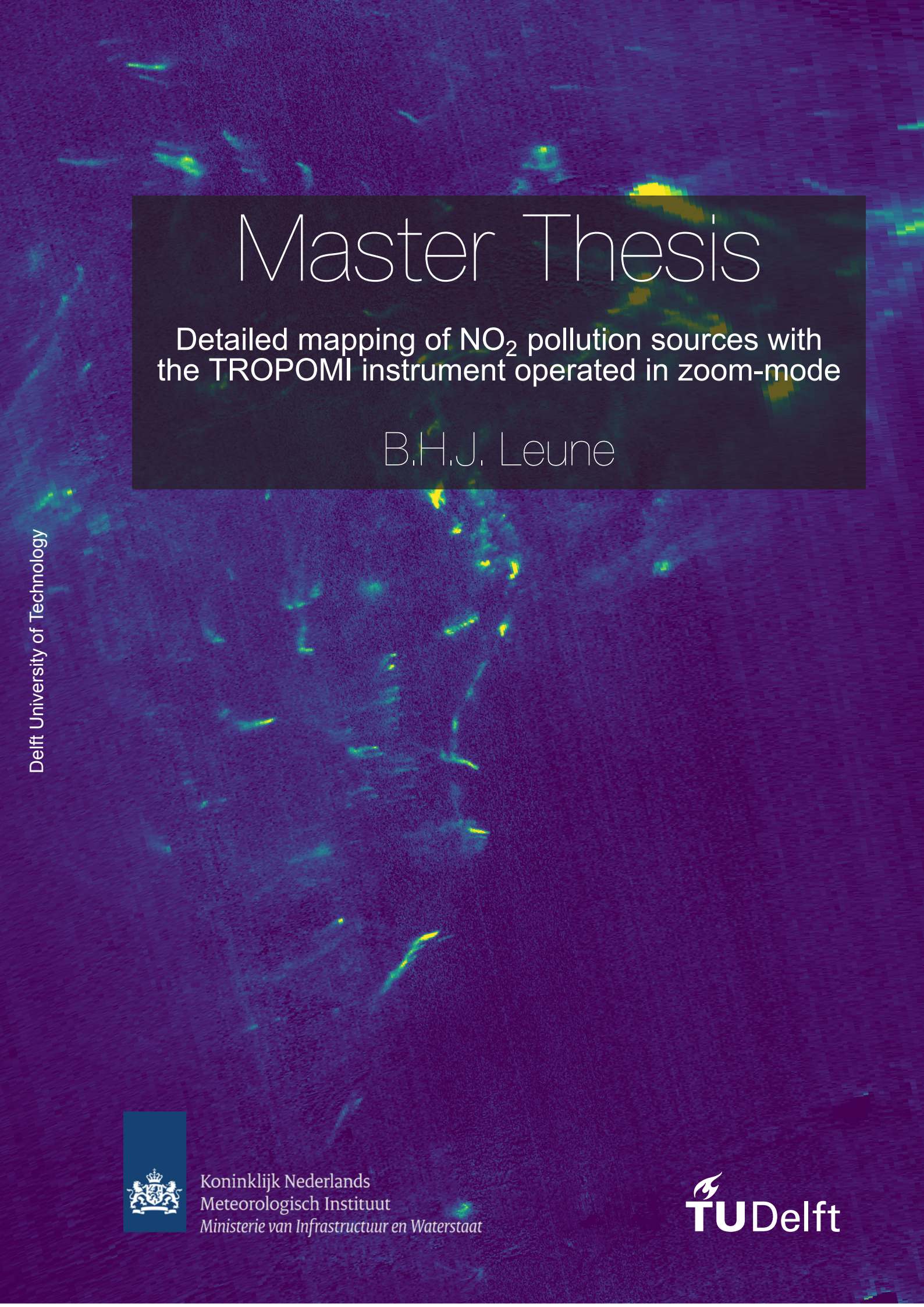

Master Thesis

Detailed mapping of NO_2 pollution sources with the TROPOMI instrument operated in zoom-mode

B.H.J. Leune

Delft University of Technology

Koninklijk Nederlands Meteorologisch Instituut
Ministerie van Infrastructuur en Waterstaat

TU Delft

Master Thesis

Detailed mapping of NO_2 pollution sources with the TROPOMI instrument operated in zoom-mode

by

B.H.J. Leune

to obtain the degree of Master of Science
at the Delft University of Technology,
to be defended publicly on Friday November 8, 2019 at 13:00 hour.

Student number:	4221125	
Project duration:	November 6, 2018 – November 8, 2019	
Thesis committee:	Dr. T. Vlemmix	KNMI, daily supervisor
	Dr. J.P. Veefkind	KNMI / TU Delft, supervisor
	Dr. D.M. Stam	TU Delft, supervisor
	Prof.dr. L.L.A Vermeersen	TU Delft, chair
	Dr.ir. J.M. Kuiper	TU Delft

Koninklijk Nederlands
Meteorologisch Instituut
Ministerie van Infrastructuur en Waterstaat

TU Delft

Abstract

Anthropogenic nitrogen dioxide (NO_2) in the troposphere is mainly produced by combustion engines in traffic, industry and energy production, and continues to affect air quality, human health and environment. Daily global measurements of tropospheric NO_2 columns are obtained by satellites with increasing spatial resolution and signal-to-noise levels, to improve monitoring of emission sources and air quality forecasting. The recently launched TROPOMI instrument on-board ESA's Sentinel-5 Precursor satellite measures tropospheric NO_2 with a spatial resolution of 7.1 km by 3.6 km. During its commissioning phase, the instrument was temporarily operated in 'zoom-mode' to measure at a resolution of 2.4 km by 1.8 km. This research presents the processed results from this unique data-set, which allows mapping NO_2 pollution sources from space with unprecedented detail. Comparison to measurements at operational resolution shows the improvement in spatial information content, at the cost of increased noise and uncertainty. The benefits and possibilities of measuring tropospheric NO_2 at high resolution are explored with several case studies. Comparisons with chemical transfer model forecasts show the improved ability of these measurements to capture local NO_2 enhancements and possibly improve emission inventories. The found correlations with co-located space-borne CO_2 column observations and the performance of a plume detection algorithm applied to the data-set provide additional support for simultaneous high resolution measurements of co-emitted CO_2 and NO_2, planned for future satellites to improve CO_2 emission monitoring. Finally, test retrievals with the zoom-mode data, using experimental high resolution surface reflectivity and NO_2 profile shape input, demonstrate the potential impact of high resolution a priori databases on the retrieval performance.

Preface

This master thesis is part of an individual Double Master's Degree programme, combining the Space Flight track from the Aerospace Engineering MSc programme at the Faculty of Aerospace Engineering with the Geoscience and Remote Sensing track from the Applied Earth Sciences MSc programme at the Faculty of Civil Engineering and Geosciences, both at TU Delft. The thesis research took place at the R&D Satellite Observations department of the KNMI (Royal Netherlands Meteorological Institute). The project lasted from November 2018 to November 2019.

First of all, I would like to thank the RDSW department of the KNMI for giving me the opportunity to do my research with them during the past year. I wish to thank Tim, my daily supervisor at the KNMI, for introducing me to the topic and providing me with advice, guidance and lots of enthusiasm. I would like to thank Maarten, Robert and the colleagues at DLR for transferring the terabytes of TROPOMI zoom mode data to the KNMI in creative ways. I also want to thank Maarten for showing me the ropes of the TROPOMI processing software, helping me to solve bugs and other advice. I would like to thank Henk for doing a NO_2 model run for me and providing me with the ECMWF data and John for providing me with the CAMS model data. Furthermore, I want to thank Daphne and Pepijn, my university supervisors, for their constructive feedback during the project and the rest of my thesis committee members for their contributions and efforts. I thank the other interns at the department for the nice lunch walks and the occasional ice cream we have had. Finally, I want to thank Eva for keeping me company in the second class compartment on the many train rides during this project.

Enjoy the read!

Benjamin Leune
Delft, October 2019

Contents

List of Figures

List of Tables

List of Abbreviations

AAI	Aerosol absorption index
AMF	Air mass factor
CAMS	Copernicus Atmospheric Monitoring Service
CCD	Charged-coupled device
CH_4	Methane
CKD	Calibration Key Data
CMOS	Complementary metal–oxide–semiconductor
CO	Carbon mono-oxide
CO_2	Carbon dioxide
CTM	Chemical transport model
DAK model	Doubling-Adding KNMI (DAK) radiative transfer model
DEM	Digital elevation model
DISAMAR	Determining Instrument Specifications and Analyzing Methods for Atmospheric Retrieval
DOAS	Differential Optical Absorption Spectroscopy
DOMINO	Dutch OMI NO_2
EC	European Commission
ECMWF	European Centre for Medium-Range Weather Forecasts
EEA	European Environmental Agency
ENVISAT	Environmental Satellite
ESA	European Space Agency
FRESCO	Fast Retrieval Scheme for Clouds from Oxygen absorption bands

GCM	General Circulation Model
GMES	Geostationary Environmental Monitoring Spectrometer
GMES	Global Monitoring for Environment and Security, now called Copernicus
GOME	Global Ozone Monitoring Experiment
GRIB	General Regularly-distributed Information in Binary form
H_2O	Water
HCHO	Formaldehyde
HNO_2	Nitrous acid
HNO_3	Nitric acid
ICID	Instrument configuration ID
IPCC	Intergovernmental Panel on Climate Change
ISRF	Instrument spectral response function
KNMI	Royal Netherlands Meteorological Institute (Koninklijk Nederlands Meteorologisch Instituut)
LER	Lambertian equivalent reflectance
LUT	Look-up table
MAX DOAS	Multi AXis DOAS
MODIS	Moderate-resolution Imaging Spectroradiometer
N_2O	Nitrous oxide
NASA	National Aeronautics and Space Administration
NetCDF	Network Common Data Form
NIR	Near-infrared
NISE	Near-real-time Ice and Snow Extent
NO	Nitrogen oxide
NO_2	Nitrogen dioxide
NO_x	Nitrogen oxides
NO_y	Oxidised nitrogen
NRT	Near real time
NSO	Netherlands Space Office
$O(^3P)$	Atomic oxygen
O_2	Oxygen
O_3	Ozone
OCO-2	Orbiting Carbon Observatory 2
OFFL	Offline
OMI	Ozone Monitoring Instrument
PAN	Peroxyacyl nitrate
PM	Particulate matter
QA value	Quality assurance value

QA4ECV	Quality Assurance for Essential Climate Variables
RO_2	Aldehydes
RPRO	Re-processing
S5P	Sentinel-5 Precursor
SCD	Slant column density
SCIAMACHY	European SCanning Imaging Absorption SpectroMeter for Atmospheric ChartographY
SNR	Signal-to-noise ratio
SO_2	Sulfur dioxide
SRON	Netherlands Institute for Space Research
Suomi-NPP	Suomi National Polar-orbiting Partnership
SWIR	Short-wave infrared
SZA	Solar zenith angle
TEMPO	American Tropospheric Emissions: Monitoring of Pollution
TM5-MP	Trace Model 5 massively parallel version
TOA	Top of the atmopshere
TOMS	Total Ozone Mapping Spectrometer
TROPOMI	TROPOspheric Monitoring Instrument
UV	Ultaviolet
VCD	Vertical column density
VIIRS	Visible/Infrared Imager and Radiometer Suite
VIS	Visible
VOC	Volatile organic compound
VZA	Viewing zenith angle
WHO	World Health Organisation
XCO_2	Vertical CO_2 column

1

Background and Introduction

Nitrogen oxides (NO_x) is the common name of nitrogen oxide (NO) and nitrogen dioxide (NO_2), which are trace gases affecting air quality. Anthropogenic NOx in the troposphere is primarily produced by combustion engines, mainly motor vehicles, shipping, power stations and (heavy) industry. Satellite measurements of tropospheric NO_2 columns can be used to monitor and forecast air quality, and to estimate the NO_x emission of pollution sources. Using satellite measurements in a so called 'top-down' or 'inversion' emission estimation approach, which often makes use of a chemical transport model, could be used to verify the emission inventories provided by governments and industry, called the 'bottom-up' approach, which may not be temporally resolved sufficiently enough or may not include all sources. The TROPOMI instrument aboard the Sentinel-5 Precursor satellite, launched October 2017, is providing a significant step forward to high spatial and temporal resolution NO_2 measurements with its daily global coverage, nadir ground pixel size of approximately 7 x 3.5 km and signal-to-noise ratio (SNR) in the NO_2 band of 1400-1500.

During the commissioning phase between 01-03-2018 and 07-03-2018 of the TROPOMI instrument, measurements were performed in a 'science zoom' mode with the detector bands required for NO_2 retrievals. Through modification of instruments settings, such as the detector binning scheme and integration time, the spatial resolution in nadir was increased to 2.4 x 1.8 km, a factor 6 better than the nominal resolution. The zoom mode settings caused the swath-width to be narrower due to limited CCD read-out data rates as well as a lower SNR because of less averaging on the detector. This master thesis research project will focus on the processing, analysing and interpreting this unique data-set and gaining new insights from it for future space-borne NO_2 measurements at high spatial resolution.

This chapter introduces the reader to the theory and background relevant to this thesis study. First, the atmospheric trace gas NO_2 and its role in air quality will be discussed in Section 1.1. The history of measuring atmospheric trace gases with ground-based and space-borne instruments is covered in Section 1.2. The underlying technique for retrieving trace gas columns, specifically for the UV-VIS-NIR part of the spectrum, is discussed in Section 1.3. The mission and instrumental characteristics and processing chain of the instrument at hand, TROPOMI, is introduced in Section 1.4. An overview of the used NO_2 retrieval algorithm for TROPOMI is given in Section 1.5. Uncertainty estimation in the NO_2 retrieval is covered

in Section 1.6. Section 1.7 mentions the chemical transfer models relevant to this thesis. Section 1.8 provides some insights regarding the role of spatial resolution in satellite-based NO_2 measurements. Advances in enhancing CO_2 emission quantification using NO_2 data for plume detection are listed in Section 1.9. An overview of future missions relevant to this study is given in Section 1.10. Finally, Section 1.11 provides the outline of this thesis: the scope, relevance and research questions.

1.1 Nitrogen oxides

Nitrogen oxides (NO_x), the name given to nitrogen oxide (NO) and nitrogen dioxide (NO_2) combined, are an important trace gas species in atmospheric chemistry. These gases can be found in the troposphere and in the stratosphere. NO_x is emitted in the troposphere mainly as NO (95%) by anthropogenic sources, which are predominantly combustion engines that run on fossil fuels, but also biomass burning. Figure 1.1 shows the contribution per sector to the total NOx emissions in Europe, where the road transport sector is the main contributor. During the combustion of fuel, high temperatures arise, which starts the reaction between nitrogen and oxygen, producing nitrogen oxide. This reaction follows the (extended) Zel'dovich mechanism, first discovered by Zeldovich et al. (1947), described in the following equations:

$$\begin{aligned} N_2 + O &\longrightarrow NO + N, \\ N + O_2 &\longrightarrow NO + O, \\ N + OH &\longrightarrow NO + H \end{aligned} \tag{1.1}$$

NO_x can also be produced by natural sources, such as soils, wildfires and lightning (Murray, 2016).

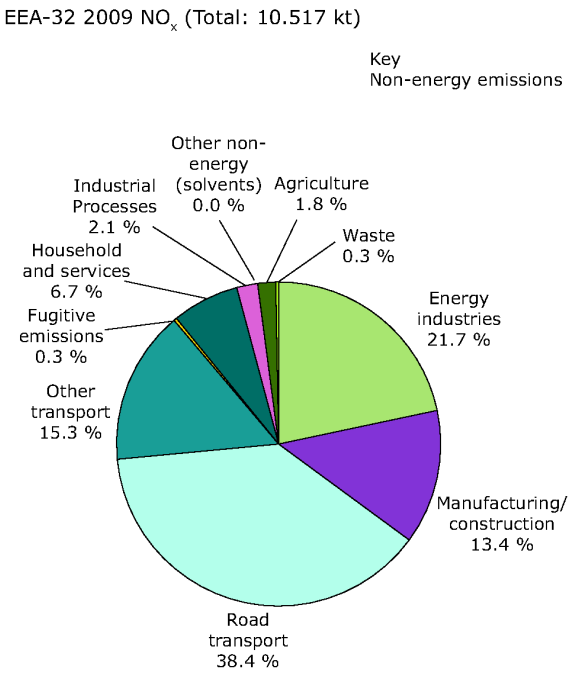

Figure 1.1: Contribution per sector to NOx emissions in the EEA-32, 2009. Source: European Environmental Agency.

After emission, NO reacts with tropospheric O_3 (ozone) to form NO_2 on a time-scale of minutes. In the presence of sunlight, the produced NO_2 is photolysed to NO, which releases $O(^3P)$ (atomic oxygen) and reacts with O_2 (oxygen) to form O_3. The produced O_3 reacts with NO to form NO_2, completing the photochemical cycle. This mechanism is described by the Leighton relationship as following (Jacob, 1999):

$$\begin{aligned} NO_2 + h\nu &\longrightarrow NO + O(^3P), \\ O(^3P) + O_2 + M &\longrightarrow O_3 + M, \\ NO + O_3 &\longrightarrow NO_2 + O_2 \end{aligned} \tag{1.2}$$

The reaction rates of NO, NO_2 and O_3 depend on their concentration and the amount of solar radiation, which creates a diurnal cycle. For example, urban areas experience a NO_x peak in the morning due to rush hour and lack of solar radiation and an O_3 peak around mid-day when the solar intensity increases.

NO_x can also react with volatile organic compounds (VOCs), the common name of organic chemical compounds that evaporate under room temperature, to form one of the main components of smog: peroxyacyl nitrate (PAN). The other main component being ozone. Nitrogen oxides are mostly removed from the atmosphere by dry deposition of nitric acid (HNO_3), formed by the reaction of NO_2 with hydroxyl (OH radicals) or nitrate (NO_3^-). A simplified overview of the various reactions oxidized nitrogen (NO, NO_2 and HNO_3 together, called NO_y) can undergo in the atmosphere is given in Figure 1.2.

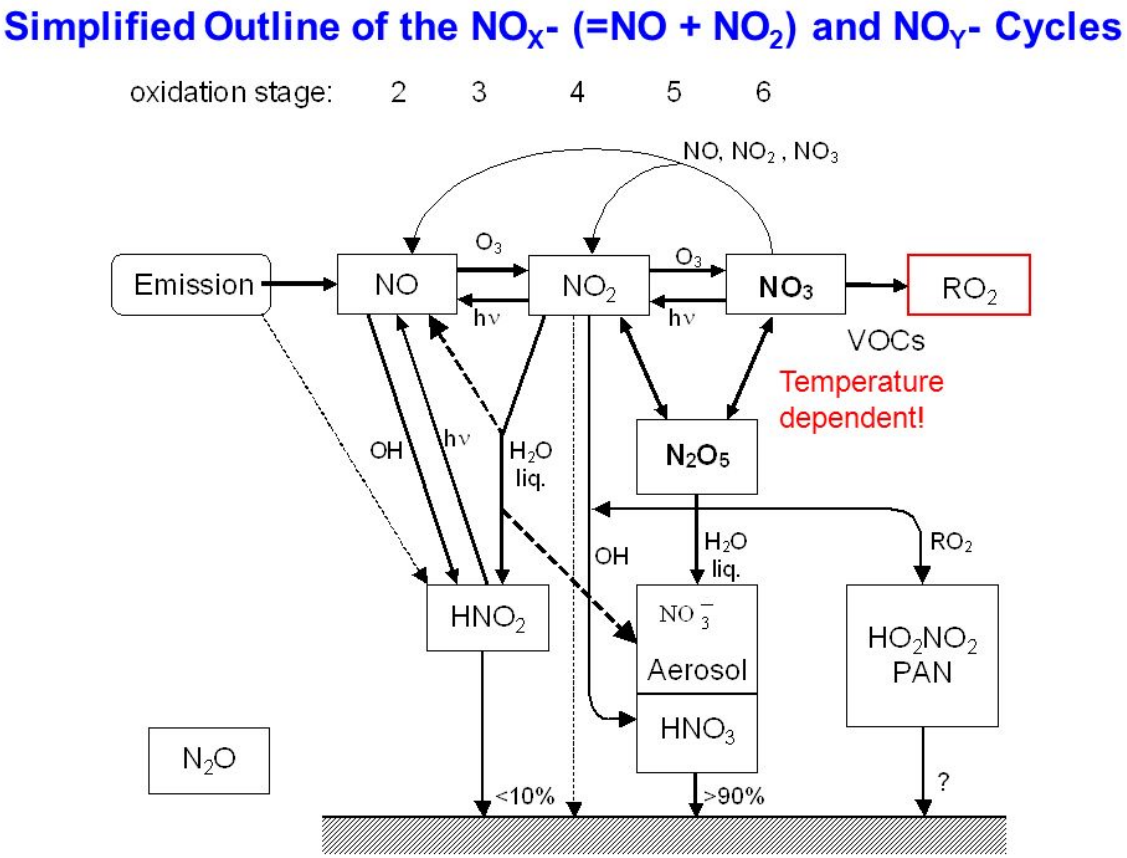

Figure 1.2: Simplified overview of the various reactions of oxidized nitrogen (NO_y) in the atmosphere, obtained from Platt and Stutz (2008): emitted NO_x (nitrogen oxides) forming O_3 (ozone) and secondary pollutants HNO_2 (nitrous acid), HNO_3 (nitric acid), RO_2 (aldehydes)(temperature dependent) and peroxyacyl nitrates (PANS).

NO_2 itself is a toxic pollutant, just like tropospheric ozone and other secondary products from NO_2 (Mauzerall et al., 2005). These pollutants have adverse health effects, for example potential lung growth issues in children (Arther et al., 2003) and premature mortality (Dockery et al., 1993). The European Environmental Agency (EEA) estimated in their latest Air Quality in Europe report (European Environment Agency, 2018) that NO_2 alone was the cause of 1900 premature deaths and/or 119 lost years of life per 100,000 inhabitants in the Netherlands in 2015. The European standards, adopted from the WHO (World Health Organisation) air quality guidelines, for NO_2 ground concentration are an hourly value of 200 $\mu g/m^3$ and yearly average of 40 $\mu g/m^3$ (European Environment Agency, 2018).

Furthermore, NO_x is a precursor of tropospheric ozone, which is considered an air pollutant (European Environment Agency, 2018) and a greenhouse gas. Not only humans, but also nature can be harmed by NO_x emissions. NO_x emissions lead to increased atmospheric deposition of oxidized nitrogen, which causes eutrophication of ecosystems (Bouwman et al., 2002). For example, an abundance of nitrogen in natural waters causes plants to flourish, leading to oxygen depletion, causing starvation of fish and other water animals.

Besides affecting air quality, NO_2 emissions have a net cooling effect on the climate. NO_2 itself is a weak greenhouse gas, however, several atmospheric constituents produced by NO_2 emissions do have an effect on the climate. The tropospheric ozone produced by NO_2 emissions has a positive radiative forcing and causes warming (Fuglestvedt et al., 1999). However, NO_x influences the amount of OH radicals and thereby reduces the methane (CH_4) concentration, which decreases radiative forcing. Both these effects are approximately equal in magnitude and cancel each other out, however, the methane effect occurs on a global scale on a time scale of decades, while the ozone effect occurs regionally with a time span of weeks (Fuglestvedt et al., 1999). Finally, direct and indirect aerosol radiative effects from the aerosols created by NO_x emissions, i.e. nitrate aerosols, result in a net negative radiative forcing (Shindell et al., 2009). Furthermore, NO_2 abundances can be considered a proxy for emissions of the greenhouse gas CO_2, or other pollutants such as particulate matter (PM) and carbon mono-oxide (CO), since these are also emitted by combustion engines and power plants (Bryan N. Duncan, 2015).

NO_x in the troposphere has a relative short life-time of a few hours to half a day, dependent on the amount of solar radiation and OH. For example, areas near the equator experience a relative high solar flux, thus shortening the life-time due to the increased photochemistry rates. Furthermore, NO_x is emitted by inhomogenously distributed sources, for example power plants, factories and traffic. This makes it possible to attribute emitted pollutants to their sources using remote sensing from space. NO is primarily emitted and within minutes to hours a photo-stationary equilibrium is achieved with NO_2, which shifts between day and night. Therefore, a measure of NO_2 is a robust measure for the amount of nitrogen oxides. Figure 1.3 shows the tropospheric NO_2 column (total abundance in the lowest vertical layer of the atmosphere, see Figure 1.4) over Europe, averaged over April 2018, as measured by TROPOMI. In this figure, the pollution in the Netherlands, Belgium and the Ruhr area stands out compared to the rest of Europe due to the large extent of the connected area with increased NO_2 values. Local NO_x concentrations in cities such as Paris, Moscow, London are significantly higher, however, covering a smaller area and thus less visible in this figure.

NO_2 in the stratosphere is formed by the oxidation of nitrous oxide (N_2O), emitted by the soil. In the stratosphere, NO_2 could be linked to destruction and/or creation processes of ozone (e.g. Hendrick et al., 2012). The NO_2 amount present in the stratosphere varies due to atmospheric dynamics. In clean areas the stratospheric contribution dominates the total atmospheric column, while in polluted regions the tropospheric contribution is significantly larger.

The troposphere is the lowest vertical layer of the atmosphere, which ends at approximately 11 km with the tropopause, where the stratosphere begins (see Figure 1.4). The part of the troposphere closest to the surface is called the planetary boundary layer (PBL), depicted in Figure 1.5, of which the temperature, moisture and wind is influenced by interaction of the air with the Earth's surface. Friction of the wind with the terrain and solar radiative forcing causes turbulence in this layer which leads to strong vertical mixing of the air (and pollutants) throughout the layer. The PBL is of variable height and is capped by an inversion layer, with a stable layer above, called the free atmosphere (or free troposphere).

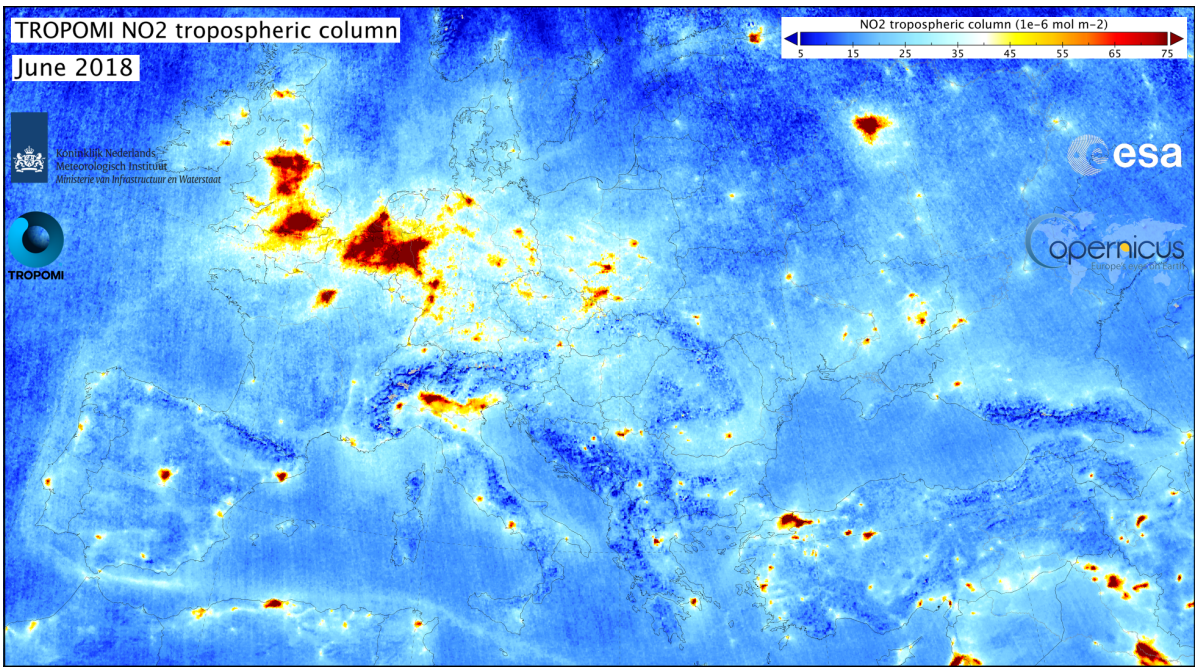

Figure 1.3: Monthly average tropospheric NO_2 columns over Europe, April 2018, derived from TROPOMI measurements. Obtained from van Geffen et al. (2019).

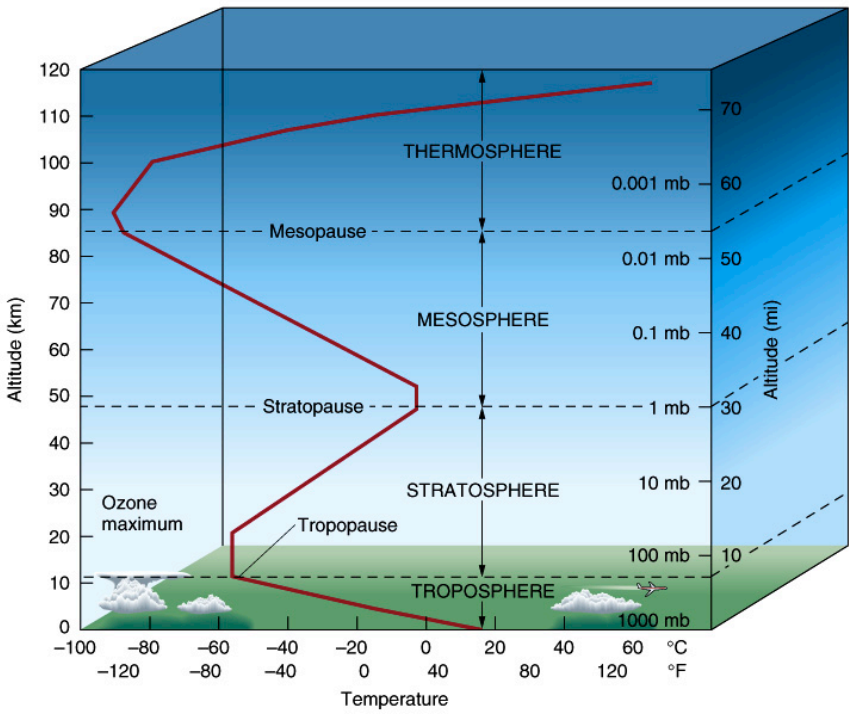

Figure 1.4: Vertical structure of the standardized atmosphere of Earth, obtained from Aguado and Burt (2013).

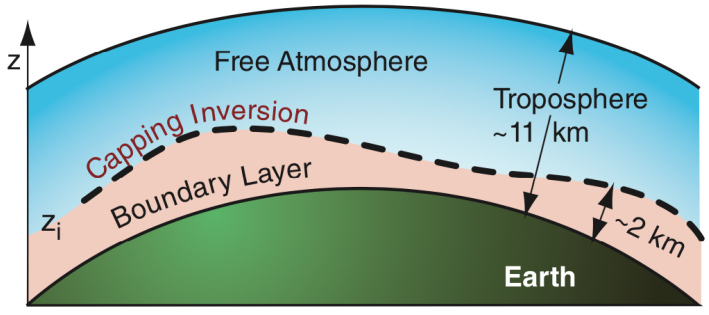

Figure 1.5: Division of the troposphere into boundary layer and free atmosphere/troposphere, adapted from Stull and Ahrens (2000).

1.2 Heritage remote sensing of atmospheric trace gases

Retrieval techniques in the ultraviolet, visible, near-infrared (UV-VIS-NIR) part of the spectrum relate spectral signatures in scattered and/or reflected sunlight directly to absorption spectra from atmospheric gases or particles. In this spectral range thermal emission features are insignificant and can be neglected (Burrows et al., 2011). The observed spectra from space are affected by constituents in the entire atmosphere, i.e. from the surface to the top of the atmosphere, and thus give information about the composition of an entire atmospheric column. Usually little to no information is obtained from space-borne measurements on the vertical distributions of trace gases.

In 1924 Dobson invented a new spectrometer, which was the first instrument able to measure the total column of atmospheric ozone (Dobson, 1957) from the ground. Later on, Alan Brewer was the first to measure the atmospheric NO_2 vertical density column in 1973 using his newly developed spectrometer (Brewer et al., 1973), based on the Dobson spectrometer. Brewer used it to measure radiances at wavelengths around 450 nm, a spectral region where NO_2 absorption occurs, however, strongly varying. In 1976 the DOAS (Differential Optical Absorption Spectroscopy) method was invented (Platt et al., 1979). This method would fit the absorption spectra of multiple trace gases simultaneously, after removing the low frequency signal from the spectrum. In this way spectral interference of multiple trace gas absorption signatures would be avoided. After the discovery of the ozone hole in 1985, a network of Brewer instruments was used to monitor stratospheric NO_2, which is involved in the stratospheric ozone chemistry. Nowadays, ground measurements are being performed, often measuring at a range of line of sights to retrieve information on the vertical distribution within the troposphere, called Multi AXis DOAS (MAX DOAS) observations.

The first atmospheric trace gas observations from space were done in 1970 by the US satellite Nimbus 4 (Heath et al., 1973), which measured ozone similarly to the Dobson instruments. Then came the TOMS (Total Ozone Mapping Spectrometer) instruments, which continuously mapped the ozone layer between 1979 and 1992, focusing on the state of the ozone hole (Bowman and Krueger, 1985). The first DOAS instrument in space was the European Global Ozone Monitoring Experiment (GOME) in 1995, which measured a wide spectrum compared to the previous instruments (Burrows et al., 1999). Using the DOAS method many trace gases and other atmospheric properties could be measured, such as NO_2, HCHO, SO_2, aerosols, clouds, et cetera. With the launch of the European SCanning Imaging Absorption SpectroMeter for Atmospheric ChartographY (SCIAMACHY) in 2002, it was possible for the first time to measure several greenhouse gases (CO_2, CH_4, N_2O) and CO from space (Bovensmann et al., 1999). The spatial resolution until then was relatively coarse, which changed with the Ozone Monitoring Instrument (OMI) in 2004, which had a spatial resolution of 13 x 24 km in nadir (Levelt et al., 2006). In combination with daily global coverage, OMI gave insight into the spatial and temporal variability of trace gases. Newer versions of the GOME instruments, the GOME-2 series, have been launched in 2006. The successor of OMI is TROPOMI, launched in 2017, further increasing the capabilities to image trace gases in the atmosphere (see Section 1.4). This thesis is based on a special data-set obtained by the most recent instrument: TROPOMI.

1.3 Retrieval of trace gas columns in the UV-VIS-NIR

The spectral regions to which trace gas retrievals are applied are: the ultra-violet, visible and near-infrared bands. Figure 1.6 shows a solar irradiance spectrum measured at the top of the atmosphere and at the surface of the Earth. The maximum energy from the Sun is located at the visible wavelengths, which is the spectral region our eyes are sensitive to. As light propagates through the atmosphere, some of it is absorbed by gases at specific wavelengths, visible in the figure as absorption bands. Furthermore, scattering events can occur, modifying the light path of the incoming light. For example, Rayleigh scattering by molecules which gives the sky its blue colour, or scattering by aerosols or clouds which can be seen sometimes as haze. Figure 1.7 illustrates the different absorption, scattering and reflection effects in the atmosphere and at the surface. Trace gases, such as NO_2, CO_2, SO_2, etc., have a very low concentration and a relatively small spectral fingerprint. Retrieval algorithms try to eliminate all other factors modifying the solar spectrum, just leaving the absorption signature of the target trace gas to estimate the amount of that trace gas in the atmosphere. The measurement geometry of backscattered radiation measurements by satellites is depicted in Figure 1.8. This section discussed the different steps taken in the trace gas retrieval algorithms: the DOAS spectral fitting technique, the separation of the stratospheric and tropospheric signal and the conversion of slant to vertical columns.

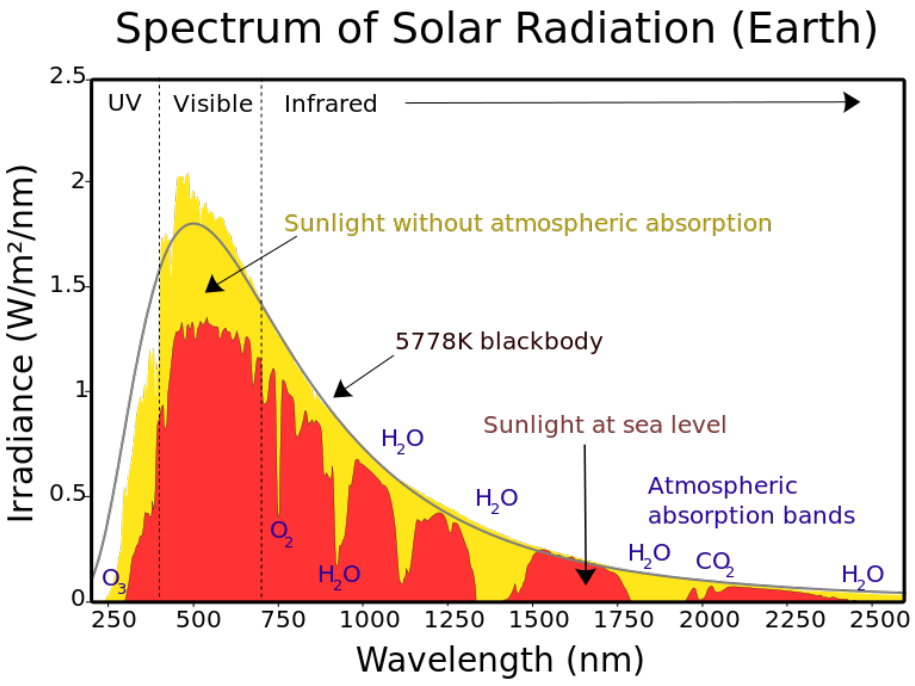

Figure 1.6: Solar irradiance spectrum at top of atmosphere (TOA) in yellow and at the Earth's surface in red, source: Wikipedia https://commons.wikimedia.org/wiki/File:Solar_spectrum_en.svg.

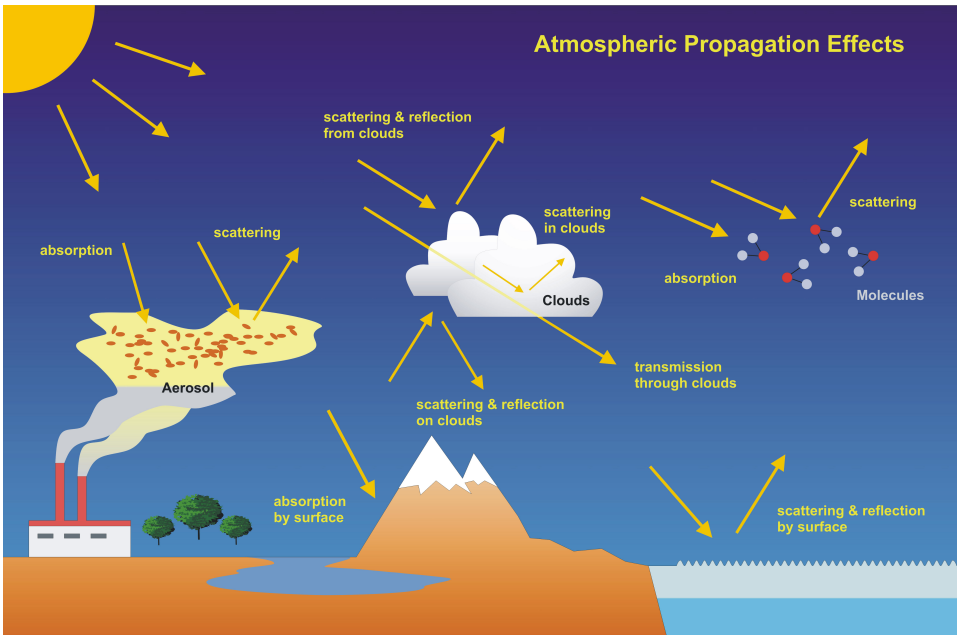

Figure 1.7: Light path interactions in the atmosphere, courtesy: DLR-IMF.

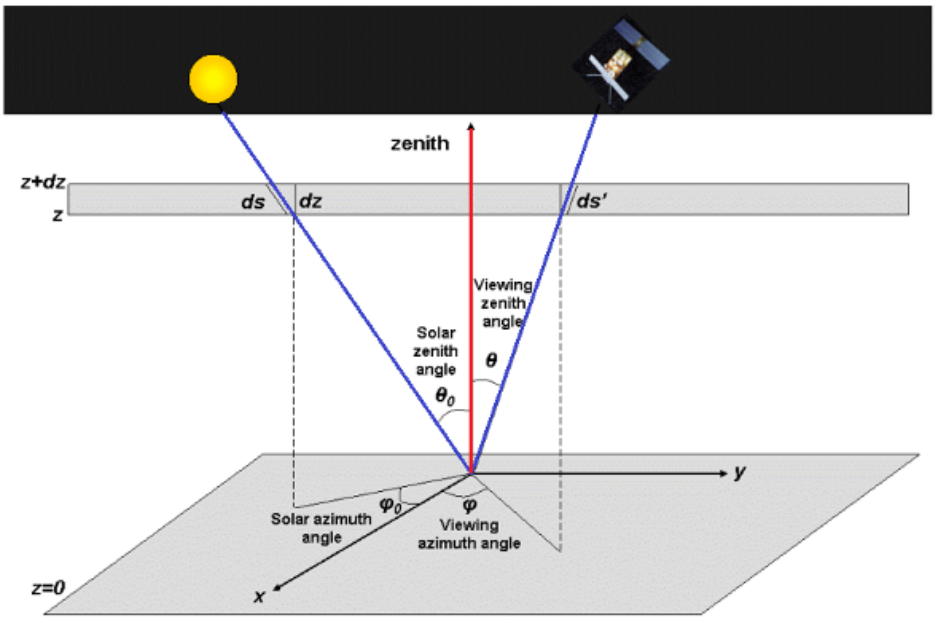

Figure 1.8: Geometry of satellite radiation measurements, source: ESA https://earth.esa.int/web/sentinel/technical-guides/sentinel-5p/level-2/doas-method. z denotes the height, dz the infinitesimal height difference of a layer in the atmosphere and ds the infinitesimal light path length for that layer.

1.3.1 DOAS technique

The starting point for retrievals of some suitable atmospheric trace gases columns in the UV-VIS-NIR spectral region from solar back scattered radiation is the Lambert-Beer law (Burrows et al., 2011):

$$dI(\lambda) = -I(\lambda)\sigma(\lambda)\rho(s)ds \tag{1.3}$$

where:

λ = wavelength
dI = change in light intensity
σ = absorption and scattering cross-section
ρ = absorber number density
ds = infinitesimally small light path element

We will limit ourselves to retrievals for nadir viewing space-borne measurements. Equation 1.3 is then integrated along the light path, the path the light follows from the sun through the atmosphere, reflected by the surface (or ocean, water, clouds, etc.), again through the atmosphere, into the satellite instrument (depicted in Figure 1.8). Along the way, trace gases absorb a tiny part of the light, leaving behind a spectral fingerprint. Scatterers, such as molecules, aerosols or cloud droplets, can absorb or reflect the light into a different direction, out of the light path or into the light path. An illustrative overview of the different interactions of the light in the atmosphere is given in Figure 1.7. The absorption and scattering cross-section quantifies the probability that a particle will absorb or scatter incident light at a specific wavelength, as illustrated in Figure 1.9. The radiation is measured at a certain band of wavelengths, where in the spectrum the target trace gases show the most pronounced differential absorption features.

Assuming only one gas is a significant absorber, Equation 1.3 can be rewritten into the integrated form:

$$I(\lambda) = c(\lambda)I_0 e^{-\int \sigma(\lambda)\rho(s)ds} \tag{1.4}$$

where:

c = scattering efficiency; the effect of surface reflectance, scattering events and clouds combined
I_0 = initial light intensity (Sun)

The number density ρ integrated along the light path s is called the slant column density SCD, which is the parameter we want to retrieve:

$$SCD = \int \rho(s)ds \tag{1.5}$$

Taking into account the Rayleigh and Mie scattering and absorption (together called extinction), and assuming the absorption cross-sections not to vary along the light path, Equation 1.4 expands to:

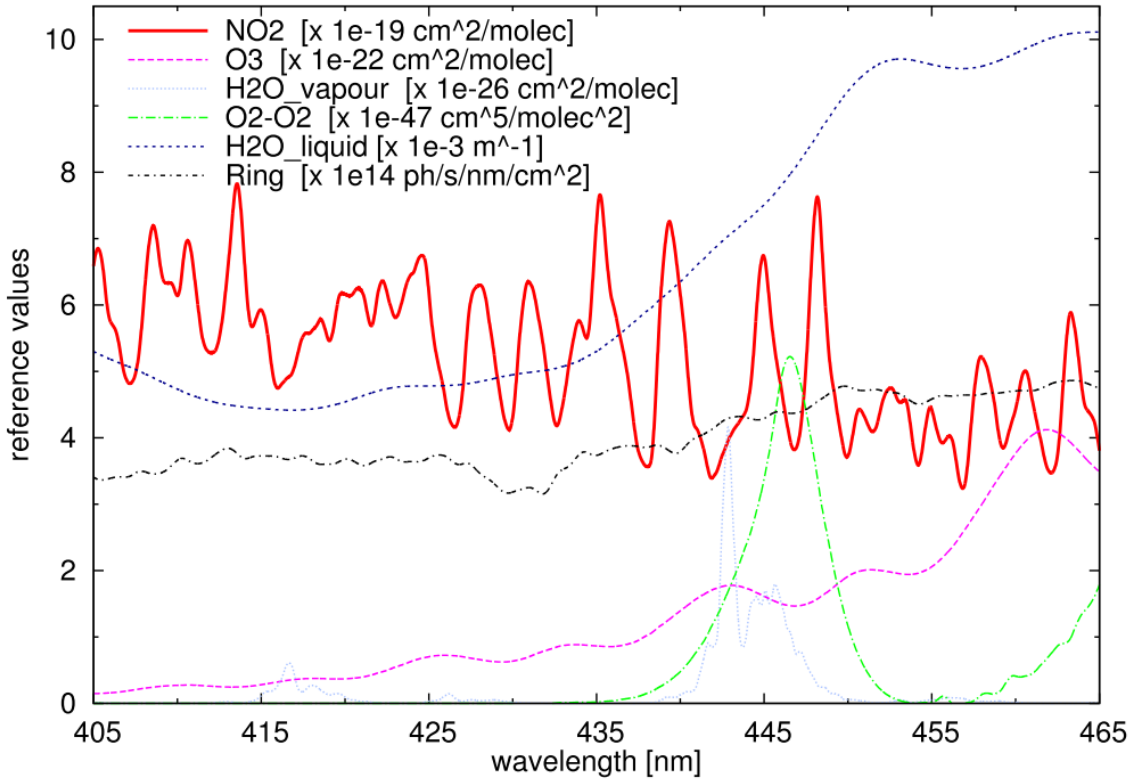

Figure 1.9: Absorption cross-section spectra of NO_2, O_3, water vapour, O_2-O_2, liquid water and the Ring spectrum, the pseudo-absorber accounting for the Ring effect (inelastic rotational Raman scattering). Reference spectra have been scaled to make them visible in one plot. Obtained from van Geffen et al. (2019).

$$I(\lambda) = cI_0(\lambda)exp\left(-\sum_i \sigma_i(\lambda)SCD_i - \sigma_{Rayleigh}(\lambda)SCD_{Rayleigh} - \sigma_{Mie}(\lambda)SCD_{Mie}\right) \tag{1.6}$$

Where the SCD is inserted according to Equation 1.5 and the different absorption trace gases are denoted by index i.

The Differential Optical Absorption Method (DOAS) technique now comes into play, as the cross-sections of the absorbers will be separated into a low and high frequency part. The high frequency part, called the differential component, contains the absorption feature from the trace gases and will be used for the retrieval. The low frequency part, called the continuum component, is fitted with a low order polynomial and subtracted, and serves as a closure term. In this way, signatures of weak absorbers (such as NO_2) can be retrieved, which decrease the light intensity only by a few percents. The choice of wavelength fitting window is a trade-off of including as many differential absorption structures of the target molecule as possible, while keeping the window narrow to reduce the impact of interfering signals. Furthermore, scattering effects are not constant over a large spectral range, which would cause errors due to light path differences. For example, the TROPOMI NO_2 fitting window is between 405 and 465 nm.

$$\sigma(\lambda) = \sigma^*(\lambda) + \sigma'(\lambda) \tag{1.7}$$

where:

$\sigma^*(\lambda)$ = continuum part
$\sigma'(\lambda)$ = differential part

Substitution in Equation 1.6 gives:

$$\begin{aligned} I(\lambda) =& cI_0(\lambda) \cdot exp\left(-\sum_i \sigma_i'(\lambda) SCD_i - \sum_i \sigma_i^*(\lambda) SCD_i \right. \\ & \left. -\sigma_{Rayleigh}(\lambda) SCD_{Rayleigh} - \sigma_{Mie}(\lambda) SCD_{Mie} \right) \end{aligned} \tag{1.8}$$

The Mie and Rayleigh scattering can be captured with the same polynomial as for the continuum trace gas absorption component, resulting in:

$$I(\lambda) = cI_0(\lambda) exp\left(-\sum_i \sigma_i'(\lambda) SCD_i - \sum_n a_n \lambda^n \right) \tag{1.9}$$

Where n is the order of the fitting polynomial. The left-hand-side of the equation can be rewritten as the optical depth, defined as $ln(I_0/I)$:

$$ln \frac{I_0(\lambda)}{I(\lambda)} = \sum_i \sigma_i'(\lambda) SCD_i + \sum_n c_n \lambda^n \tag{1.10}$$

The scattering efficiency is captured by the polynomial as c_p. Systematic errors in the intensities (I and I_O) measured by the same instrument are cancelled out in this equation, which lowers the requirements for the radiometric calibration of the instrument. This linear relation can be set up for all wavelengths in the measurement, creating a linear system of equations which can be solved using a least-squares technique. This allows for retrieval of SCD's of multiple trace gases simultaneously in a fast manner. Uncertainty in the slant columns arise from instrument noise and spectral fitting errors. For NO_2 the uncertainty in the SCD is in the order of 10%.

1.3.2 Separating the stratospheric and tropospheric signal

The DOAS retrievals do not provide vertical profile information of the trace gas and thus the stratospheric and tropospheric signals (for relevant gases) are combined in the slant column density. Separating these signals is possible by using limb measurements of the stratosphere (Rozanov et al., 2005), as performed by SCIAMACHY. However, current trace gas instruments are restricted to nadir measurements, thus one usually relies on approximations. For example, using chemical transport models (CTM's) in combination with assimilated observations over remote regions to simulate the stratospheric NO_2 field. The tropospheric slant column can then be calculated by subtracting the estimated stratospheric column from the measured total slant column.

1.3.3 Converting to vertical column density using air-mass factors

The next step in the NO_2 retrieval scheme is to convert the tropospheric and stratospheric slant column densities into their respective vertical column density (VCDs). The air mass factor (AMF) is the ratio between the SCD and VCD, see Equation 1.11, thus essentially the ratio between the light path of the incident sunlight to the satellite, and the light path vertically up from the measurement location (Burrows et al., 2011). For a measurement with negligible atmospheric scattering and only backscatter of the Earth's surface, this quantity is primarily determined by the viewing geometry: the solar zenith angle (SZA) and the viewing zenith angle (VZA) of the satellite, see Equation 1.12 (neglecting the Earth's curvature). Since the light path crosses the atmosphere twice, the geometric AMF is always larger than 2.

$$AMF = \frac{SCD}{VCD} \tag{1.11}$$

$$AMF_{geometric} = \frac{1}{\cos(SZA)} + \frac{1}{\cos(VZA)} \tag{1.12}$$

However, some radiation is scattered out of the light path or into the light path on its way through the atmosphere. Scattering events thus alter the average light path and have an effect on the AMF. Trace gases, including the target trace gas, also alter the light path through scattering. Furthermore, the surface albedo has an effect on the AMF computation since this determines the amount of light reflected by the surface. A higher albedo will increase the sensitivity close to the surface, because relatively more light paths have gone through the surface layer due to more light being reflected off the surface. This effect is shown in Figure 1.10, where the increase in sensitivity per increase of albedo is the highest for low albedo surfaces and decreases for increasing albedo. The AMF in Equation 1.11 is usually referred to as the *total* AMF.

The *box*-AMF or altitude-dependent AMF quantifies the measurement sensitivity as function of altitude. This is used to express the contribution of a certain layer to the total measurement. For example, when an optically thick cloud or aerosol layer is present, the measurement becomes less sensitive to the trace gas below the layer. Figure 1.11 shows an example of a vertical profile of a box-AMF and the dependency of the wavelength and albedo. Figure 1.10 illustrates this further, showing the dependency of the box-AMF for varying albedos. For optically thin absorbers it can be assumed that the light path does not depend on the absorber concentration. This simplification allows for Equation 1.13, where the total AMF can be calculated from the box-AMF profile ($BAMF_i$) and the trace gas profile (VCD_i) defined at vertical levels i. This equation makes it possible to pre-calculate box-AMF scenarios with a radiative transfer model for varying viewing geometry, wavelength, surface pressure, albedo, cloud and aerosol parameters in a look-up table for a fast retrieval. In the algorithm a modelled trace gas profile or profile shape (VCD_i/VCD), also called 'a priori profile', can be plugged in, resulting in a total AMF that can be used to convert the slant column to a vertical column.

$$AMF = \frac{\sum_{i=0}^{TOA} BAMF_i \cdot VCD_i}{VCD} \tag{1.13}$$

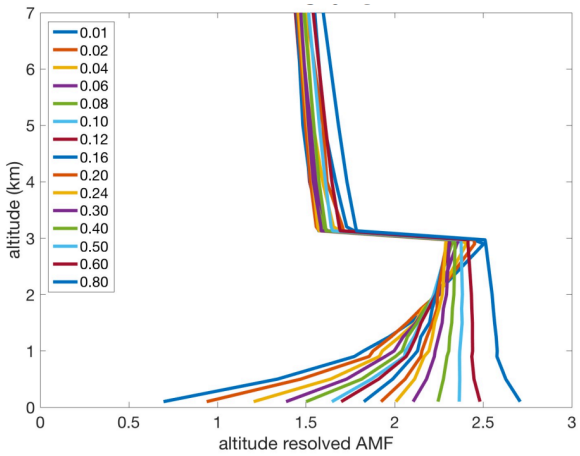

Figure 1.10: Example of the dependency of vertical profiles of box-AMF on surface albedo. Obtained from Vlemmix et al. (2017), simulated for aircraft at 3.1 km height for VZA=0°and SZA=0°.

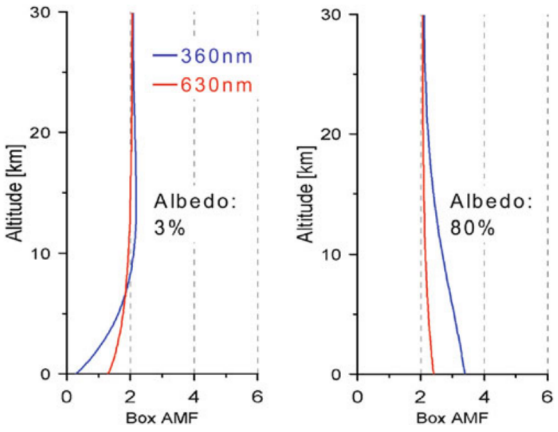

Figure 1.11: Satellite measurement height-dependent sensitivity expressed with vertical profile of box-AMF with effect of varying albedo and wavelength, obtained from Burrows et al. (2011).

Dividing the box-AMF through the total AMF results in the averaging kernel, shown in Equation 1.14. This quantity can be used to describe the vertical dependence of the measurement sensitivity for a trace gas of a certain instrument. Applying the averaging kernel to a trace gas profile simulates how the instrument would have measured the profile as a column, which allows for comparison of collocated data-sets. This quantity also removes the dependency on the a priori profile shape (Eskes and Boersma, 2003).

$$AK_i = \frac{BAMF_i}{AMF} \tag{1.14}$$

The methods described here to retrieve trace gas columns in the UV-VIS-NIR spectral region are used in the TROPOMI retrieval algorithms, of which the specifics are discussed in Section 1.5.

1.4 The TROPOMI instrument

The Sentinel-5 Precursor (S-5P) mission is part of a joint Earth observation programme by the European Commission (EC) and the European Space Agency (ESA), called Copernicus (previously known as Global Monitoring for Environment and Security (GMES)) (de Vries et al., 2016). The payload on-board, called TROPOspheric Monitoring Instrument (TROPOMI), is funded by the Netherlands Space Office (NSO) and ESA, and developed by Airbus DS Netherlands and TNO. KNMI (Royal Netherlands Meteorological Institute) and SRON (Netherlands Institute for Space Research) are principal investigators.

The mission's goal is to provide daily global information on concentrations of trace gases and aerosols, important for studies in air quality, climate forcing and the ozone layer. The instrument is to provide a continuation of data records from SCIAMACHY onboard the ENVISAT satellite and to prepare for the planned Sentinel-5 mission by measuring atmospheric constituents including ozone, nitrogen dioxide, carbon mono-oxide, methane, formaldehyde and aerosol properties with unprecedented spatial resolution (7 x 3.5 km in nadir) and signal-to-noise levels (Veefkind et al., 2012). A large improvement with relation to the 15-year old Ozone Monitoring Instrument (OMI) (Levelt et al., 2006, 2017), which had a spatial resolution of 13 x 24 km and a SNR of a factor 2-3 times lower. Furthermore, due to the smaller ground pixels, more cloud-free retrievals can be made, which reduces the error in the NO_2 estimates. The TROPOMI measurements can be used for operational services such as air quality forecasting, scientific research on climate change, monitoring emissions and for many other purposes.

The satellite was launched successfully on October 13th, 2017. The data processing has been running operationally for most products since summer of 2018. Several first results have already been presented or published and look successful: overview (Veefkind et al., 2018), CO (Borsdorff et al., 2018), CH_4 (Hu et al., 2018), NO_2 (van Geffen et al., 2018; Eskes et al., 2018a), clouds and aerosols (Stammes et al., 2018), formaldehyde (De Smedt et al., 2018), SO_2 (Theys et al., 2018) and O_3 (Lerot et al., 2018). Currently, all Level-2 data products have been released to the public, except for the ozone profile product.

1.4.1 Mission characteristics

Science goals

The TROPOMI science objectives are stated by Van Weele et al. (2008), as following:

1. *To better constrain the strength, evolution, and spatio-temporal variability of the sources of trace gases and aerosols impacting air quality and climate.*

2. *To improve upon the attribution of climate forcing by a better understanding of the processes controlling the lifetime and distribution of methane, tropospheric ozone, and aerosols.*

3. *To better estimate long-term trends in the troposphere related to air quality and climate from the regional to the global scale.*

4. *To develop and improve air quality model processes and data assimilation in support of operational services including air quality forecasting and protocol monitoring.*

Orbit characteristics

The S-5P mission is orbiting the Earth in a sun-synchronous polar orbit. This orbit has the sun in a fixed position relative to the orbit, which results in a constant local mean solar time for each measurement position on Earth and a constant illumination of the solar panels. The mean local solar time of TROPOMI is 13:33, which means that every ascending equator crossing is at approximately the same moment during the day. This is useful for backscatter radiation instruments, such as trace-gas measurements, since this way the variation of the solar angle is minimized, which allows for better comparisons. However, it also limits the temporal coverage of air quality measurements, for example, the diurnal cycle cannot be studied when all measurements are taken at the same local time. Several other orbital parameters are listed in Table 1.1. The S-5P is flying in close formation with the Suomi-NPP of US National Oceanic and Atmospheric Administration. High resolution cloud data from the Visible/Infrared Imager and Radiometer Suite (VIIRS) on-board this satellite is used in the TROPOMI methane processing. TROPOMI spends half of its time on the day-side of Earth and the other half on the night-side. The ascending part of the orbit is on the day-side, when Earth radiance measurements are taken. During the descending part on the night-side, measurements are carried out required for calibrating the instrument. Solar irradiance measurements are taken once a day, when crossing the terminator from night to day during a specified orbit.

Table 1.1: Orbit parameters of Sentinel-5P mission, adapted from Loots (2015).

Orbital parameter	**Reference value**
Repeat cycle	16 days
Cycle length	227 orbits
Semi-major axis	7205.919 km
Altitude	835 km
Eccentricity	0.001148
Inclination	98.7462 deg
Argument of Perigee	90.00 deg
Mean local solar time	13:33
Launch date	13-10-2017
Mission life-time	7 years

Technical specifications

TROPOMI measures solar radiation reflected and scattered back by the Earth's surface and atmosphere towards the instrument. It has four spectrometers, each consisting of two detectors, resulting in eight wavelength bands. Table 1.2 lists the different measurement bands and their specifications.

The instrument makes use of the 'pushbroom' measurement principle, where the detector scans the whole swath ($\approx$ 2600 km) simultaneously as the satellite moves across the Earth. After approximately 1 second a new scan is started, resulting in the pixel size in the along-track direction to be approximately 7 km. The 2D detectors are registering the spectral content by mapping the different wavelengths on pixels in the along-track dimension, as dispersed by the spectrometers. The measurement swath is mapped by the pixels in the across-track dimension. An illustration of the measurement principle is shown in Figure 1.12.

Table 1.2: TROPOMI spectrometer specifications (Loots, 2015; Sneep, 2019).

Spectrometer	Band	Wavelength [nm]	Spectral resolution [nm]	Species
UV	1	270-300	0.5	O_3
	2	300-320	0.5	O_3
UVIS	3	310-405	0.5	Cloud, aerosol
	4	405-500	0.5	Cloud, aerosol, NO_2
NIR	5	675-725	0.5	Aerosol
	6	725-775	0.5	Cloud, aerosol, CH4
SWIR	7	2305-2345	0.23	CO, CH_4
	8	2345-2385	0.23	CO, CH_4

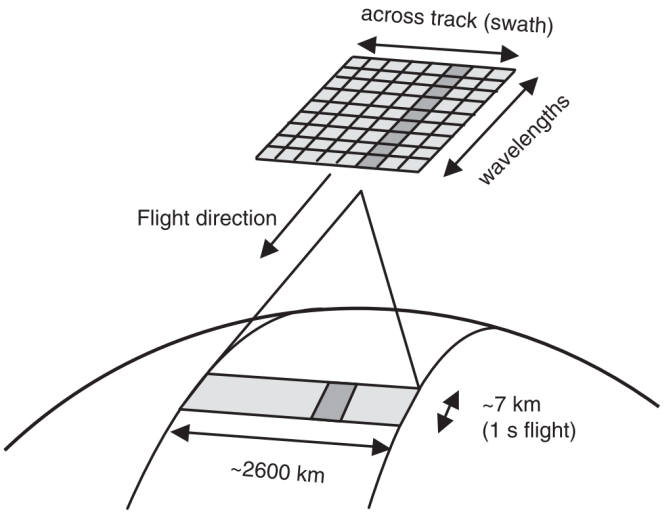

Figure 1.12: Measurement principle of the TROPOMI instrument, obtained from Veefkind et al. (2012).

1.4.2 Data processing

Processing levels

For most Earth observation missions the data processing is divided into several levels, ranging from raw instrument data to model analysis results. An overview of these data processing levels are given here[1]:

- **Level 0** - The full resolution, unprocessed telemetry data consisting of the instrument data (measurements and calibration) and housekeeping data (status of the satellite bus, altitude and attitude). This data is time-ordered, duplicates and overlaps are removed.
- **Level 1A** - Time-referenced Level 0 data with ancillary information, such as geolocation and radiometric data. For TROPOMI a product does not exist for this data level.

[1]Source: https://sentinel.esa.int/web/sentinel/missions/sentinel-5p/data-products and https://science.nasa.gov/earth-science/earth-science-data/data-processing-levels-for-eosdis-data-products

- **Level 1B** - Geo-referenced and calibrated Level 1A data converted to sensor units. For TROPOMI this data level consists of top of the atmosphere Earth radiances and solar irradiances for all detector bands.

- **Level 2** - Geophysical parameters extracted from the Level 1 data, in the same grid as the Level 1 data. TROPOMI Level 2 data consists of geo-located total columns/ tropospheric columns/vertical profiles of the measured trace gases and cloud and aerosol information.

- **Level 3** - The measured variables from Level 2 mapped on a grid, usually spatially and temporally averaged.

- **Level 4** - The output from models applied to a multitude of Level 3 data.

The S-5P mission delivers Level 1B and Level 2 data as products, available to the public.

Processing types

In the TROPOMI processing chain there are three different types of Level 2 products:

- **Near real time (NRT)** - This product type has to be available within 3 hours after sensing and is being used for operational purposes, such as numerical air quality forecasting models. NRT is or will be available for most of the Level 2 products.

- **Offline (OFFL)** - For this type the availability of the products ranges from half a day to about five days after sensing. The major difference between near real time and offline products is the different meteorological fields used in the processing, the NRT product used forecast fields due to time constraints, while the offline product uses analysis fields.

- **Re-processing (RPRO)** - Whenever a large improvement in the product is made, the offline data-set might be re-processed, resulting in a better data product. For scientific analysis this is the preferred data type, when available.

Processor overview

A high level overview of the TROPOMI L2 processor of the KNMI and SRON is shown in Figure 1.13. The input data consists of TROPOMI Level 1B radiances and irradiances, Level 2 products, calibration data, configuration files and static reference data and dynamic auxiliary data. For the NO_2 processor the Level 2 output from the KNMI cloud support product (FRESCO) and Aerosol Absorption Index (AAI) algorithms are required as input. The description of the static and dynamic input data in this section is limited to those needed for the NO_2, cloud and AAI processors.

Static input

The static input data are reference files that are used in the TROPOMI Level 2 processors and are either not subject to change or only change when instrument settings are adjusted. The static input data consists of the following (Sneep and Pedergnana, 2015; van Geffen et al., 2019):

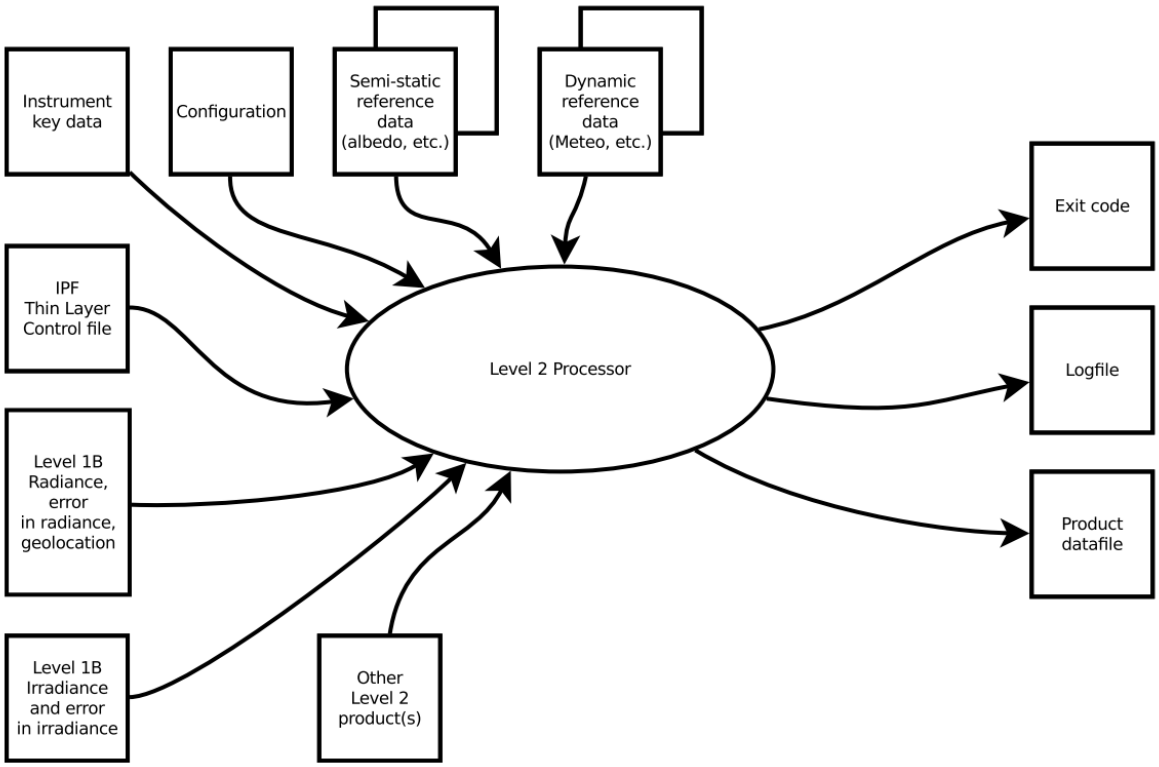

Figure 1.13: TROPOMI KNMI and SRON Level 2 processor overview, obtained from Sneep (2019).

- **Spectroscopic reference data** - Reference cross section spectra for various trace gases, such as O_3, NO_2, O_2, O_2-O_2, H_2O, and liquid H_2O. Furthermore, a high resolution solar reference spectrum is required for wavelength calibration and a Ring effect spectrum is required to account for inelastic rotational Raman scattering. These spectra are used in the DOAS fit, as explained in Section 1.3. All spectra are convolved with the TROPOMI instrument spectral response function (ISRF), which differs for each viewing direction or detector row, thus leading to different reference spectra for each detector row.

- **Surface elevation** - A high resolution (15 arc-second) Digital Elevation Model (DEM) of the Earth's surface is used, the Global Multi-resolution Terrain Elevation Data 2010 (GMTED2010) data set. The surface elevation is used in the algorithm, for example, in the air mass factor calculations.

- **Surface albedo** - The OMI LER database is used as source of the surface albedo at the wavelength range the measurements take place. This data-set is generated from three years of OMI reflectivity measurements, containing monthly and yearly albedo averages, sampled globally at 0.5°x 0.5°. The surface albedo needs to be known to calculate how much of the measured radiance was reflected by the Earth's surface and also used in the AMF calculation. The resolution of this database is considered coarse compared to the TROPOMI pixel resolution, and currently a LER database is being developed from TROPOMI data with a resolution of 0.5° x 0.5°.

- **ISRF** - The instrument spectral response function (ISRF) or 'slit function' is a key calibration data-set characterizing the response of each instrument detector pixel to a monochromatic (single wavelength) light point-source for varying wavelengths. This way it is known what spectral signal the detector pixels produce for specific wavelengths. Convolving the ISRF with the reference spectra results in modified reference spectra as it would be seen by the instrument.

- **AMF LUT** - The air-mass factor (AMF) look-up table (LUT) provides the altitude-dependent AMFs used to convert NO_2 slant columns into vertical columns (see Section 1.3). These altitude-dependent AMFs depend on the viewing geometry, surface albedo, surface pressure and atmospheric pressure.

- **Cloud fraction LUT** - Look-up table used by the NO_2 processor to calculate cloud fractions and cloud radiance in the NO_2 window.

- **FRESCO LUT** - Look-up table used by the FRESCO (Fast Retrieval Scheme for Clouds from the Oxygen A band) algorithm to retrieve cloud fraction, height and albedo. It consists of TOA reflectance at 440 nm as function of the viewing geometry and the retrieval parameters.

- **AAI LUT** - Look-up table used for the aerosol absorption index (AAI) calculation, which contains radiative transfer calculations for a range of measurement scenarios.

- **O_3 database** - An O_3 profile shape and temperature profile climatology: TOMS version 8. Used in the retrieval of clouds and aerosol absorption index.

Dynamic input

Several auxiliary data-sets are needed for the Level 2 algorithm that change every day or even every few hours. There are the following (Sneep, 2019; van Geffen et al., 2019):

- **NO_2 profiles** - NO_2 profile estimates are required as a priori for the calculation of the AMF in the NO_2 algorithm. This estimate is obtained as model field from the TM5 chemical transfer model running at the KNMI, which produces forecasts using TROPOMI observations in an assimilation system. TM5 profile output has a grid resolution of 1°x1°and a temporal resolution of 30 minutes.

- **Meteorological fields** - Several meteorological fields are needed at multiple stages in the processor: temperature profiles, wind and pressure surface fields. These model fields are obtained from the European Centre for Medium-Range Weather Forecasts (ECMWF) as forecast fields for the near real-time processor and as analysis fields for the offline processor. These fields are gridded on a N640 reduced Gaussian grid, which is effectively 16 x 16 km on the surface. For the profile 91 model levels are used. The temporal resolution is 3 hours.

- **Snow and ice cover** - Snow and ice cover change the surface albedo of the measurements, which needs to be known by the algorithm. The Near-real-time Ice and Snow Extent (NISE) data-set is used for this, which has a spatial resolution of 25 km.

1.5 TROPOMI NO_2 retrieval algorithm

Over the years the KNMI has developed an NO_2 retrieval algorithm for NO_2 retrievals for the OMI satellite, called DOMINO (Boersma et al., 2007). This algorithm uses a DOAS retrieval method, an altitude-dependent AMF look-up table and a data assimilation using the TM5-MP CTM on a $1^\circ \times 1^\circ$ grid to split the stratospheric and tropospheric NO_2 signal. The TROPOMI NO_2 processing algorithm is based on DOMINO v2 and recommendations from the Quality Assurance for Essential Climate Variables (QA4ECV) project (Boersma et al., 2018). Several NO_2 retrieval algorithms from other institutes are: the OMNO2 algorithm from NASA (Goldberg et al., 2017), Berkeley High-Resolution (BeHR) NO2 algorithm (locally for U.S.) (Russell et al., 2011) and POMINO (locally for China) (Lin et al., 2015).

The TROPOMI NO_2 retrieval algorithm is briefly described below in three main steps, adapted from van Geffen et al. (2019):

1.5.1 DOAS spectral fit

The reflectance R is calculated by correcting the measured TOA radiance I for the solar zenith angle (SZA) and dividing by the measured solar irradiance E_0. The solar irradiance (radiation from all directions with units $W \cdot m^{-2}$) has to be converted to a radiance (flux from one direction with units $W \cdot sr^{-1} \cdot m^{-2}$) by dividing by the solid angle of the sky (π sr).

$$R(\lambda) = \frac{\pi\, I(\lambda)}{\cos(SZA)\, E_0(\lambda)} \tag{1.15}$$

Then the DOAS algorithm tries to obtain a spectral fit with the smallest possible difference between the measurement reflectance and a modelled spectrum by minimising a chi-square cost function:

$$\chi^2 = \sum_{i=1}^{N_\lambda} \left(\frac{R_{meas}(\lambda_i) - R_{model}(\lambda_i)}{\sigma_{R_{meas}}(\lambda_i)} \right)^2 \tag{1.16}$$

where:

N_λ = number of spectral points in the fitting window
$\sigma_{R_{meas}}(\lambda_i)$ = precision of the reflectance

The precision of the reflectance is calculated from the precision of the radiance and irradiance from the L1B product:

$$\sigma_{R_{meas}}(\lambda_i) = \frac{1}{I(\lambda)} \sqrt{(\sigma_I(\lambda_i))^2 \left(\sigma_{E_0}(\lambda_i)\right)^2 \cdot (R_{meas}(\lambda_i))^2} \tag{1.17}$$

The non-linear fitting function $R_{model}(\lambda)$ used is as following:

$$R_{model}(\lambda) = P(\lambda) \exp\left(- \sum_{k=1}^{N_k} \sigma_k(\lambda) SCD_k \right) \left(1 + \frac{C_{ring} I_{ring}(\lambda)}{E_0(\lambda)} \right) \tag{1.18}$$

where:

$P(\lambda)$ = polynomial, usually order 5
N_k = slant column density of molecule k
k = index of the molecule considered in the fit
$\sigma_k(\lambda)$ = absorption cross-section of molecule k
C_{Ring} = Ring fitting coefficient
$I_{Ring}(\lambda)/E_0(\lambda)$ = sun-normalised synthetic Ring spectrum

Included in the fit is absorption from NO_2, ozone, water vapour, liquid water and O_2-O_2 collision-induced absorption. The polynomial P accounts for slow-varying spectral structures from molecular and aerosol scattering and surface albedo effects. The remaining high frequency spectral signatures are used together with the absorption cross-section spectra to fit the slant column densities SCD. The last term in this equation accounts the influence of the Ring effect (inelastic rotational Raman scattering) on the reflectance spectrum, where C_{Ring} is used as fitting parameter. Note that the DOAS fitting equation used is non-linear and is set up in terms of reflectance, in contrast to the general DOAS equation (Equation 1.10), which is linear and describing optical depth. The non-linear system is then solved using optimal estimation, a regularized matrix inverse method.

1.5.2 Separation of tropospheric and stratospheric NO_2

In the KNMI TROPOMI NO_2 processor a data assimilation method is performed of the slant columns using the TM5-MP chemical transfer model (CTM) (Williams et al., 2017). In this data assimilation, recently measured NO_2 slant columns are fed into the CTM simulation to obtain a realistic 3D model of the current coupled tropospheric and stratospheric NO_2 field. For areas that are known for their negligible tropospheric NO_2 column, such as the Pacific ocean, the stratospheric NO_2 field in the model is nudged to the observed slant column measurements. The location and time of these areas is based on the model prediction. This model has a resolution of 1° x 1° and uses time steps of 30 minutes. ECMWF forecast and analysis meteorological fields (pressure, temperature, wind humidity, etc.) are used as input with 3-hourly intervals. The balance between the model and observations is achieved by means of a Kalman filter. The model estimates the stratospheric signal over areas that do have a significant amount of tropospheric NO_2 and subtract this from the total column to arrive at the tropospheric column. The stratospheric column is taken as the column from the tropopause up to the upper layer of the CTM.

1.5.3 Conversion to vertical columns with air-mass factors

The box-AMFs used in the conversion from slant column to vertical column are obtained from a look-up-table containing pre-calculated box AMFs for different combinations of parameters at a predefined wavelength. These box AMFs have been calculated by the Doubling-Adding KNMI (DAK) radiative transfer model (de Haan et al., 1987), simulating the light path with a model atmosphere as function of the viewing geometry, albedo and pressure profiles. Aerosol effects are not directly taken into account in the model, and a Lambertian reflectance climatology is used for the albedo, thus not taking anisotropic effects into account. Included in the AMF calculation are an effective cloud correction (combined effect of clouds and aerosols) for pixels that are (partly) covered in clouds and a temperature correction for the NO_2 fit to

account for the temperature dependency of the absorption cross-section of NO_2. Besides the box-AMF, an a priori vertical NO_2 profile or profile shape is required to convert the slant column to the vertical column (see Section 1.3.3), for which the profile output from the TM5 CTM run is used (see previous section).

1.5.4 Data quality flags

To indicate the quality of the TROPOMI data products, a data quality flag is given to each ground pixel, called the 'QA value' (quality assurance). Several criteria are used to assess the quality: cloud cover, snow cover, viewing geometry, air mass factor, sun glint possibility, missing data etc., see van Geffen et al. (2019) for the complete description. The QA value ranges from 0 to 1, where 0 means a processing error occurred. Filtering for a value larger than 0.50, leaves only good quality retrievals, including cloud or snow contaminated pixels. Above QA value of 0.75, also cloudy pixels (cloud fraction above 50%) and snow/ice covered pixels are filtered out, which is the recommended pixel filter for most use cases.

1.6 NO_2 column retrieval uncertainty

The measurement uncertainty of trace gas retrieval from space is important for the interpretation and quality of the data product. However, obtaining this error estimate is not trivial, since there are many steps in the processing chain which introduce errors or noise. According to the International vocabulary of metrology (IEC BiPM et al., 2012), measurement uncertainty is a "*non-negative parameter characterizing the dispersion of the quantity values being attributed to measurand, based on the information used.*", which includes systematic error and random error. The uncertainty contributors for NO_2 retrievals can be divided into three groups (Boersma et al., 2004):

1. Slant column error - errors originating from instrument noise and spectral fitting, which appear in the retrieved slant column density

2. Stratospheric slant column error - errors introduced by the separation between stratospheric and tropospheric signal

3. Air-mass factor error - errors in the air mass factor caused by uncertainty in clouds, surface albedo and a priori profile shape

The instrument noise consists of shot noise and read-out noise. Shot noise is a quantum noise effect and originates from the particle-like behaviour of light and the discreteness of photons and electrons. The shot noise follows a Poisson distribution and its standard deviation is equal to the square root of the number of electrons generated by the photons hitting the detector (Loots, 2015). Read-out noise is caused by the physical electronic detector chain, when converting the photons to electron, electrons to volts and volts to digital numbers. The ratio between the measured signal and the instrument noise is called signal-to-noise ratio (SNR). For TROPOMI the SNR in the 400-500 nm range is approximately 1400-1500, when operating in the nominal mode (van Geffen et al., 2019). During the spectral fitting systematic errors of a few percent are introduced by the inaccuracy of reference spectra and

instrument calibration, however, they are relatively small compared to other errors in the retrieval (Boersma et al., 2004). From forward retrievals with synthetic spectra, slant column uncertainties were found in the range of 10-15% for background and 5-10% for polluted NO_2 cases (van Geffen et al., 2019).

The error introduced in the separation of stratospheric and tropospheric NO_2 columns is mainly caused by uncertainty in the forecasted stratospheric columns. The uncertainty in the stratospheric column is then in the order of 0.1-0.2·10^{15} molec./cm² (van Geffen et al., 2019), approximately 10%. Errors in the AMF calculation are mainly caused by errors in the cloud fraction, cloud pressure, surface albedo and a priori NO_2 profile shape. Each of them has can cause an AMF error roughly between 0 and 10%, which sums up to approximately 15-25% AMF error (van Geffen et al., 2019).

The total error in the tropospheric NO_2 column is a sum of these groups, and is calculated according to Equation 1.19 (Boersma et al., 2004):

$$\sigma(VCD_{tropo}) = \sqrt{\left(\frac{\sigma(SCD)}{AMF_{tropo}}\right)^2 + \left(\frac{\sigma(SCD_{strato})}{AMF_{tropo}}\right)^2 + \left(\frac{(SCD - SCD_{strato}) \cdot \sigma(AMF_{tropo})}{AMF_{tropo}^2}\right)^2} \tag{1.19}$$

where:

$\sigma(SCD)$ = the slant column error; (group 1)
$\sigma(SCD_{strato})$ = the stratospheric slant column error; (group 2)
$\sigma(AMF_{tropo})$ = the error in the tropospheric air-mass factor; (group 3)

This error differs from measurement pixel to pixel due to retrieval parameters as cloud fraction, surface albedo, etc. that are variable. For small tropospheric NO_2 columns, the uncertainty is dominated by the random errors from the spectral fitting. For polluted pixels, with large tropospheric columns, the error is dominated by uncertainty associated with the AMF. Errors in the AMF originate mainly from the albedo dataset and a priori NO_2 profiles, due to their low spatial resolution relative to the measurement resolution. Over polluted hotspots tropospheric TROPOMI NO_2 retrievals have an uncertainty in the range of 15 - 50%. Over unpolluted areas this is typically more than 100%. The overall error budget can be approximated with Equation 1.20 (van Geffen et al., 2019).

$$\sigma(VCD_{tropo}) = 0.5 \cdot 10^{15} + [0.2\ to\ 0.5] \cdot VCD_{tropo}\ \ [molec/cm^2] \tag{1.20}$$

The SCD uncertainty estimates reported in data are subject to the error propagation in prior steps in the L1B processor and the DOAS method in the L2 processor. An independent method to analyse SCD uncertainty is looking at the a posterior statistical SCD uncertainty. This method is explained in (Zara et al., 2018) and references therein. In this approach the spatial variability of the SCD over an unpolluted area is calculated and assumed to be a statistical indicator of the random component of the SCD uncertainty. The difference between the statistical and propagated uncertainty could provide a lower limit on the systematic error.

1.7 Chemical transfer models

Chemical Transfer Models (CTMs) are used to simulate the atmospheric chemistry and to forecast air pollution. CTMs do not calculate the meteorology, they use the output from General Circulation Models (GCMs) which use Navier-Stokes equations for numerical weather prediction and climate modelling. The retrieval of trace gases from remote sensing data makes use of CTM data as well. For example in the TROPOMI NO_2 retrieval, the a priori profile shape and stratospheric column are obtained from a CTM called TM5-MP (Trace Model 5 massively parallel version). On the opposite, satellite trace gas retrievals are used as input for operational forecasting with CTMs. For example, TROPOMI data is planned to be used in the data assimilation system of the European air quality forecasting CAMS (Copernicus Atmospheric Monitoring Service)[2]. Tests are being performed, for example with the total ozone column (Inness et al., 2019). CAMS is part of the Europeans Commission's Copernicus program and is implemented by the ECMWF, and provides operational global and European air quality forecasts. These forecasts are made by using 7 models (CHIMERE, EMEP, EURAD, LOTOS-EUROS, MATCH, MOCAGE and SILAM) from different institutions and are combined in one ensemble hourly forecast up to 4 days for several atmospheric constituents at a grid size of 0.1°x 0.1°.

1.8 Spatial resolution of space-borne NO_2 measurements

OMI provides NO_2 measurements with a spatial resolution of 13 x 24 km (Levelt et al., 2017). Its successor, TROPOMI, delivers an operational NO_2 product with, at the moment of writing, ground pixels of 7.1 x 3.6 km in nadir. The measurements performed in the zoom mode of TROPOMI have a resolution six times higher: 2.4 x 1.8 km in nadir.

In (Valin et al., 2011b) the effect of the model resolution of NO_2 columns on the interpretation of satellite measurements is analysed. This study focuses on the resolution required for modelling emissions based on satellite observations, which suggests a resolution in the range of 4-12 km is sufficient to predict the NO_2 column and lifetime accurately enough. Simulations run in this study shows how coarse resolution measurements over a polluted area introduce a negative bias in the maximum and average measured NO_2 column. Especially of interest for this thesis are the differences between 12 x 12 km, 4 x 4 km and 2 x 2 km, which have a negligible effect on the area column average, however, do show the importance of resolution to identity point sources inside a polluted background.

(Loughner et al., 2007) developed a method to determine the spatial resolution required to observe air quality from space, using variogram analysis in combination with model simulations and an emissions inventory. This study concludes that air-quality fields have a smallest length scale of roughly 50 km in the boundary layer for tropospheric ozone, which would require observations to have a resolution in the range of 10-15 km. However, NO_2 sources

[2] https://atmosphere.copernicus.eu/

already influence the surrounding area on length scales smaller than 1 km, so to separate emissions from sources such as high-ways or factories from the surroundings, observation resolutions should be an order of magnitude smaller, thus in the range of 1-1.5 km.

A recent aircraft campaign from NASA compared high resolution (250 x 250 m) aircraft NO_2 column retrievals to ground-based column measurements (Judd et al., 2019). These two data-sets compare well (r^2=0.91 and slope of 1.03) for two polluted urban regions in the Unites States. To assess the effect of the spatial resolution of the data, the measurements were down-scaled to the approximate resolution of the satellites TEMPO (3 x 3 km), TROPOMI (5 x 5 km) and OMI (18 x 18 km). The spatial averaging resulted in aircraft to ground measurements slopes of 0.88, 0.77 and 0.57, respectively, indicating that satellite products representativeness is degrading with coarser resolution. This implies that biases found between ground and satellite measurements in validation efforts have a spatial representativeness dependency, meaning that biases do not necessarily indicate a discrepancy in the instrument data but are caused by a difference in spatial scale. Also, biases found for satellites with different spatial resolution cannot be fairly compared to each other without correcting for this dependency. Distinct spatial features in the aircraft data, such as signals from sea breeze and industrial areas, were only distinguishable at the TEMPO resolution scale and roughly at the TROPOMI resolution scale, indicating the importance of high spatial resolution measurements. Furthermore, this study demonstrated the benefit of high resolution albedo database and NO_2 a priori profiles by comparing different a-priori products to the ground-based measurements. Multi-variable linear regression of this data indicates that the variability in tropospheric AMF could be explained for 64% by the surface albedo and for 16% by the a priori NO_2 profiles.

The OMI instrument performed measurements in a so called super-zoom mode in late 2004 for 85 orbits (Valin et al., 2011a). In operational setting, OMI retrieves slant column NO_2 with a nadir footprint of 13 x 24 km, where eight detector rows are averaged. In the zoom-mode, without the detector averaging, the spatial resolution becomes 13 x 3 km. Due to data transmissions limits, the spatial coverage was reduced from the nominal 2600 km to 180 km. Methods used in the exploration of this OMI data-set can be used as well in the analysis of the TROPOMI zoom mode data-set.

In the study describing the zoom-mode measurements (Valin et al., 2011a), the spatial response of the single detector pixels was determined by comparing the measured reflectance to a co-located reflectance with known resolution. The decay in reflectance at a sharp boundary was used for this, in this case a coastline. Furthermore, downwind plumes of an isolated point sources of NO_2 give a good estimate of the measured resolution. The upper limit was put at 9 km, in agreement with the calibrated value of 7 km.

Since the resolution went up by a factor 8 for the same instrument, the uncertainty in the slant column would theoretically be a factor $\sqrt{8}$ smaller because no averaging is applied anymore. This holds only when the uncertainty is dominated by random noise and has a small systematic error. The statistical uncertainty of the zoom measurements was indeed approximately a factor $\sqrt{8}$ smaller, which indicates the retrieval does not suffer much from a systematic error and is shot-noise limited. This statistical uncertainty was obtained by taking the 1-σ standard deviation of a measurement set above a uniform region with little NO_2 emission, in this case a remote desert and ocean.

Furthermore, the increased performance of the zoom measurements was illustrated with several case studies that looked at point sources. For some cases, individual sources could be distinguished in the zoom measurements, whereas in the normal case it appeared as one source. Also higher maxima could be measured with the increased spatial resolution for the same sources. Compared to a 6-day average of normal measurements, the zoom resolution cases shows more spatial variability, due to the spatial smoothing caused by meteorological effects.

1.9 Enhancing CO_2 emission quantification with NO_2 plume detection

As introduced in Section 1.10, the planned European CO_2 mission will image CO_2 plumes from individual sources such as power-plants and cities with a spatial resolution of 2 x 2 km (Kuhlmann et al., 2018a). Cities account for 70% of the CO_2 emission and have potential for large emission reduction, as stated in the Paris agreement and IPCC reports. Previous satellite instruments that measured atmospheric CO_2 columns (called XCO_2) are SCIAMACHY, GOSAT, OCO-2 and MicroCarb. These measurements were mostly averaged over time and used to study the meso-scale CO_2 signals originating from natural sources. Due to the long lifetime of CO_2 in the atmosphere and the high global average background (approximately 400 ppm), the signal from local anthropogenic sources is relatively small (<1% or 0-2 ppm) and therefore require measurements with high precision.

Studies have shown the feasibility of quantifying point source CO_2 emissions from power-plant plumes using airborne measurements (Krings et al., 2018) and satellite measurements (Nassar et al., 2017) (using OCO-2 measurements), (Bovensmann et al., 2010) (using simulations). Increased resolution, sampling and accuracy should enable quantification of CO_2 emissions from measurements of individual plumes using single overpasses.

The CO_2 mission might use NO_2 measurements to better constrain the shape and size of CO_2 plumes, of which the signal is close to the detection limit. Using a co-emitted species, such as NO_2, which plume is easier to detect due to higher SNR and smaller background, helps to detect and identify CO_2 plumes and improves the quantification of CO_2 emissions. Furthermore, since NO_2 is usually not influenced by biospheric fluxes, which is the case for CO_2, NO_2 measurements could help to separate the anthropogenic CO_2 signal from the background gradient. In addition, NO_2 algorithms are still able to perform good quality retrievals with light cloud cover (<30%) while CO_2 retrieval algorithms require cloud free pixels.

Several studies have shown the benefit of combining CO_2 and NO_2 with either co-located measurements from different instruments or simultaneous measurement from one instrument. For example, the technique of combining the measurements have been demonstrated using NO_2 data from TROPOMI and XCO_2 data from OCO-2 to identify plumes and estimate CO_2 emissions (Reuter et al., 2019). Furthermore, an ESA-funded study called SMARTCARB, showed the added value of NO_2 measurements by quantifying emissions from power plant and city plumes using one year of synthetic satellite observations with and without NO_2 measurements for different resolutions, instrument noise levels and number of satellites. Using

Berlin as test case, their plume detection algorithm detects 20-30% of the cloud-free plumes with only CO_2, while adding the simultaneously measured NO_2 results in a detection of about 70%. Using the NO_2 measurements from Sentinel 5, only 39% of the plumes are detected, due to a overpass time difference of two hours. Using a power-plant as test case, two to three times more plumes could be detected per year compared to Berlin, which increased by 50% when using the NO_2 plume detection. Furthermore, by using the NO_2 plume detection the extent of the plume is better estimated, decreasing systematic biases in estimating the CO_2 background, used in emissions analysis. This study suggests a NO_2 instrument with a resolution of 2 x 2 km and precision of $2{\cdot}10^{15}$ molecules cm^{-2}.

1.10 Future relevant missions

Sentinel-5 Precursor has an operational lifetime of minimum seven year to bridge the gap towards the launch of the first Sentinel-5 on-board meteorological satellites MetOp-SG around 2021 in Low Earth Orbit (LEO). The instrument onboard Sentinel-5, will be very similar to the TROPOMI instrument and deliver similar data products. A multitude of Sentinel-5's will provide operational long-term global daily nadir atmospheric composition measurements at least until 2035/2040 (Bézy et al., 2014; Pérez Albiñana et al., 2017).

The Sentinel-4 satellite family will provide operational hourly atmospheric composition measurements over Europe from geostationary orbit (Gulde et al., 2014). This scanning instrument will measure O_3, NO_2, SO_2, HCHO and aerosol optical depth above Europe and North Africa at a spatial resolution of 8.9 km (N/S) by 11.7 km (E/W) with a repeat cycle of one hour. The data from this missions will contribute to air quality forecasting and monitoring. The first satellite is schedules for launch in 2019 and the second one in 2027. There are two similar geostationary instruments which are to monitor air quality on an hourly basis, both targeting areas with high pollution. Scheduled for launch in 2019, the American Tropospheric Emissions: Monitoring of Pollution (TEMPO) instrument (Zoogman et al., 2017) to monitor greater North America at a spatial resolution of 2 km (N-S) by 4.5 km (E-W). And scheduled to launch in 2019, South-Korean Geostationary Environmental Monitoring Spectrometer (GMES) for East-Asia (Hong et al., 2015).

The European Commission and ESA are considering to expand the Copernicus project with a CO_2 mission (also called Sentinel 7 or CO2-M), which is to monitor anthropogenic carbon emissions, in support of the Paris agreement and other (inter)national policies. This missions aims to measure atmospheric CO_2 columns (XCO_2), with a spectrometer using CO_2 absorption in the near infra-red band, at high spatial resolution, to enable imaging the plumes of individual power-plants and cities. The requirements at this moment are a spatial resolution of 2 x 2 km, revisit time of 2-3 days, swath width of 250 km and high measurement precision, which needs a constellation of 3 satellites (Meijer, 2018). The launch target is set for 2025. In addition, the spectrometer might have a VIS channel to measure NO_2, which will be used to enhance the measurement of CO_2 plumes, by constraining the plume location and size (Kuhlmann et al., 2018a). The results of this thesis might be relevant for the design

of this new instrument, since the ground pixels are of similar size as the TROPOMI zoom measurements. The performance of the zoom measurements could be insightful for the requirements of the NO_2 spectrometer.

1.11 Thesis outline

The initial objective of this thesis project is to apply the KNMI TROPOMI Level-2 retrieval algorithm to the high spatial resolution Level-1B (ir)radiance spectra, obtained by the TROPOMI instrument in zoom science mode, to estimate NO_2 tropospheric columns. This task is more technical of nature and requires the regeneration of input databases for the algorithm, as they are dependent on the used binning scheme in the instrument detector. Further analysis of the retrieved NO_2 columns will focus on the quality of the data in terms of spatial resolution and measurement uncertainty. Case studies on polluted scenes, for example plumes from power plants and cities, will give insight in the improved capabilities of these high resolution measurements compared to the nominal resolution. These polluted scenes furthermore provide opportunities for several case studies, such as simulating coarser resolution measurements, plume detection algorithms tests, correlation studies with CO_2 measurements and comparisons to air quality forecast models. A measure for the amount of information content in a retrieved NO_2 field will be set-up and tested, which allows for a quantitative comparison of the effects of the spatial resolution increase. Finally, the effect of high spatial resolution a priori NO_2 profiles and high spatial resolution surface albedo databases on the retrieval performance will be looked into.

The processed zoom mode measurements are scientifically relevant, since they show the potential of TROPOMI and future tropospheric air quality monitoring satellites with its unprecedented spatial resolution. This work could help future NO_2 instruments in their design choices, such as the desired spatial resolution and required signal-to-noise ratios. Furthermore, it might give insight into the added value of increased spatial resolution of tropospheric NO_2 in terms of information content, plume detection capabilities, a priori profile dependencies, model validation and so forth. Increased spatial resolution NO_2 measurements could improve emission estimation and top-down emission inventories, contributing to efforts at improving air quality, decreasing the human impact on the environment and limiting emissions to slow down climate change.

The following main research question has been formulated:

What is the additional value of the high spatial resolution NO_2 measurements obtained by TROPOMI in zoom mode compared to the nominal resolution measurements?

With the following sub-questions:

- *Sub-question 1: What is changed in the instrument settings for TROPOMI in the special zoom science mode and what are the consequences of that?*
  I.e. different integration-time, binning scheme, measurement bands causes different spatial resolution, different uncertainty and different viewing angles. What input re-

quired for the NO_2 Level-2 processor needs to be re-generated? What is the actual measured spatial resolution on the ground? (Method from (Valin et al., 2011a), explained in Section 1.8). And what is the effect on the instrument noise and thus uncertainty of the measurements? (Method from (Zara et al., 2018), as explained in Section 1.6).

- *Sub-question 2: What is the increase in NO_2 pollution mapping capabilities due to the spatial resolution increase in the zoom-mode measurements compared to the nominal measurements?*
  A measure for the amount of information content has to be defined to allow for quantitative comparisons of different resolution measurements. Qualitative comparisons can be based on distinguish-ability of pollution sources, plume detection capabilities, increased level of detail within polluted areas, etc. Comparisons can be done between zoom mode and nominal measurements, and between zoom mode measurements and zoom mode measurements simulated at nominal spatial resolution.

- *Sub-question 3: How well do high spatial resolution NO_2 measurements compare to model forecasts from CAMS and what can be learned from it?*
  Comparison for scenes containing enhanced NO_2 columns, such as plumes, between the high resolution measurements and forecasted air quality fields from chemical transfer models can give insights into the performance of these models and what the strong and weak points are for these scenarios. The CAMS model fields could be used as an alternative to the coarse TM5 model to produce a priori profiles for the NO_2 retrieval.

- *Sub-question 4: How well do high resolution NO_2 column measurements correlate with co-located CO_2 column measurements and how much do they increase plume detection capabilities?*
  Spatially and temporally co-located high resolution measurements of NO_2 and CO_2 could improve the understanding of the relation between these two emission species. Furthermore, CO_2 plume detection algorithms can be significantly enhanced by using NO_2 measurements, according to simulations at this spatial resolution ((Kuhlmann et al., 2018b), see Section 1.9). Using actual high resolution NO_2 measurements could provide more evidence for this claim.

- *Sub-question 5: What is the effect of using higher spatial resolution a priori input for high spatial resolution NO_2 retrievals in polluted areas?*
  It has been argued that coarse a priori profiles together with coarse surface albedo databases lead to significant error in the AMF and thus in the retrieved tropospheric vertical NO_2 columns, especially for polluted areas (see Section 1.6 and 1.8). The a priori profiles from the TM5 model could be replaced with a high resolution alternative from the CAMS models, it should be investigated how the profiles from these models compare for polluted areas. Then using the high resolution profiles for the AMF calculation, what is the effect on the total AMF and the retrieved NO_2 columns compared to using the nominal coarse NO_2 profiles? This can be done for different levels of NO_2 pollution and different albedo scenes using the polluted scenes available in the zoom mode data-set. This could provide insight in the required resolution of the a priori profiles. Similarly, the impact of the coarseness of the surface albedo databases can

be investigated by using an experimental high resolution surface albedo database in the retrieval process. Then, differences between the surface albedo databases could be linked to potentially observed discrepancies in the retrieved cloud fraction and NO_2 columns.

It should be noted that process to obtain NO_2 estimates from space-borne measurements is complex, where a large amount of data from different sources converges. In this thesis not all aspects of the retrieval are covered in depth, as it would simply become too much. The parts that are relevant for this work are explained in more detail. Besides, the performed analysis is not comprehensive, as they focus on specific components of the retrieval and data that were deemed useful for assessing the impact of the spatial resolution improvement.

Chapter 2 covers the processing efforts and tries to answer sub-question 1. In Chapter 3 the results are analysed, which covers sub-question 2. Sub-question 3 and 4 are examined in Chapter 4, where the results are compared to other data-sets. Chapter 5 attempts to use high resolution a priori input in the retrieval process and investigates sub-question 5. Finally, in Chapter 6, the found conclusions are discussed and based on that recommendations are made.

Disclaimer:
The operational spatial resolution of the TROPOMI instrument was increased in the along track direction from 7.2 km to 5.6 km starting from 6 August 2019 onwards[3]. Since most of the analysis of this thesis was already performed by that time, the original along track dimension (7.2 km) is used in the text and in the comparison cases.

[3]Source: http://www.tropomi.eu/mission-status

2

Processing the L1B zoom-mode data

This chapter describes the steps taken in processing the TROPOMI Level-1B zoom mode measurements. First, the data-set itself is described and the differences relative to the nominal TROPOMI measurements are explained in terms of instrument settings, measurement geometry and data properties. Then, the required static and dynamic input databases for the TROPOMI Level-2 processing software are discussed. Finally, the processing scheme is provided and a brief overview of the resulting Level-2 data is given. Meanwhile, the first knowledge is gained to answer sub-question 1, by understanding the changes in the instrument settings and their effect on the measurements.

2.1 TROPOMI Level-1B zoom data

This thesis is built on the unique series of high resolution zoom measurements performed by TROPOMI. This section starts with a description of the general TROPOMI Level-1B product, whereafter the differences between the nominal data product and the zoom measurements will be discussed.

The TROPOMI instrument consists of four spectrometers, each divided into two bands, resulting in a total of 8 bands, where each band has its own spectral range. Bands 1 to 6 (the UV, VIS and NIR bands) are CCD detectors and band 7 and 8 (the SWIR bands) are CMOS detectors. The instrument measures the sunlight reflected by the Earth in a pushbroom configuration, meaning that the detectors image the whole swath simultaneously while moving along in the spacecraft's orbit, (see Figure 1.12). The along track dimension of the detector represents the range of measured wavelengths, as dispersed by the spectrometers. The across track dimension of the detector image is the swath of the image, consisting of an array of ground pixels. Figure 2.1a shows how the wavelengths are mapped on the detector image for band 4, where the wavelengths in the visible spectrum are visualized by true colours. The dispersed wavelengths do not map perfectly onto the detector, there is a spectral distortion present called the 'spectral smile', as visualized with the contour plot in Figure 2.1b. The CCD detectors are subject to a binning scheme, where the signal of detector rows (across track) are added together before the detector is read out. The binning scheme is nominally adding pixels together around nadir, so they become effectively the same size as ground pixels towards the edge of the swath, which are larger due to the viewing angle and the spherical Earth.

In addition, the binning of pixels averages the individual measurements, which reduces the measurement noise and decreases the data volume for read-out and down-link. The incoming radiation is integrated over time, while the spacecraft orbits the Earth, thus realizing the along-track dimension of the ground pixels.

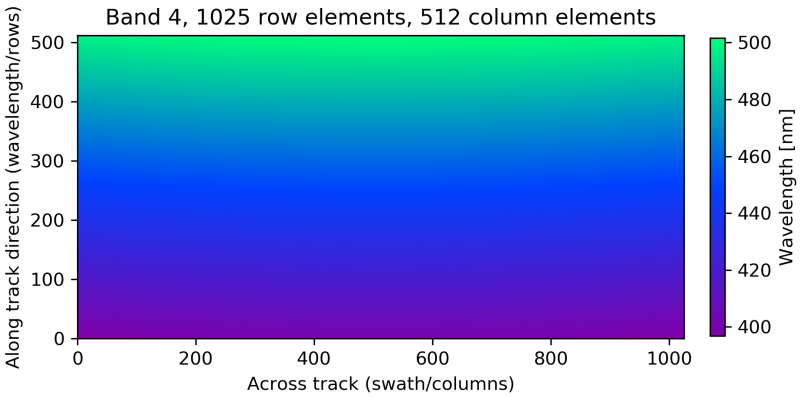

(a)

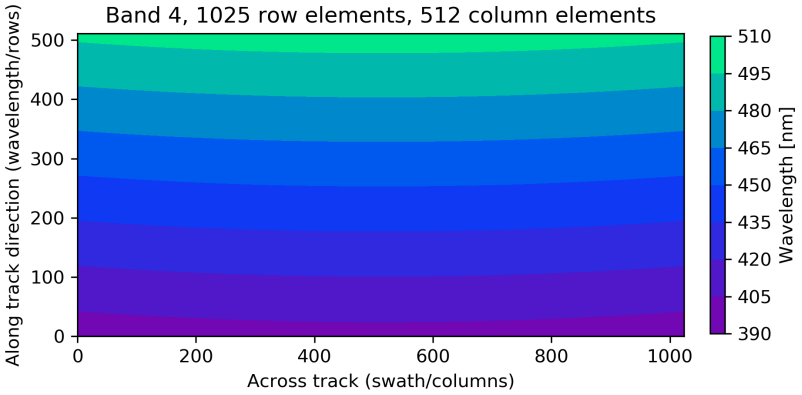

(b)

Figure 2.1: TROPOMI band 4 detector wavelength map (a) and contour plot of the same map to increase visibility of the spectral distortion (b). The chosen colorscale represents the perceived color of these wavelengths.

The raw instrument data (Level-0) is calibrated and processed to a geolocated Level-1B product by the L01B processor. The L1B product contains, among other data, the measured radiances for a specific band during a specific orbit or granule (part of orbit). For each measured ground pixel it consists of a radiance spectrum, where the spectral range is determined by the detector band. Table 2.1 shows an example of several relevant specifications of a typical standard mode TROPOMI L1B granule for UVIS band 4.

The special measurement mode, called 'Zoom Science Mode' (or simply 'zoom mode'), was used during the E1 Commissioning Phase of the mission for about a week (01-03-2018 to 07-03-2018 and several separate orbits). The zoom measurements available are orbit number 1970 to 2059, resulting in a total of 88 granules. In this mode the measurements were only performed for 4 out of 8 detector bands due to data volume restrictions: bands 3, 4, 6

Table 2.1: Specifications of a typical standard mode and a zoom mode L1B radiance file. Note that data compression is currently applied on the nominal data product, reducing the file size further compared to the zoom mode.

TROPOMI Band 4 L1B file		
Property	**Nominal mode (orbit 6738)**	**Zoom mode (orbit 1972)**
Scanlines	3245	6846
Ground pixels	450	456 (172 zoom)
Spectral elements	497	497
Number of measurements	725M	1551M
Swath size	2700 km	2700 km (310 km zoom)
Pixel size (nadir)	7.1 x 3.6 km	2.4 x 1.8 km
Co-addition time	1.08 s	0.36 s
File size	2.6 GB	12 GB

and 7. The adjusted instrument configuration (with instrument configuration ID (ICID) 0114) incorporated several changes to the nominal instrument setting during Earth radiance measurements. The binning scheme of the CCD detectors was changed in a way that no binning was applied in the centre of the swath, decreasing the ground pixel width by a factor 2 in nadir. Towards the edge of the swath, the binning increased, averaging more pixels together, to reduce the data volume that had to be read from the CCD. There is no binning applied to the CMOS detector of band 7, so no binning changes occurred there. Furthermore, the integration time was shortened by a factor three, from 1.08 s to 0.36 s, resulting in a three times smaller ground pixel length. In total the pixel size of the CCDs thus reduced by a factor 6. In Table 2.1 several relevant specifications are shown for a zoom mode TROPOMI L1B granule of band 4. When comparing the specifications of the standard mode and the zoom mode, it can be noted that the number of spectral elements, number of ground pixels and swath size are mostly unchanged. The number of scanlines and the binning factor do change and result in the decrease in pixel size and increase in file size.

The effect of the different binning scheme is shown in Figure 2.2, where the cross-track pixel sizes are imaged on the TROPOMI swath. Where on the top figure (nominal mode), the cross-track pixel size remains constant and gradually increases towards the edge of the swath, on the bottom figure (zoom mode) it goes up in discrete steps. The high resolution pixel sizes only hold for a limited part of the swath, the middle strip, which is approximately 310 km out of the total 2700 km swath . Figure 2.2 illustrates this further, as the cross-track pixel dimensions of both modes are plotted as a function of the ground pixels.

The result of the different binning scheme and shorter integration time is an increase in spatial resolution in the zoom mode (2.4 x 1.8 km), relative to the nominal mode (7.1 x 3.6 km). The decrease of the ground pixel size is visualised in Figure 2.4, where rasters are plotted onto South Holland, Netherlands. Whereas cities in the nominal mode consisted of only a few pixels, in the zoom mode this amount is multiplied by 6, which increases the detail within and around cities significantly. As has been mentioned in Section 1.8, (Loughner et al., 2007) states that in order to distinguish point sources, such as factories, from the surroundings,

NO_2 measurements with resolution in the order of 1-1.5 km are needed. The zoom mode measurements approach this required resolution. Looking at Figure 2.4, a factory NO_2 plume just outside a city would not be resolved by the nominal resolution, however, under the right meteorological conditions, this could be possible with the increased zoom mode resolution.

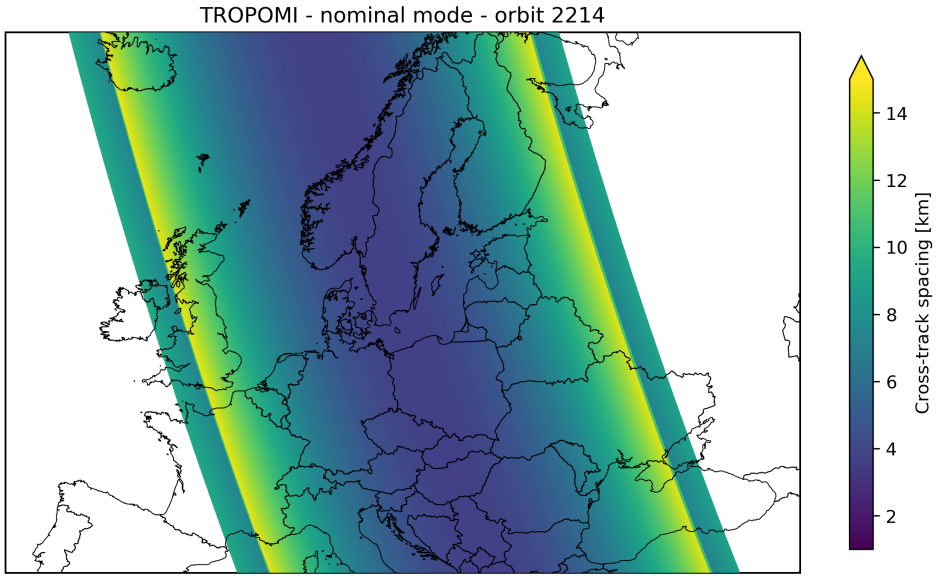

(a)

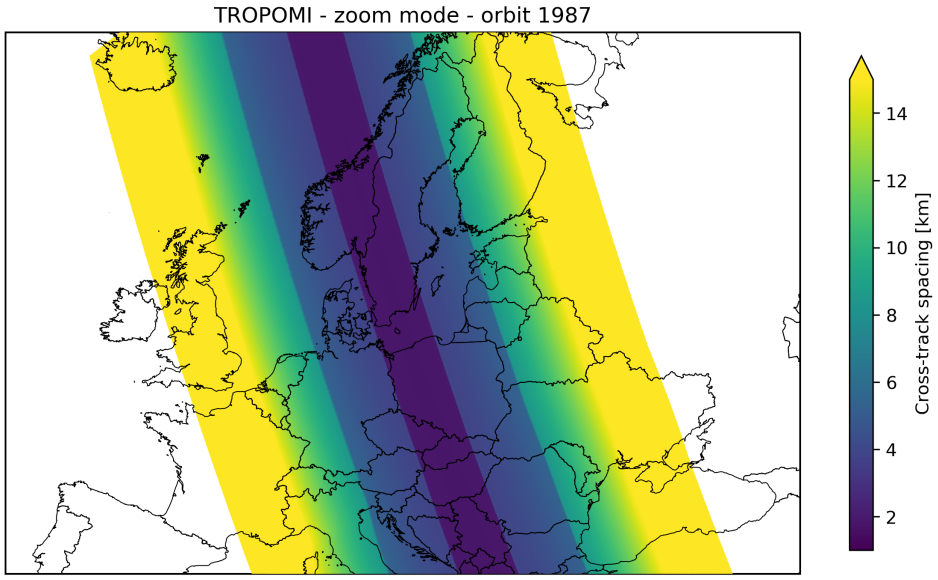

(b)

Figure 2.2: TROPOMI detector band 4 cross-track pixel size mapped on swath: (a) nominal mode. (b) zoom mode.

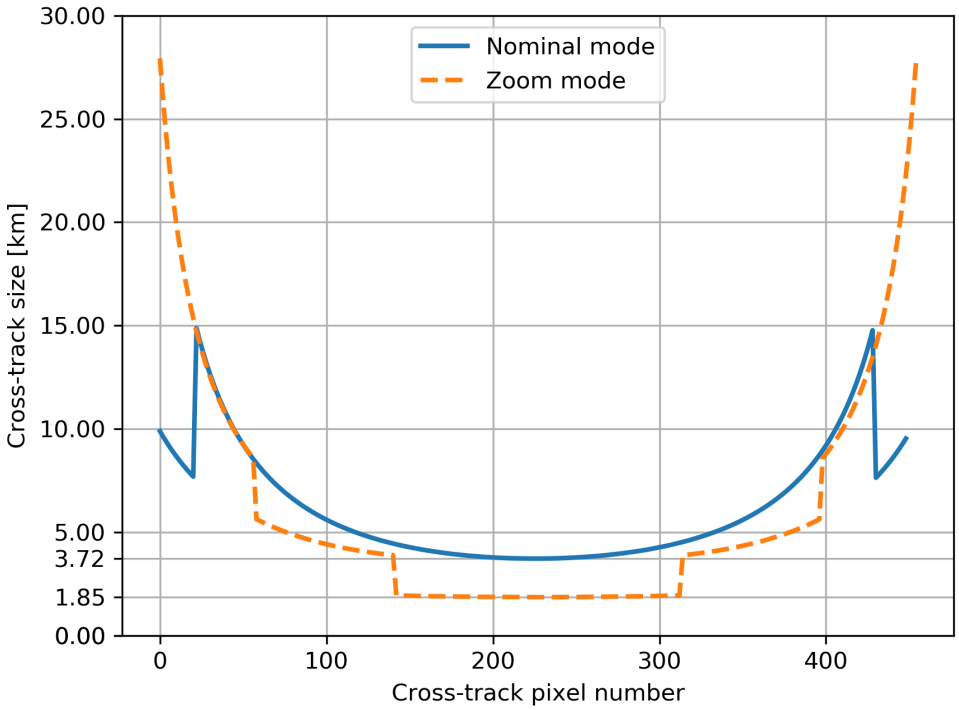

Figure 2.3: TROPOMI detector band 4 cross-track pixel size plot comparing the nominal and zoom mode.

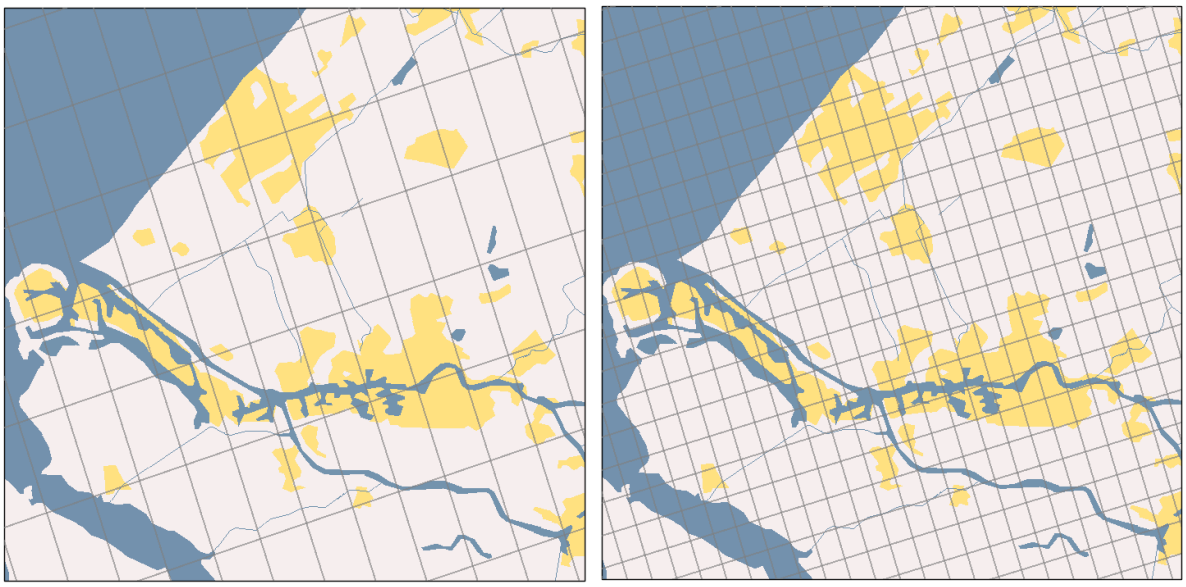

(a) (b)

Figure 2.4: Ground pixel raster of TROPOMI plotted on South Holland, Netherlands: (a) nominal mode, 7.1 x 3.6 km. (b) zoom mode, 2.4 x 1.8 km. Flight direction from south to north.

2.2 Regenerated static input

The KNMI TROPOMI L2 processors require multiple static input databases (see Section 1.4.2) of which some have to be regenerated. The radiances in the L1B product are measured according to a certain binning scheme. During the processing steps from L1B to the L2 product several input databases are used, which are convolved with the binned Instrument Response Function (ISRF) or 'slit function'. Since the binning scheme was changed for the zoom measurements, the databases depending on the binned ISRF have to be regenerated. Furthermore, adjusting the binning scheme changes the viewing angle that corresponds to a certain ground pixel. The consequence is that input databases which are calculated per ground pixel for the corresponding nominal viewing angle scheme have to be made again as well. The original scripts for generating the static input, described in Sneep (2018), are modified in order to generate the zoom mode version of the input databases. Below the static input that has to be re-generated for the analysis of the zoom-mode data is listed:

Instrument spectral response function (ISRF)

The ISRF contains for each detector pixel the response to a point-source of monochromatic light as function of the source wavelength. When changing the binning scheme, the binned ISRF has to be regenerated and all databases depending on it as well. The unbinned ISRF for the TROPOMI instrument is created by pre-flight calibration measurements (Kleipool et al., 2018) and is part of the Calibration Key Data (CKD). The binned ISRF can be calculated from the unbinned ISRF when the binning scheme and wavelength map are known (Sneep, 2018).

Solar reference spectrum

The measured solar irradiance spectrum is shifted in wavelength to the measured Earth's radiance spectrum due to the Doppler effect caused by the motion of the satellite. The solar irradiance spectrum is brought to the wavelength grid of the Earth's radiance spectrum by using spline interpolation on a high resolution solar reference spectrum to find the corresponding wavelength (van Geffen et al., 2019). This high resolution reference spectrum, obtained from Chance and Kurucz (2010), has to be convolved with the ISRF, so it represents the solar spectrum as measured by the instrument. The convolution of the newly binned ISRF with the solar reference spectra is performed with line by line calculations with the DISAMAR program (de Haan, 2011).

Absorption cross-section reference spectra

The absorption cross-section reference spectra are used in the DOAS algorithm to fit the spectral signature of several species. These spectra have to be convolved with the binned ISRF and the convolved solar spectrum for band 4. The used reference spectra are: NO_2 (Vandaele et al., 1998), O_3 (Serdyuchenko et al., 2014), O_2-O_2 (Thalman and Volkamer, 2013) and H_2O vapour/liquid (Pope and Fry, 1997).

FRESCO look-up table

The FRESCO algorithm retrieves cloud information from the O_2-A absorption band in TROPOMI band 6, for which a look-up table is used. This look-up table contains the TOA reflectance at 758 nm as function of the retrieval cloud parameters (cloud fraction, height and albedo) and the viewing geometry. Due to the different binning scheme, the ground pixels have different corresponding viewing angles and this look-up table has to be regenerated.

2.3 Dynamic input

Several input data files are needed in the NO_2 retrieval algorithm that are dynamic of nature and are only valid for a certain time interval. The following dynamic input was used for the zoom measurements (01-03-2018 to 07-03-2018):

NO_2 profiles

Vertical NO_2 profile estimates are needed in the retrieval algorithm to separate the stratospheric and tropospheric signal and to convert the slant column to a vertical column. Forecast NO_2 profiles are obtained from a chemical transport model, TM5-MP (Huijnen et al., 2010; Williams et al., 2017). Operationally, a data assimilation approach is followed, where the model is updated with slant column measurements, such that the modelled stratospheric field matches with the observed column over unpolluted remote regions. However, for the zoom-mode this was not possible, and the TM5-MP model was ran without assimilation. A TM5-MP start field was used for the initial state for the model run, which was assimilated using TROPOMI slant columns. The total reactive nitrogen in the stratosphere is a well-conserved quantity, and the information obtained from the assimilated observation can be stored in the model over long periods (van Geffen et al., 2019). Therefore, the start field should be adequate for the simulation of the stratospheric field for the short time period of the zoom mode (approximately 7 days), and the impact due to the lack of assimilated observations should be relatively small. The model was run for the time period spanned by the zoom mode measurements using ECMWF meteorological fields.

In the nominal TROPOMI NO_2 product, small systematic across-track features in the NO_2 slant columns are removed, called 'de-striping' (van Geffen et al., 2019). The de-striping was initially turned off, since the striping amplitude was found much smaller than in OMI, however, was turned on later to slightly increase the data quality. These across-track biases (stripes) result from calibration errors that are viewing angle dependent and are generally within 5% of the slant column density. The de-striping correction factors are determined for each viewing angle using the measured slant columns from the past 7 days over the Pacific ocean, performed by the NO_2 CTM assimilation system. For the zoom-mode measurements the viewing angles are different, and this had to be changed in the settings of the CTM run to obtain the NO_2 field. However, this was not the case, and it was decided to omit the de-striping correction for the zoom mode measurements, to avoid a lengthy rerun of CTM, and because the de-striping would only have a minor effect on the slant columns.

Meteorological fields

Meteorological data, such as surface pressure, is needed in the retrieval algorithms. From the ECMWF data catalogue 12-hourly forecasts of the global surface fields (2D) are obtained. These files contain the required parameters at 3-hour intervals. The forecast data-set is used, since this provides 3-hour intervals, while the analysis data-set only contains 6-hour intervals. The provided files are in GRIB format, which are converted to NetCDF files by a conversion tool described in (Sneep, 2019).

Snow and ice cover

Daily snow and ice cover information is provided by the Near-real-time Ice and Snow Extent (NISE) data-set (Brodzik and Stewart, 2019). The files for the relevant dates are obtained from their data portal and can be directly used by the TROPOMI L2 processor to correct the surface albedo climatology for snow, where needed.

2.4 Processing scheme

The KNMI TROPOMI L2 processors are used to retrieve the tropospheric NO_2 columns from the L1B zoom data (see Section 2.1). Figure 2.5 shows a simplified overview of the used processing scheme in this study. The static reference data is covered in Section 1.4, of which some had to be regenerated, covered in Section 2.2. The dynamic input data used is described in Section 2.3, and more generally in Section 1.4. The flow chart shows that the cloud product and the aerosol absorbing index (AAI) product have to be generated first, since these are used as input for the NO_2 retrieval algorithm.

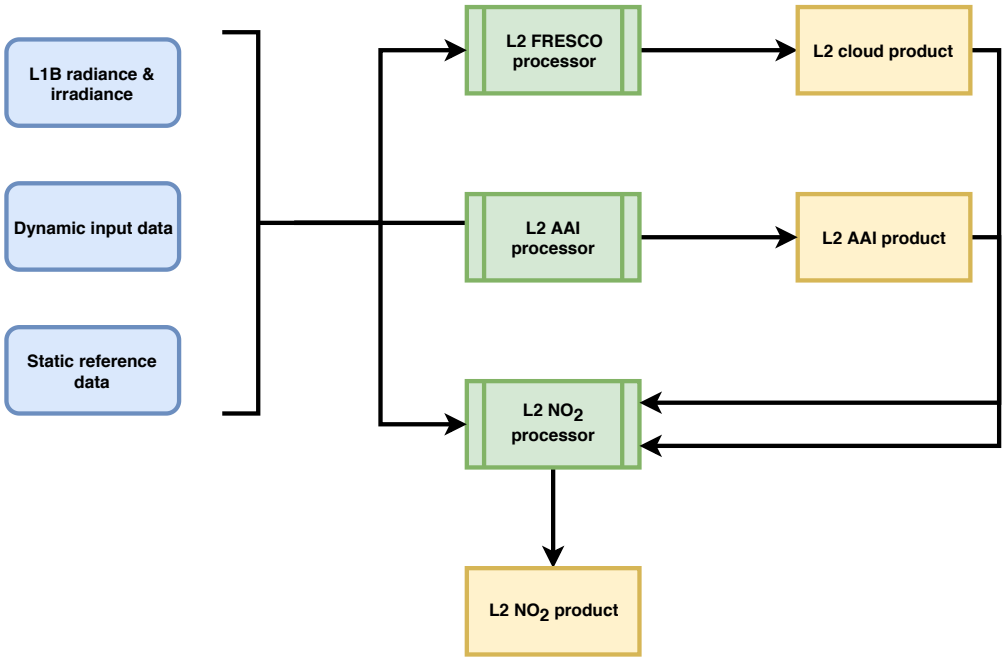

Figure 2.5: Simplified overview of the used Level-2 processing scheme.

2.5 Overview results

The processing scheme has been applied the TROPOMI zoom mode measurements of orbit 1970-2059. From the Level-2 output the cloud fraction, aerosol absorption index (AAI) and NO_2 tropospheric column is plotted in Figure 2.6. Note that only the high resolution ground pixels are plotted. This plot contains roughly 7 days of the zoom mode measurements from TROPOMI, which in its normal has daily global coverage and thus the globe would be completely covered. However, due to the limited part of the swath that measures in the high resolution, the coverage is significantly lower. Thick cloud cover prohibits good quality tropospheric NO_2 retrievals, which are filtered out by the algorithm. The AAI map (Figure 2.6b) shows oval gaps for each orbit around the equator above ocean, this is due to the possibility of sun-glint geometry, where the sunlight is specularly reflected of the sea surface, possibly affecting the retrieval quality and thus a lower QA-value is assigned. Clear-sky overpasses of interesting (polluted) regions are sparse in this data-set due to the limited swath. From Figure 2.6c multiple polluted areas can be recognised: Europe, Middle-East, India and China. In Section 3.1 several scenes are identified and studied in more detail.

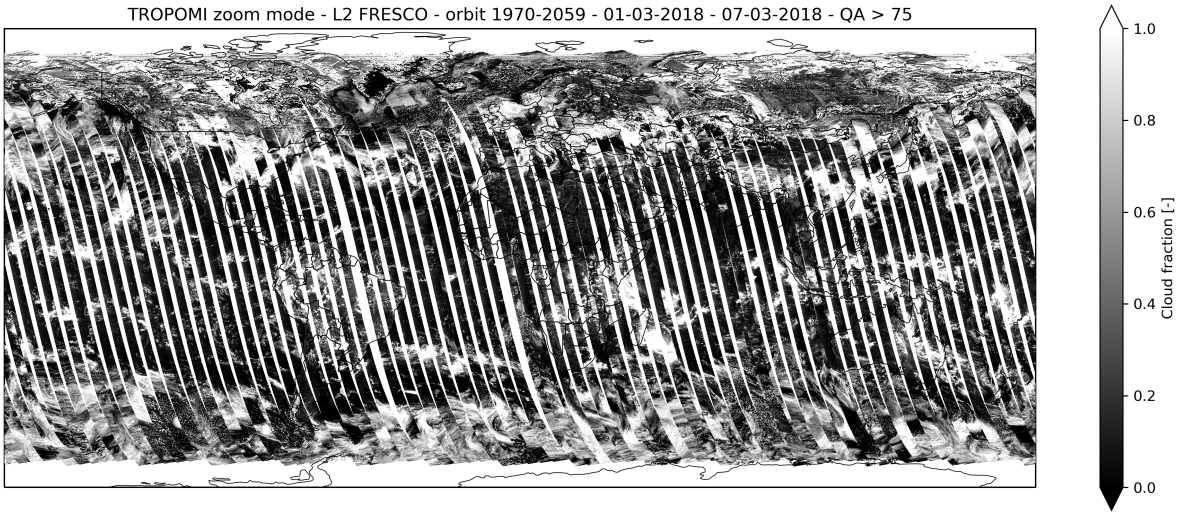

(a)

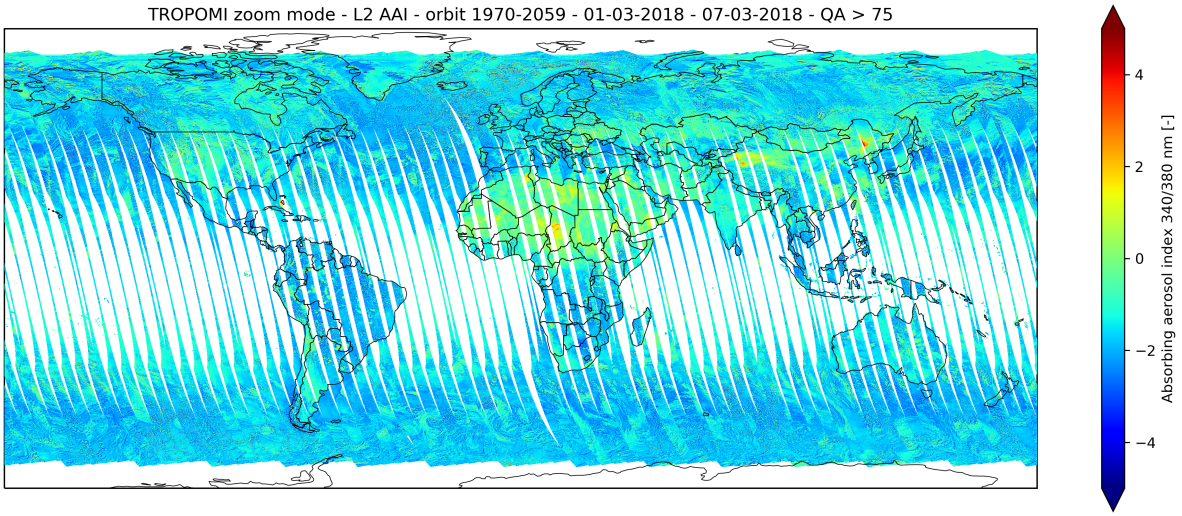

(b)

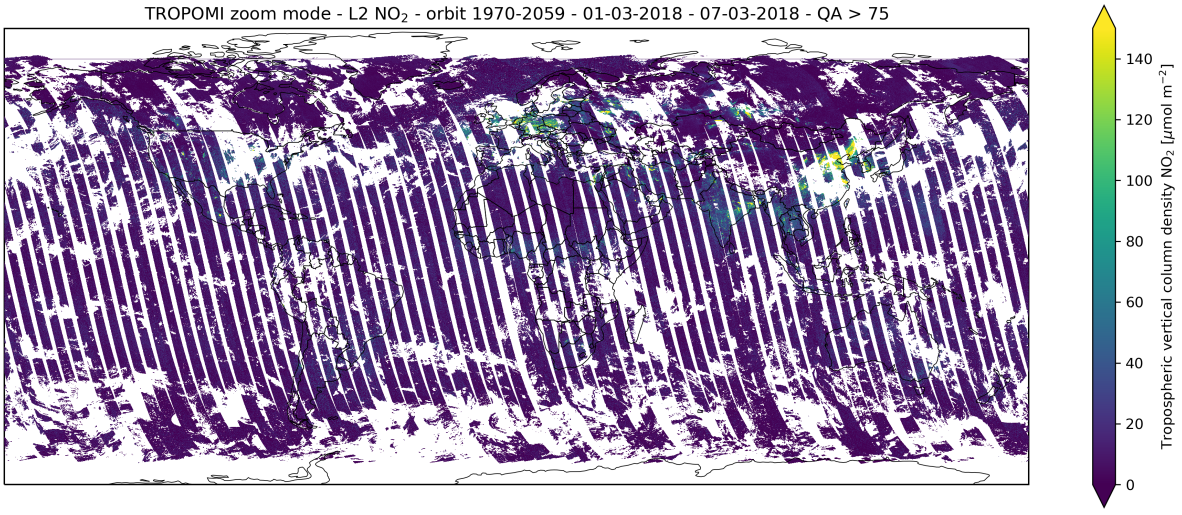

(c)

Figure 2.6: Overview map of L2 zoom mode data from orbit number 1970-2059, taken from 01-03-2018 to 07-03-2018, QA value > 75. (a) FRESCO cloud fraction. (b) AAI 340/380 nm. (c) Tropospheric NO_2 column.

3

Analysis of the zoom-mode NO_2 results

The TROPOMI L1B zoom mode data-set has been processed to a Level-2 NO_2 product, as described in the previous chapter. Within those 7 days of zoom mode measurements, several interesting cloud-free scenes with pollution sources were found. These polluted scenes are then used to assess the added value of the increased resolution by comparing them to lower resolution scenes, with the goal to answer the second sub-question. Furthermore, an analysis of the spatial resolution is done, and the changes in measurement uncertainty is looked into. Both to further understand the effect of the adjusted instrument settings on the measurements and to answer sub-question 1.

3.1 Polluted scenes

In this section several polluted scenes are shown which demonstrate the high resolution of the zoom mode NO_2 measurements, with a pixel size of 2.4 x 1.8 km. First, five scenes of plumes from point sources are discussed located in the Middle-East and East-Europe. Then, the measured NO_2 column maps of two mega cities are shown: Mumbai and Mexico City. For easily identifiable point sources a search was done for a matching entry in the Global Power Plant Database from the World Resources Institute (Byers et al., 2018). The location of the identified power plants are indicated on the maps. For the mega-cities no power plants were indicated, since no individual sources were identified using the database.

3.1.1 Point source plumes

Riyadh

Riyadh is the capital of Saudi Arabia with a population of over 7.5 million. Figure 3.1 shows the retrieved tropospheric NO_2 column, measured on 01-03-2018, overlaying a map from OpenStreetMaps. Included is a scale-bar (5 km), which gives a feeling of the size of the ground pixels. This scene catches a fine and sharp long-stretched plume on the top right, which indicated the instrument is able to detect a signal on individual pixels, without visible smearing. Apart from the plume from city itself, two point sources can be identified. The source marked with the upper red dot appears to be the combined oil and gas power plant Riyadh PP 9, with a capacity of 3617 MW. The lower red dot is at the location of a similar

plant: Riyadh PP 10, capacity of 3160 MW. There are several more power plants located in this scene according to the Global Power Plant Database database. However, these are not clearly visible in this measured NO_2 columns, either because they are not operational, have too low signal or are masked by the plume from the city.

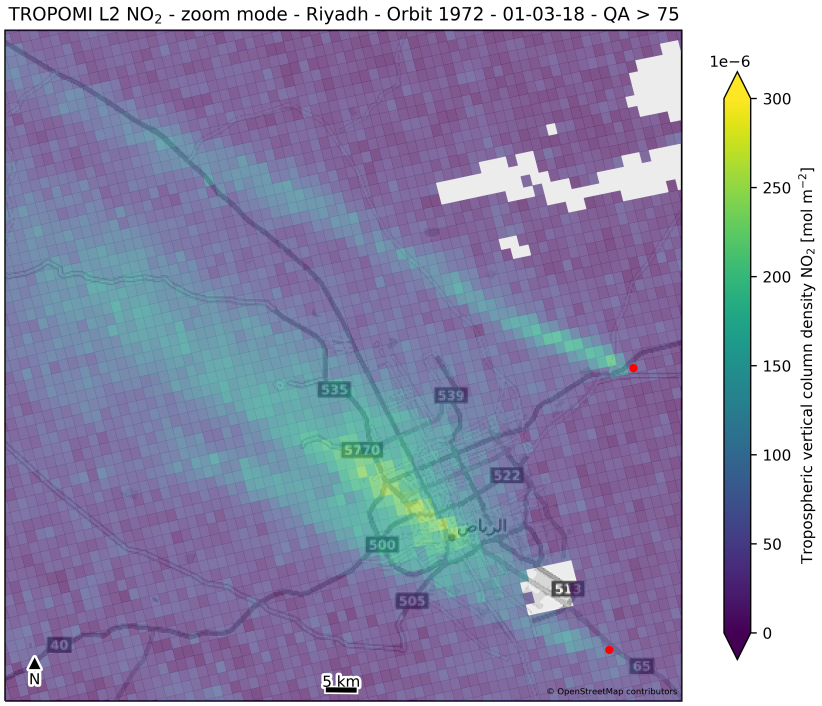

Figure 3.1: TROPOMI zoom mode L2 tropospheric NO_2 at 01-03-2018, Riyadh (Saudi Arabia), with known power plants indicated with red dots.

Ahwaz

Ahwaz is a city in Iran, near the corner of the Persian Gulf, with 1.3 million inhabitants. In Figure 3.2 the surrounding area of Ahwaz is shown, taken on 02-03-2018. The plume originating from the power plant indicated with the red dot, is the oil fuelled Ahwaz Ramin power station, with a capacity of 1903 MW. The broad and relatively weak plume below is originating from Ahwaz itself. The bright plume at the bottom belongs to a harbour town with houses a petrochemical complex. This scene shows the plumes in the north being redirected by the wind.

Jubail

Jubail is a city on the East coast of Saudi Arabia, housing the largest petrochemical company in the country. Figure 3.3 shows the NO_2 plume coming from the cities industry, mainly petrochemical and steel production, on the left. The right plume originates from a combined power and desalination plant (indicated with the red dot), producing 2744 MW and 800 million litres of drinking water per day.

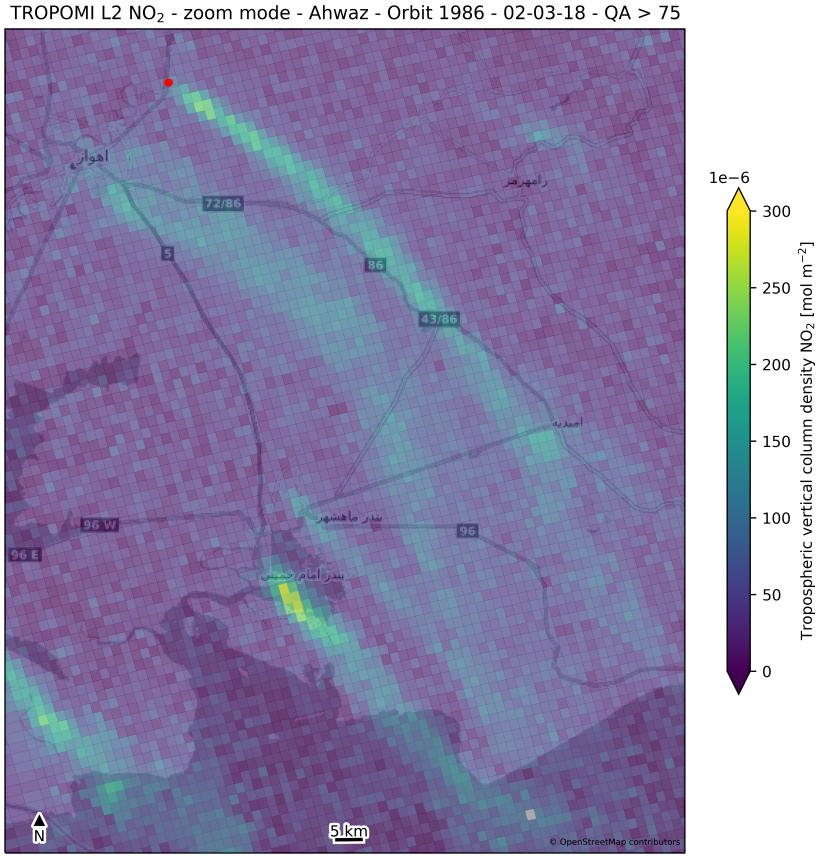

Figure 3.2: TROPOMI zoom mode L2 tropospheric NO_2 at 01-03-2018, Ahwaz (Iran), with power plant indicated by the red dot.

Bełchatów

Bełchatów is the name of Europe's largest thermal power station, and second largest fossil-fuel power station in the world, producing 5472 MW. It is located in Poland, below Łódź, and runs on brown coal (lignite). In 2014, the European Commission had ranked Bełchatów as "the most climate-damaging power plant in the European Union", with CO_2 emissions of roughly 37.2 million tonnes in 2013[1]. Figure 3.4 shows the NO_2 plume emitted by Bełchatów (indicated by the red dot) on 02-03-2018. The plume remains visible over a significant distance, while keeping its width constant, as it is transported by a westward wind.

Ukraine

Figure 3.5 shows multiple clear plumes located above Eastern Ukraine on 06-03-2019. Most of these plumes appear to have their source at the location of a power plant (indicated with the red dot). This image appears to be sharper and less noisy than the other scene in Europe (the Belchatow power plant in Poland). This can be explained by the snow cover in Ukraine on this day, which increases the albedo and the amount of light reflected by the surface and thus the SNR. At the Black Sea in the bottom, the noise increases again, as water has a much lower albedo.

[1]Source: https://www.spiegel.de/wirtschaft/unternehmen/kohlekraftwerke-in-deutschland-stossen-mehr-co2-aus-als-im-eu-schnitt-a-962028.html.

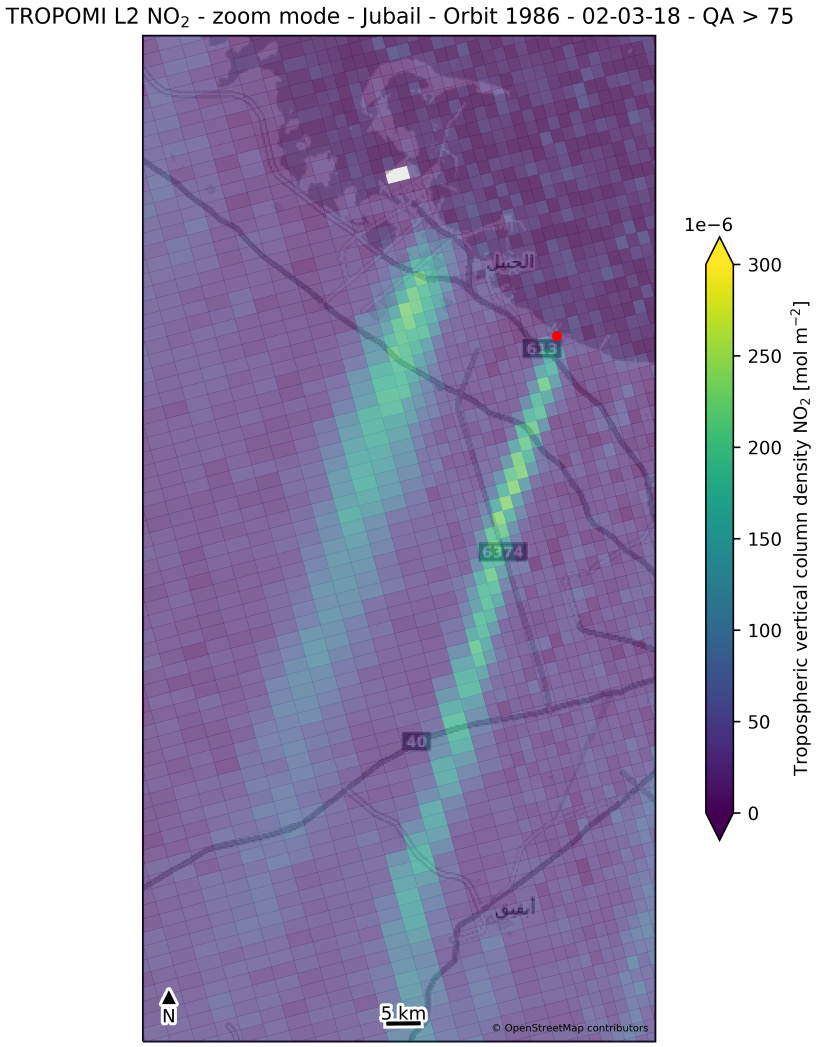

Figure 3.3: TROPOMI zoom mode L2 tropospheric NO_2 at 02-03-2018, Jubail (Saudi Arabia), with desalination plant indicated with the red dot.

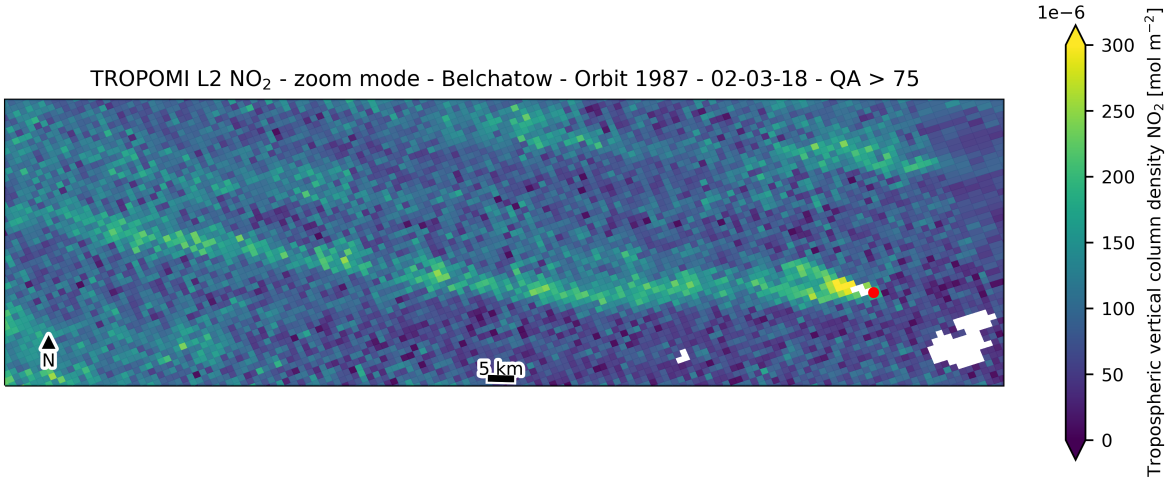

Figure 3.4: TROPOMI zoom mode L2 tropospheric NO_2 at 02-03-2018, Bełchatów (Poland), with power plant indicated with the red dot.

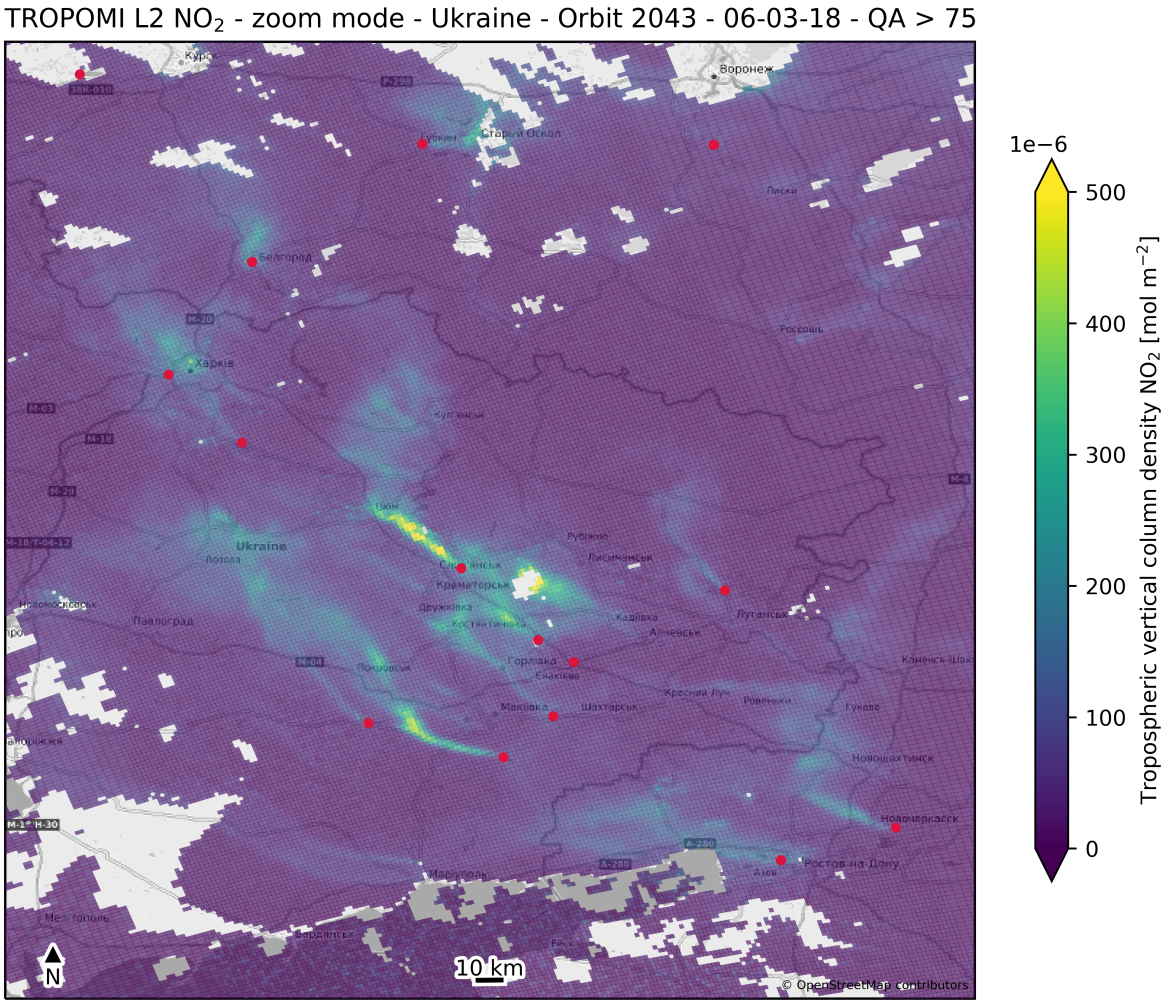

Figure 3.5: TROPOMI zoom mode L2 tropospheric NO_2 at 06-03-2018, East Ukraine, with known power plants indicated with the red dots.

3.1.2 Mega cities

Mumbai

Mumbai is India's most populated city, with 12.4 million inhabitants in the proper city, and 21.3 million in the Mumbai Metropolitan Region. Figure 3.6 shows the NO_2 measured above Mumbai on 01-03-2018. The city is situated on the thin lower part of the peninsula, the eastern and northern part are suburban area, where the majority of the pollution is located. An outflow of pollution to the sea is visible, which is due to the south-east wind at that moment. ECMWF data indicate a mean wind speed at 10 m of approximately 4 m/s. The peak on the right side of the city cannot be assigned to a known power plant, perhaps it originates from an industrial source.

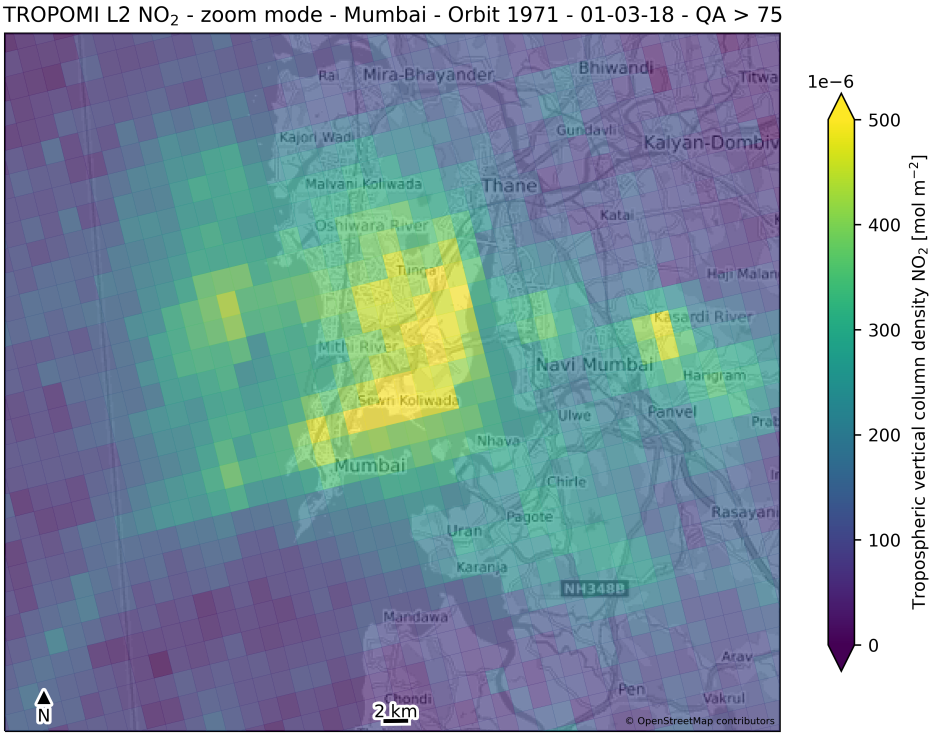

Figure 3.6: TROPOMI zoom mode L2 tropospheric NO_2 at 01-03-2018, Mumbai (India).

Mexico City

Mexico City is the capital of Mexico, with a population of 8.84 million (21.3 million in Greater Mexico City). Figure 3.7 shows the NO_2 as measured by TROPOMI on 02-03-2018. The measurements show a maximum tropospheric NO_2 vertical column of 713 μmol/m^2. No plumes are visible, and it appears the emitted pollution is trapped above the city, closed in by the boundary layer inversion and surrounding mountains. An elevation map of Mexico city is shown in Figure 3.8, where the mountains surrounding the city are visible. Increased NO_2 values are seen above the highways going out and in the city, especially the highway to the north and the highway through the mountains in the south-west.

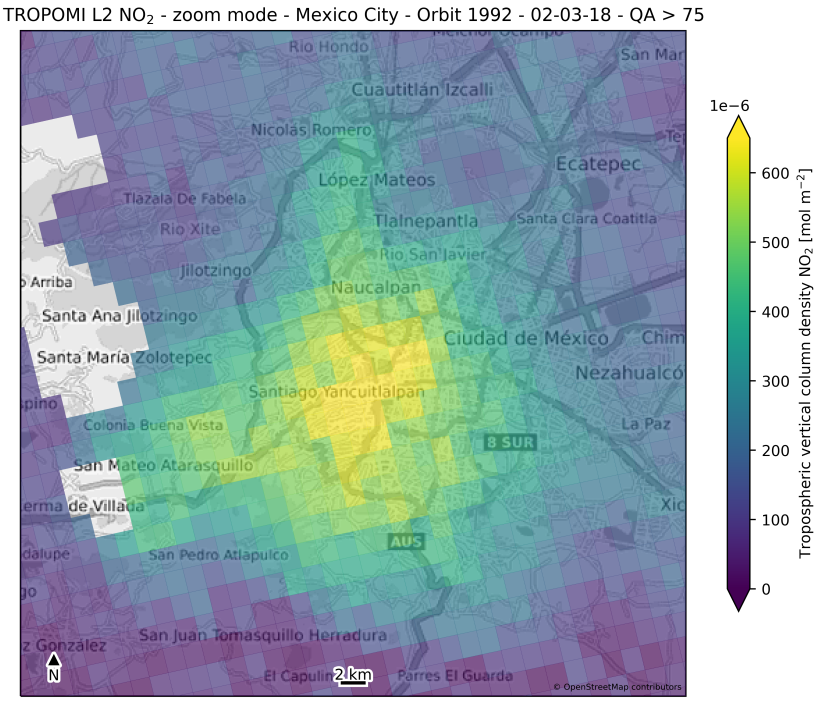

Figure 3.7: TROPOMI zoom mode L2 tropospheric NO_2 at 02-03-2018, Mexico City (Mexico).

Figure 3.8: Elevation map of Mexico City (Mexico) and surrounding mountains, map data source: Esri, USGS.

3.1.3 Remarks

The discussed scenes show the detailed NO_2 column maps, as imaged at high resolution by TROPOMI operated in zoom-mode. Multiple sharp plumes are visible in the scenes, where signals are detected on individual pixels. These findings indicate there is limited to no smear or memory effect of the detector pixels present due to the zoom mode instrument settings. It should be noted that most of the scenes were taken at measurement conditions that are well above average, increasing the visibility and detail of the plumes. For example, the scenes in the Middle-East have a high signal-to-noise ratio due to the high scene albedo caused by the desert sand and enhanced sensitivity due to a low solar zenith angle (SZA) close to the equator. Furthermore, the scene above Ukraine shows clear plumes and low noise due to the snow cover at that moment, increasing the albedo and the SNR. A more realistic example for a snow- and cloud-free mid-latitude area would be the Bełchatów scene, where more noise is present and the plume is less visible.

3.2 Comparison with down-scaled resolution

The dimensions of the ground pixel in zoom mode are two times smaller in cross-track direction and three times smaller in along-track direction than in nominal mode. To simulate what TROPOMI would have measured at the polluted scenes of Section 3.1 in its nominal measurement mode, the zoom mode measurements were averaged over two by three pixels to arrive at a pixel size of approximately 7.1 x 3.6 km. Doing this allows for comparison of the scenes in the two modes and to investigate the effect of the increased resolution. Qualitatively this is done by assessing how well point sources can be distinguished to another, how well the shape of power plant plumes is captured and how much detail can be seen in polluted cities. A more quantitative approach of comparison is attempted by making use of two methods: a local entropy method and a method using an image sharpness measure. Several scene comparisons are selected and discussed in this section.

3.2.1 Qualitative comparison

Figure 3.9 shows the original zoom measurement and downscaled resolution version of Riyadh. The plume from upper power plant appears pixelated and the shape of the plume is less clear in the downscaled version. Furthermore, the origin of the plume is harder to identify and the gradient of NO_2 abundance within the plume is not visible. The plume from the bottom power plant is harder to notice and could be mistaken as part of the plume produced by the city.

Figure 3.10 shows the original and downscaled version of the power-plant Bełchatów (Poland). Also in this case, the meandering of the plume is less clear from the downscaled version. The peak value measured in the plume in the original case is 392 μmol m^{-2}, while in the downscaled version that is reduced to 276 μmol m^{-2}. A higher measured peak value would be expected from a smaller pixel size, because a smaller area is imaged and less spatial averaging occurs.

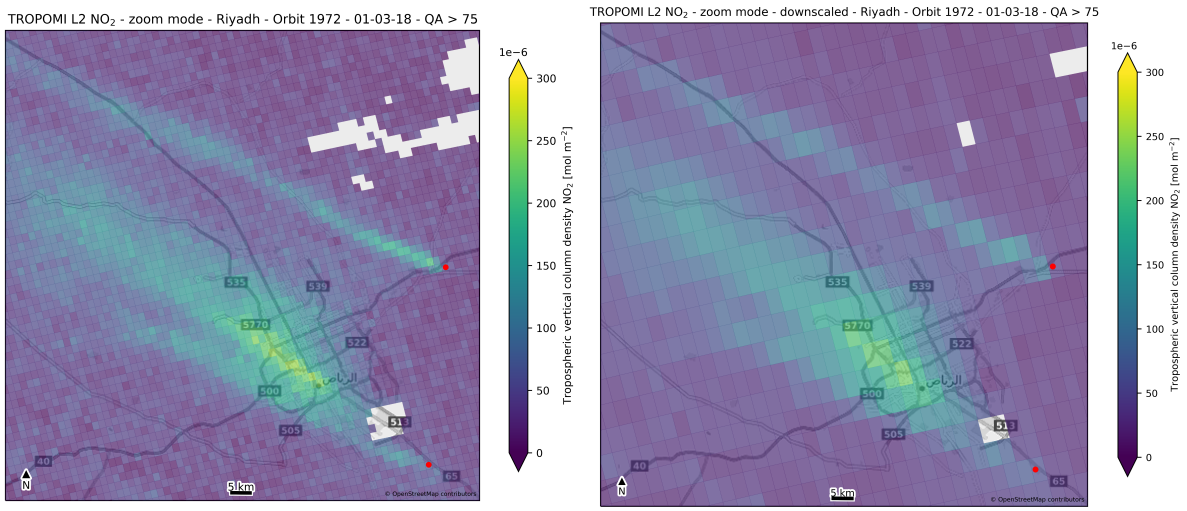

(a) (b)

Figure 3.9: TROPOMI zoom mode L2 tropospheric NO_2 at 01-03-2018, Riyadh (Saudi Arabia), with known power plants indicated with the red dots. Original zoom measurement (a) and downscaled to nominal TROPOMI resolution (b).

Figure 3.11 shows the comparison for the city of Mumbai. Comparing the two versions, the overall detail in spatial features over the city is considerably less in the downscaled version. Especially the plumes in the centre and on the left of this city, over the sea, do not show much structure, while they do in the original plot. Furthermore, the source right of the city might be mistaken to be part of the city in the downscaled version.

Figure 3.12 shows the comparison for a measured scene of the Rihand Power Station (India) and surrounding coal thermal power plants around the Govind Ballabh Pant Sagar reservoir. In the zoom mode version four plumes can be distinguished from another, originating from power plants. The wind direction causes the plumes from the middle three power plants on the left side of the reservoir to overlap with the power plant on the right side of the reservoir, where after the plumes appear to have merged into one another. In the downscaled version this would still be noticeable, although harder to spot, as the plumes of all power plants could be mistakes as one large plume. Furthermore, the detail of the plume shape and gradient in the plumes is significantly less in the downscaled version.

Figure 3.13 shows the comparison for the city of Lahore (Pakistan) and surrounding power plants. The level of detail of the zoom mode makes it easier to spot the power plants and the shape of the plumes is again better captured. The plume from the power plant next to Lahore passes over the city and seems to join the plume of the city, which would be harder to capture in the downscaled version.

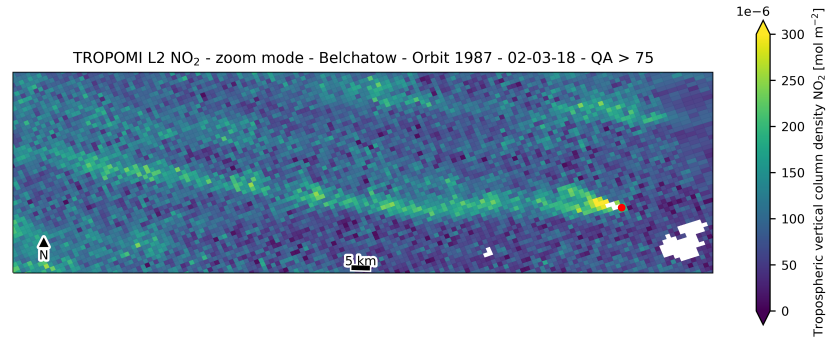

(a)

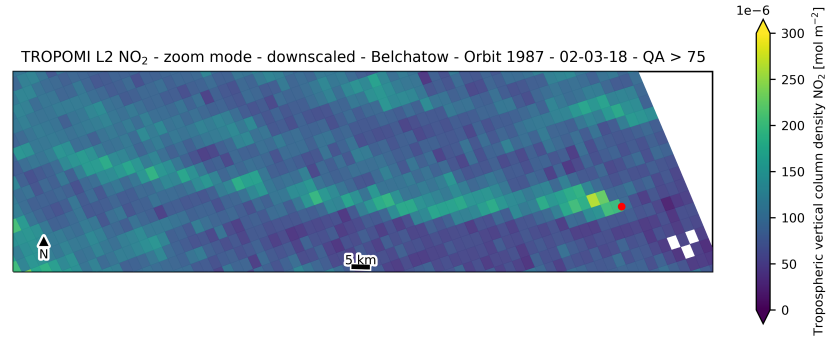

(b)

Figure 3.10: TROPOMI zoom mode L2 tropospheric NO_2 at 02-03-2018, Bełchatów (Poland), with known power plant indicated with the red dot. Original zoom measurement (a) and downscaled to nominal TROPOMI resolution (b).

Figure 3.14 shows the comparison of the plume originating from the neighbouring border cities Blagoveshchensk (Russia) and Heihei (China). This plume contains relatively low columns of NO_2 (maximum 80 μmol m^{-2}), however, is still well visible among the background noise. In the downscaled version the gradient within the plume is not as clear, and the shape is not as sharp as in the zoom mode version.

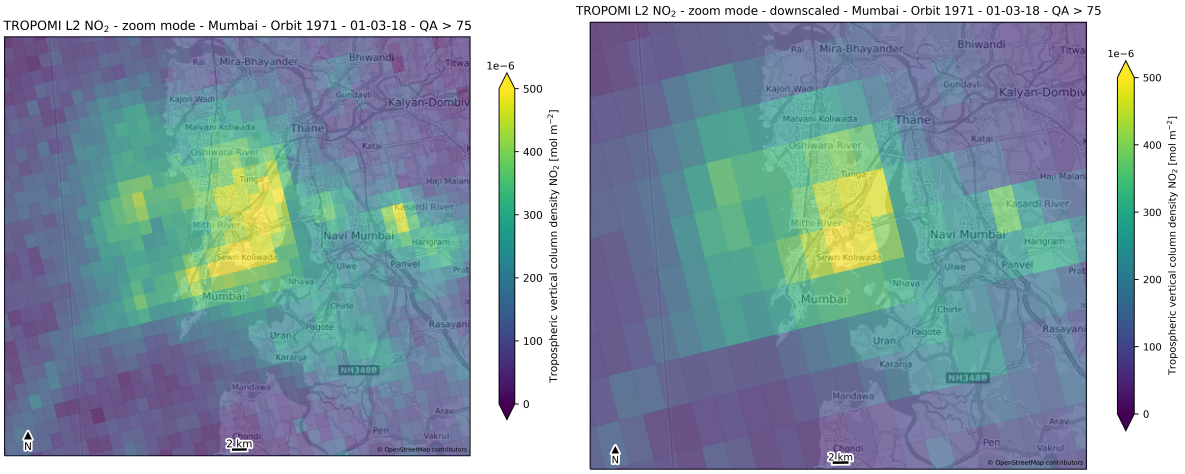

(a) (b)

Figure 3.11: TROPOMI zoom mode L2 tropospheric NO_2 at 01-03-2018, Mumbai (India). Original zoom measurement (a) and downscaled to nominal TROPOMI resolution (b).

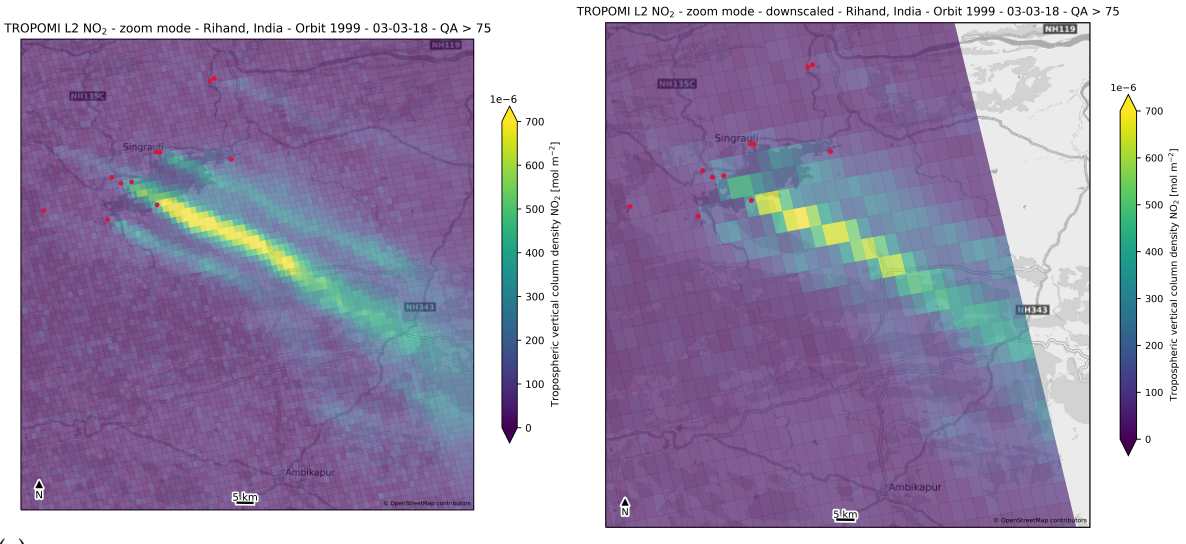

(a) (b)

Figure 3.12: TROPOMI zoom mode L2 tropospheric NO_2 at 03-03-2018, Rihand (India). Original zoom measurement (a) and downscaled to nominal TROPOMI resolution (b), with known power plants indicated with the red dots.

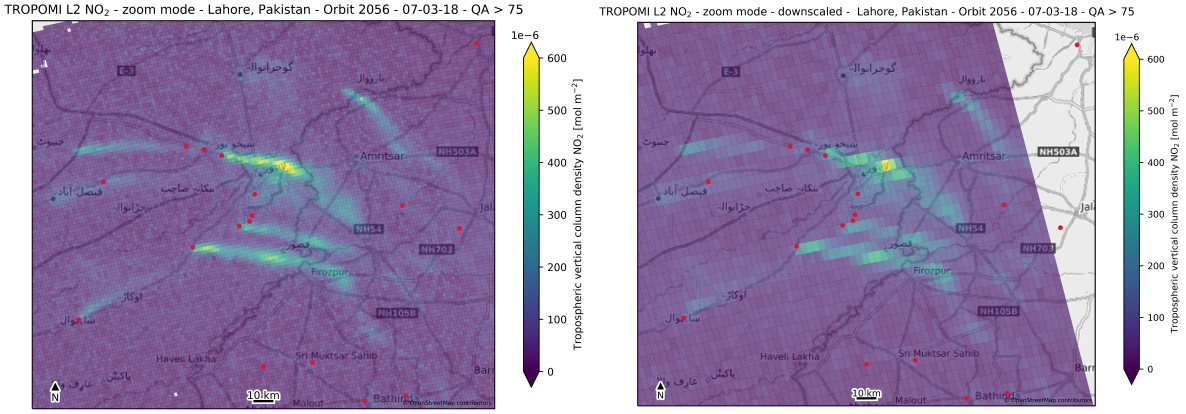

(a) (b)

Figure 3.13: TROPOMI zoom mode L2 tropospheric NO_2 at 07-03-2018, Lahore (Pakistan). Original zoom measurement (a) and downscaled to nominal TROPOMI resolution (b), with known power plants indicated with the red dot.

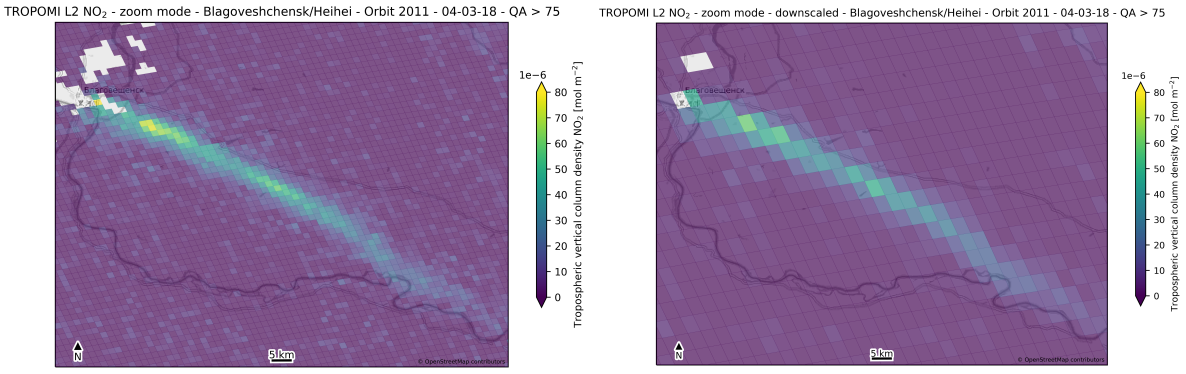

(a) (b)

Figure 3.14: TROPOMI zoom mode L2 tropospheric NO_2 at 04-03-2018, Blagoveshchensk (Russia) / Heihei (China). Original zoom measurement (a) and downscaled to nominal TROPOMI resolution (b).

To visualize the increase further, a 3D surface plot was made for the original zoom case and the downscaled resolution version. Figure 3.15 shows the comparison for Riyadh. The downscaled version resolved fewer peaks and has less detail than the original case, however, the background is smoother due to the noise being averaged out. Figure 3.16 shows the comparison for Mexico City, where the increase in detail is even more pronounced. Several peaks on the right side of the plot cannot be distinguished from one another in the downscaled version.

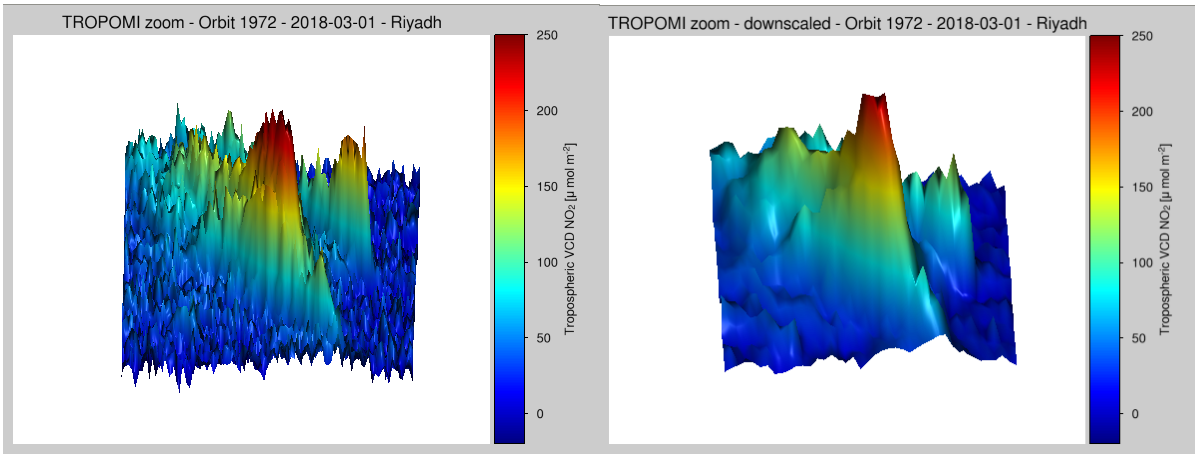

(a) (b)

Figure 3.15: TROPOMI zoom mode L2 tropospheric NO_2 at 01-03-2018, Riyadh (Saudi Arabia). 3D surface plot of original (a) and downscaled to nominal TROPOMI resolution (b).

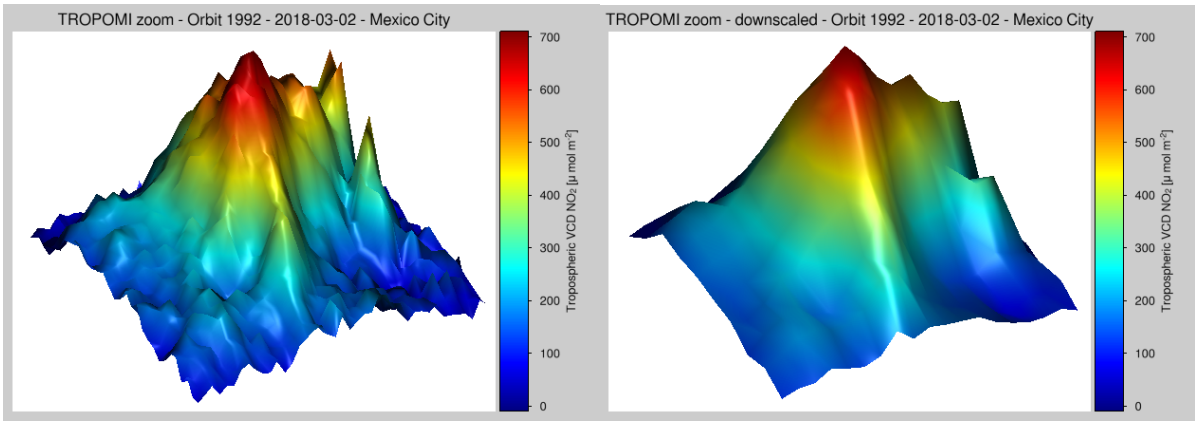

(a) (b)

Figure 3.16: TROPOMI zoom mode L2 tropospheric NO_2 at 02-03-2018, Mexico City. 3D surface plot of original (a) and downscaled to nominal TROPOMI resolution (b).

3.2.2 Quantitative comparison

To compare the effect of the increased spatial resolution on the retrieved tropospheric NO_2 column fields more quantitatively, two methods were found to be insightful. Both methods originate from the field of image processing and were not designed for this purpose, however, the essence of the method remains the same: to quantify the increase of information captured by a resolution change. After introducing the two methods, the methods are applied to several measurement cases and a comparison is made of their behaviour.

The first method is to use the Shannon entropy, which is defined in information theory as the expected amount of information in a message or the log-base-2 of the number of possible outcomes (Feixas et al., 2014). In an image the entropy can be calculated for a neighbourhood of pixel values, resulting in a local entropy per pixel. The local entropy map of an image gives a measure of the distribution of complexity[2]. Applied to our case, the local entropy is calculated for each pixel with a neighbourhood in the shape of a circle with a radius of 10 pixels. This shape and size seemed to capture the structures in the pollution plumes well. Then, the mean is taken of the local entropies to arrive at one measure for the image. This is done for the original zoom mode image and the downscaled version, re-sampled at the original pixel grid to preserve the amount of pixels. The change in mean local entropy can be used to quantify the change in information content. When comparing the zoom mode resolution to the nominal resolution, the differences in local entropy can be used as a measure for how much more information is captured by increasing the spatial resolution. Figure 3.17 shows the local entropy for zoom mode and the downscaled version of the previously shown Riyadh case (Figure 3.9). In this image the plumes have a higher local entropy than the background, since the measured values are distributed over a larger range. Comparing the two versions, the plume has a lower local entropy in the downscaled version than in the original. The background value also decreased in the downscale version, probably because the measurement noise of the original version is averaged out. A histogram of these two local entropy maps is shown in Figure 3.18, which shows the impact of the downscaling on the local entropy distribution. The mean of downscaled distribution is lower than the mean of the zoom mode distribution, while the shape remains relatively constant. Hence, the change in mean of the local entropy can be used as an indicator for the change in local entropy.

[2]Method obtained from: https://scikit-image.org/docs/dev/auto_examples/filters/plot_entropy.html.

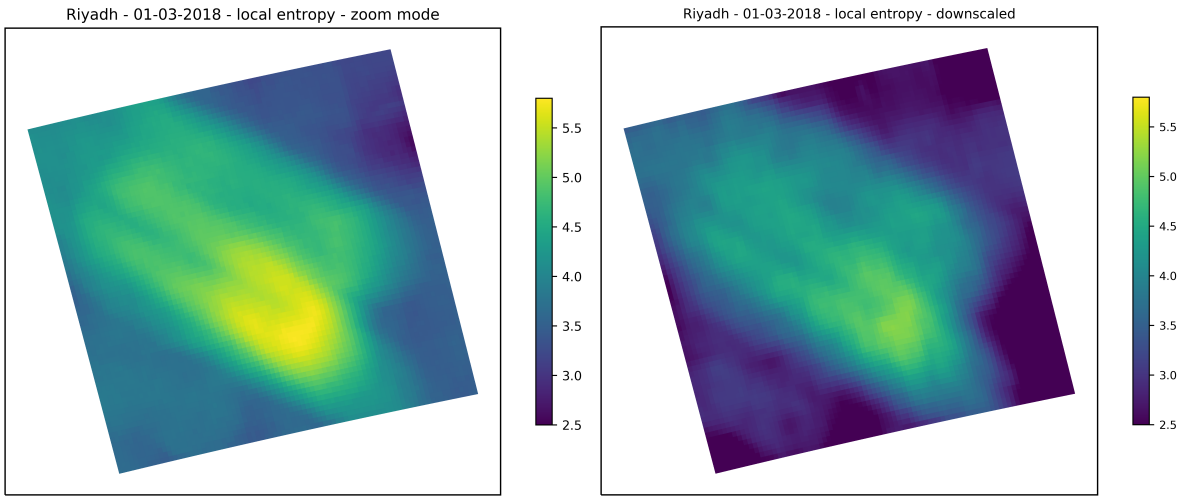

(a) (b)

Figure 3.17: Local entropy calculated for L2 tropospheric NO_2 at 01-03-2018, Riyadh (Saudi Arabia) (see Figure 3.9): Original zoom measurement (a) and downscaled to nominal TROPOMI resolution (b).

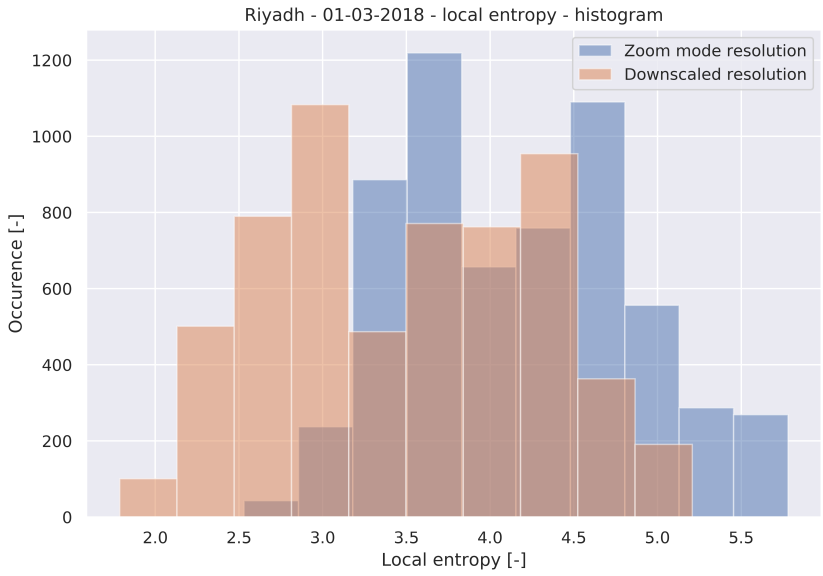

Figure 3.18: Histogram of local entropy for L2 tropospheric NO_2 at 01-03-2018, Riyadh (Saudi Arabia) (see Figure 3.9), original zoom measurement and downscaled to nominal TROPOMI resolution.

The second method is based on the image sharpness measure described in De and Masilamani (2013), which quantifies the quality of an image in terms of sharpness/blurriness using a Fourier analysis. The idea is that a sharper image contains higher frequency components than a blurry image. The algorithm to calculate this measure first computes the 2D Fourier Transform of the image of which the maximum value of the frequency component is defined as M. The measure is then defined as the percentage of pixels in the image in the frequency domain with a value higher than the threshold: $M/1000$. The threshold determines the scale of the measure and this value was taken from De and Masilamani (2013), which claims that experiments show that this particular threshold gives an accurate sense of image quality. To apply this to the retrieved NO_2 field, the downscaled version is resampled to the original grid

to preserve the amount of pixels. Figure 3.19 shows the centred Fourier spectrum for zoom mode and the downscaled version of the Riyadh case (Figure 3.9). In this figure, the centre of the plot shows the lowest frequency components, where the orientation of the increased values indicate the direction in the image that needs higher frequencies to describe (in this case perpendicular to the plume). The downscaled version shows a similar, yet slightly weaker, feature in the centre. However, artefacts are visible, probably caused by artificial patterns from the sampling and averaging. The pixels are averaged and then re-sampled to the original grid, creating blocks of pixels with equal pixel value, which appear as high frequency signals in the Fourier spectrum.

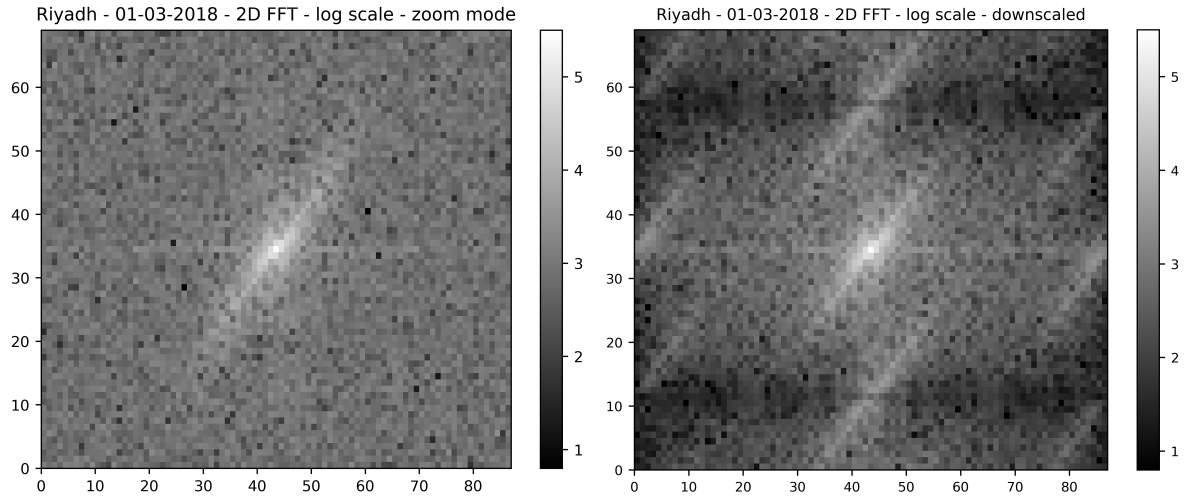

Figure 3.19: Image sharpness measure calculated for L2 tropospheric NO_2 at 01-03-2018, Riyadh (Saudi Arabia) (see Figure 3.9): Original zoom measurement (a) and downscaled to nominal TROPOMI resolution (b).

The two methods, referred to as *mean local entropy* and *image sharpness measure*, are applied to the downscaled version and original zoom mode version of the cases presented earlier in this section. Table 3.1 shows the results of these two methods applied to the downscaled resolution comparison cases. For all cases, both methods show a higher information content for the zoom mode resolution compared to the downscaled resolution, confirming the qualitative visual comparison. The *mean local entropy* method shows less increase between the two resolutions than the *image sharpness measure*. The *mean local entropy* method shows more or less the same values for the relative differences, while the values from the *image sharpness measure* are quite divergent. For the latter method, the lowest relative change is seen in the Blagoveshchensk (Russia) / Heihei (China) (indicated as *B. / H.*) and Mumbai cases, and the highest relative change in the Bełchatów and Lahore cases. When comparing the zoom-mode and downscaled versions of NO_2 column maps for the same cases in Section 3.2, the found results can be explained to some extent. For example, the Lahore case (Figure 3.13) does indeed show larger difference in plume detail than the Blagoveshchensk / Heihei case (Figure 3.14) or the Mumbai case (Figure 3.11), although opinions on this matter are rather subjective.

One interesting observation is that the scene with the largest relative increase for the *mean local entropy* method (Blagoveshchensk / Heihei case), has the smallest increase for the other method. This might be due to the relative small NO_2 columns in this scene (see Figure 3.14), which increases the relative contribution of the background noise on the mean local entropy. Neither of the methods show a clear differentiation between the information content increase for cities (Mumbai, Riyadh) and power plants.

The last row contains a *background test*, where a remote unpolluted area over the Pacific Ocean was chosen where no tropospheric NO_2 signals are present except for measurement noise. Therefore, the change in information content in this scene will be solely due to changes in the background noise, where the downscaled version contains less noise due to averaging. This test shows us that the *mean local entropy* method sees a large increase when resolution is increased, because the noise increases the entropy. The *image sharpness measure* shows a small decrease when increasing resolution, which is closer to the desired behaviour that is being sought (i.e. no change), since the goal is to quantify information content and not noise.

The *image sharpness measure* method thus experiences less influence from the background noise and, although resulting in quite diverging values, resembles the differences in information content as appear from visual comparisons. Therefore, the *image sharpness measure* method seems more suitable for the purpose of quantifying gain in information content of polluted NO_2 column fields due to resolution changes,

Table 3.1: Two methods applied to the original zoom mode image and the downscaled resolution version that quantify the change in information content. The *downscaled* and *zoom* columns present the quantity as obtained from applying the method to the downscaled resolution and original version, respectively. The columns *Diff.* and *Diff [%]* denote the absolute and relative difference, respectively, between the two versions. *B. / H.* denotes the Blagoveshchensk (Russia) / Heihei (China) case.

Scene	**Mean local entropy**				**Image sharpness measure**			
	Downscaled	Zoom	Diff.	Diff. [%]	Downscaled	Zoom	Diff.	Diff. [%]
Riyadh	3.50	4.18	0.68	19	0.15	0.34	0.19	127
Bełchatów	3.80	4.65	0.85	22	0.12	0.32	0.20	167
Mumbai	4.75	5.72	0.97	20	0.24	0.35	0.11	46
Rihand	3.88	4.73	0.85	22	0.21	0.38	0.17	81
Lahore	3.70	4.59	0.89	24	0.17	0.50	0.33	194
B. / H.	0.78	1.21	0.43	55	0.37	0.47	0.10	27
Background test	0.85	1.57	0.72	85	0.55	0.50	-0.05	-9

3.3 Comparison with nominal measurements

In this section three scenes from the zoom mode dataset are compared to nominal TROPOMI measurements of that area. After comparing the zoom mode data to synthetic low resolution scenes in the previous section, the next step is to compare the data-set to actual low resolution scenes from TROPOMI. However, since these are different scenes, with different emissions and meteorological conditions, the comparison is more qualitative of nature. The scenes, Riyadh, Mumbai and Mexico City were chosen because they have a relative low cloud probability, are strong NO_2 sources and experience low inflow from other sources. Scenes were selected based on their similarity to the pollution patterns and levels in their corresponding zoom mode scenes, while also minimizing the possible effect of seasonality, to allow for a better comparison. The used data-sets are available from the Copernicus Open Access Hub (https://scihub.copernicus.eu/), from which the reprocessed (*RPRO*) or offline (*OFFL*) streams where chosen of the TROPOMI Level-2 NO_2 products.

For the three scenes, maps are shown for the zoom mode and nominal measurements in Figures 3.20, 3.23 and 3.25, to demonstrate the effect of the increased resolution. To compare the effect further, the pixels of each image are sorted in ascending order of NO_2 vertical column density in Figures 3.21, 3.24 and 3.26, including their measurements precision, which gives insight into the distribution of the measured values.

Figure 3.20 shows the comparison plots for Riyadh, Saudi Arabia, as presented before in Figure 3.1, with two power plants indicated. In the nominal measurement, the wind direction is almost opposite, exposing another point source left of the city. Apart from the wind direction change, the scenes look quite similar, also the measured maxima do not differ much. Similar to the comparison between the zoom mode measurements and the downscaled resolution simulated measurements in Section 3.2, the level of detail of the enhanced NO_2 plumes is significantly higher at higher spatial resolution. The plume shape and the gradient within the plumes are better captured.

In Figure 3.21 the comparison is made between the two resolutions by means of plotting the measured vertical column densities sorted by ascending value. Since the higher resolution mode has six times more measurements, the measurement number is normalised with the total number of measurements, to allow for a more meaningful comparison. The measurement precision (1-sigma) is shown as shaded area around the line. The left-hand side shows the complete plot and the right-hand side shows a cut-out of the highest measured values. The change in shape of the curve can be explained by the increase of background noise in the zoom mode. This leads to more dispersion of the background measurements with low VCD value, tilting the curve counter-clockwise. In the final part of the curve, where the polluted pixels are located, the two resolutions show similar behaviour. The zoom mode is expected to measure higher maximum values than the nominal mode, since the pixel size is smaller, and peaks are better captured. It should be noted that analysed scenes were measured on different days, which was unavoidable because of the different instrument settings. Therefore, interpretation is more difficult, and comparisons of this behaviour is better done with simulations than with real measurements, since real scenes are never identical on different days. One thing that can be noticed is the increasing measurement uncertainty of the nominal mode for the top VCD values, up to the same value of the zoom mode measurements.

At these relatively high NO_2 column values the contribution from the air mass factor uncertainty increases, as this quantity scales with the column value and is indifferent of the spatial resolution. This causes the uncertainty of the two modes to be more or less equal for this part of the curve.

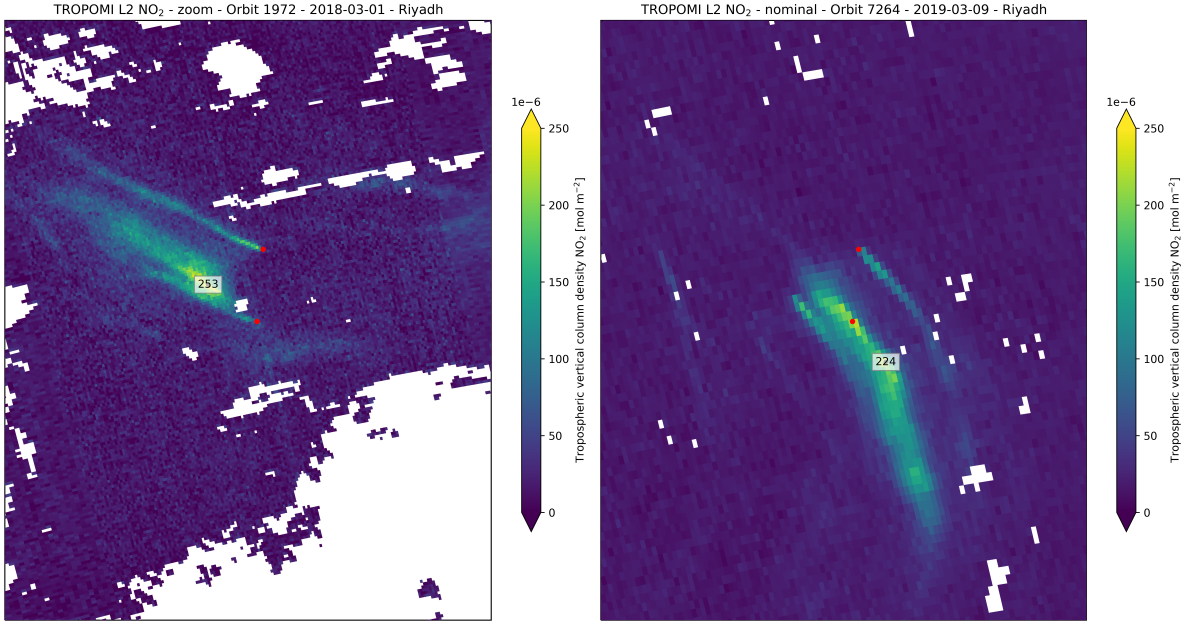

(a) (b)

Figure 3.20: TROPOMI L2 tropospheric NO_2 VCD measurements of Riyadh (Saudi Arabia). Zoom mode measurements at 01-03-2018 (a) and nominal measurements at 09-03-2019 (b). Power plants and maximum measured value indicated.

Figure 3.22 shows the VCD uncertainty of the zoom and nominal mode scenes in Figure 3.20, as propagated by the retrieval algorithm (see Section 1.6). Comparing the VCD with the VCD uncertainty, the plots seem identical, except for the values on the colorbar. This is due to the scaling behaviour of the VCD precision with the VCD value itself. In the zoom mode plot the effect of changes in the binning scheme are visible as a line where the uncertainty experiences a jump. Furthermore, the background value of the uncertainty is higher due to the increased noise.

In Figure 3.23 the comparison is shown for the Mexico City scene, as seen before in Figure 3.7. A high increase in detail is visible, as emissions from neighbourhood and motor ways are significantly more visible in the high resolution measurements compared to the nominal ones. It should be noted that the pixels in the nominal measurements are located towards the edge of the swath, which leads to increased pixel size compared to nadir. Nonetheless, this data is used in the daily global NO_2 product. The measured maximum is reasonably higher in the zoom mode, however, this can also be explained by the difference in scene. The plot containing the sorted VCD curve for these scenes are shown in Figure 3.24. Again, the zoom mode curve is tilted counter-clockwise due to the increased background noise. However, the hinge-point is located more to the left than in the Riyadh case, since there are relatively fewer background pixels. High VCD values occur more frequently in the zoom mode than in the nominal mode scene. The increase of measurement error for increasing VCD value is

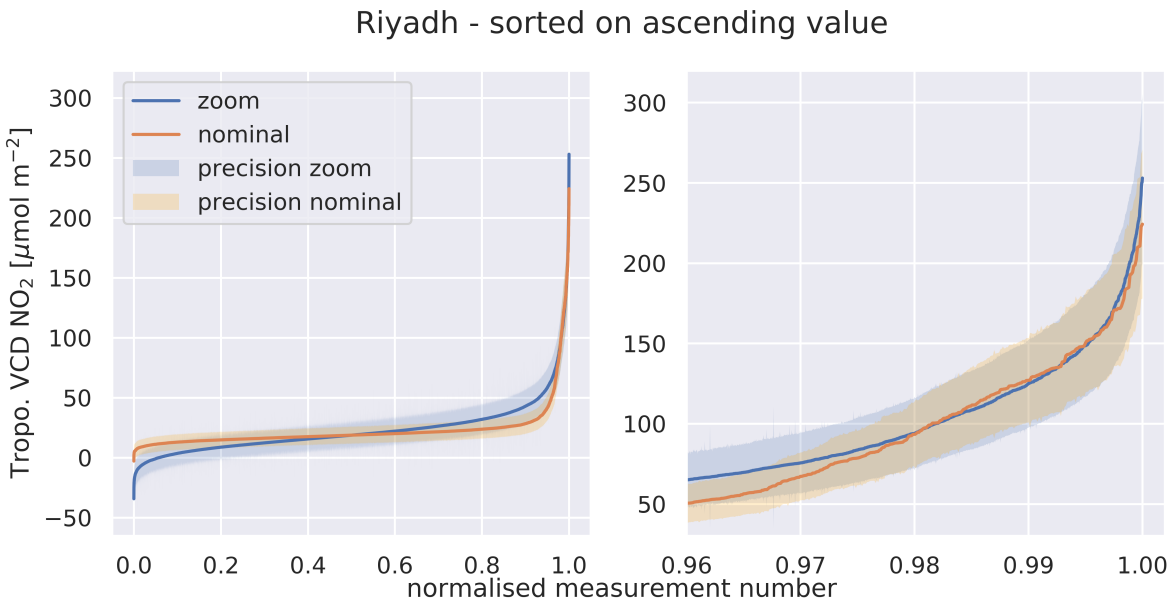

Figure 3.21: Comparison of VCD measurements sorted in ascending order for Riyadh (Saudi Arabia) on 01-03-2018 in zoom mode and on 09-03-2019 in nominal mode. Left figure shows complete plot, right figure shows cut-out of highest VCD values.

well visible in both modes, where the zoom mode has an overall larger error because of the lower SNR. The difference in uncertainty is larger in this case than in the previous case for Riyadh, since the pixel size of the nominal mode is larger. The uncertainty for high column values is larger for the zoom mode than for the nominal mode, unlike the Riyadh case. This can be caused by different air mass factors between the two scenes and the larger difference in pixel size between the two modes.

Finally, the comparison is made for Mumbai (India) in Figure 3.25, previously shown in Figure 3.6. The scenes do look quite different from one another, however, comparing the two still demonstrates the effect of resolution increase. The nominal mode scene pixels are located more towards the edge of the swath, increasing the pixel size. Significantly more detail is visible in the higher resolution, within the city suburbs, the plume shape and point source on the right. The measured maxima are approximately the same. The sorted VCD curve in Figure 3.26 shows the tilting behaviour less pronounced as the previous two cases, most likely because the there are relatively even fewer background pixels and the two scenes of this case are less comparable to each other. The right part of the curve shows more frequent high VCD values for the higher resolution case, with again increased measurement error. The highest VCD values measured in the nominal scene show a sudden increase in value and error, which can be explained by Figure 3.25b, where there is a large difference in column value between the pixels with the largest column and the surrounding pixels. For these large columns the air mass factor error contribution becomes larger, which increases the measurement precision of the nominal mode to similar values as from the zoom mode.

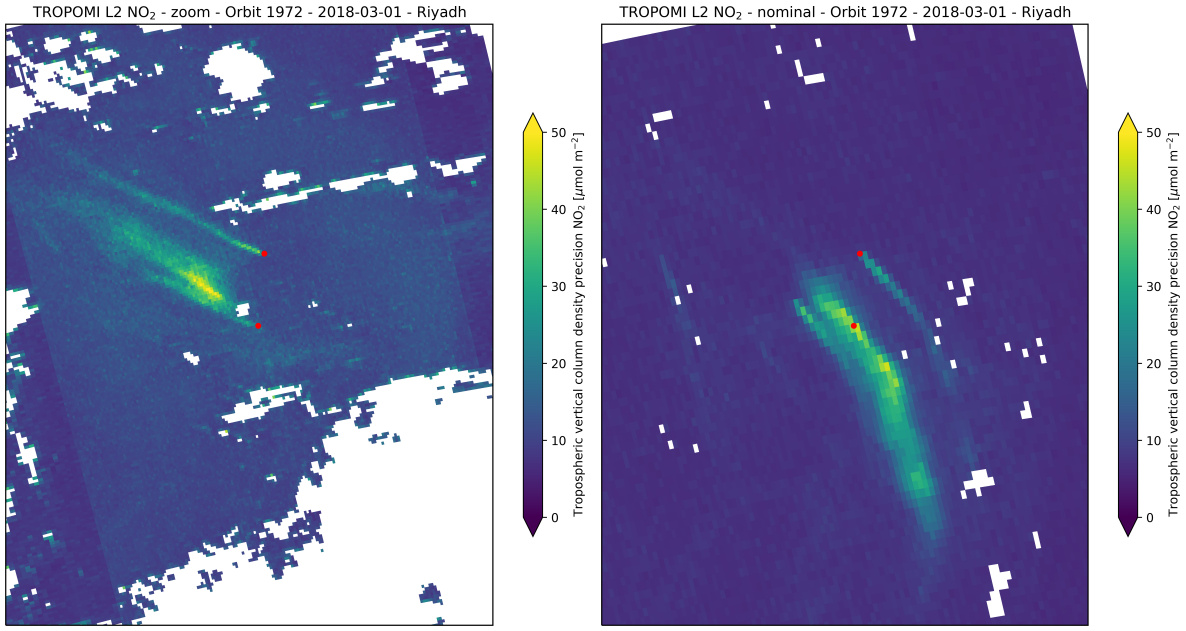

(a) (b)

Figure 3.22: Uncertainty of TROPOMI L2 tropospheric NO_2 VCD measurements of Riyadh (Saudi Arabia). Zoom mode measurements at 01-03-2018 (a) and nominal measurements at 09-03-2019 (b).

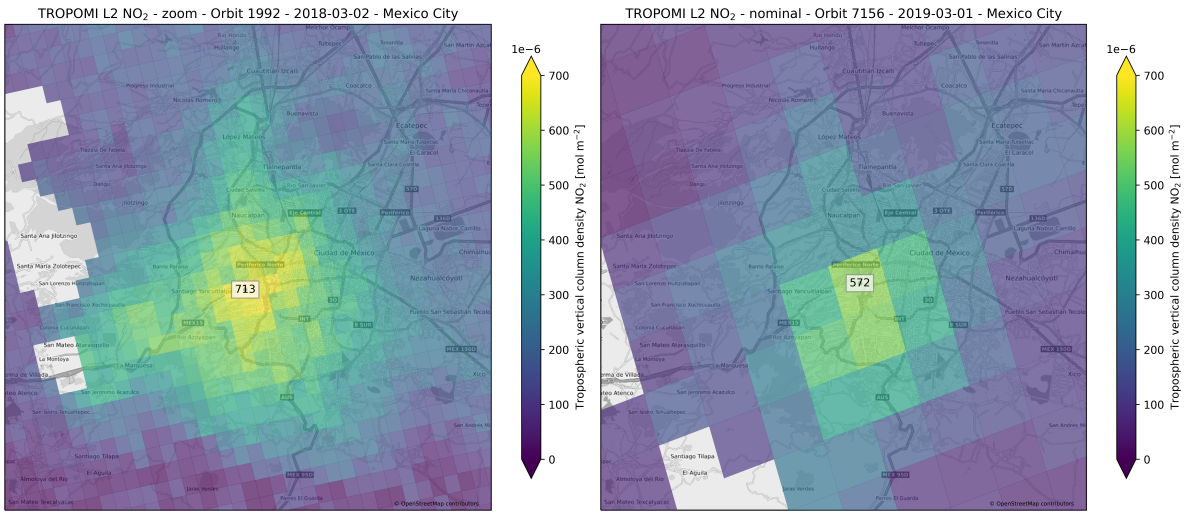

(a) (b)

Figure 3.23: TROPOMI L2 tropospheric NO_2 VCD measurements of Mexico City. Zoom mode measurements at 01-03-2018 (a) and nominal measurements at 03-03-2019 (b). Maximum measured value indicated.

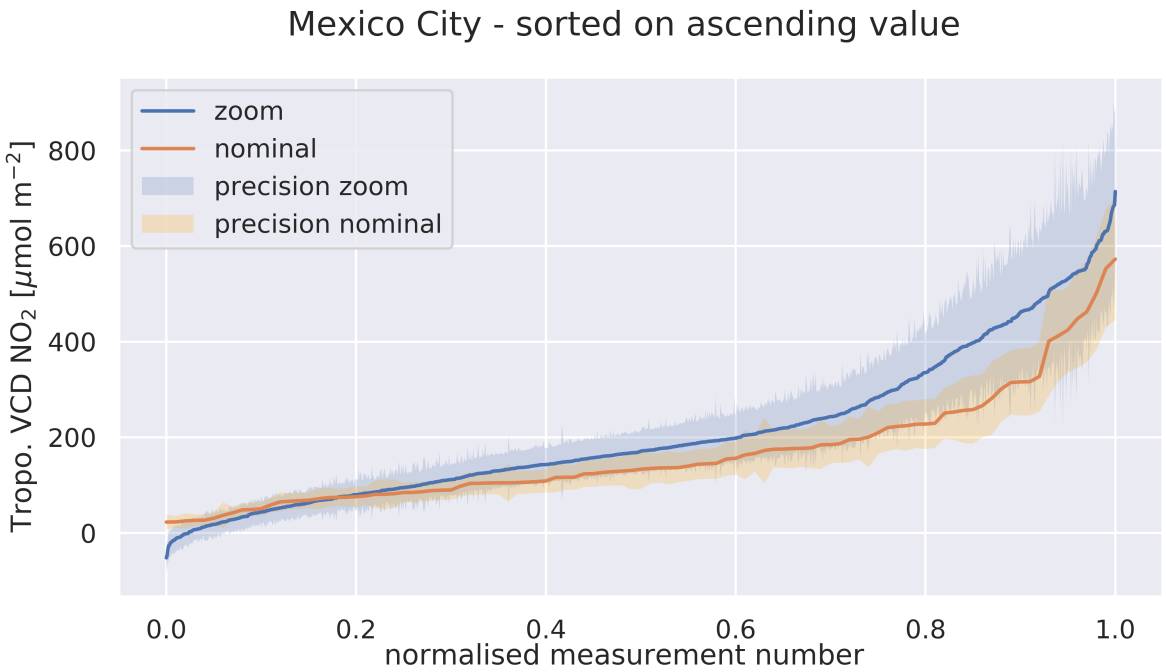

Figure 3.24: Comparison of VCD measurements sorted in ascending order for Mexico City on 01-03-2018 in zoom mode and on 03-03-2019 in nominal mode.

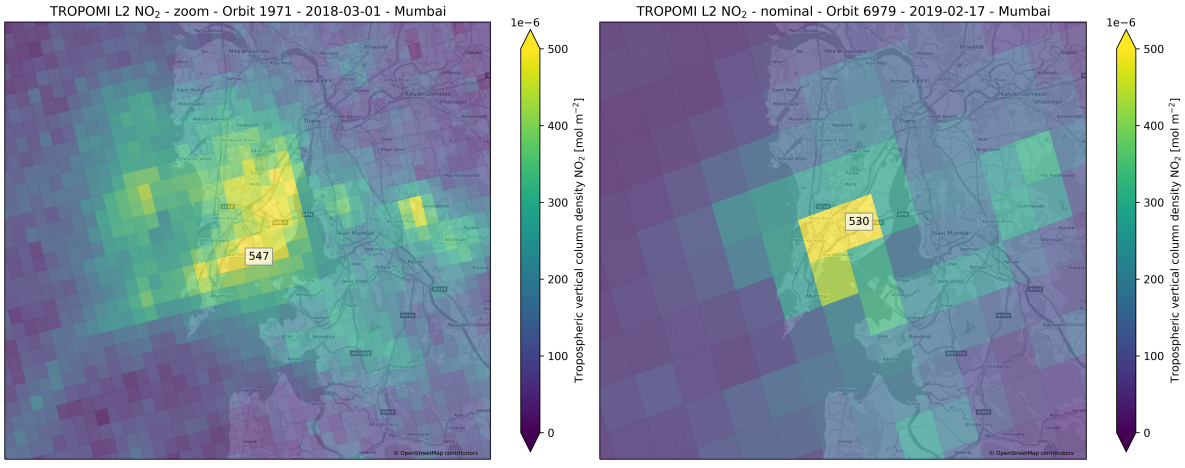

(a) (b)

Figure 3.25: TROPOMI L2 tropospheric NO_2 VCD measurements of Mumbai (India). Zoom mode measurements at 01-03-2018 (a) and nominal measurements at 17-02-2019 (b). Maximum measurement value indicated.

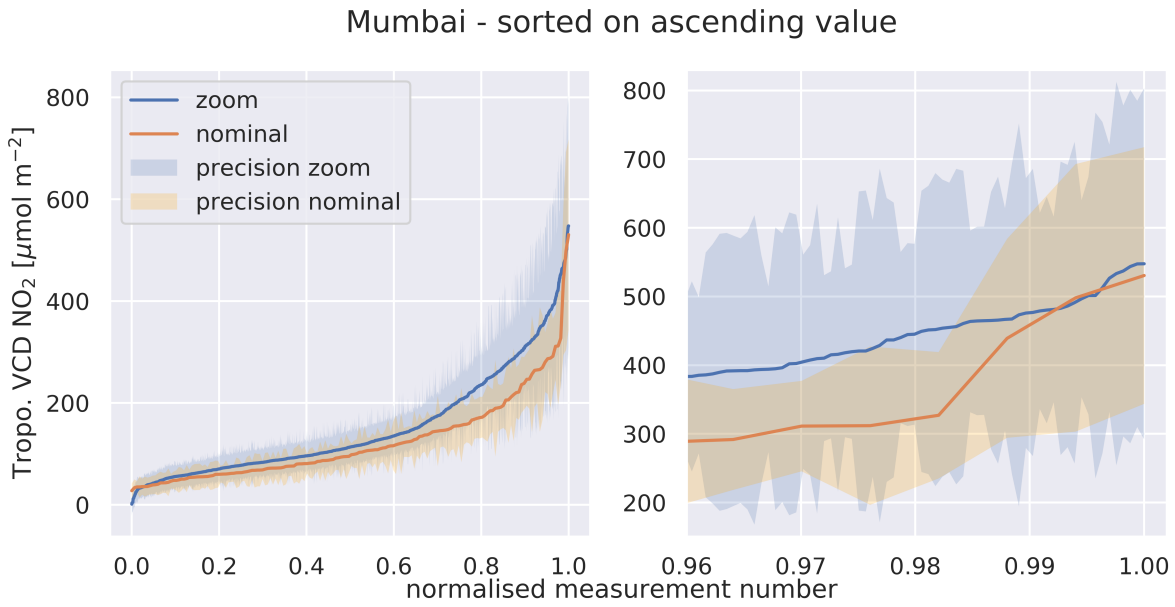

Figure 3.26: Comparison of VCD measurements sorted in ascending order for Mumbai (India) on 01-03-2018 in zoom mode and on 17-02-2019 in nominal mode.

3.4 Spatial resolution analysis

The TROPOMI zoom mode observations provide the ideal data-set for a close examination of the response of a single detector pixel. By using the zoom mode, the instrument settings are set to allow for read out of single detector pixels, with a minimum integration time. Since these settings seek out the limit of the detector, effects such as smearing or memory effect/hysteresis of the frame read-out could occur. In this section it is investigated if this was the case for the zoom mode instrument settings.

In the study describing the zoom-mode measurements of OMI, (Valin et al., 2011a), the spatial response of the single detector pixels was determined by comparing the measured reflectance to a higher spatial resolution co-located data-set. For this case top-of the-atmosphere (TOA) reflectances from the MODIS satellite instrument were used. The shift in reflectance at a sharp boundary, for example a coastline, was compared to the MODIS reflectance, to put an upper limit on the spatial resolution of the OMI detector.

A similar approach is followed for the TROPOMI zoom measurements. Reflectance measurements from the Visible Infrared Imaging Radiometer Suite (VIIRS) instrument, on-board the Suomi National Polar-orbiting Partnership (Suomi-NPP) satellite, are used as resolution benchmark. Sentinel-5P flies in close formation with Suomi-NPP, with an offset of less than 5 minutes in overpass time and overlapping swath, which allows for close temporal and spatial co-location of both measurement sets. The VIIRS moderate resolution band M2 has an overlapping wavelength range with TROPOMI band 4, so the reflectance is taken for the same spectral range. This eliminates the spectral dependency of the measured surface reflectance. The VIIRS band has a spatial resolution of 750 m (NASA Goddard Space Flight Center, 2018). First, the applied operations are discussed for the TROPOMI and VIIRS data, after which the method is applied for the along-track and cross-track dimensions using suitable scenes.

The reflectance of the TROPOMI zoom mode is calculated using the radiance and irradiance from the L1B zoom mode data-set from band 4. The reflectance spectrum R is calculated by dividing the measured TOA radiance I by the measured solar irradiance E_0 and correcting for the solar zenith angle (SZA) per detector pixel:

$$R(\lambda) = \frac{\pi\, I(\lambda)}{\cos(SZA)\, E_0(\lambda)} \tag{3.1}$$

The reflectance of the VIIRS data-set is taken from the VIIRS L1B product, where the M2 band is used. This broadband has one reflectance value integrated for the wavelength range of 436-454 nm. The TROPOMI bands are hyperspectral, meaning it is sampling many wavelengths in a certain wavelength band. For example, band 4 has a wavelength range of 405-500 nm with a spectral resolution of 0.5 nm. To compare the two reflectances fairly, the subset of the TROPOMI band 4 spectral reflectance, overlapping with the VIIRS broadband M1 reflectance, is integrated over the wavelength range. The spectral response function of the VIIRS M2 band is not block shaped Moeller and Moyer (2011) and thus the measured radiance and irradiance differ from the ones measured by TROPOMI. However, since we only consider the Earth's surface reflectance, which is the Earth's radiance divided by the solar irradiance measured with the same instrument, these differences cancel out and are irrelevant for this analysis.

The best case for this method has a sharp boundary in the topography, resulting in a sudden jump in reflectance. For example a sharp coastline, where the contrast in reflectance between the ocean and the land is high, for instance, desert land. For a decomposition in the along-track dimension of the detector, a coastline perpendicular to the direction of flight is best. Analogous, a coastline parallel to the direction of flight is best suited for analysis of the cross-track direction. Once a suitable area is chosen by using the TROPOMI reflectance, the matching VIIRS pixels are selected. The selected area is reduced in one dimension by taking the average of the pixels perpendicular to the direction of interest, so the two reflectances can be compared in a line plot. The distance used for the line plot is calculated from a arbitrary point along the line plot to indicate the spatial resolution.

For the along-track direction the southern coastline of Jemen was chosen (Figure 3.27), observed by TROPOMI at 01-03-2018 (orbit 1972). The area indicated in red in the lower two plots show the area used for the calculation. The coastline is quite sharp and nearly perpendicular to the direction of flight. Just besides the coastline is a strip of vegetation, which results in a spot of high reflectance in this band. Figure 3.28 shows a scatter-plot of the two reflectance sets across the coastline. The VIIRS pixel resolution of 750 m is three times smaller than the along-track dimension of the TROPOMI zoom pixel, as approximately 4 VIIRS points span the same distance as two TROPOMI points. The two data-sets are generally in good agreement with only some scatter in the vegetated area (the second peak). The first 'jump' shows an instantaneous response to the coastline in the TROPOMI points, with one pixel half-way the jump, indicating a good response of the pixel in the along-track direction. The jump spans 2 TROPOMI pixels and between 6.5 VIIRS pixels, which agrees approximately with 2.4 km. The along-track pixel dimension is determined by the integration time of the detector. Between two consecutive frames a memory effect can occur, which means the pixel value of the preceding readout is affecting the current readout. If this had occurred, signs of this effect could have been visible in the downward section of the second peak in the line plot. In that section the TROPOMI pixel readings would have been higher than the VIIRS pixels, as the preceding pixel values are higher. Since this is not the case, there seems to be no substantial memory effect present in the detector pixel readout for the decreased integration time of the zoom mode.

For the cross-track direction the coastline of Libya was chosen, measured at 01-03-2018 (TROPOMI orbit 1973). Figure 3.29 indicates the location of the coastline and shows the measured reflectances of the coastline. The coastline is not perfectly straight, however, is in good alignment with the direction of flight and has a reasonable sharp boundary. Figure 3.30 shows the reflectances in the cross-track direction across the coastline. It seems there is less agreement between the two data-sets than in the Jemen case, however, the range of the y-axis is much smaller, amplifying the differences. The pixel size of VIIRS (750 m) is 2.4 times smaller than the across-track dimension of the TROPOMI zoom pixel (1.8 km). When looking at the jump in reflectance across the coastline, VIIRS spans 7 pixels, while TROPOMI spans 3 pixels, which translated to resolution corresponds approximately with 1.8 km. The jump in reflectance is not instantaneous in either of the data-sets, but distributed over several pixels, which makes it hard to say something about TROPOMI's pixel smear in the cross-track direction. However, there are no obvious signs of smear between the unbinned pixel rows,

which would appear as a smoothing of the jump, since it follows the VIIRS measurements quite well. A sharper jump from a more suitable coastline or other natural feature would provide more insight, however, this was not found in the data-set.

According to the Sentinel 5P L1B product requirements, the geolocation knowledge shall be better than 0.1 spatial sampling distance (SSD) for all spatial samples (requirement *MR-LEO-SYS-10* in (ESA Mission Science Division, 2017)). Since this is the requirement for the nominal pixel size (7.1 x 3.6 km), this results in a geolocation accuracy requirement of, at least, 710 m in along-track direction and 360 m in cross-track direction. Using the relatively small pixels of the zoom mode data, this geolocation accuracy can be studied in more detail. The VIIRS pixel size of 750 m is close to the geolocation accuracy requirement of the TROPOMI L1B pixel in the along-track direction of 710 m, which allows for an assessment of the geolocation accuracy. The two reflectance data-sets in the line plot (Figure 3.28) show a good spatial alignment when resolving the coastline reflectivity jump. If the geolocation accuracy would not have met the requirement, the alignment of the two data-sets would have been off. From this qualitative comparison it appears the accuracy requirement of the geolocation in the along-track direction is met. Since the required accuracy in the cross-track direction is smaller (360 m), the VIIRS data-set could not provide further insight into the validation of the geolocation performance.

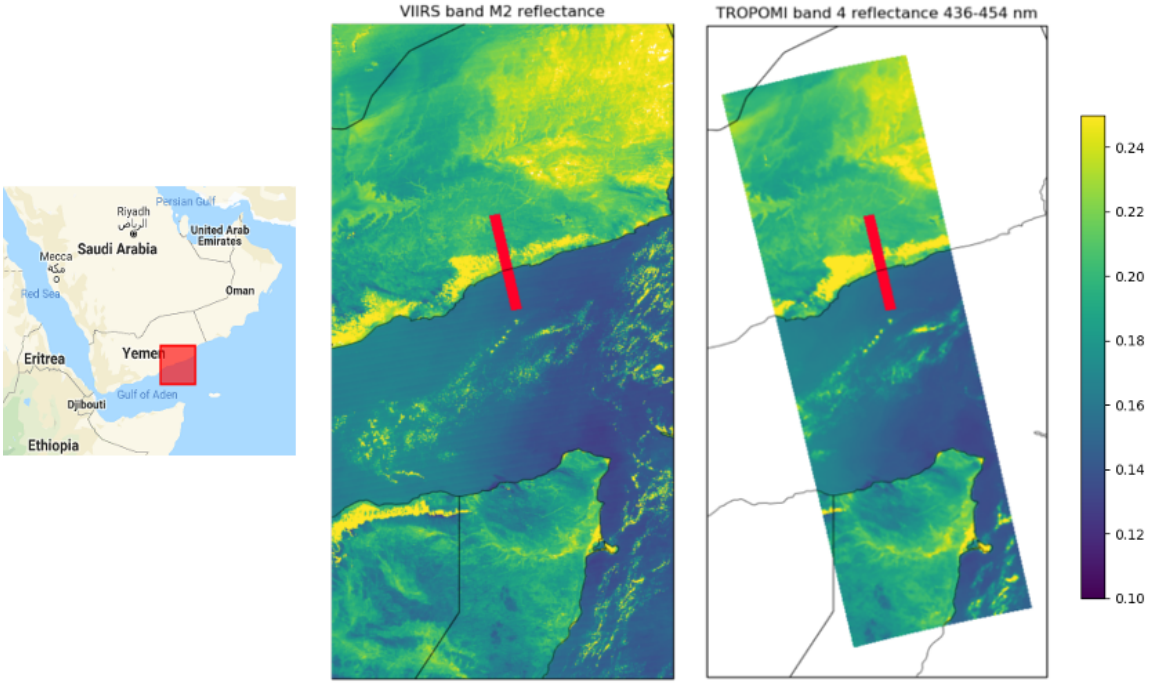

Figure 3.27: Map of TROPOMI and VIIRS L1B reflectances across Jemen coastline. Direction of flight is northwards.

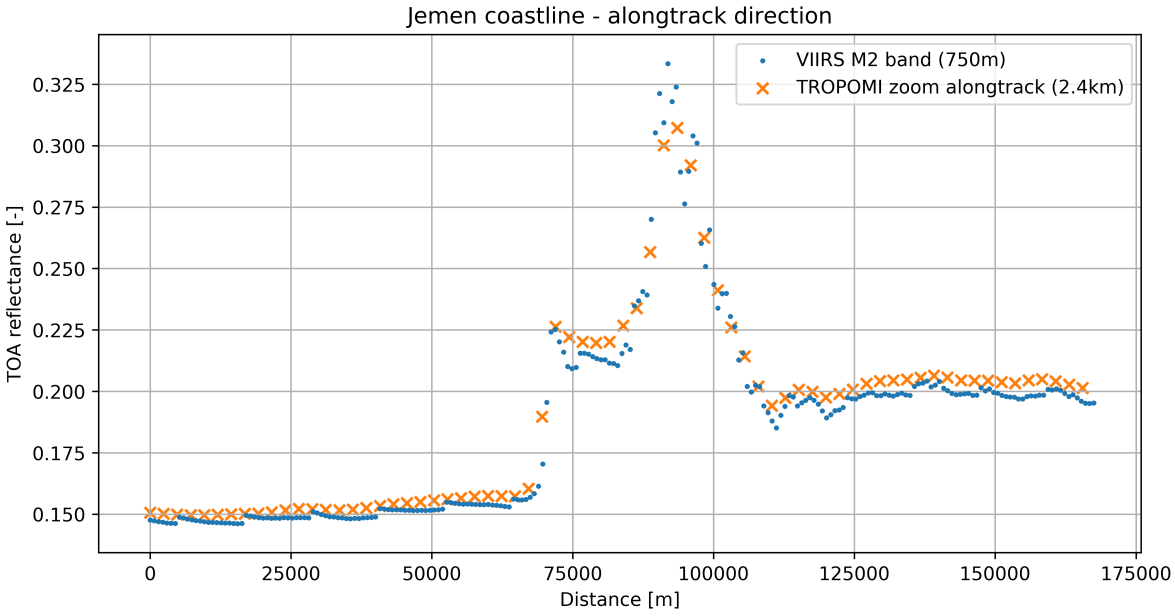

Figure 3.28: Comparison of TROPOMI and VIIRS L1B reflectances across Jemen coastline, plotted from south to north.

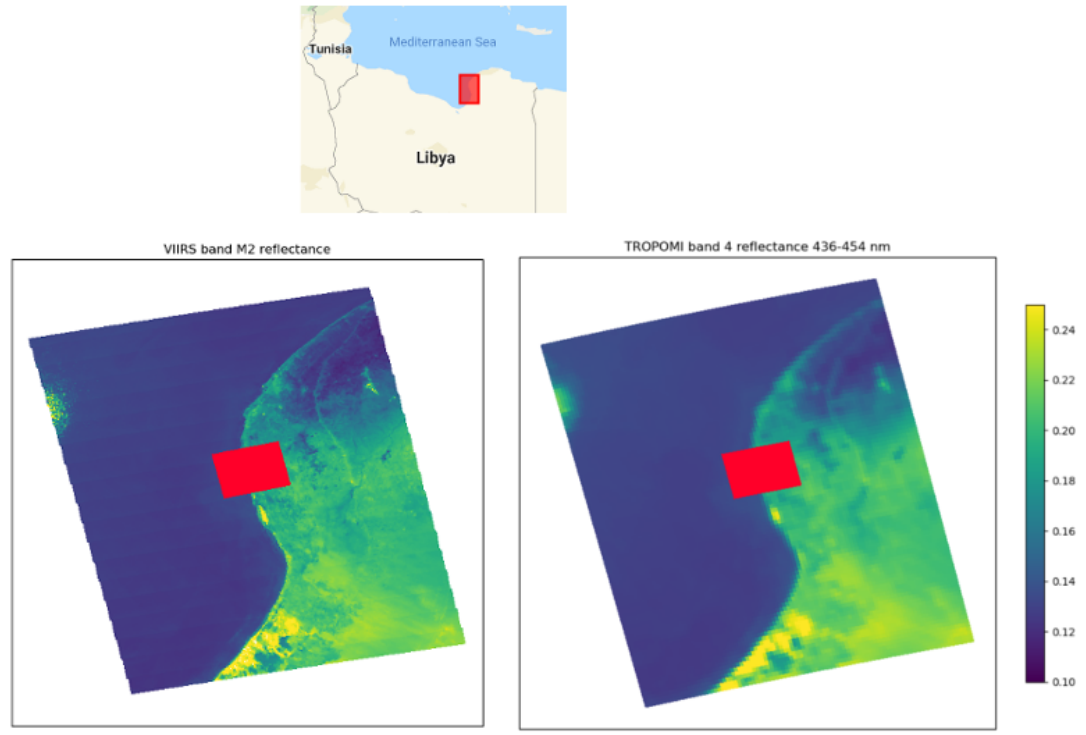

Figure 3.29: Map of TROPOMI and VIIRS L1B reflectances across Libya coastline. Direction of flight is northwards.

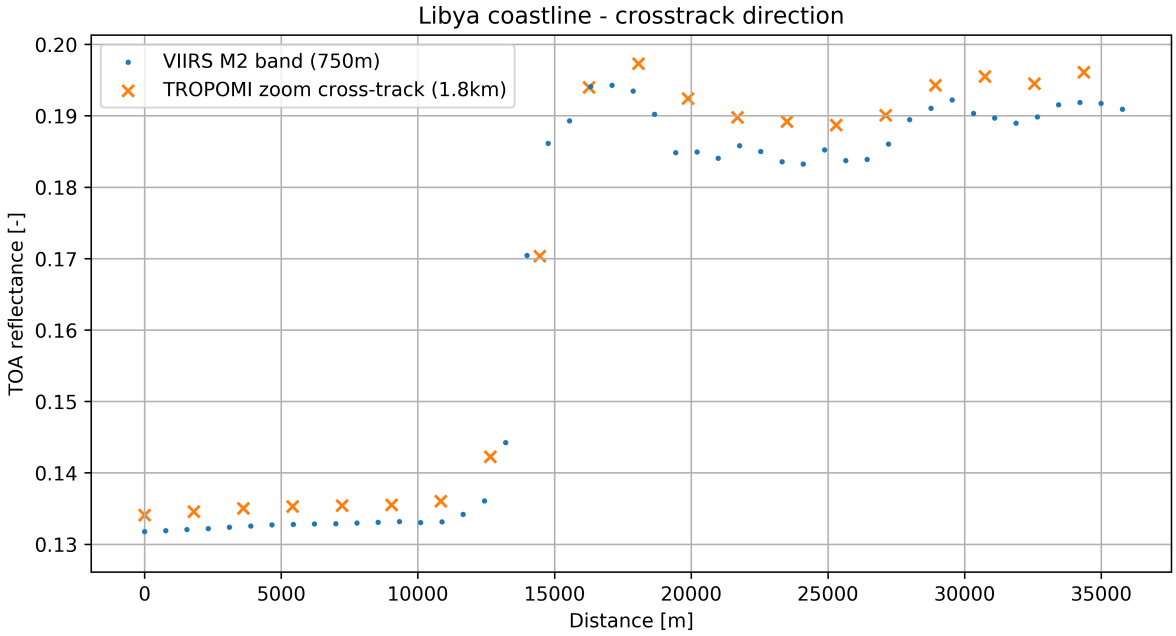

Figure 3.30: Comparison of TROPOMI and VIIRS L1B reflectances across Libya coastline. Plotted from west to east.

3.5 NO_2 VCD error analysis

The total error in the retrieved tropospheric vertical NO_2 column densities is calculated in the algorithm from the slant column error, the stratospheric column error and the tropospheric air-mass factor error (see Section 1.6). For small tropospheric columns the error is dominated by random error in the spectral fitting, while for larger columns the uncertainty from the air-mass factor dominates. The total tropospheric VCD error can be approximated to first order as $8.3 + [0.2\ to\ 0.5] \cdot VCD_{tropo}\ \mu mol/m^2$ (van Geffen et al., 2019). In this section a comparison is made between the VCD error of the TROPOMI L2 zoom mode measurements and a set of nominal mode measurement, to assess the impact of the zoom mode instrument settings on the measurement uncertainty.

The zoom mode measurements of orbit 1971 to 1994 are compared with normal measurements of orbit 2198 to 2221. These two sets are separated by one orbital cycle, approximately 16 days, which results in the same measurement locations and viewing geometry. These two datasets contain different states of the atmosphere and different NO_2 columns, thus instead of investigating the VCD error itself, the relation between the VCD error and the measured VCD is looked into. The tropospheric NO_2 VCD error, also called 'precision', is plotted against the VCD measurement as a scatter plot for the zoom and nominal modes in Figure 3.31. The points of the two data sets are each fitted with a simple linear regression model. From first sight, the zoom mode seems more scattered than the nominal mode at small columns and larger in general. The regression results in the following fits: zoom mode $y = 0.179x + 11.7$ ($R^2 = 0.75$) and nominal mode $y = 0.193x + 5.66$ ($R^2 = 0.90$). In these relationships, the slope is approximately the same (factor 0.92), however, the interception point is about twice as large (factor 2.08) for the zoom mode as for the nominal mode. There appears to be a segregation of the error for each mode into two branches, which could be caused by a discretization or split somewhere along the error propagation, however the exact cause remains unknown. Figure 3.32 shows the same data in a box-plot, which better visualizes the distribution of the points. The two data-sets again show a similar slope and a positive offset of the zoom mode relative to the nominal mode.

Referring to Equation 1.19, the air-mass factor error contribution scales with the measured vertical column. Between the nominal mode and the zoom mode there is only a small difference in slope of the fit, which indicates the air-mass factor is not the prime source of the increased error. This can be expected, since the air mass factor is highly dependent on a priori input, which remained unchanged. The resolution changes in the cloud product are expected to have a relatively small impact on the air mass factor. The stratospheric column error also is unlikely to be the source of error, since the chemical transfer model used for estimating the stratospheric field is the same for both modes and not dependent on the pixel size. Most probably the differences are caused by a change in the slant column error due to increased measurement noise. An analysis of the slant column density error is done in Section 3.6.

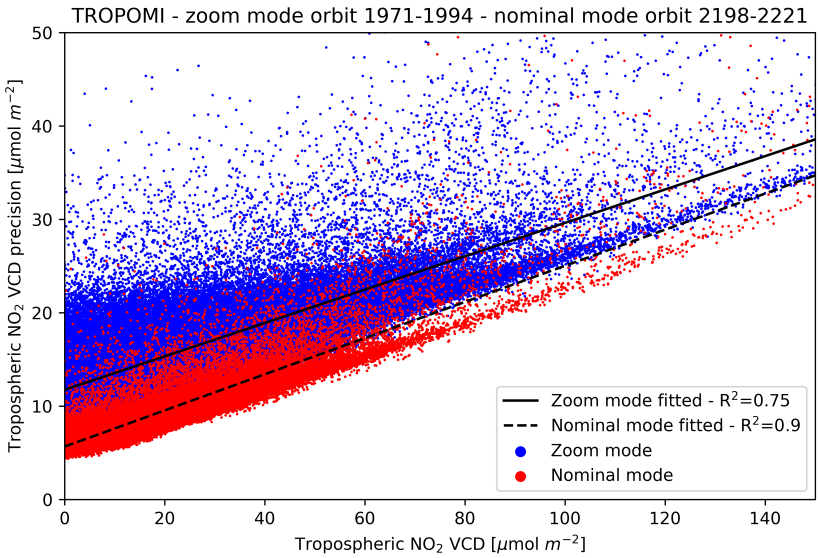

Figure 3.31: Propagated tropospheric NO_2 vertical column density error as function of the vertical column density for TROPOMI zoom and nominal mode. Zoom mode orbit 1971-1994, nominal mode orbit 2198-2221. QA=100

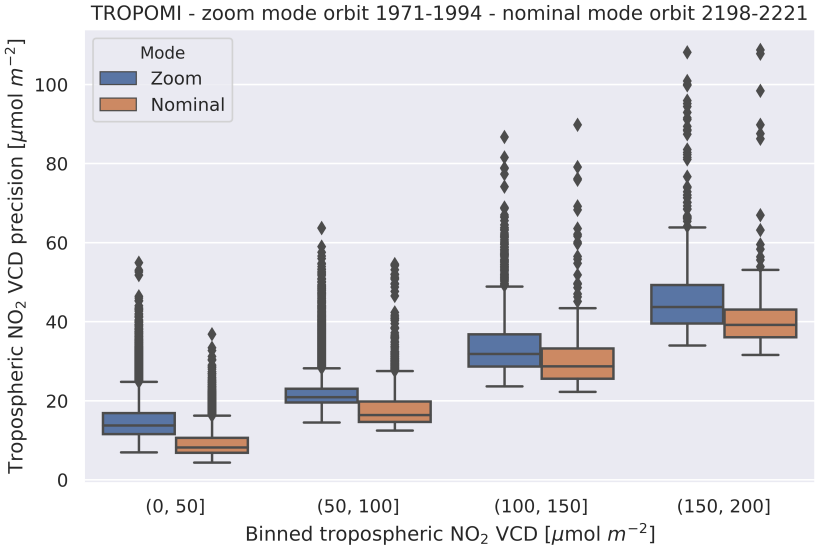

Figure 3.32: Box-plot of the propagated tropospheric NO_2 vertical column density error as function of the vertical column density for TROPOMI zoom and nominal mode. Zoom mode orbit 1971-1994, nominal mode orbit 2198-2221. QA=100

3.6 NO_2 SCD error analysis

In the retrieval algorithm, the L1B radiance and irradiance uncertainties are propagated to a reflectance uncertainty (using Equation 1.17). Then, using the DOAS technique, the retrieval parameters are fitted to the spectrum and the uncertainty is propagated. The result is an estimate on the uncertainty of the retrieved slant column density (SCD). This uncertainty depends on the instrument noise, which is dominated by random error, and errors in the fitting model and wavelength calibration, which are considered to be systematic errors. The increase of spatial resolution leads to a factor 6 increase in spatial sampling density, as the pixels are 6 times smaller. In a system dominated by random noise, an increase of the sampling density by a factor 6 should theoretically lead to an increase in noise by a factor $\sqrt{6} \approx 2.45$, as seen in the OMI zoom measurements (Valin et al., 2011a). The effect of the spatial resolution increase will be investigated in this section using zoom mode and nominal slant column NO_2 measurements from TROPOMI.

Figure 3.33 shows the SCD uncertainty for TROPOMI orbit in nominal mode. The colorbar is saturated at 33 μmol/m^2 and pixels exceeding this limit are marker red, usually located around thick clouds where the retrieval failed. In this granule several can be seen near the west coast of southern Africa. One of the selection criteria of the QA-value is the SCD uncertainty, with a threshold of 33 μmol/m^2 in the TROPOMI L2 NO_2 standard product. This criterion appeared to be very sensitive to saturation in the detector pixels caused by bright scenes, for example high thick clouds in the tropics (van Geffen et al., 2019). Because of this sensitivity, the slant column error is used as a quality criterion to filter out saturated pixels.

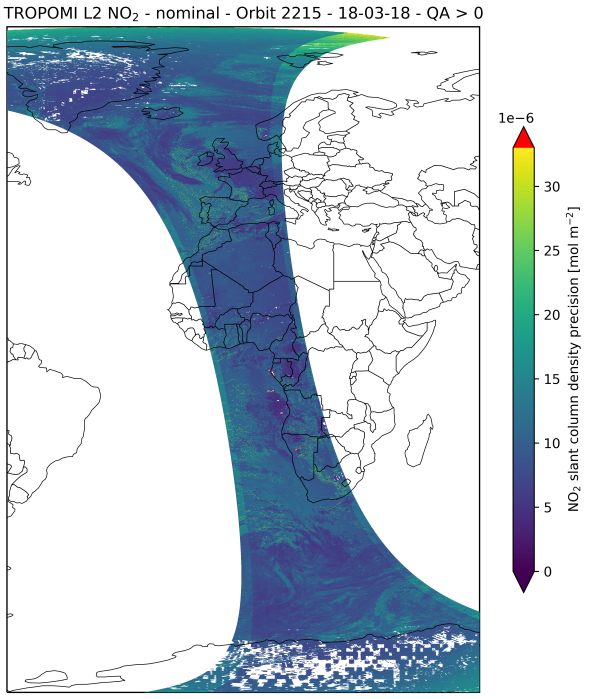

Figure 3.33: TROPOMI nominal mode, slant column density precision: cut-off at 33 μmol/m^2.

Figure 3.34 shows the SCD uncertainty for a TROPOMI orbit in the zoom mode, with the same measurement area as the previous case. In the left plot the saturation is set at 33 μmol/m^2, while at the right plot it is set at 66 μmol/m^2. The plot clearly shows effect the binning scheme, as the SCD error increases in discrete steps towards the zoom part of the swath in the middle. Comparing the left plot with the nominal plot (Figure 3.33), it appears significantly more pixels are exceeding the threshold. The red pixels are not only located around thick clouds, as in the nominal plot, but also scattered throughout the rest of the field. As a test the threshold was doubled to 66 μmol/m^2, shown in the right plot, which seems to have removed most of the threshold exceeding scattered pixels, while the cloud structures above the south of the African continent are excluded. This is still conservative, since the theoretical increase in SCD uncertainty is even higher: 2.45, as explained in the beginning of this section. The threshold value was then also modified in the QA value parameters in the algorithm settings for the zoom mode measurements. This prevents that pixels are too easily discarded as saturated pixels.

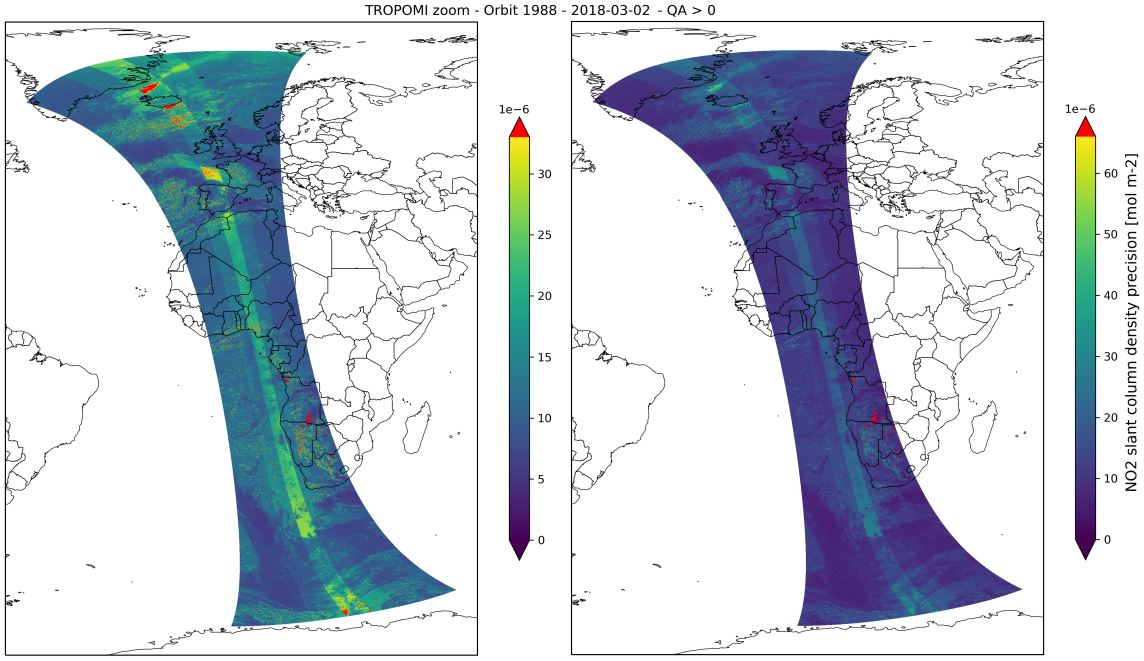

Figure 3.34: TROPOMI zoom mode, slant column density precision: cut-off at 33 (left) and 66 μmol/m^2 (right).

The two cases of SCD error shown would make an unfair comparison between the nominal and zoom mode, since it does not concern the same day and thus not the same NO_2 columns above polluted area. A more robust method to compare these two modes is to use the posterior statistical SCD uncertainty, a method explained in (Zara et al., 2018), and references therein, applied to OMI. In this approach the spatial variability of the SCD over an unpolluted area is calculated and assumed to be a statistical indicator of the random component of the SCD uncertainty. A similar method is used in (Valin et al., 2011a), where the uncertainty of the slant column zoom measurements for OMI is determined from observations above a remote ocean and desert. The SCD variability within this area then consists of the instrument noise, geophysical spatial variability, reflectance and viewing geometry variability. The goal is to isolate the first component and limit the effect of the others. The

method in (Zara et al., 2018) uses part of the Pacific Ocean as unpolluted remote area, defined by a bounding box of +60 and -60 degrees latitude and -180 to -150 degrees longitude. This area is divided into boxes of 2°x 2° longitude and latitude, to limit the effect of natural geospatial variability in the stratospheric NO_2 field and acquire an adequate amount of samples for statistical analysis. Pixels with a cloud fraction larger than 0.5 are filtered out, since this might affect the measurement. For each box the variability of the AMF in that box is calculated and when exceeding 5% the box is discarded. Finally, if a box contains less than 100 pixels, it is discarded because of low representativeness. Per box the measurements are aggregated and the mean SCD column and standard deviation are calculated. This method with the same area and filtering parameters were used for the analysis of the TROPOMI measurements. Furthermore, measurements with a QA-value lower than 75 are filtered out as well.

The method was applied to the zoom mode measurements from TROPOMI orbit 1970 to 1959 taken between 01-03-2018 and 07-03-2018, from which the measurements were selected based on the selection criteria. For comparison, the same method is applied to TROPOMI measurements with nominal resolution from orbit 7191 to 7280. These measurements were taken approximately one year later, between 03-03-2019 and 10-03-2019, at the same viewing geometry as the zoom mode measurements. Figure 3.35 shows two maps depicting the mean NO_2 SCD over the 2° x 2° boxes in the analysis area above the Pacific Ocean for the zoom mode and the nominal measurements. Both maps shows that there are a sufficient amount of boxes that passed the filtering, ensuring there is enough data for a robust statistical analysis. The latitudinal gradient visible in the SCD is caused by the stratospheric NO_2 field. Figure 3.36 shows the zonal mean taken over the SCD boxes for both modes, where the gradient is visible as well. From both the map and the mean plot it can be seen that the gradient has moved southward between the two datasets. The two subsets of data have show comparable latitudinal behaviour in NO_2 slant column measurements and have almost the same mean SCD value (107 and 106 μmol/m^2), which allows for a fair comparison.

In Figure 3.37 the zonal mean of the statistical uncertainty, calculated as the spatial variability of the SCD per box, and the propagated uncertainty, estimated by the processing algorithm, are shown for the zoom mode and the nominal mode datasets. For both modes it seems the propagated uncertainty is conservative, as the statistical uncertainty is on average 5% and 18% smaller than the propagated uncertainty for the zoom mode and nominal mode, respectively. The zoom mode uncertainty shows less longitudinal stability than the nominal mode, especially at latitudes of 50 degrees and higher. On average the statistical uncertainty of the zoom mode is a factor 2.3 higher than for the nominal mode. For the propagated uncertainty it is a factor 2.6 higher. Coincidently, the average of these two factors is equal to the predicted theoretical multiplication factor of 2.45, as explained earlier in this section. The underestimation of the predicted factor 2.45 by the statistical uncertainty increase could be explained by systematic errors in the uncertainty, which do not multiply with the increase in measurements as the random error does. Thus only the random component of the uncertainty is multiplied with 2.45, resulting in a overall multiplication factor less than that. The fact that the obtained factors are close to the theoretical random noise factor shows that the measurement uncertainty of the TROPOMI NO_2 slant column densities are dominated by random error and have little contribution from systematic errors.

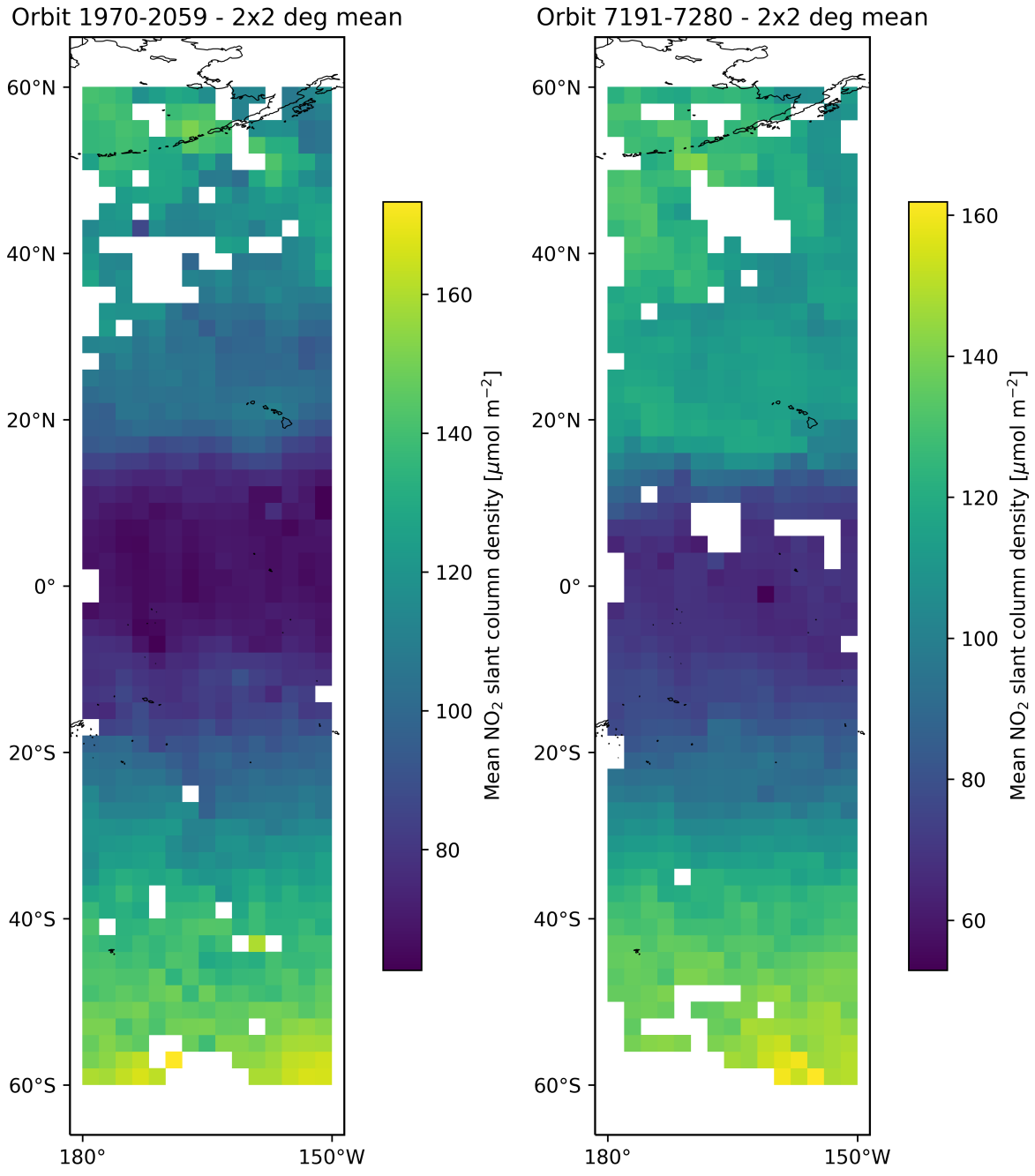

(a) (b)

Figure 3.35: TROPOMI L2 NO_2 mean SCD over Pacific Ocean: (a) zoom mode, orbit 1970-2059, 01-03-2018 to 07-03-2018 and (b) nominal mode, orbit 7191-7280, 03-03-2019 to 10-03-2019. Mean taken over 2x2 degree boxes.

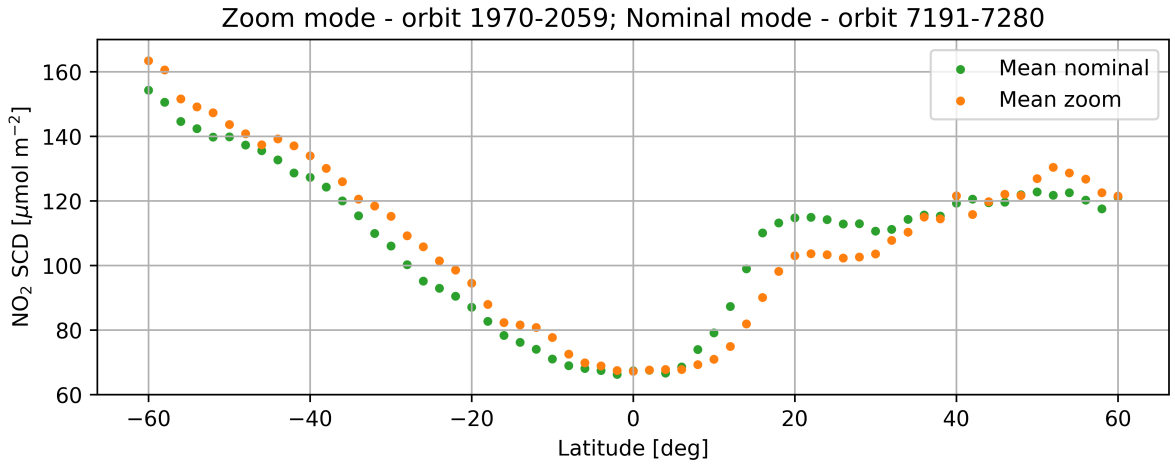

Figure 3.36: Zonal mean of mean SCD boxes for zoom and nominal mode, as shown in Figure 3.35.

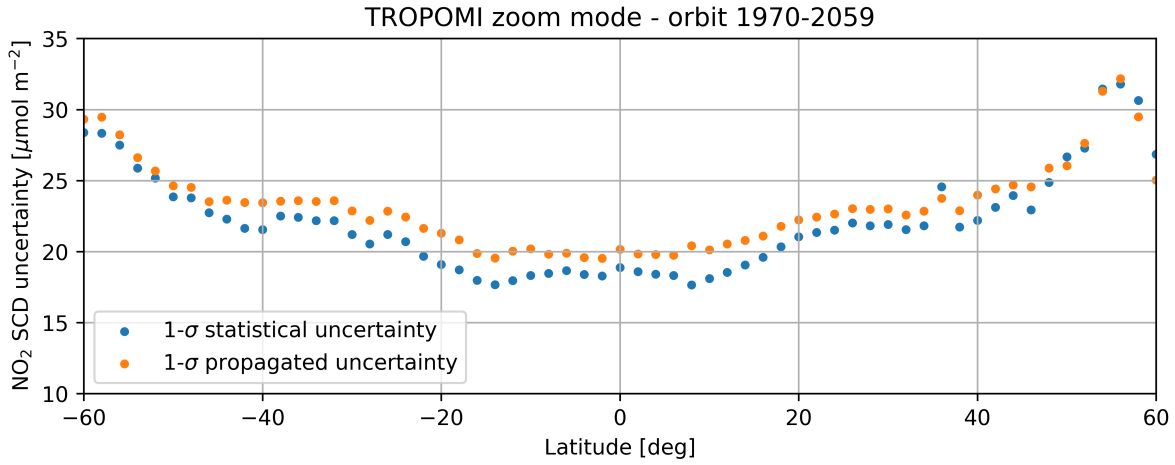

(a)

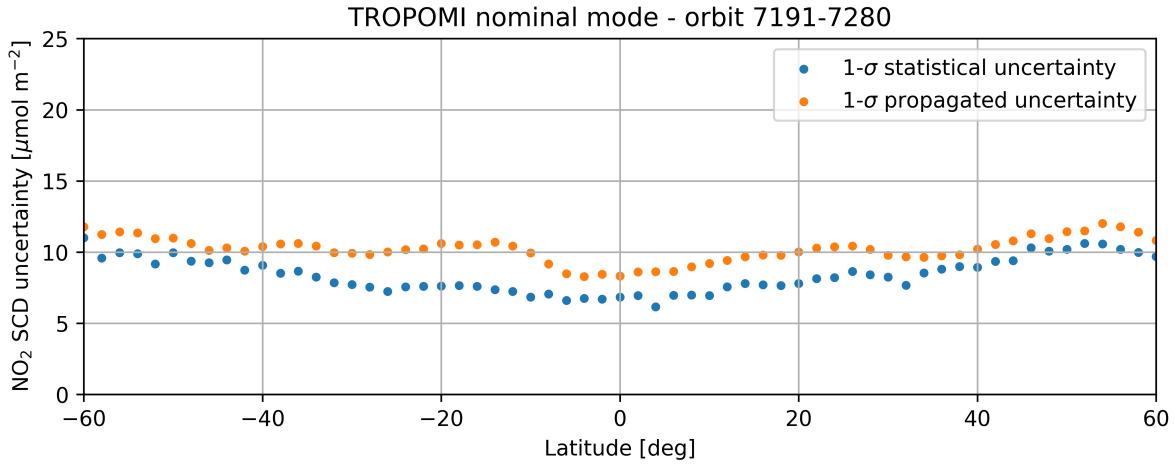

(b)

Figure 3.37: Comparison of the statistical and propagated SCD uncertainty of TROPOMI NO_2 measurements in (a) zoom and (b) nominal mode. Zonal mean taken over the boxes as shown in Figure 3.35.

4

Comparison of the zoom-mode results to other data-sets

The Level 2 products retrieved from the zoom-mode measurements have been analysed in the previous chapter. In this chapter the high resolution results are compared to other data-sets. In Section 4.1 the comparison to model predictions of the NO_2 pollution from the CAMS models are discussed, to assess how well the models can capture the measured pollution plumes. The correlation between space-borne measurements of NO_2 by TROPOMI and CO_2 by OCO-2 at high spatial resolution is investigated in Section 4.2. This correlation could be useful to improve the detection of CO_2 plumes by using plume detection algorithms on high resolution NO_2 measurements. The detecting capabilities of a plume detection algorithm is demonstrated using the zoom-mode results in Section 4.3.

4.1 Comparison to forecasted NO_2 from CAMS models

The European air quality forecasting service CAMS (Copernicus Atmospheric Monitoring Service) provides global forecasts for air pollutants, including tropospheric NO_2. The prediction is created by assimilation of in-situ and satellite measurements and runs from chemical transfer models. In the future TROPOMI measurements are to be included in this assimilation system. CAMS is part of the European Commission's Copernicus program and is implemented by the ECMWF, and provides operational global and European air quality forecasts. For Europe, these forecasts are made by 7 models (CHIMERE, EMEP, EURAD, LOTOS-EUROS, MATCH, MOCAGE and SILAM) from different institutions and are combined in one ensemble hourly forecast for every hour up to 4 days for several atmospheric constituents at a grid size of 0.1° x 0.1° (roughly 10 x 7 km in Europe). These models each have their own horizontal and vertical grids and time steps, however, their output is converted to a uniform grid for CAMS. In this section, a comparison is made between the CAMS forecast and TROPOMI zoom mode measurements for several case studies: the Bełchatów power plant, the cities of Charkov and Madrid, East-Ukraine and the Netherlands. Any discrepancies between the satellite data and the predicted fields could be of interest for both atmospheric models and satellite retrievals. The high resolution zoom data provides a detailed plume shape, which

allows for validation of the predicted plumes in the forecast. Furthermore, this comparison analysis allows for identification of good cases to use for the test retrieval with modified high resolution a priori NO_2 profiles in Section 5.1.

The CAMS data-set with a 1 day forecast field is used for the comparison, which is temporally the closest available prediction. Afterwards, an analysis version is released for the same field, however, this includes measurements of the actual air composition, which would not be fair for the analysis of forecasting performance since it includes posterior knowledge. The data-set consists of forecasted NO_2 concentration fields from each of seven models and the ensemble, sampled to hourly time-steps at a 0.1° x 0.1° field with eight vertical levels. In order to compare these fields to the TROPOMI vertical columns, the model data has to be integrated vertically. The NO_2 concentration is given at the seven model levels in [kg/m³]. By vertical integration with the trapezoid rule using the model level heights, one arrives at the approximation of vertical column in [kg/m²]. Using the molar mass of NO_2 (46.005 g/mol) the vertical column can be converted to the same units as the TROPOMI vertical columns: [mol/m²]. Finally, the model values are interpolated to the TROPOMI measurement time using linear interpolation of the time-steps.

Bełchatów

The first case is the plume of the Polish power plant Bełchatów on 02-03-2018, shown before in Figure 3.4, the largest thermal power plant in Europe and the second largest fossil-fuel station in the world. An overview of the vertical column density derived from different models for the Bełchatów scene is shown in Figure 4.1, where the power plant location is indicated. The models already show quite some variability among themselves in intensity, direction and location of the plume.

In order to compare the derived vertical columns from the model data to the TROPOMI measurements, the model data was re-sampled to the finer TROPOMI grid. Then for each pixel the difference could be calculated. The result is shown for the model ensemble and the LOTOS-EUROS model, one of the models in CAMS.

Figure 4.2a shows the result for the model ensemble, where the first panel contains the re-sampled model data, the second panel the TROPOMI measurements and the third panel the difference between model and TROPOMI. The model ensemble has an overall positive bias compared to TROPOMI. At the start of the plume, the direction is slightly too much to the South, however, the overall plume shape is well captured. The measurement plume has no real visible diffusion, whereas in the model ensemble the plume fades away already quite fast. This might be due to the nature of the model ensemble, as it is the average of the seven models, resulting in smoothing due to the different plume directions in the different models.

Figure 4.2b shows the result for the Dutch model LOTOS-EUROS. This model seems to have a wrong wind direction in at least one of the model levels, as there is a small plume going westward, as well as a large one going north-west. Also, it predicts increased column values east of the power plant. To investigate the plume direction offset further, instead of the total column, the partial columns are calculated per vertically integrated layer, shown in Figure 4.3. These partial columns show the contribution per layer to the total column. Furthermore, the original model level concentrations are included. It can be seen that the lower model levels have the highest NO_2 concentration. However, because these levels have

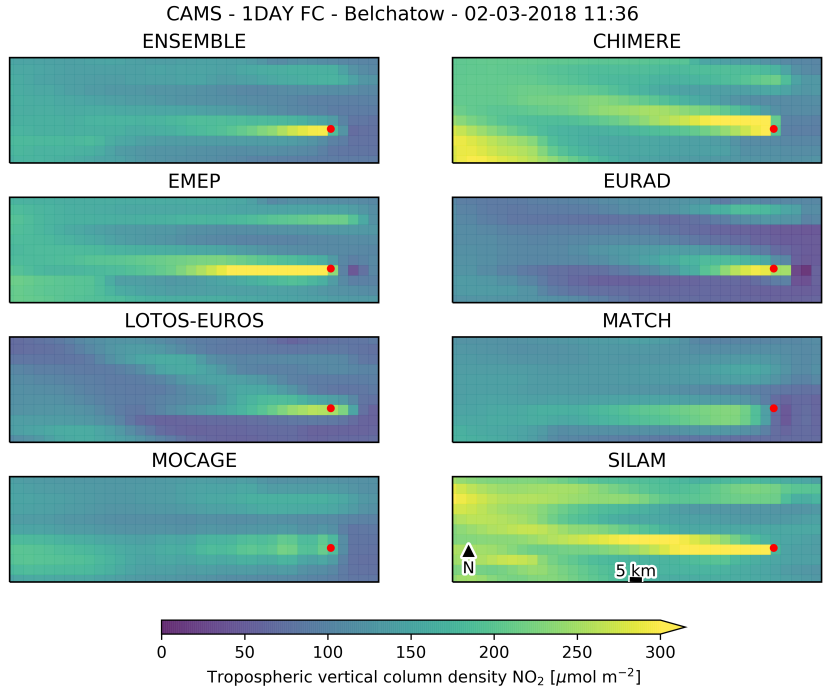

Figure 4.1: One day forecast from the different CAMS models of power plant Bełchatów (Poland) on 02-03-2018. Power plant location indicated with red dot.

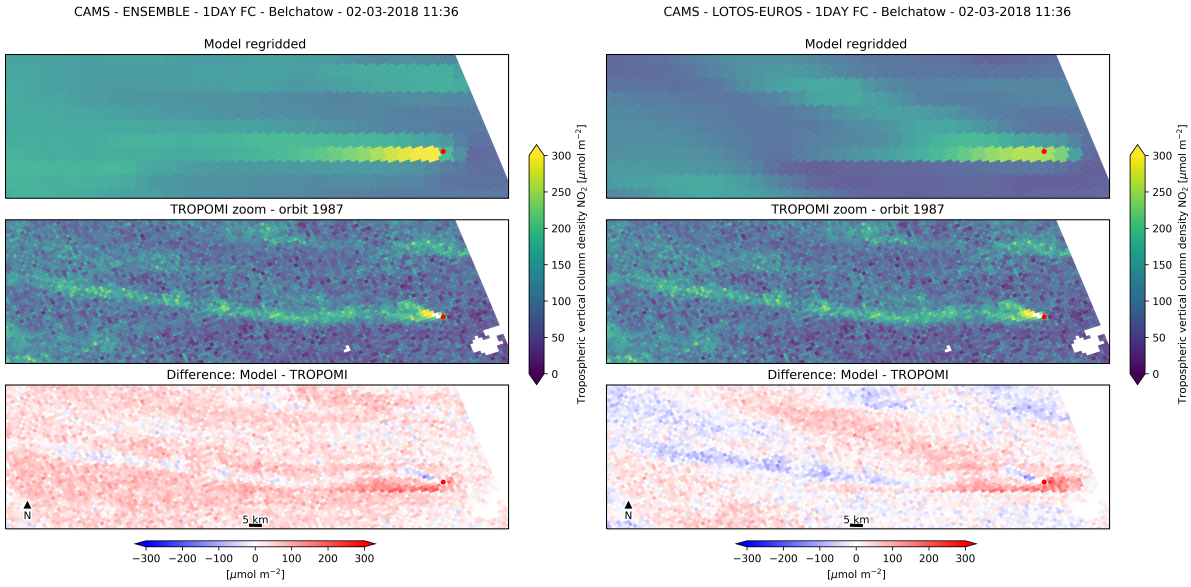

(a) (b)

Figure 4.2: Comparison of the CAMS model ensemble (a) and LOTOS-EUROS model (b) and TROPOMI zoom mode data of power plant Bełchatów (Poland) on 02-03-2018.

a smaller layer thickness, the integrated partial column becomes less significant in comparison to the other layers. The higher levels show little concentration, but have a larger layer thickness, resulting in larger partial columns. The plume with the erroneous direction seems to originate from level 1000 m and 2000 m, which due to the thickness of those layers, integrates to a significant part of the derived total column. It seems there must be an deviation in the vertical wind profile or the modelled plume height in the LOTOS-EUROS model for this specific case.

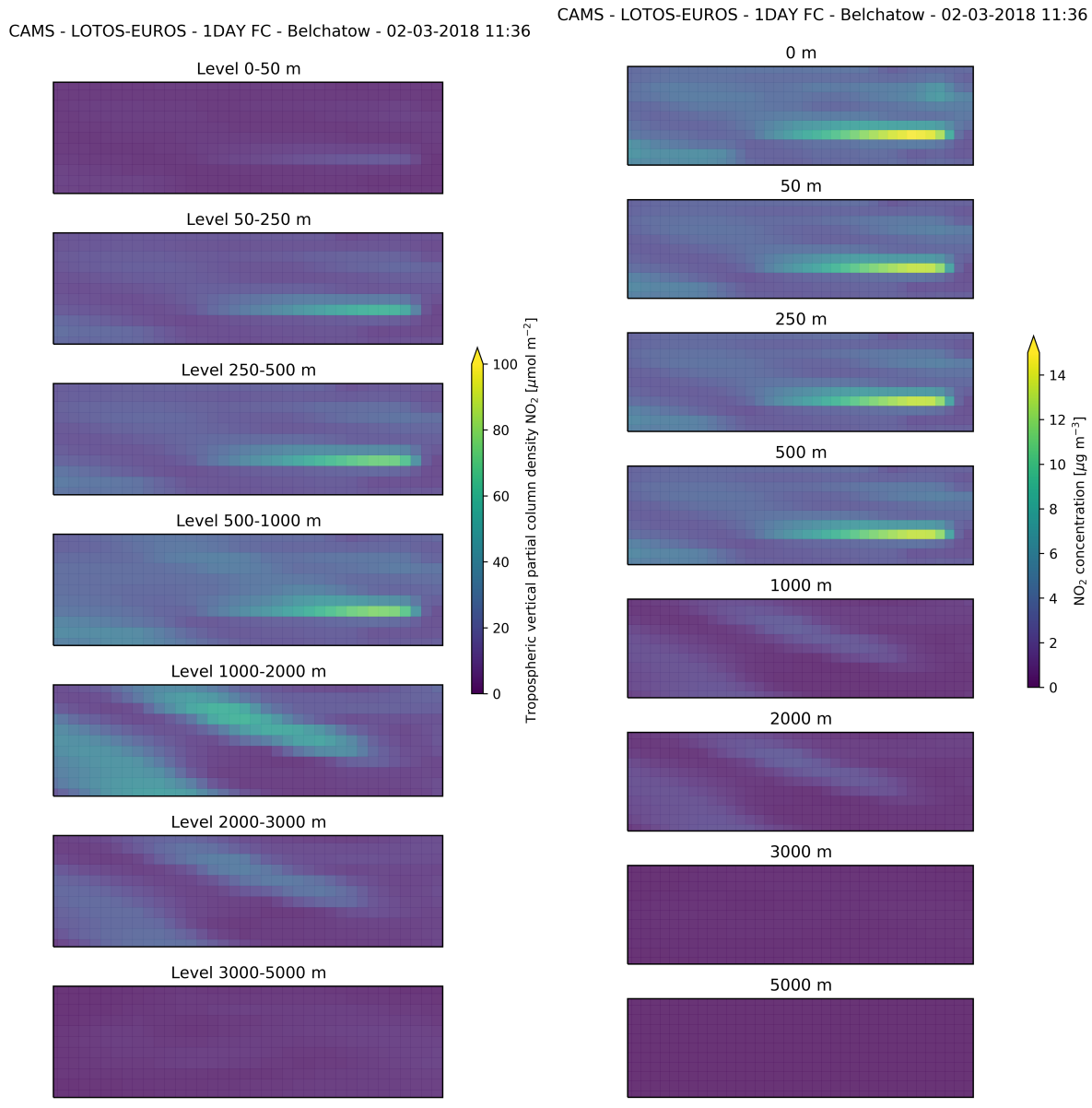

Figure 4.3: One day forecast LOTOS-EUROS model for power plant Bełchatów (Poland) on 02-03-2018. (a) the integrated partial columns. (b) the original model levels.

Charkov

Charkov is the second largest city of Ukraine with a population of approximately 2.1 million (greater area). Figure 4.4a shows the forecasted NO_2 for Charkov on 06-03-2018 by the different CAMS models. Most models seem to capture the city's pollution, except for LOTOS-EUROS. The CHIMERE model seems to perform well on this scene, thus a comparison between the CHIMERE model and the TROPOMI zoom measurements is shown in Figure 4.4b. The location and orientation of the plume matches quite well, however, the extent of the plume is too large in the model causing an overestimation of the columns. The background value shows a good match as well.

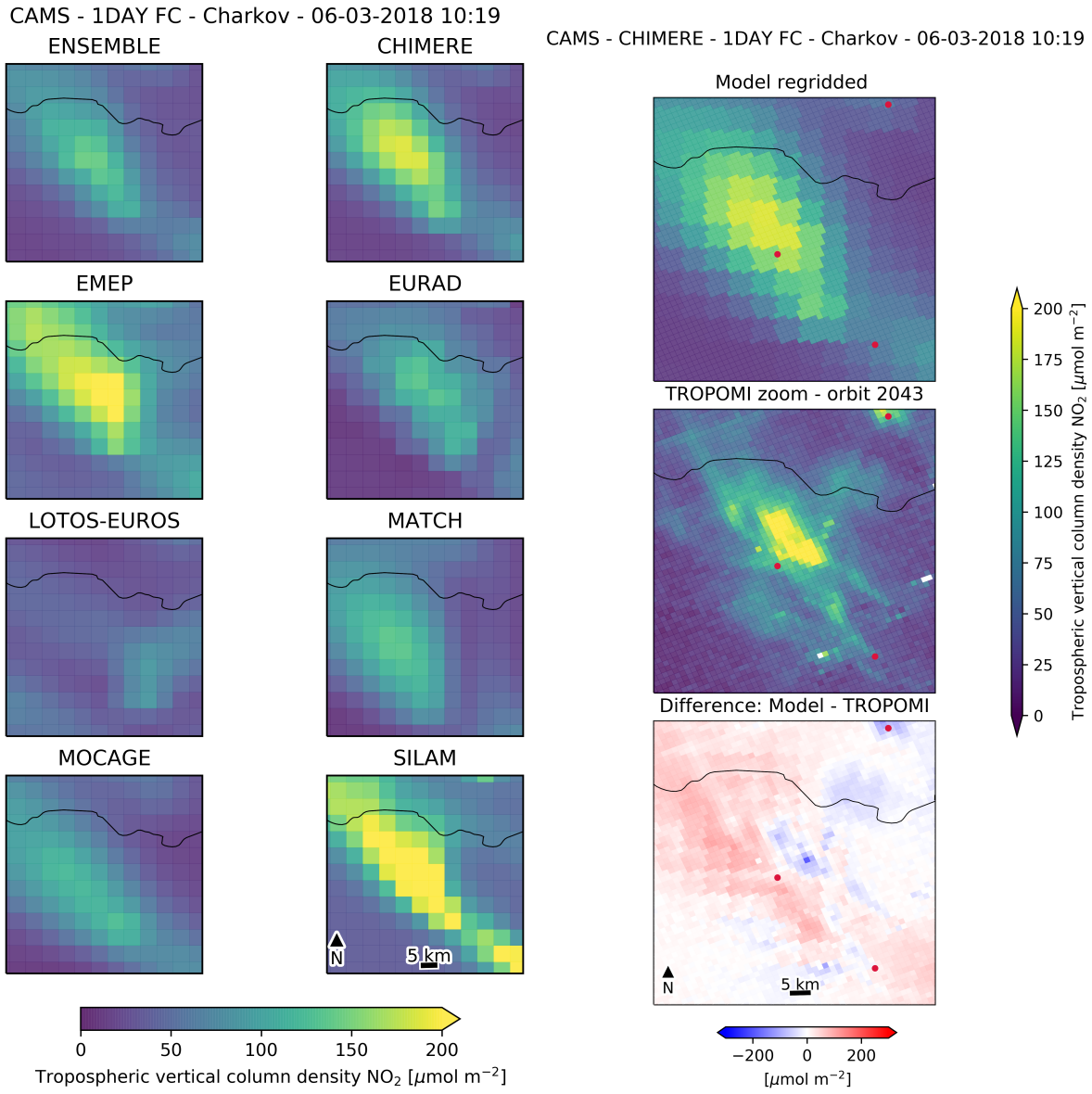

(a) (b)

Figure 4.4: (a) One day forecast from the different CAMS models of Charkov (Ukraine) on 06-03-2018. (b) Comparison of the CHIMERE model and TROPOMI zoom mode data of Charkov (Ukraine) on 06-03-2018.

Madrid

Madrid, capital of Spain, has approximately 3.3 million inhabitants, 6.5 million when including the metropolitan area. Figure 4.5a shows the forecasted NO_2 for Madrid on 07-03-2018 by the CAMS models. The models appear to agree on the plume shape and direction, with slight differences in column values. Comparing to the TROPOMI zoom measurements in Figure 4.5b to the EURAD model, shows the plume is well represented by the model in shape and columns value. The TROPOMI pixels are on the edge of the zoom swath and on the right side a different binning is visible.

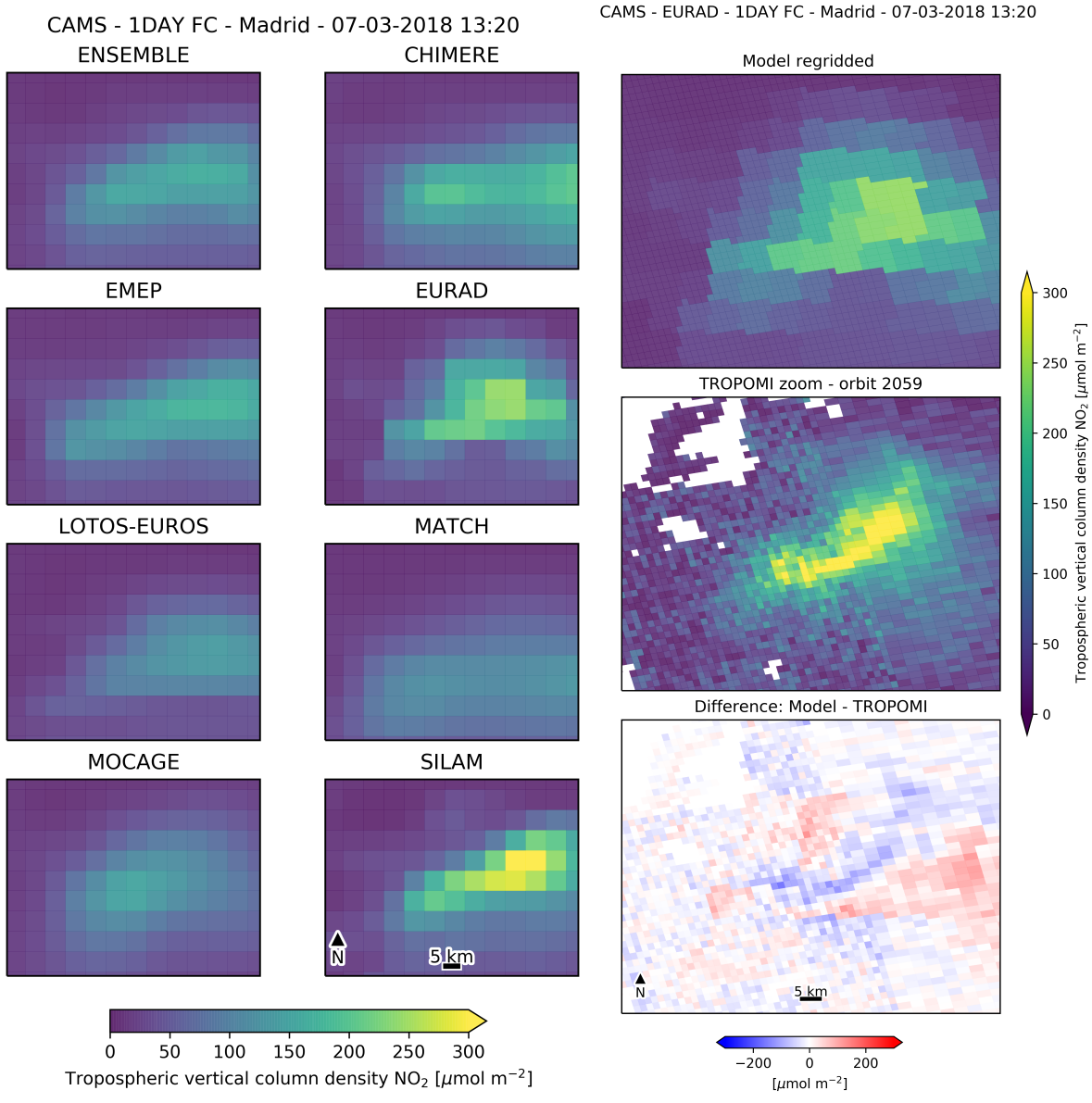

Figure 4.5: (a) One day forecast from the different CAMS models of Madrid (Spain) on 02-03-2018. (b) Comparison of the EURAD model and TROPOMI zoom mode data of Madrid (Spain) on 02-03-2018.

East-Ukraine

Figure 4.6 shows the East-Ukraine case, with Charkov in the upper left already covered as a case on its own. This area contains several power plants located close to each other, clearly visible in the TROPOMI zoom measurements by the plumes. The models seem to either underestimate the NO_2 columns or incorrectly model their shape. The comparison to the model ensemble shows the plumes are smeared out in the forecast, overestimating the background and highly underestimating the columns in the plume itself.

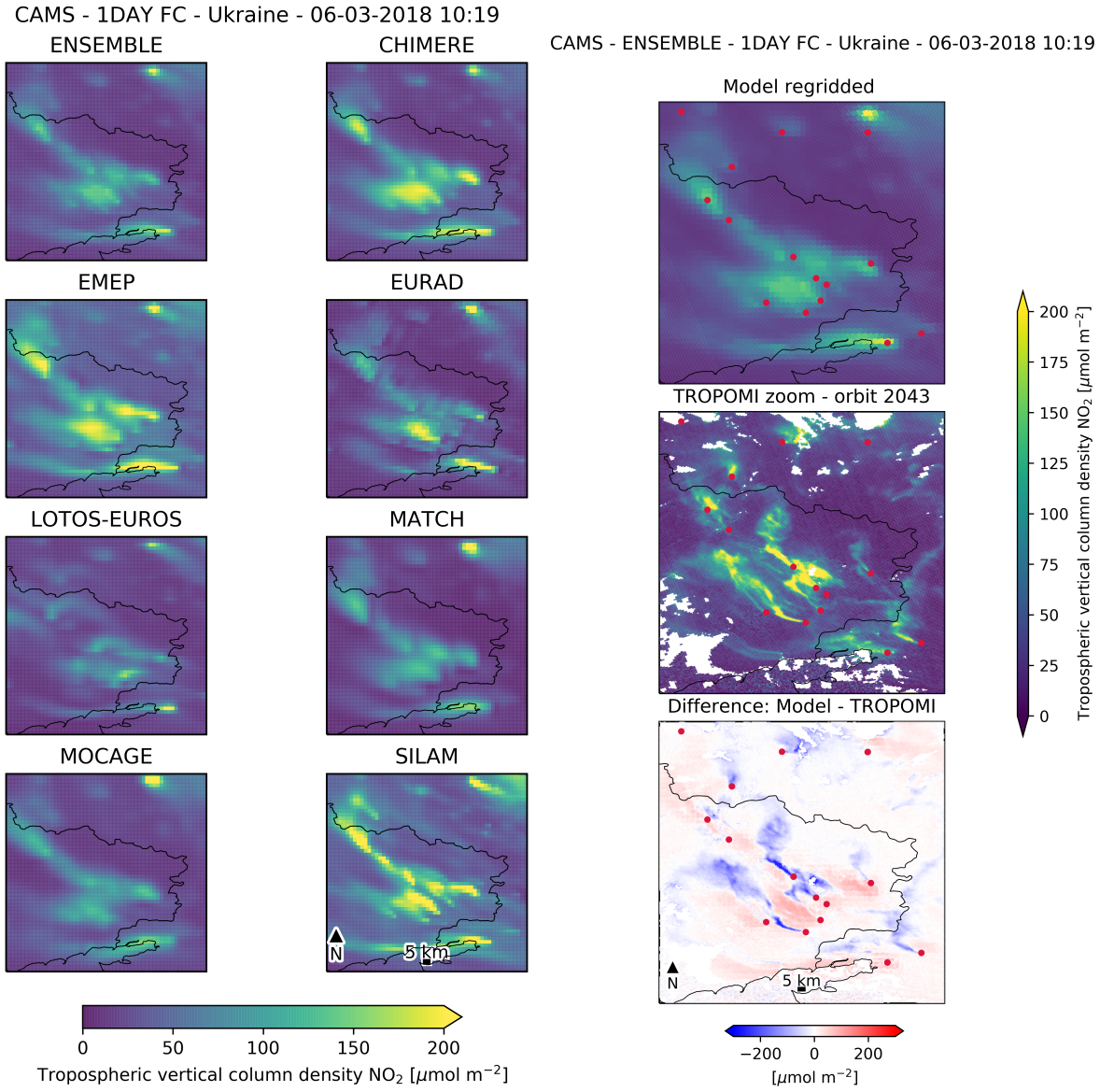

Figure 4.6: (a) One day forecast from the different CAMS models of East-Ukraine on 06-03-2018. (b) Comparison of the CAMS model ensemble and TROPOMI zoom mode data of East-Ukraine on 06-03-2018.

The Netherlands

The last case is a scene above the Netherlands, containing NO_2 pollution from a variety of sources. The models show approximately the same behaviour, slightly differing in wind direction and column value. The TROPOMI zoom mode scene, although slightly contaminated with clouds, shows less NO_2 than predicted by most models, except for the EURAD model, shown in Figure 4.7b. The enhancement in measured NO_2 by TROPOMI above Lake Ijssel (IJsselmeer) could be an artefact due to ice cover, which caused an underestimation of the surface reflectivity and an overestimation of the air-mass factor (see Section 5.2).

Conclusion

Comparing the CAMS models with each other and with TROPOMI zoom-mode measurements have shown a wide range in performance of the models, from well represented plumes from cities to non-captured power plants. Since several power plant plumes were better resolved in the TROPOMI zoom-mode NO_2 maps than in the CAMS forecast, high resolution NO_2 satellite measurements could be useful to improve the models and emission inventories. Furthermore, besides validation with in-situ measurements, high resolution NO_2 measurements could benefit the validation of the models, as substantial differences occur between NO_2 forecasts of the models.

On the other hand, the TROPOMI NO_2 retrieval can learn from the CAMS models, as high spatial resolution profiles could potentially benefit the retrieval quality. This comparison has provided several cases where the CAMS models represented the measured plume well: the cases of Bełchatów, Charkov, Madrid and the Netherlands. The NO_2 profiles from these case-model combinations can be used in testing the retrieval with high spatial resolution NO_2 a priori profiles in Section 5.1.

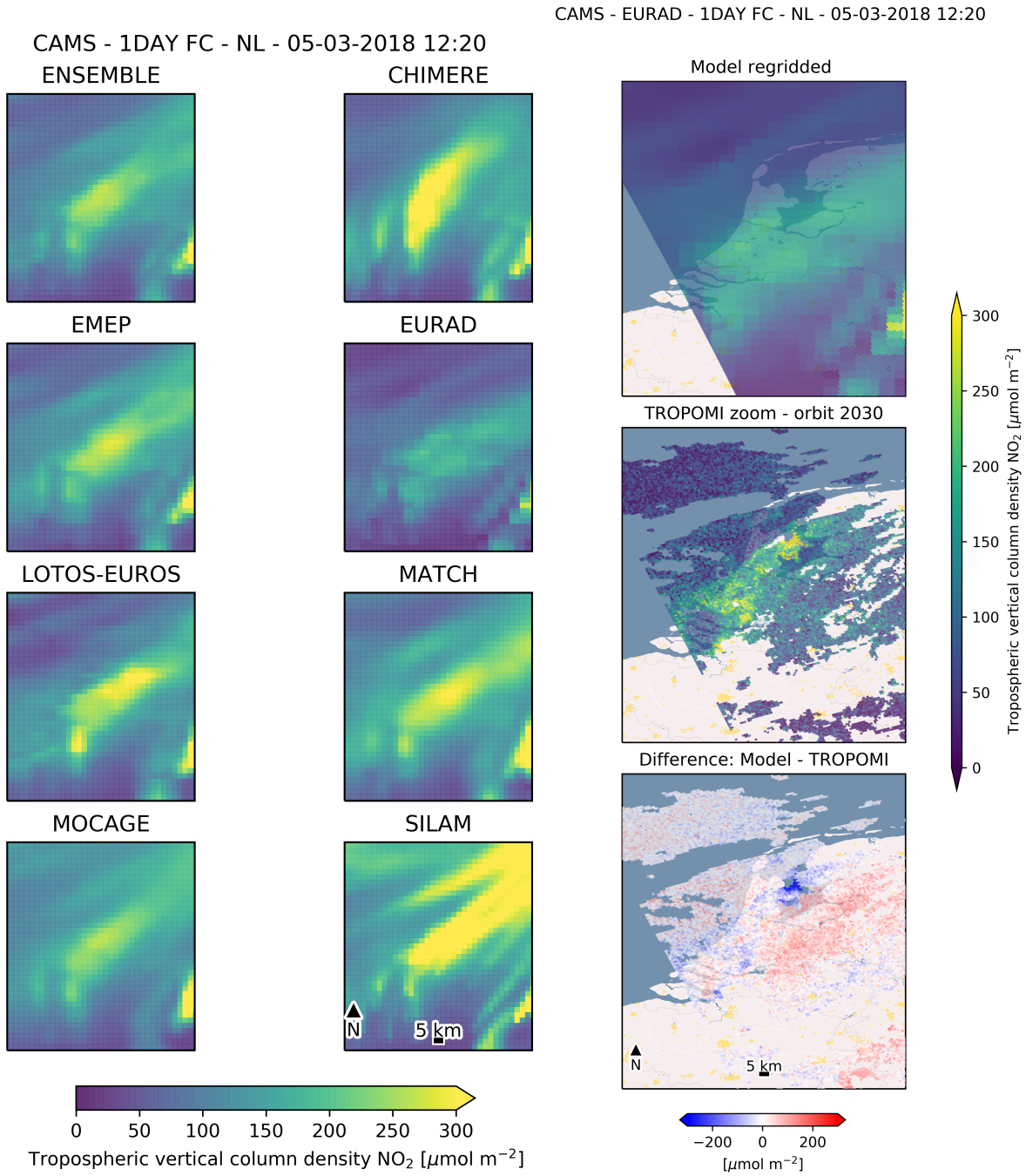

(a) (b)

Figure 4.7: (a) One day forecast from the different CAMS models of the Netherlands on 05-03-2018. (b) Comparison of the EURAD model and TROPOMI zoom mode data of the Netherlands on 05-03-2018.

4.2 Comparison with CO_2 measurements by OCO-2

Whenever combustion of fossil fuels is involved, NO_2 and CO_2 can be considered co-emitted species. However, CO_2 has a much longer lifetime and therefore a higher background value than tropospheric NO_2, making it easier to identify sources using NO_2 measurements. As mentioned in Section 1.9, NO_2 can be used to better identify local enhancements (or plumes) of CO_2 for single overpass emission estimation. Estimating emitted CO_2 abundances from NO_2 measurements is difficult, since the ratio of emitted NO_2 to CO_2 is variable per emission source. Furthermore, the lifetime of both species in the atmosphere is meteorologically dependent, increasing the uncertainty of the conversion.

This section contains a case study investigating the correlation of NO_2 enhancements in the TROPOMI zoom mode data-set and co-located CO_2 measurements from NASA's Orbiting Carbon Observatory (OCO-2) satellite. Similar studies have been done by (Hakkarainen et al., 2019) and (Reuter et al., 2019) to show the potential benefit of measuring NO_2 and CO_2 simultaneously using the nominal TROPOMI and OCO-2 data. OCO-2 has a spatial resolution of approximately 2.25 km x 1.29 km, slightly higher than the resolution of the TROPOMI zoom data (2.4 km x 1.8 km). Unfortunately, co-located measurements are sparse, since OCO-2 has a small swath width (10.3 km) causing the cross-over frequency of the ground tracks to be low.

For this study the OCO-2 Level 2 bias corrected XCO_2 lite product (version 8r) (OCO-2 Science Team et al., 2017) is used. The TROPOMI pixels with a QA-value lower than 75 are filtered out, as recommended by the TROPOMI user guide (Eskes et al., 2018b). The OCO-2 measurements with a warning level of 4 or 5 are excluded, resulting in a subset with the best 80% of the data. The used warning level threshold was chosen by finding a balance between the amount of pixels available for statistical analysis and the measurement uncertainty, as instructed in the OCO-2 product description (Osterman et al., 2017).

Poland

The first co-located, clear-sky measurements containing NO_2 enhancements were over Poland on 02-03-2018. The measurements are 18 minutes apart. Figure 4.8 shows the column averaged dry air CO_2 mole fraction (XCO_2), measured by OCO-2, mapped on top of the vertical tropospheric NO_2 column, measured by TROPOMI. The OCO-2 track crosses several NO_2 enhancements, which also seem to be visible as enhancements in the measured XCO_2.

To compare the two measured quantities, a co-location was performed by selecting all TROPOMI pixels with their pixel centre inside the OCO-2 pixel vertices. Then, a coordinate transformation was done on both data subsets, so the measurements could be plotted as function of the distance along the OCO-2 ground track. Figure 4.9 shows the two data subsets combined in one plot, where the distance is measured along the OCO-2 ground track northward. The two peaks at the middle of the track, visible in the map plot, are visible in the scatter plot as well in the XCO_2 data.

In order to quantify the correlation between the two measurement sets a line plot is made along the OCO-2 track. The measurements are binned in boxes of approximately 2.4 km along-track, which matches the along-track size of the TROPOMI ground pixel, and over the swath width in the cross-track direction (10.3 km / 8 OCO-2 pixels). The measurements are then averaged per bin, normalised per species and plotted as function of the distance along

the OCO-2 track from south to north. The result for this Poland case is shown in Figure 4.10, with the corresponding uncertainty for each measurement indicated by the shaded area. Again, the first peak in the NO_2 at 50 km is unresolved in the XCO_2, and the second and third peak at 100 and 150 km are clearly visible. For the binned datasets the Pearson correlation coefficient is calculated, with a result of $r = 0.58$, shown in Figure 4.11. This indicates a slight correlation between the NO_2 and XCO_2 measurements.

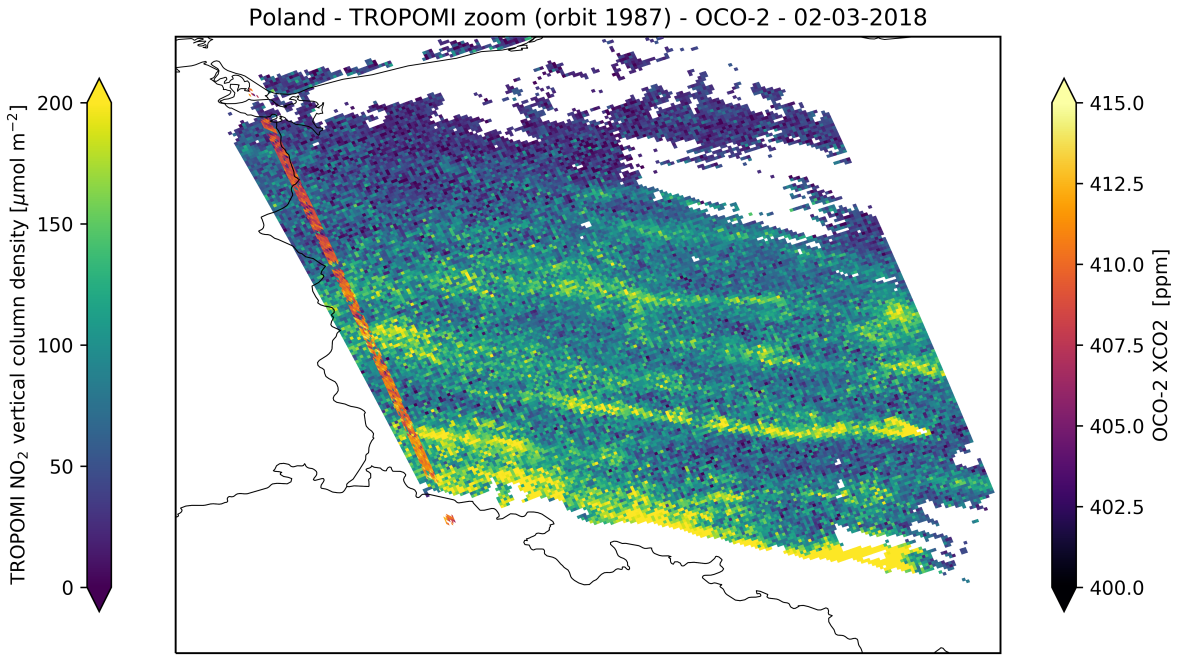

Figure 4.8: OCO-2 XCO_2 measurements mapped on top of TROPOMI zoom mode NO_2 VCD measurements, Poland, 02-03-2018.

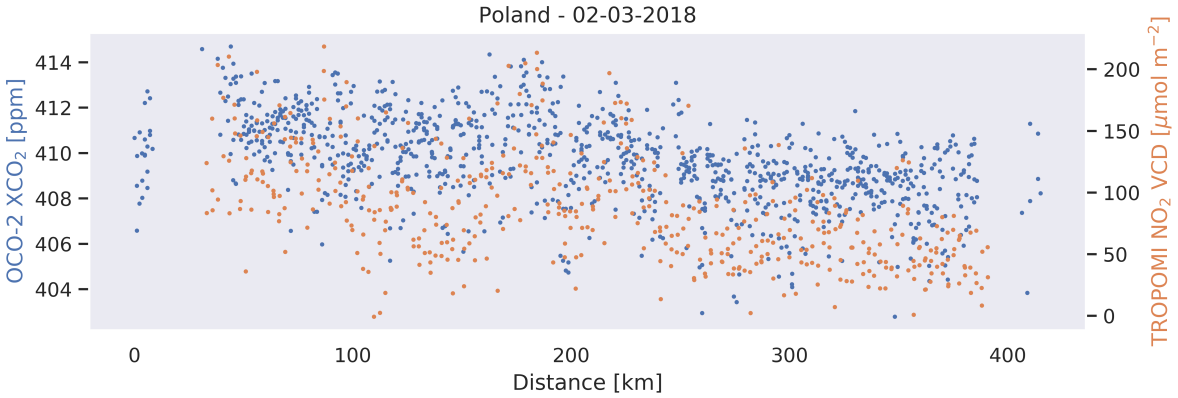

Figure 4.9: Scatter-plot of the co-located XCO_2 and NO_2 measurements over Poland, 02-03-2018.

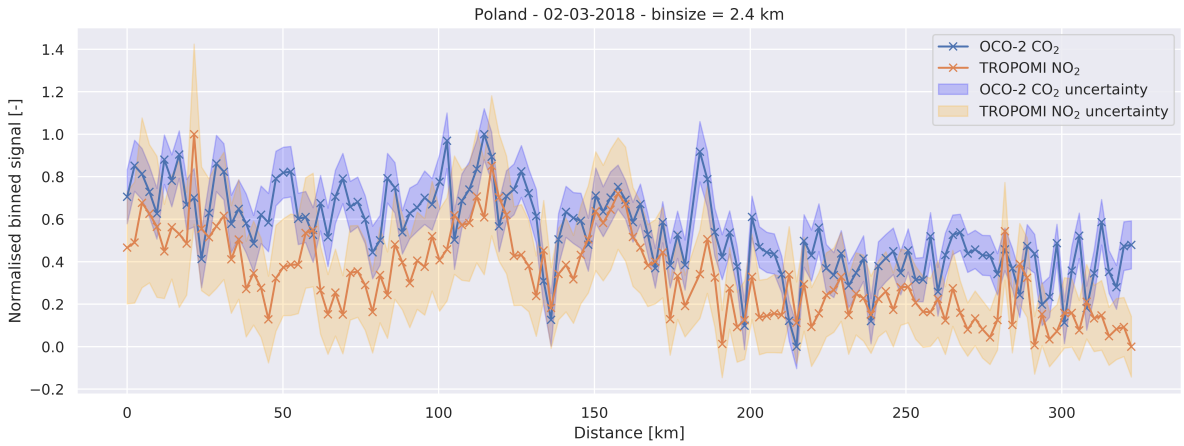

Figure 4.10: Line plot of normalised and binned co-located XCO_2 and NO_2 measurements over Poland, 02-03-2018.

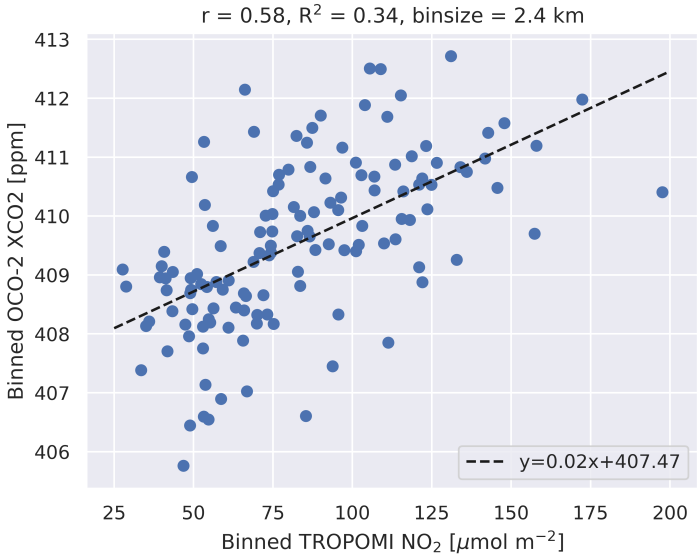

Figure 4.11: Correlation plot of binned co-located XCO_2 and NO_2 measurements over Poland, 02-03-2018.

China

The second case is located in the Inner Mongolia region in the north of China, sharing a border with Mongolia. Figure 4.12 shows the co-located TROPOMI zoom NO_2 and OCO-2 CO_2 measurements, taken approximately 16 minutes apart. From first sight, enhancements in both measurements can be seen, which seem to occur at the same locations. The visible NO_2 plumes cannot be easily assigned to point sources, they probably originate from small cities, factories and roads. Figure 4.13 shows the scatter plot of both measurements along the OCO-2 ground track. The first two peaks in NO_2 are slightly visible in the CO_2 measurements. However, the peak around 150 km to be well represented in both data-sets. Binning and normalizing the measurements results in the line plot shown in Figure 4.14, where the two measurements sets follow each other quite well. This is confirmed with the correlation plot in Figure 4.15, resulting in a strong correlation coefficient of 0.85.

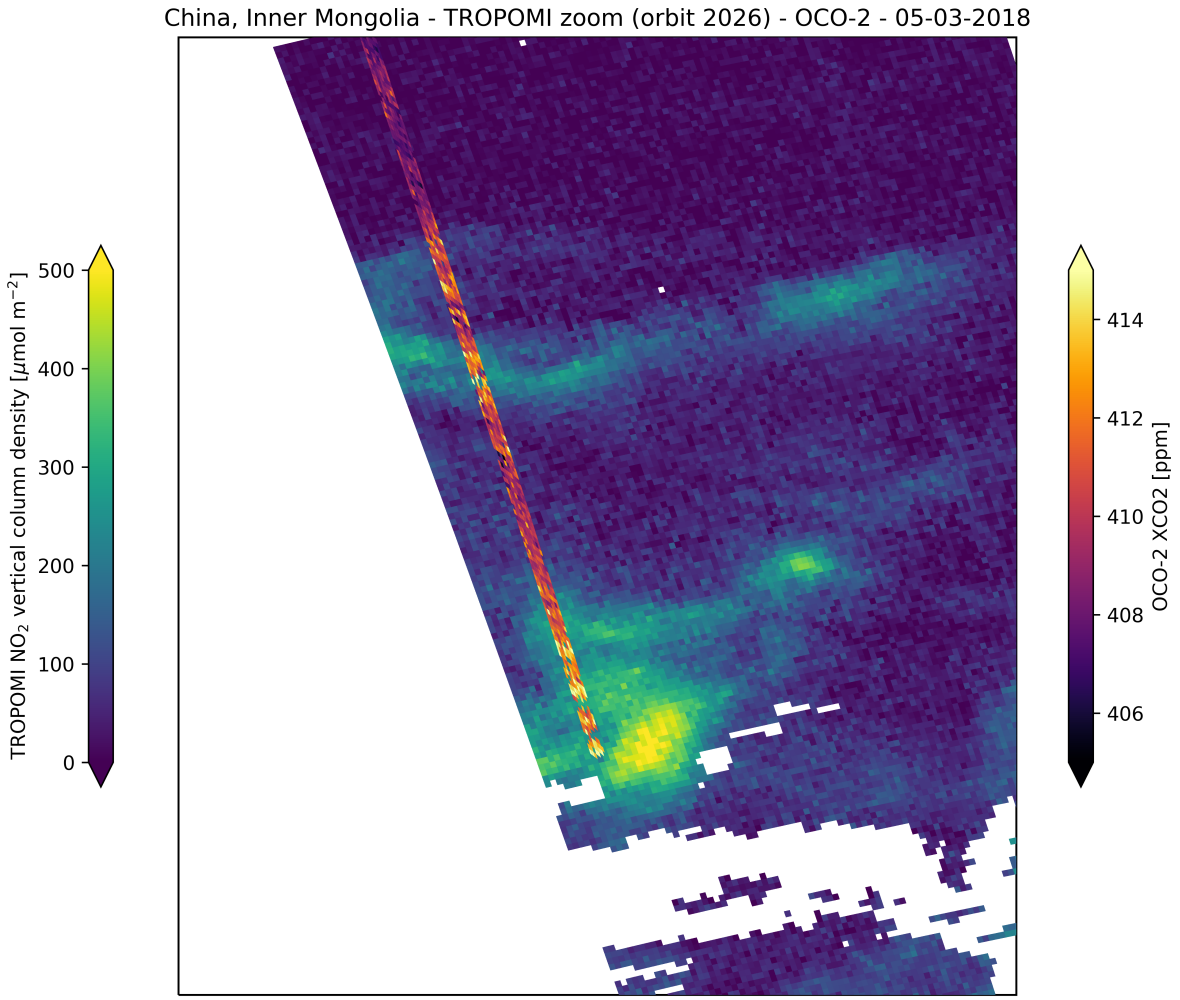

Figure 4.12: OCO-2 XCO_2 measurements mapped on top of TROPOMI zoom mode NO_2 VCD measurements, China, Inner-Mongolia, 05-03-2018.

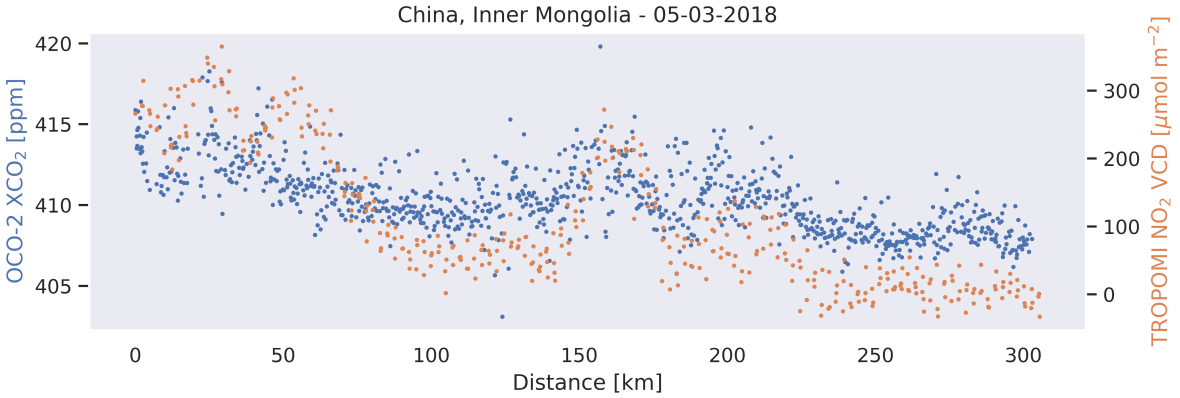

Figure 4.13: Scatter-plot of the co-located XCO_2 and NO_2 measurements over China, Inner-Mongolia, 05-03-2018.

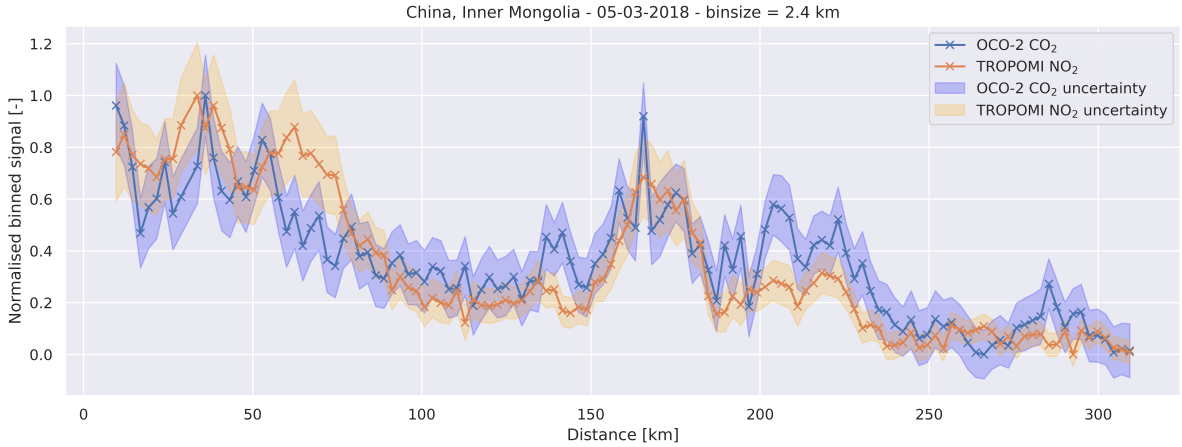

Figure 4.14: Line plot of normalised and binned co-located XCO_2 and NO_2 measurements over China, Inner-Mongolia, 05-03-2018.

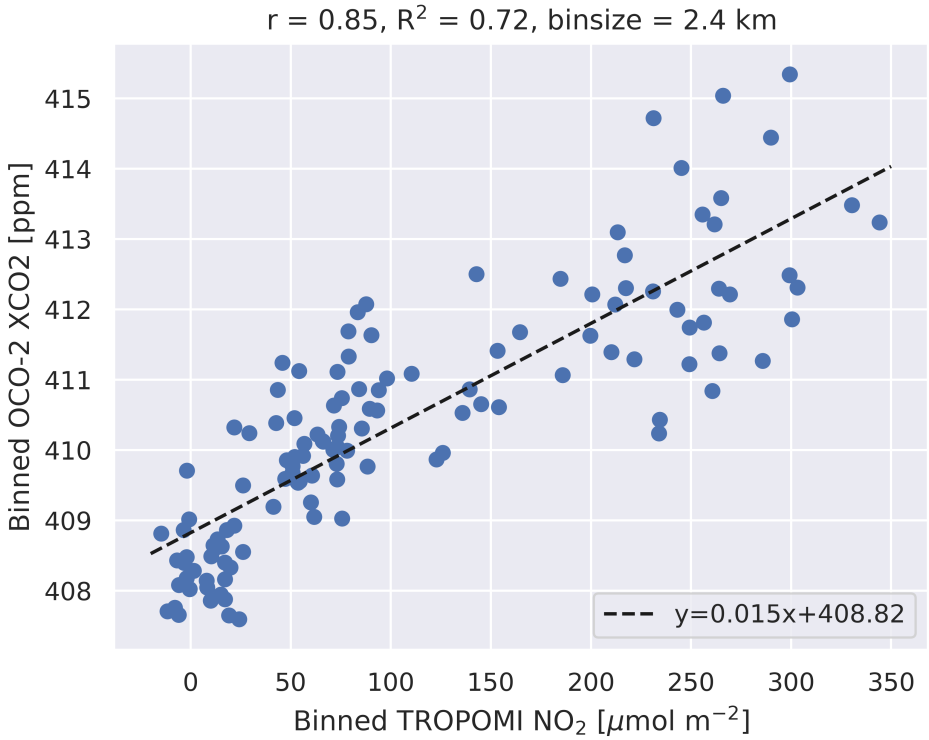

Figure 4.15: Correlation plot of binned co-located XCO_2 and NO_2 measurements over China, Inner-Mongolia, 05-03-2018

Mary

Figure 4.16 shows the NO_2 plume from the Mary Power Plant, located just below the city of Mary in Turkmenistan. This power plant is a combined gas and steam turbine producing 1680 MW (Byers et al., 2018). The clearly visible NO_2 plume in this plot does not appear to be captured by OCO-2, which also follows from the scatter plot in Figure 4.17. The observations were taken 10 minutes apart. From the line plot in Figure 4.18 it becomes clear that the main and first NO_2 peak measured by TROPOMI is poorly resolved by the CO_2 measurements from OCO-2. There seems to be a peak present at this location in the CO_2, however, it is too wide and too early compared to the NO_2 peak. Calculating the correlation between the two line-plots results in a poor $r = 0.24$.

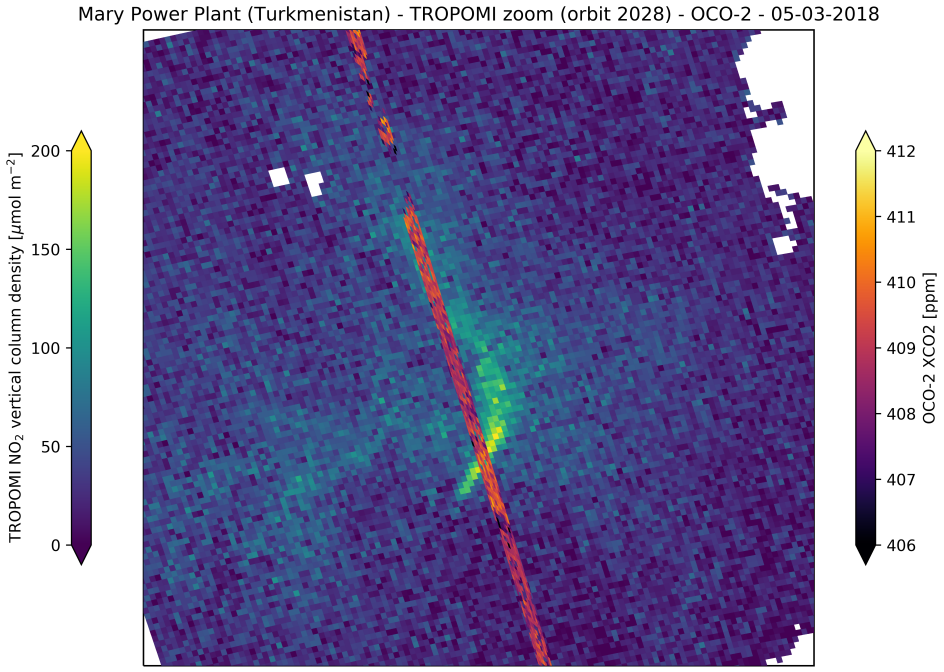

Figure 4.16: OCO-2 XCO_2 measurements mapped on top of TROPOMI zoom mode NO_2 VCD measurements, Mary Power Plant (Turkmenistan), 05-03-2018.

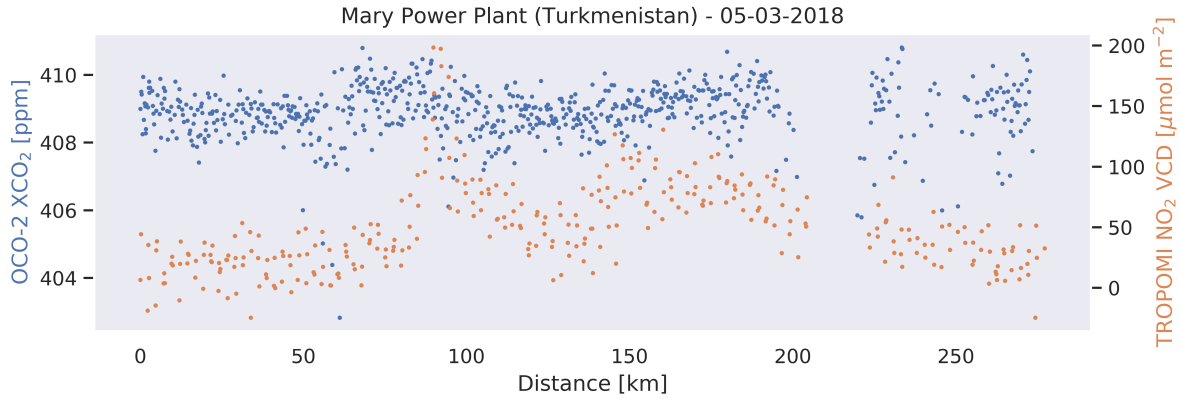

Figure 4.17: Scatter-plot of the co-located XCO_2 and NO_2 measurements over Mary Power Plant (Turkmenistan), 05-03-2018.

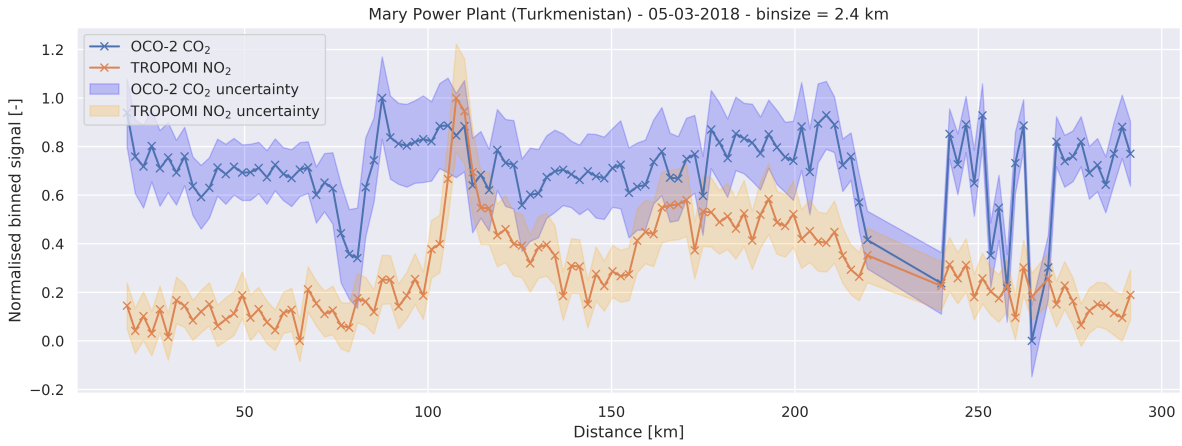

Figure 4.18: Line plot of normalised and binned co-located XCO_2 and NO_2 measurements over Mary Power Plant (Turkmenistan), 05-03-2018.

Discussion

One possible cause for the varying correlation between the different scenes could be the amount of turbulent diffusion that occurs in the atmosphere between the overpasses of the two satellites. For example, the China case shows a strong correlation between measured NO_2 and CO_2 with a difference in overpass time by TROPOMI and OCO-2 of 16 minutes, while the Mary case shows poor correlation with a overpass difference of 10 minutes. Figures 4.19 and 4.20 show the ECMWF 10 m wind vectors mapped on the scenes of China and Mary, respectively. These wind vectors are included in the TROPOMI Level-2 output. Note the difference in the quiver length in the plot legend. From these plots it can be seen the China case is almost windless at the ground track of OCO-2 and that the wind velocities for the Mary case are higher, especially in the plume. The average wind speed in the OCO-2 ground track is 2.1 m/s for the China case and 5.5 m/s for the Mary case. The stronger wind could cause the pollution plume to change shape during the time between the overpasses, resulting in a poor correlation between the measured trace-gas species. For a scene with weak wind as in China, the emitted pollution experiences less atmospheric transfer and the location and shape of the plume remains more or less constant, allowing for a good correlation. The change in shape of the plume over time could be modelled with a Large Eddy Simulation (LES) to confirm these findings, however, are out of the scope of this thesis.

The good correlation found for the two cases with weak wind velocities provide further evidence of the benefit of using NO_2 measurements at high spatial resolution (near 2 x 2 km) for identifying local CO_2 enhancements. The effect of the turbulent diffusion shows the importance of NO_2 and CO_2 measurements to occur simultaneously, in order for them to be more useful in detection analysis. Section 4.3 continues on the topic of plume identification.

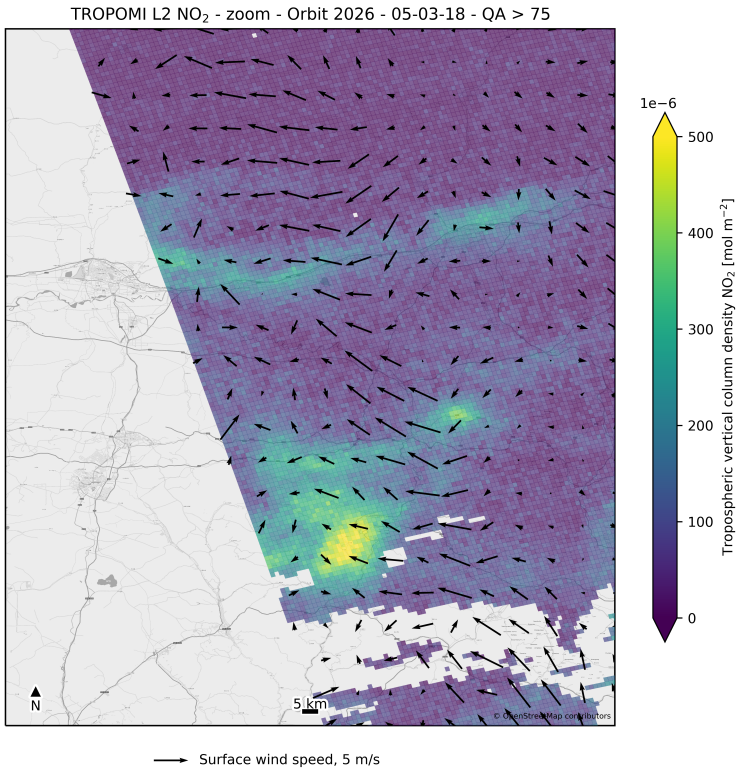

Figure 4.19: ECMWF 10 m wind vector mapped on top of TROPOMI zoom mode NO_2 VCD measurements, China, Inner-Mongolia, 05-03-2018.

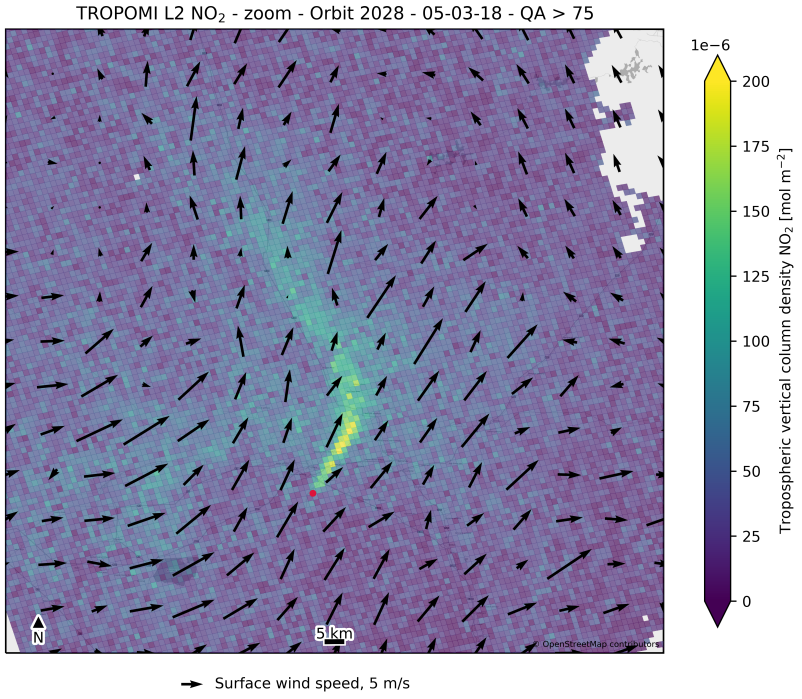

Figure 4.20: ECMWF 10 m wind vector mapped on top of TROPOMI zoom mode NO_2 VCD measurements, Mary Power Plant (Turkmenistan), 05-03-2018.

4.3 Plume detection algorithm

As explained in Section 4.2, measurements of NO_2 plumes can be used to enhance the detection of CO_2 plumes, since they are often co-emitted by the fossil fuel burning. For satellite measurements, retrieved NO_2 columns have a lower signal-to-noise ratio than retrieved CO_2 columns. Furthermore, CO_2 enhancements by emissions are only a few percent higher than the background field, due to the long lifetime of CO_2. Contrary, NO_2 has a lifetime of only several hours and sources are clearly visible against the background field. This causes enhancements (or plumes) of NO_2 to be easier detectable than the CO_2 ones. As shown in Section 4.2, there is a good correlation between the measured XCO_2 and NO_2 abundance for low wind speeds.

A new Copernicus mission is being developed, which is to monitor CO_2 emissions of cities and power plants. Besides high resolution CO_2 measurements, the instrument will likely have a NO_2 detector to measure NO_2 plumes at a resolution of 2 x 2 km, in order to enhance the CO_2 detection. Adding the NO_2 measurements would decrease the requirement on the instrument precision of the CO_2 detector. A preparatory study, called SMARTCARB, showed the added value of NO_2 measurements by quantifying emissions from power plant and city plumes using one year of synthetic satellite observations with and without NO_2 measurements for different resolutions, instrument noise levels and number of satellites (Kuhlmann et al., 2018b). This study concluded that a NO_2 instrument with a high noise ($2{\cdot}10^{15}$ molecules cm^{-2} or $33{\cdot}10^{-6}$ μmol m^{-2}) and a spatial resolution of 2 x 2 km would be sufficient. In the recommendations of this report it is stated: *"A matter of concern is the fact that little is known about the realism of the plumes simulated in the SMARTCARB project. Other settings of the transport model may have led to more or less rapidly dispersing plumes with potentially significant effects on plume structure and detectability (...) Direct comparisons with airborne CO_2 observations e.g. during the C-MAPExp or COMET campaigns or with NO_2 plumes detected by the recently launched Sentinel-5P satellite could provide further valuable insight."*.

The TROPOMI zoom mode data-set, with a spatial resolution in the order of 2 x 2 km, could be used to validate the simulated plumes in the SMARTCARB study. In this section the plume detection algorithm from the project is re-implemented in code and applied to the TROPOMI zoom mode measurements for several cases. Since the data-set only has a limited number of use cases, which is not sufficient for a statistical analysis as performed in the study, the purpose is only to demonstrate the algorithm on real NO_2 measurements with similar spatial resolution and noise as the simulated measurements. It would be interesting to also include CO_2 measurements to the plume detection, however, these are not available with a swath and resolution comparable to the simulated CO_2 measurements. For example, OCO-2 measurements, which have a narrow swath (see Section 4.2), would be unsuitable for this plume detection algorithm. First, the method of the plume detection algorithm will be explained. Then, the results of the algorithm applied to several zoom mode scenes are shown. Furthermore, a comparison of the algorithm performance is done for the zoom mode resolution and a simulated downscaled resolution (as seen in Section 3.2). To asses the impact of measurement noise on the algorithm outcome, also a test was done with measurements with added noise.

4.3.1 Method

The plume detection algorithm, developed in the SMARTCARB study, selects measurements pixels where NO_2 values are significantly larger than the background, using a Z-test (Kuhlmann et al., 2018b). A Z-test is a statistical test, where the test statistic can be approximated as a normal distribution. The test compares the normalized difference between the mean value of a neighbourhood of pixels and the background value to the z-value as following:

$$\frac{x_p - x_{bg}}{\sqrt{\frac{\sigma_{ssp}^2}{n_p} + \sigma_{bg}^2}} > z(q) \tag{4.1}$$

where:

x_p = the mean value of n_p pixels
x_{bg} = the mean value of the background field
σ_{ssp} = the single sounding precision of the satellite measurement
n_p = the number of pixels
σ_{bg} = the standard deviation of the background field
$z(q)$ = the test statistic, with probability q

Since most plumes consist of multiple pixels, it can be beneficial to use the mean value of a local neighbourhood. In the SMARTCARB study, neighbourhoods ranging from 1 to 121 pixels in different shapes were tested. For the 2 x 2 km measurement resolution, the neighbourhood with 5 pixels (cross-shaped, one pixel with the four surrounding pixels connected by edge), gave the best results. The significance level was set at q=0.99 (P=0.01), resulting in z=2.33. In the simulation study, the background mean and standard deviation values were calculated from the chemical transfer model over an area of 100 x 100 km around power plants and 200 x 200 km around cities, excluding the sources itself. For the TROPOMI measurements, the same neighbourhood of 5 pixels was chosen and the same significance level was used. The TROPOMI background statistics are determined over an area of 50 rows by 50 scanlines, approximately 100 x 100 km, of the L2 measurements from the orbit at hand. For simplicity, sources are filtered out by excluding pixels with a value deviation from the mean by more than $\pm$1-sigma. The Z-test results in a binary image of pixels labelled as 'plume' or 'non-plume'. The 'plume' labelled pixels that can be grouped by 8-connectivity (also called Moore neighbourhood, the central cell plus eight surrounding cells) are labelled as individual plumes. For the minimum plume size, a threshold of 5 pixels is used to filter out relatively small sources without a plume spanning multiple pixels.

4.3.2 Results

Several measurement scenes have been chosen as test case for the plume detection algorithm, containing either multiple plumes from power plants (Lahore, East-India and Ahwaz cases) or a singular large city plume (Mumbai case). The comparison to the simulated low resolution version has been done for the Lahore case.

Lahore

The scene of Lahore (Pakistan) and surroundings is shown in Figure 4.21, which has been shown before in Figure 3.13. Figure 4.21a shows the measured NO_2 column with the detected plume pixels are indicated with black dots and Figure 4.21b depicts the different plumes as identified by the algorithm. This scene contains several clearly indistinguishable sources, which should be correctly identified by the algorithm, if it behaves as described in (Kuhlmann et al., 2018b). For the relatively small plumes, label number 2, 4 and 7 this is indeed the case. The plume from the city Lahore and the power plant plume upwind of the city are identified by the algorithm as one plume (label number 3), together with several small sources around the city. The plumes with label number 1 appear to be recognised as separate plumes in Figure 4.21a, however, because 8-connectivity is used group the plume labelled pixels, the plumes are erroneous identified as one by the algorithm. The tail of plume 5 is seen as separate small plumes, since their signal is likely too low compared to the background mean and noise.

Figure 4.22 shows the results for the same scene, simulated at the spatial resolution of the nominal TROPOMI measurements. The algorithm settings remain unchanged, except for the number of pixels used in the neighbourhood filter, which is reduced to 1, and the minimum pixel count threshold, which is reduced to 0, to compensate for the larger pixel size. The background mean and variability is calculated over 25 rows by 17 scanlines, to arrive at approximately the same area as in the zoom mode case.

From Figure 4.22a, it seems the small plumes on the left-hand side and being detected, however, only with a single pixel, which is insufficient to be labelled as plume. The larger plumes are similarly detected and labelled as in the zoom resolution case, although the plume shapes are captured with much less detail. Since the background variability of the downscaled simulation is lower than the zoom mode, the threshold is also lower, decreasing the amount of pixels that have a single sounding precision below the threshold and therefore labelling relatively less pixels as plume. From this comparison it seems the spatial resolution does not influence the performance of the plume detection algorithm much. However, the spatial resolution does influence how well the shape of the plumes is captured by the plume detected pixels, which decreases with increasing pixel size. From the zoom mode case it is relatively easy to visually identify the power plant plumes, while for the downscaled case this becomes much harder.

East-India

Figure 4.23 shows the results of the plume detection algorithm applied to a region in East-India, north of Calcutta. In this scene a multitude of power plants have produced a complex combined NO_2 plume, which is seen by the algorithm as two plumes (label 13 and 15). The plumes are located closely together and are mixed with each other, increasing the difficulty for the detection algorithm to correctly identify them as individual plumes. An analysis from scenes of this area with varying wind directions could perhaps be helpful to reveal the individual sources.

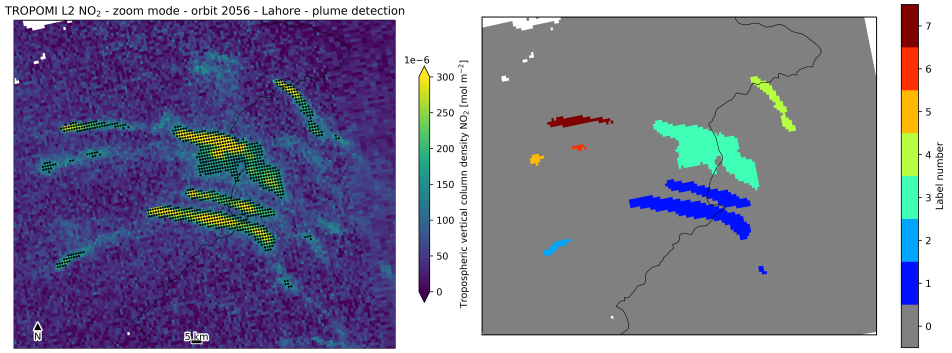

(a) (b)

Figure 4.21: Plume detection algorithm applied to TROPOMI L2 NO_2 zoom data, Lahore (India) scene at 07-03-2018: (a) VCD with pixels indicated as plume, (b) detected plume labels.

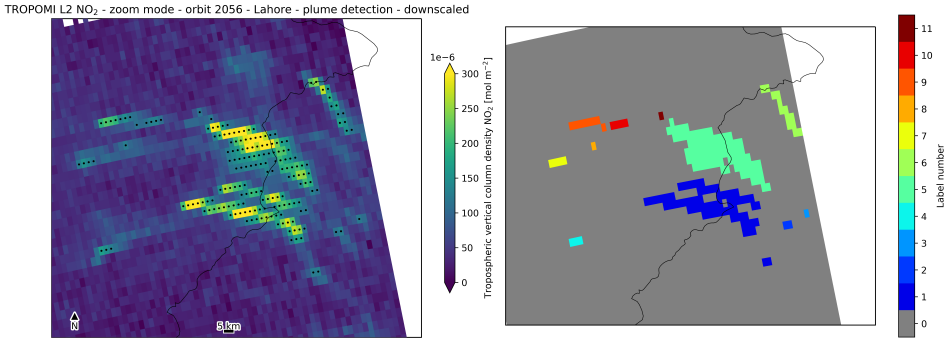

(a) (b)

Figure 4.22: Plume detection algorithm applied to TROPOMI L2 NO_2 zoom data downscaled to nominal resolution, Lahore (Pakistan) scene at 07-03-2018: (a) VCD with pixels indicated as plume, (b) detected plume labels.

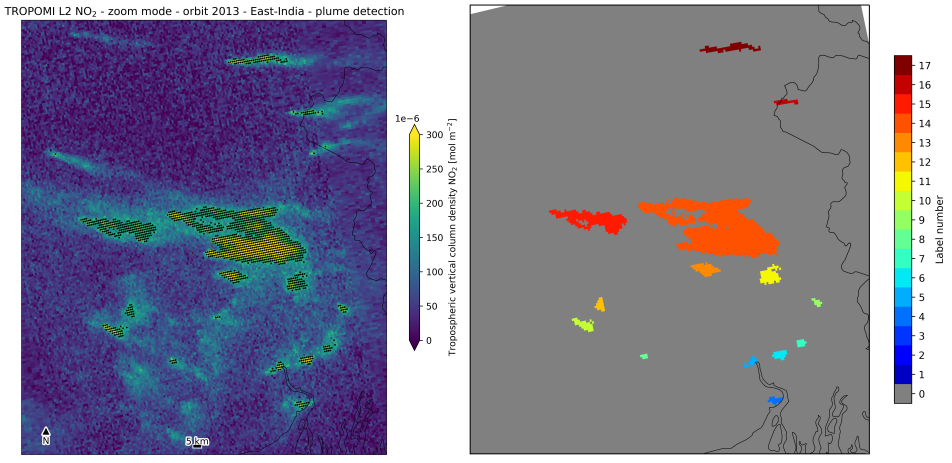

(a) (b)

Figure 4.23: Plume detection algorithm applied to TROPOMI L2 NO_2 zoom data, East-India scene at 04-03-2018: (a) VCD with pixels indicated as plume by black dots, (b) detected plume labels. Note that not all label numbers listed in the legend are within the extent of the figure.

Bełchatów

The power plant Bełchatów, covered before in Section 3.1 and Figure 3.4, was used to test the plume algorithm on a scene with relatively high noise. The results in Figure 4.24 show that the algorithm fails to correctly detect the power plant plume. The noise at this scene, which is typical for mid-latitudes, in combination with the small and weak plume, prevents the algorithm from separating the plume from the background. Individual patches of the plume are detected, however, are not linked together. Larger neighbourhood sizes were tested, which might have closed the gaps in the detected plume pixels, however, this did not improve the outcome.

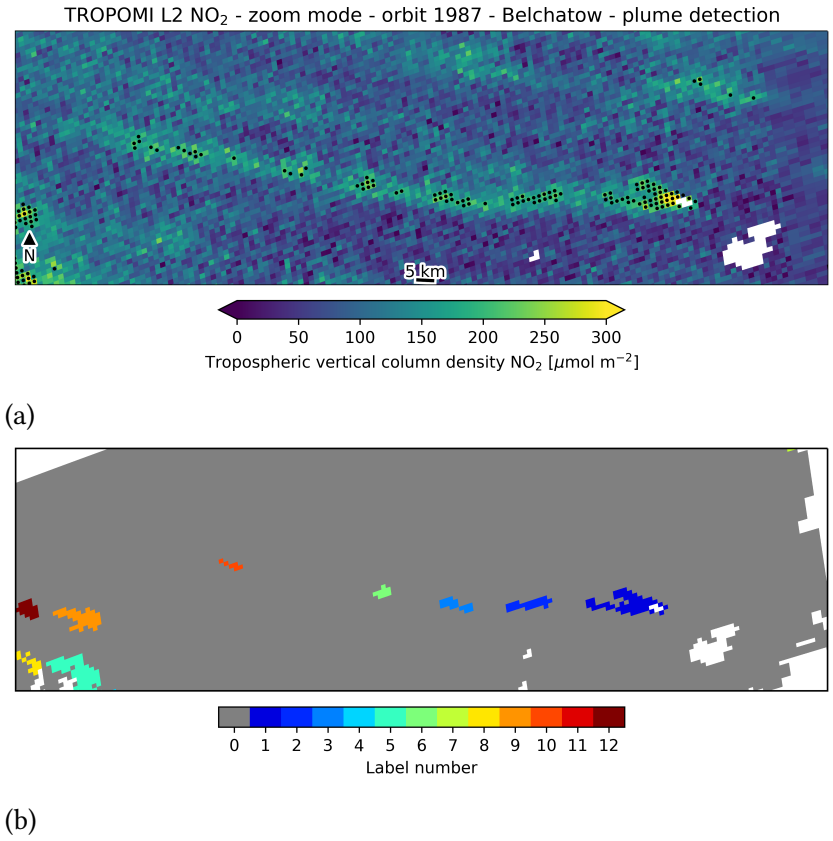

Figure 4.24: Plume detection algorithm applied to TROPOMI L2 NO_2 zoom data, Bełchatów (Poland) scene at 02-03-2018: (a) VCD with pixels indicated as plume, (b) detected plume labels.

Mumbai

The Mumbai scene, shown before in Figure 3.6 in Section 3.1, is used to demonstrate the plume detection algorithm on a complicated city plume. Figure 4.25 shows the result, where the extent of the city plume is captured quite well. The plume appendix in the south-west towards above the sea is correctly included in the city plume, as this plume is originating from the city and being blown to sea by the wind (see description is Section 3.1). For the plume appendix to the south-east it is unclear whether this belongs to the city or is a plume outside of it.

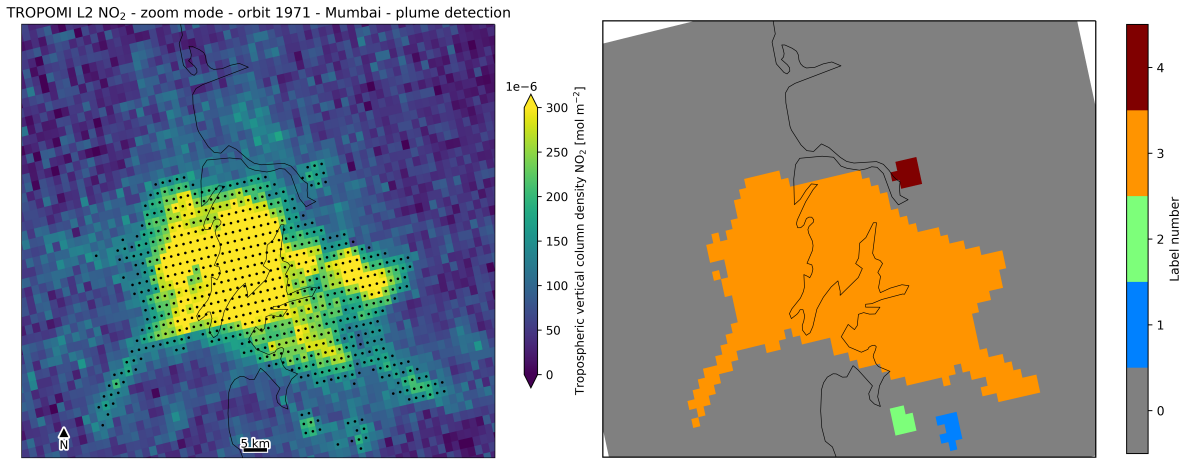

(a) (b)

Figure 4.25: Plume detection algorithm applied to TROPOMI L2 NO_2 zoom data, Mumbai (India) scene at 01-03-2018: (a) VCD with pixels indicated as plume, (b) detected plume labels.

Ahwaz

The results for the scene of Ahwaz, as seen before in Section 3.1 and Figure 3.2, is shown in Figure 4.26. The long curved plume from the power plant, label number 9, is detected correctly against the background. However, the plume from Ahwaz itself is separated into plume label 7 and 12. Although the tails of both these plumes seem to mix into one another, the algorithm manages to detect both plumes quite well.

To test plume detection capabilities on measurements with increased noise, the algorithm was tested on simulated measurements with added random error. A similar approach was followed as in the SMARTCARB study (Kuhlmann et al., 2018b), where a low and a high noise case was defined as following: a random error of 1 (low noise) / 2 (high noise) $\cdot 10^{15}$ molecules/cm^2 or 15% of the measured vertical column, whichever is the largest. The measurements in this case already contain noise, which is comparable to the low noise scenario. Hence, the noise levels under consideration for this test case are significantly larger than the noise scenarios in the SMARTCARB study. Noise affects the Z-test in the plume detection in three ways: the pixel values, variability of the background field and the single sounding precision.

The outcome of the low noise scenario is shown in Figure 4.27. The detected plumes are slightly smaller which causes several small plumes to be discarded, though overall the detected plumes are similar to the ones from the original case. The plume from Ahwaz, number 10, suffers the most from the noise, as the detected pixels become scrambled. The high noise scenario is shown in Figure 4.28a, where the results are affected by the noise more drastically. Only the centre pixels of the plume are still recognised as plume, and the shape of the plumes is not captured by the algorithm.

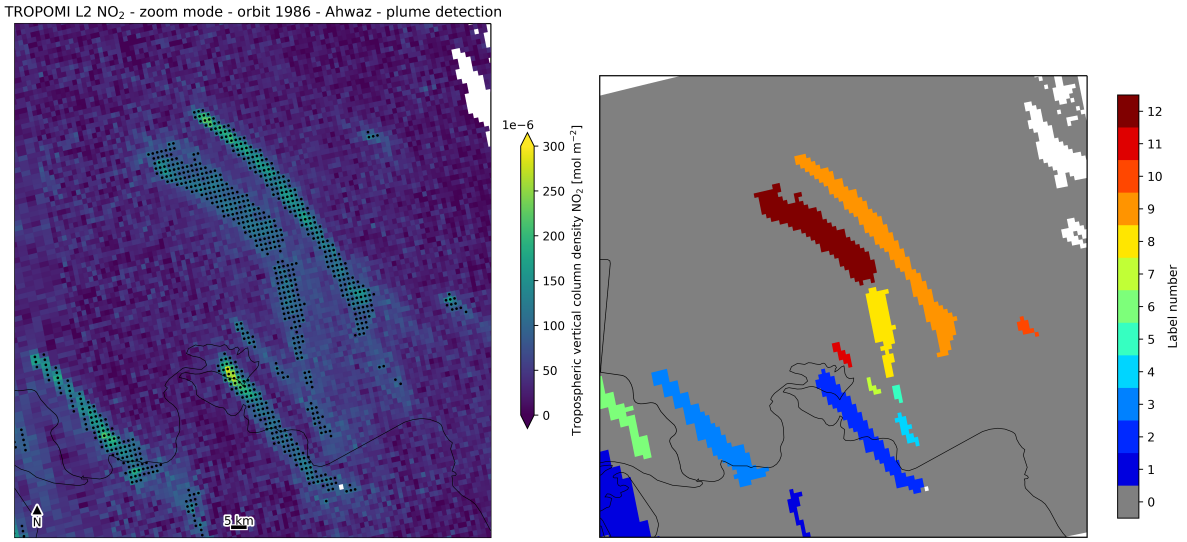

(a) (b)

Figure 4.26: Plume detection algorithm applied to TROPOMI L2 NO_2 zoom data, Ahwaz (Iran) scene at 02-03-2018: (a) VCD with pixels indicated as plume, (b) detected plume labels.

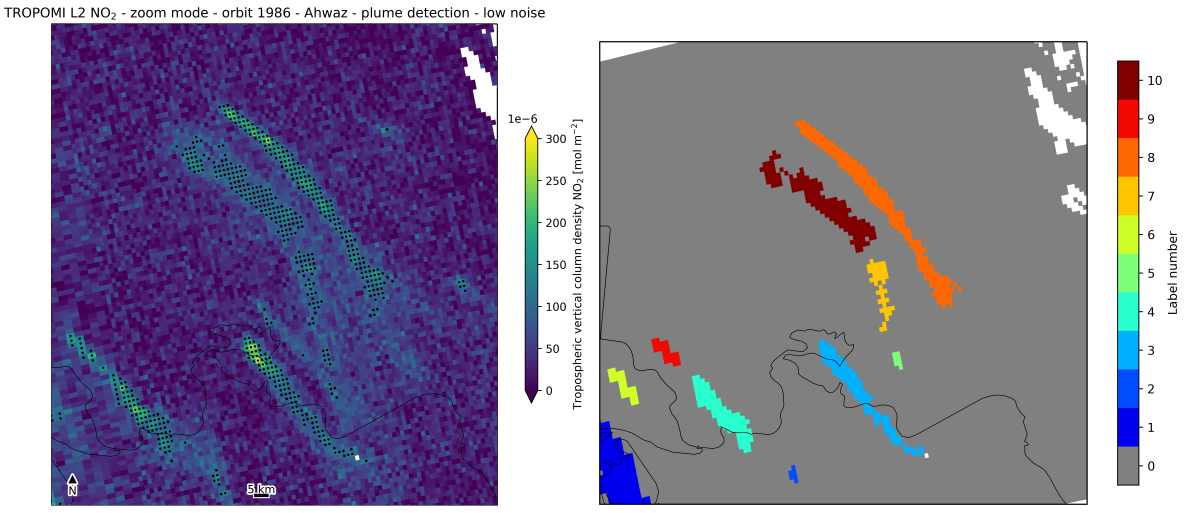

(a) (b)

Figure 4.27: Plume detection algorithm applied to TROPOMI L2 NO_2 zoom data, Ahwaz (Iran) scene at 02-03-2018. with added noise according to the low noise scenario: (a) VCD with pixels indicated as plume, (b) detected plume labels.

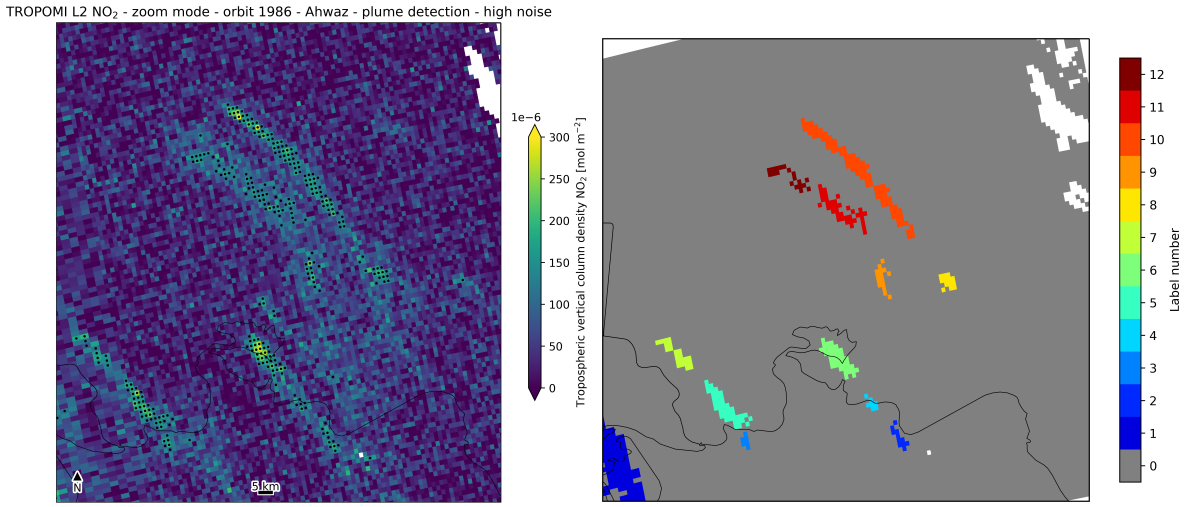

(a) (b)

Figure 4.28: Plume detection algorithm applied to TROPOMI L2 NO_2 zoom data, Ahwaz (Iran) scene at 02-03-2018. with added noise according to the high noise scenario: (a) VCD with pixels indicated as plume, (b) detected plume labels.

4.3.3 Conclusion

The presented cases have demonstrated the SMARTCARB plume detection algorithm on real TROPOMI NO_2 measurements at a spatial resolution of 2.4 x 1.8 km, close to the 2 x 2 km simulations from the study. For cases with high albedo, and thus good signal-to-noise ratios, the algorithm performs well, and most plumes are correctly detected. However, when plumes for different power plants start mixing downwind of the sources, the algorithm cannot distinguish the sources any longer. Additional noise to the measurements decreased the performance of the algorithm moderately in the low noise scenario, and significantly in the high case scenario. Applied to simulations at nominal TROPOMI spatial resolution (7 x 3.5 km), the algorithm still detects the plumes, although the shape of the plumes is captured with much less detail. For a scene typical for mid-latitudes, the algorithm did not succeed in detecting a power plant plume. This demonstration provides further support for a 2 x 2 km resolution NO_2 instrument, with an adequate signal-to-noise ratio, on the Sentinel 7 CO_2 mission to enhance CO_2 detection capabilities. However, design requirements on noise and spatial resolution cannot be drawn from these cases, as the zoom mode data-set contains too few measurements to be statistically robust.

5

Zoom-mode retrievals using high resolution a priori input

Section 4.1 in the previous chapter has shown several NO_2 polluted scenes in Europe where the measured NO_2 values are well represented by the forecasted values from the CAMS models. To show the impact of the spatial resolution of the a priori NO_2 profiles, used in the NO_2 retrieval algorithm to calculate the air mass factors, zoom-mode retrievals are attempted in Section 5.1 using the profiles from the CAMS models, instead of operationally used coarse profiles from the TM5 model. Another a-priori input used in the cloud and NO_2 retrieval algorithms, the surface albedo or LER database, is considered to be coarse in spatial resolution compared to the nominal TROPOMI pixel size. Using an experimental high resolution surface albedo database to process the zoom mode-measurements, the impact on the TROPOMI cloud and NO_2 products are demonstrated in Section 5.2.

5.1 A priori NO_2 profiles from CAMS models

In the NO_2 retrieval algorithm the slant column density follows from the DOAS spectral fit. To convert this slant column density to a vertical column density, certain atmospheric parameters have to be taken into account that can influence the light path. For example, the surface pressure, cloud and aerosol profiles, but also the viewing geometry, surface albedo and wavelength of the measurement. The effect on the light path is condensed into the box-AMF, a measure that quantifies the vertically resolved measurement sensitivity to NO_2. The VCD can then be calculated according to Equation 5.1, where VCD_i represents the a priori NO_2 profile. In the TROPOMI NO_2 retrieval algorithm a look-up table is used which contains pre-calculated box-AMF's for different combinations of viewing geometry, surface pressure, surface albedo and effective cloud cover. The a priori NO_2 profiles are obtained from the TM5-MP CTM, a 3D model with a spatial resolution of 1° x 1° (roughly 110 by 110 km) and time resolution of 30 minutes. In this section the TM5-MP CTM is referred to as 'TM5'. A more detailed description of these retrieval steps can be found in Section 1.3.3.

$$VCD = \frac{\sum_{i=0}^{TOA} BAMF_i \cdot VCD_i}{AMF} \tag{5.1}$$

Variability of the retrieved tropospheric NO_2 columns could be explained for 16% by the a priori NO_2 profiles, according to a recent NASA aircraft campaign (Judd et al., 2019). Additionally, a comparison between OMI NO_2 retrievals using TM5 model profiles at 3° x 2° resolution and at 1° x 1° resolution shows a more pronounced contrast between background and pollution sources for the higher resolution profiles (van Geffen et al., 2019). The currently used a priori profiles are spatially coarse compared to the TROPOMI pixels resolution, especially compared to the zoom mode resolution. Increasing the resolution of the a priori profiles would better resolve pollution sources and potentially provide a better reference profile for the retrievals, possibly reducing the error in the retrieved VCD.

To investigate this, profiles from CAMS models will be used for the AMF calculation for several selected scenes. These regridded model outputs have a spatial resolution of 0.1° x 0.1° (roughly 10 x 7 km in Europe) with hourly time-steps. A comparison between the NO_2 column derived from the CAMS model and the retrieved column from TROPOMI is done in Section 4.1. Cases are selected when the location, orientation and magnitude of the plume are represented correctly, to first order, by one of the CAMS models. However, it should be kept in mind that a resolution increase of the assumed profile shape is not necessarily beneficial to the retrieval. For example, if the plume would have an erroneous location, the retrieval performance would decrease, since the profiles with increased NO_2 concentration would be used at the wrong retrieved columns. In that case a profile shape averaged over a larger area would be better suitable.

First, the method of modifying the retrievals with new profiles, and how to obtain those profiles from the TM5 model and the CAMS models, will be explained. The profiles will then be compared for the selected TROPOMI scenes, before the modified CAMS profiles will be applied to the retrieval. Finally, a comparison is made using the retrieved VCD for each scene using the different profile spatial resolutions.

5.1.1 Method

The averaging kernel is included in the retrieval output (see Section 1.3.3). This allows for the a priori profile used in the retrieval algorithm to be easily replaced with the following steps (Eskes et al., 2018b):

1. Calculate the modified air mass factor:

$$AMF' = AMF \frac{\sum_l AK_l^{trop} x'_l}{\sum_l x'_l} \tag{5.2}$$

   Where x' is the alternative NO_2 a priori partial columns profile and AMF' is the modified air mass factor. This means that layers that contain NO_2 and $AK > 1$ have an increasing effect on the total AMF, whereas layers with $AK < 1$ have a decreasing effect on the total AMF.

2. Calculate the modified averaging kernel:

$$AK' = \frac{AMF}{AMF'} AK \tag{5.3}$$

3. Calculate the modified vertical column density:

$$VCD' = \frac{AMF}{AMF'} VCD \tag{5.4}$$

An increase in AMF leads to a lower VCD, and a decrease in AMF leads to a higher VCD.

Summarised: a layer containing NO_2 leads to a higher VCD when the sensitivity to that layer is low ($AK < 1$), and leads to a lower VCD when the sensitivity to that layer is high ($AK > 1$). Physically this means the following: the a priori profile shape multiplied with the averaging kernel, which can be seen as a measure for the sensitivity, scales the total air mass factor in order to correct the tropospheric NO_2 for the bias introduced by the non-uniform vertical sensitivity. Better spatially resolved a priori profiles should therefore lead to more accurate column estimates.

The averaging kernel that is used (AK^{trop}) is the tropospheric averaging kernel, which can be obtained from the total averaging kernel as following (Eskes et al., 2018b):

$$AK^{trop} = \begin{cases} \frac{AMF}{AMF^{trop}} AK & l <= l_{tp} \\ 0 & l > l_{tp} \end{cases} \tag{5.5}$$

Where l_{tp} is the tropopause layer, as given in the TM5 model output for the used vertical numbering in the model. The total AMF and tropospheric AMF are provided separately in the TROPOMI L2 output.

The NO_2 profile produced by the TM5 model is given as function of model layers, defined by two constants and the surface pressure. This model layering follows a hybrid sigma-pressure coordinate scheme, which uses sigma coordinates near the surface to follow the terrain and isobaric layers to describe the pressures higher up the atmosphere. The TM5 model pressure profile in this scheme can be calculated as following (Eskes et al., 2018b):

$$p(t,k,j,i,l) = a(k,l) + b(k,l) \cdot p_s(t,j,i) \tag{5.6}$$

where:

p = pressure
t = time index
k = layer index
j = scanline index (along track)
i = ground-pixel index (across track)
l = bottom ($l = 0$) or top ($l = 1$) of the layer
a = hybrid A coefficient: pressure
b = hybrid B coefficient: sigma
p_s = surface pressure

For each TROPOMI pixel a NO_2 profile is calculated, based on linear interpolation of the four nearest neighbour TM5 cell centres. In the calculation of the pressure profile a modified surface pressure is used which corrects the profile for the terrain height offset between the spatially coarse terrain height in TM5 and a more detailed terrain height from a digital elevation model in TROPOMI (van Geffen et al., 2019).

The NO_2 profile is given as a mixing ratio (or mole fraction) per atmospheric layer in parts per million (ppm). The modification steps require a NO_2 profile given as an integrated column per layer with units [mol/m²]. The mixing ratio can be converted to a concentration using the perfect gas law (see Equation 5.7), where the pressure and temperature profiles are obtained from the TM5 model as well. To convert to a partial column, the concentration has to be integrated over the vertical distance covered by the layer. The layer heights can be calculated from the pressure levels with the barometric formula, shown in Equation 5.8, using the temperature profile.

$$c = \frac{P \cdot r}{R \cdot T} \tag{5.7}$$

where:

c = concentration [mol/m³]
P = pressure [Pa]
r = mixing ratio / mole fraction [mole/mole] / [ppm]
R = universal gas constant (8.31446261815324) [JK⁻¹mol⁻¹]
T = temperature [K]

$$H = -ln\left(\frac{P}{P_s}\right)\frac{R_{air}}{g_0 T} \tag{5.8}$$

where:

H = Height above surface [m]
P = pressure [Pa]
P_s = surface pressure [Pa]
M_{air} = molar mass air (from TM5) [kg/mole]
g_0 = surface gravitational acceleration (9.80665) [m/s²]
T = temperature [K]

The NO_2 profiles in the CAMS models are stored with a time interval of 1 hour. When obtaining the profile for a TROPOMI pixel, the profiles are interpolated to the TROPOMI measurement time. Since the spatial resolution of the CAMS models is in the same order of magnitude as the TROPOMI resolution, it was not necessary to spatially interpolate the profiles, as was done for the TM5 profiles. The NO_2 values are given in mass concentration, which can easily be converted to molar concentration with the molar mass of NO_2. The profile is given at fixed heights above the surface: 0, 50, 250, 500, 1000, 2000, 3000 and 5000 m. The CAMS profiles are then interpolated to the TM5 level heights, since these are used in the TROPOMI Level-2 output as well, and the new profile has to be defined the same. Finally, the partial columns can be calculated by integrating over the height per layer. The profiles in the CAMS models only have data up to 5 km height, the remaining layers above are filled using the original TM5 profile. The planetary boundary layer does not exceed 5 km, therefore, the tropospheric NO_2 within the boundary layer is captured by the CAMS models. However, the relatively small amount of NO_2 present in the free troposphere might not be represented by the CAMS models. Column measurements from space are more sensitive to NO_2 in the free troposphere than to the boundary layer (Silvern et al., 2019). This raises little concern for highly polluted areas, since the free tropospheric NO_2 has a relatively small effect. However, for unpolluted areas the measured column is mostly contributed by the free tropospheric

background. In this analysis highly polluting sources are studied, and therefore the contribution of free tropospheric NO_2 that might not be captured by the CAMS model might only have a minor contribution in the results. Furthermore, by extending the profile above 5 km with the coarser profile from the TM5 model, the contribution of the free tropospheric NO_2 might be resolved, since it can be considered as a spatially uniform background value.

5.1.2 Results

The comparison of the TM5 and CAMS profiles as a priori profiles for the TROPOMI NO_2 retrieval is done for the following scenes: the power plant Bełchatów, the cities Charkov and Madrid, and the Netherlands. A comparison between CAMS models themselves and between the CAMS models and the TROPOMI columns has been done in Section 4.1. For each scene, the best performing CAMS model was chosen and used for the following analysis. First, the columns derived from the model profiles will be compared, then profiles from the polluted area and from the background are compared, and finally, the effect on the TROPOMI VCD is investigated. For the two most pronounced cases, Madrid and Charkov, a more in-depth analysis is performed.

Bełchatów

Figure 5.1 compares the integrated NO_2 profile from the TM5 model and the CAMS model ensemble for the Bełchatów power plant (Poland) at 02-03-2018. The TM5 model provides a spatial average of the area due to its coarse resolution, whereas the CAMS model does resolve the plume. The profiles from the two models are compared for an area inside the plume and for an area in the background in Figure 5.2, where the used areas are indicated in Figure 5.1b. The background profile in CAMS is lower at the surface and higher in the region 500-3000 m. For the polluted profiles, the CAMS profile shows significantly more NO_2 concentration, as expected.

The resulting effect on the VCD for this scene, shown in Figure 5.3 is not substantial, overall a slight decrease in NO_2 column is visible. At the origin of the power plant plume, a small increase can be observed for some pixels. The AMF increases in the polluted area and in the background due to the increased profile values (see Equation 5.2) and high sensitivity close to the ground.

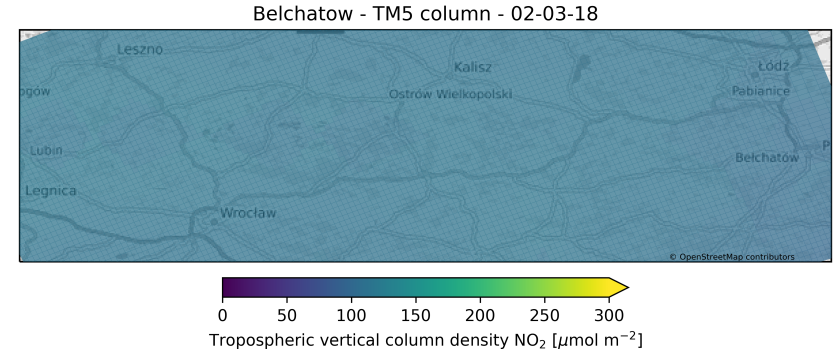

(a)

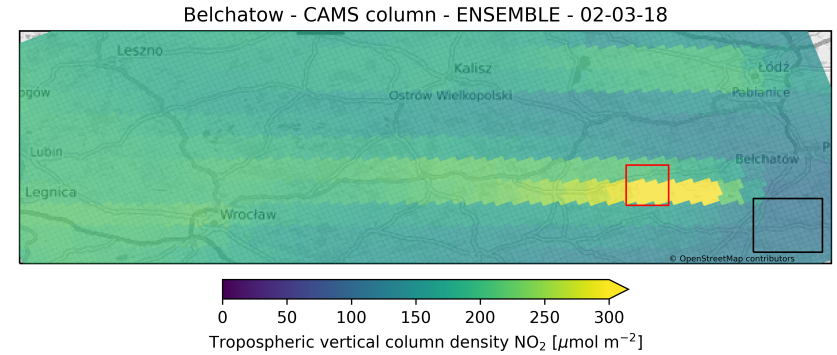

(b)

Figure 5.1: Comparison of the integrated NO_2 column of the power plant Bełchatów (Poland) on 02-03-2018 from (a) the TM5 model (b) and the CAMS model ensemble. The areas indicated with the black and red box are shown in Figure 5.2.

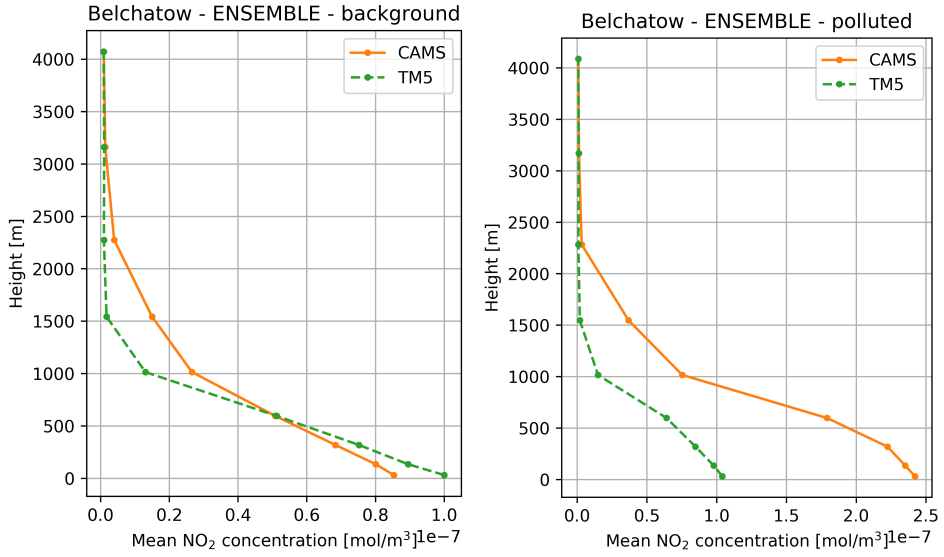

(a) (b)

Figure 5.2: Comparison of the vertical NO_2 profiles of the power plant Bełchatów (Poland) scene on 02-03-2018 for (a) polluted area (b) the background area. The average profile is taken over the areas indicated with the red and black box, respectively, in Figure 5.1b.

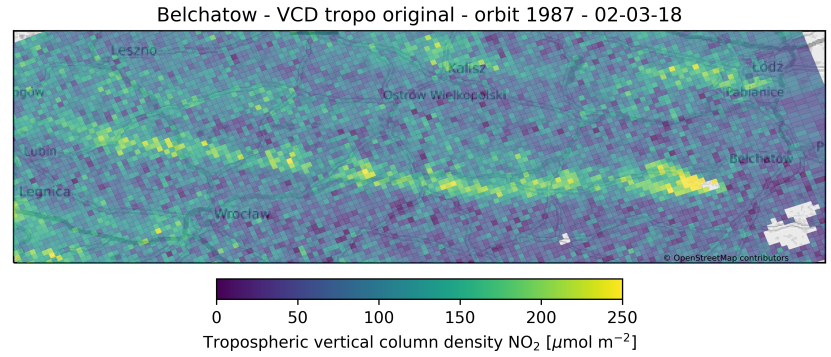

(a)

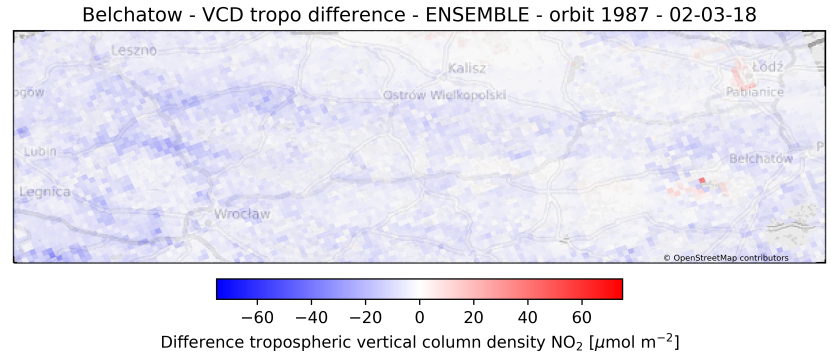

(b)

Figure 5.3: Comparison of the retrieved NO_2 VCD's of the power plant Bełchatów (Poland) on 02-03-2018: (a) the original retrieval (b) and relative difference when using the CAMS model profiles.

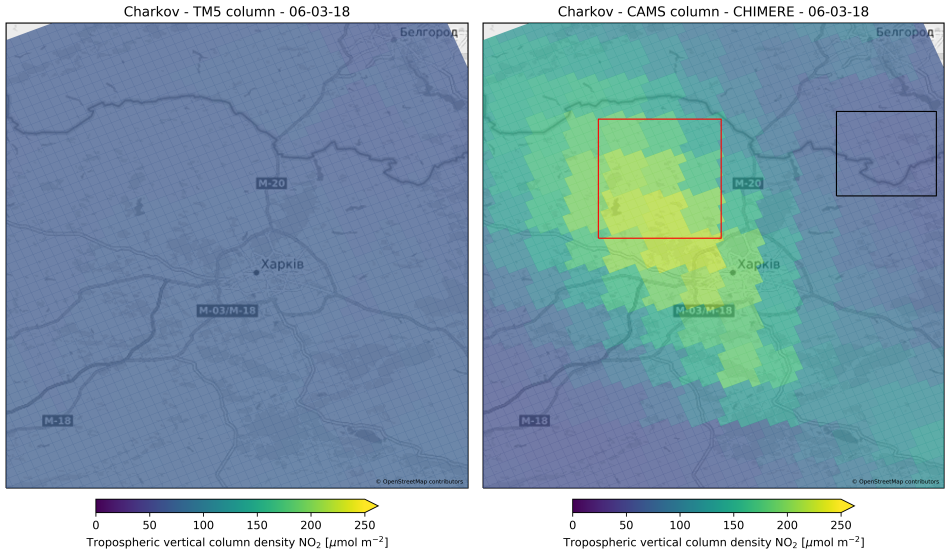

(a) (b)

Figure 5.4: Comparison of the integrated NO_2 column of Charkov (Ukraine) on 06-03-2018 from (a) the TM5 model (b) and the CAMS model CHIMERE. The areas indicated with the black and red box are shown in Figure 5.5.

Charkov

The comparison for the city Charkov (Ukraine) in Figure 5.4 and 5.5 shows similar behaviour as for Bełchatów: in the background slightly higher NO_2 values, except near the surface, and increased values for the polluted profile. The effect on the VCD is also quite similar, as shown in Figure 5.6. A slight decrease in column values, with a few outliers possibly due to cloud contamination.

Figure 5.7a shows the tropospheric averaging kernel averaged over the polluted area (red box in Figure 5.4b). It shows the averaging kernel passes the 1 threshold close to the surface, so that the retrieval is sensitive to NO_2 up to the surface. The effect of Equation 5.2 is visualised in Figure 5.7b, where $AK - 1$ times the NO_2 partial column is plotted for the polluted box. Layers with a value larger than 0 will increase the total AMF, while layers below 0 will decrease the AMF. The resulting multiplication factor of the AMF is 1.2, which then decreases the VCD with a factor 1.2.

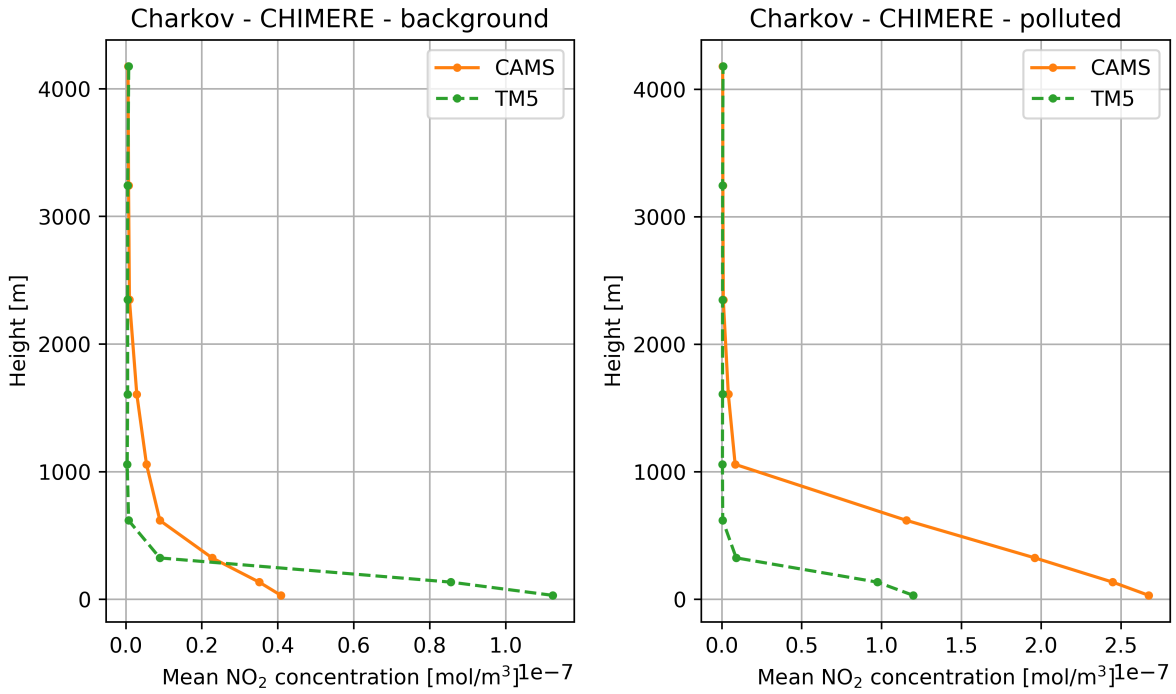

(a) (b)

Figure 5.5: Comparison of the model NO_2 profiles of Charkov (Ukraine) scene on 06-03-2018 for (a) polluted area (b) the background area. The average profile is taken over the areas indicated with the red and black box, respectively, in Figure 5.4b.

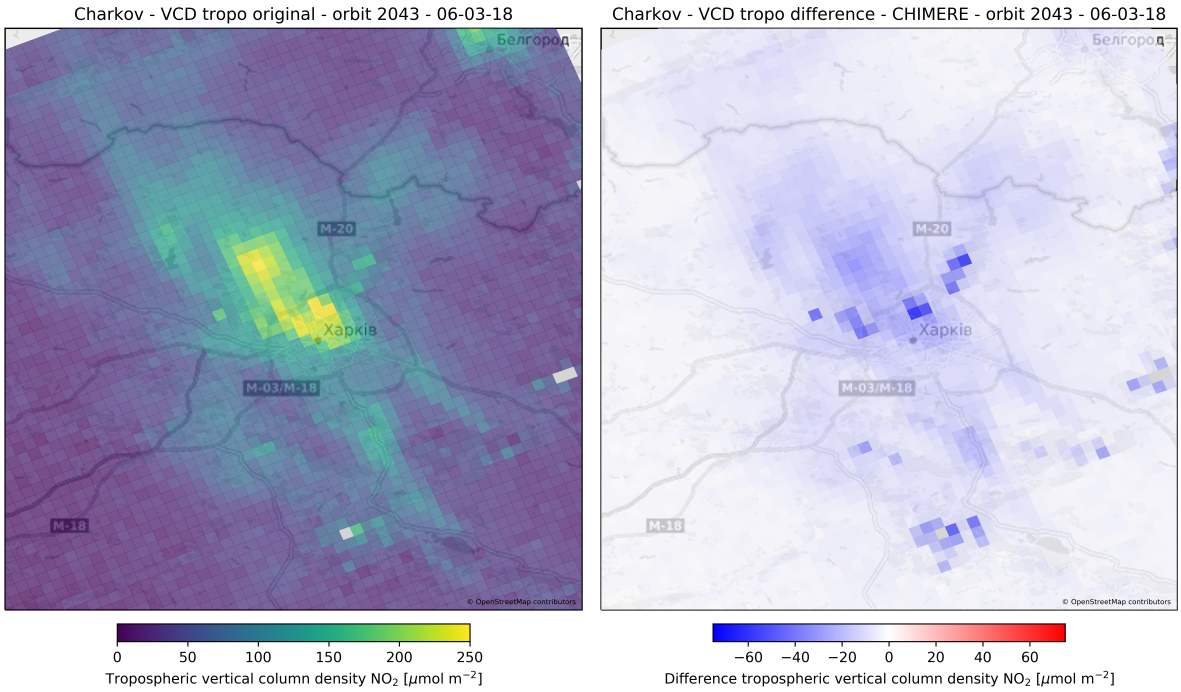

(a) (b)

Figure 5.6: Comparison of the retrieved NO_2 VCD's of Charkov (Ukraine) on 06-03-2018: (a) the original retrieval (b) and relative difference when using the CAMS model profiles.

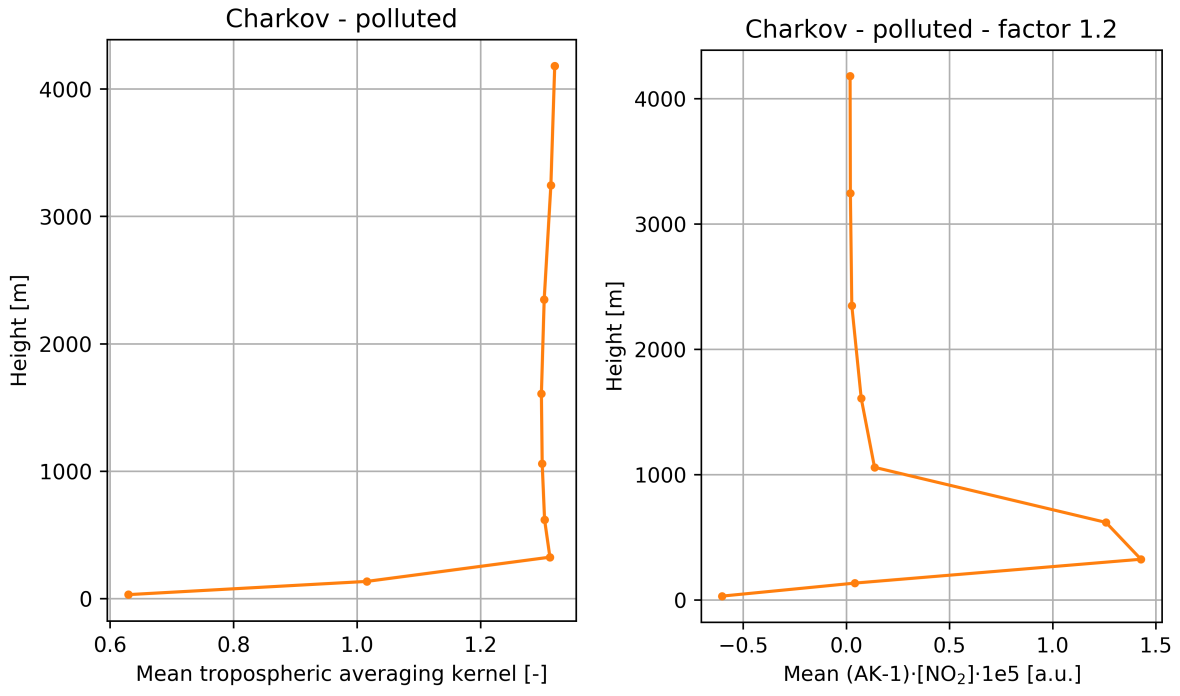

(a) (b)

Figure 5.7: Polluted area from Charkov (Ukraine) scene: (a) tropospheric averaging kernel (b) visualization of the effect of the CAMS profile on the total AMF, total AMF multiplication factor is 1.2.

Madrid

The comparison of the model derived columns for the city Madrid (Spain) is shown in Figure 5.8. A clear plume shape can be seen for CAMS (EURAD model), while the TM5 model shows a constant value. Comparing the profiles of the two models for a background area shows different behaviour than for the previous cases, since here the entire profile is smaller in value for CAMS than for TM5. For the polluted area, there is a large increase in NO_2 concentration for the CAMS model compared to TM5. The resulting effect on the VCD is a substantial increase around the peak of the plume (≈20%) and less increase for the more distant plume (≈10%). Contrary to the previous scene, there is a increase in VCD due to a priori profiles with higher concentrations. Figure 5.11 explains the cause: until 800 m height the averaging kernel is below 1, meaning the retrieval is less sensitive to NO_2 close to the surface. The new a priori profile has a decreasing effect on the total AMF (factor 0.9), which increases the VCD with approximately a factor 1.1. Essentially, the higher resolution a priori profile corrects the retrieval for the underestimated NO_2 concentration at the surface, where the retrieval has low sensitivity.

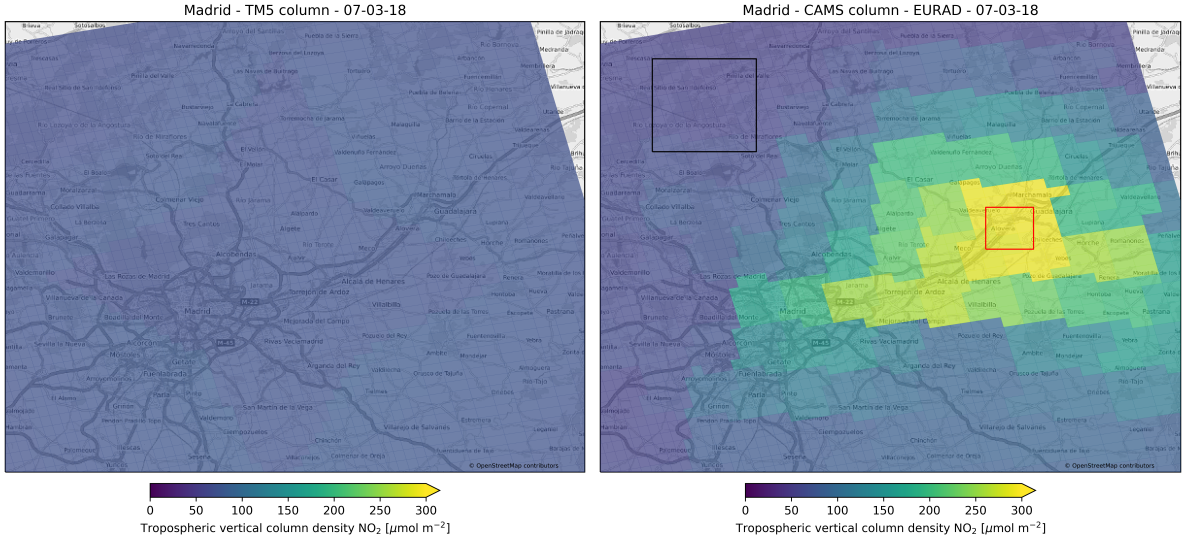

(a) (b)

Figure 5.8: Comparison of the integrated NO_2 column of Madrid (Spain) on 07-03-2018 from (a) the TM5 model (b) and the CAMS model EURAD. The areas indicated with the black and red box are shown in Figure 5.9.

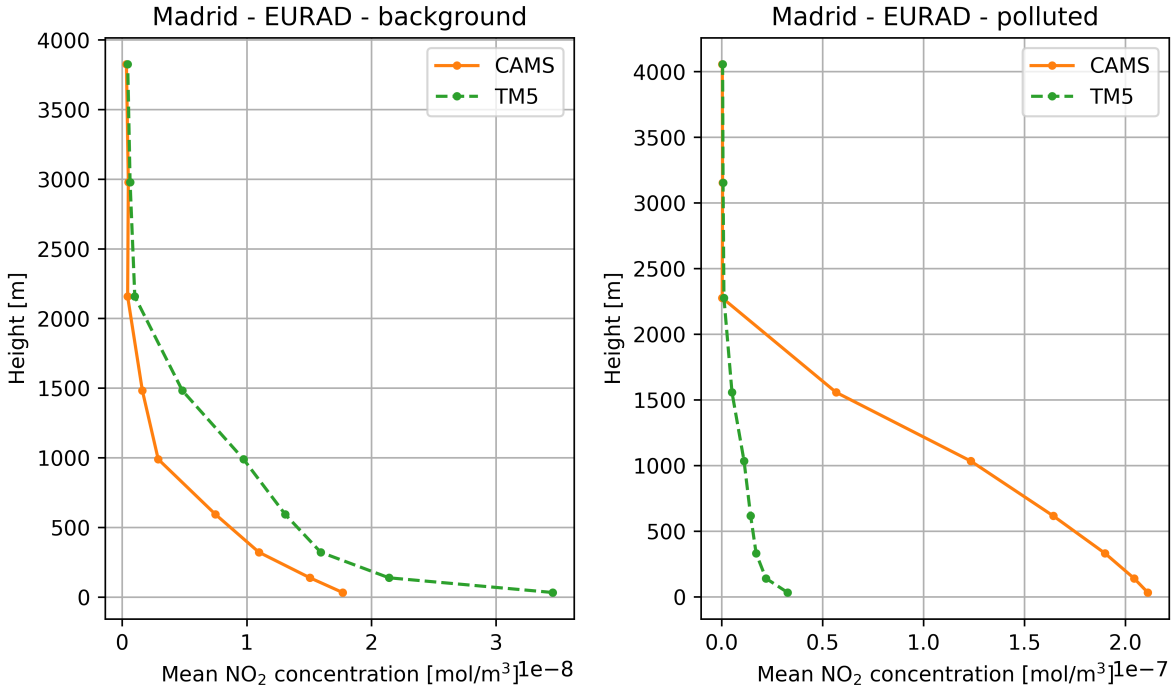

(a) (b)

Figure 5.9: Comparison of the model NO_2 profiles of Madrid (Spain) scene on 07-03-2018 for (a) polluted area (b) the background area. The average profile is taken over the areas indicated with the red and black box, respectively, in Figure 5.8b.

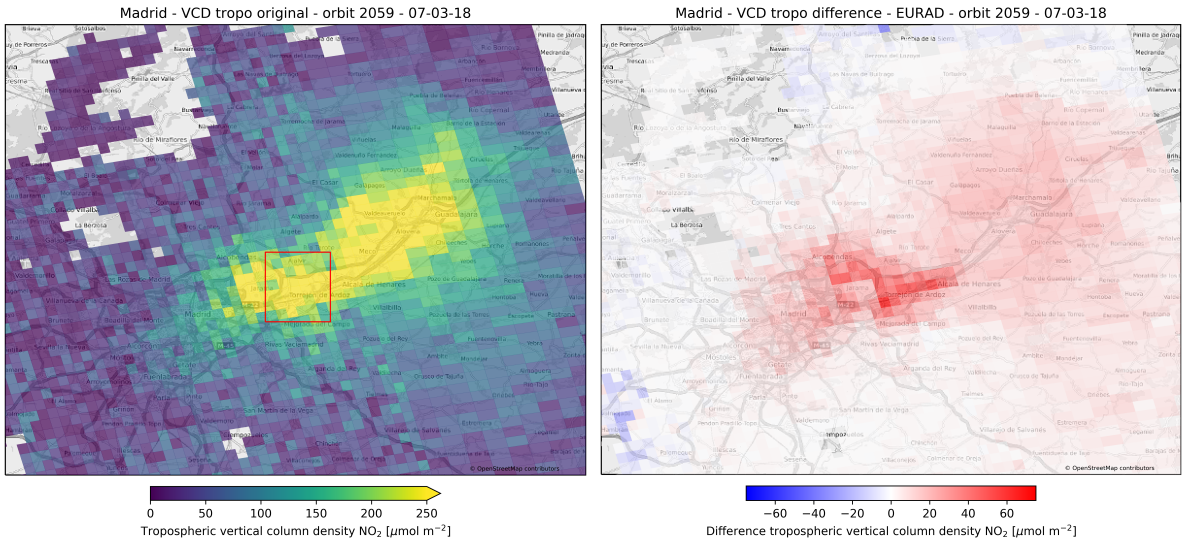

(a) (b)

Figure 5.10: Comparison of the retrieved NO_2 VCD's of Madrid (Spain) on 07-03-2018: (a) the original retrieval (b) and relative difference when using the CAMS model profiles.

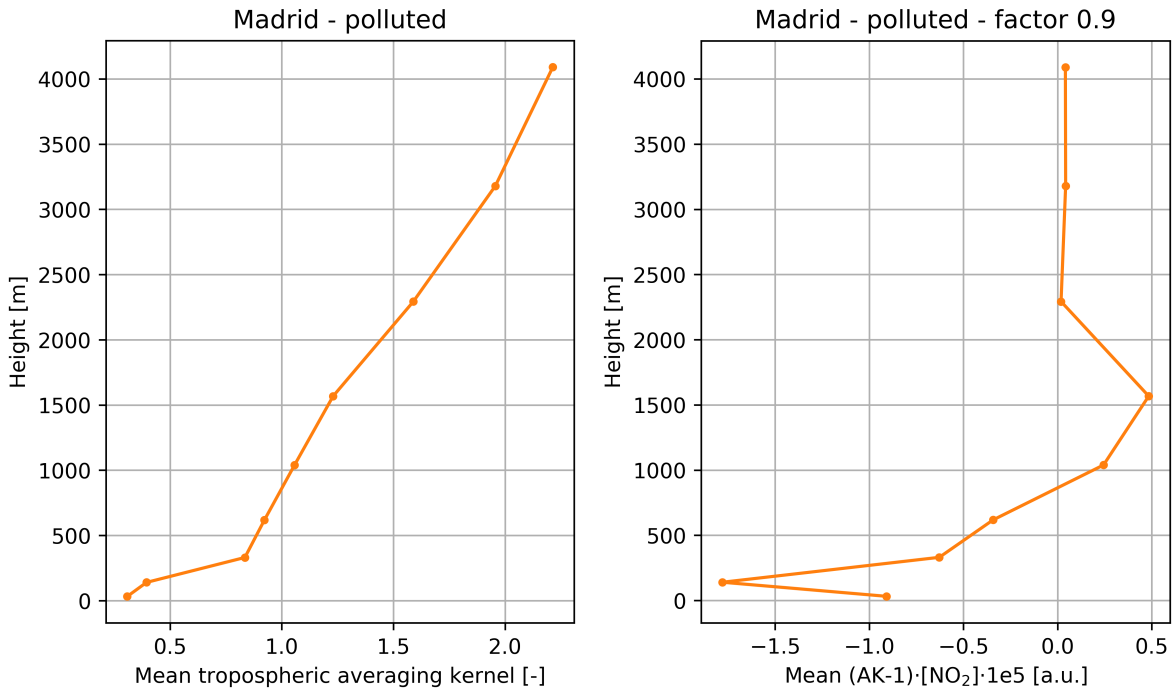

(a) (b)

Figure 5.11: Polluted area from Madrid (Spain) scene: (a) tropospheric averaging kernel (b) visualization of the effect of the CAMS profile on the total AMF, total AMF multiplication factor is 0.9

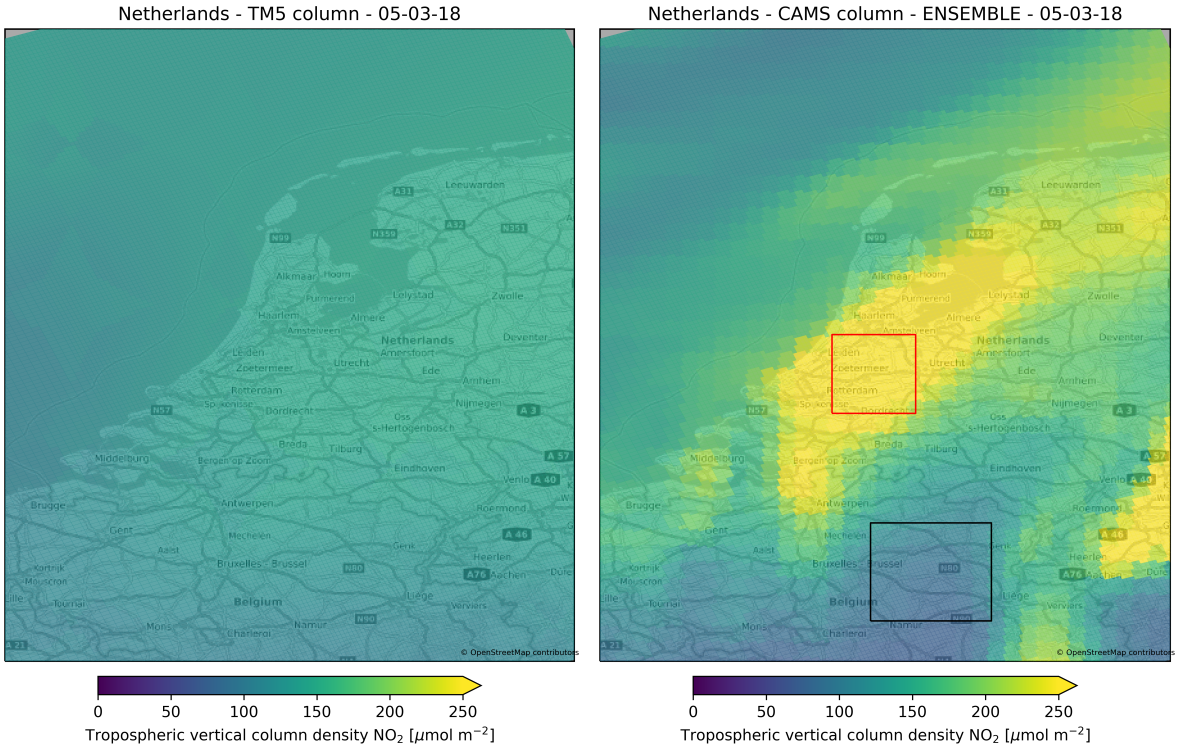

(a) (b)

Figure 5.12: Comparison of the integrated NO_2 column of the Netherlands on 05-03-2018 from (a) the TM5 model (b) and the CAMS model ensemble. The areas indicated with the black and red box are shown in Figure 5.13.

The Netherlands

The case for the Netherlands shows similar behaviour to the Madrid case. An increase in a priori profiles for polluted areas and a decrease for the background values is shown in Figures 5.12 and 5.13. This results in a decrease in AMF, causing an increase in VCD, as seen in Figure 5.14. Some local increases are visible, where the changes above the Ijssel lake stand out. The comparison between the original zoom-mode retrieval and the CAMS forecast in Figure 4.7 shows there is a large discrepancy between the two at this location, likely caused by ice cover, as discussed in Section 5.2.

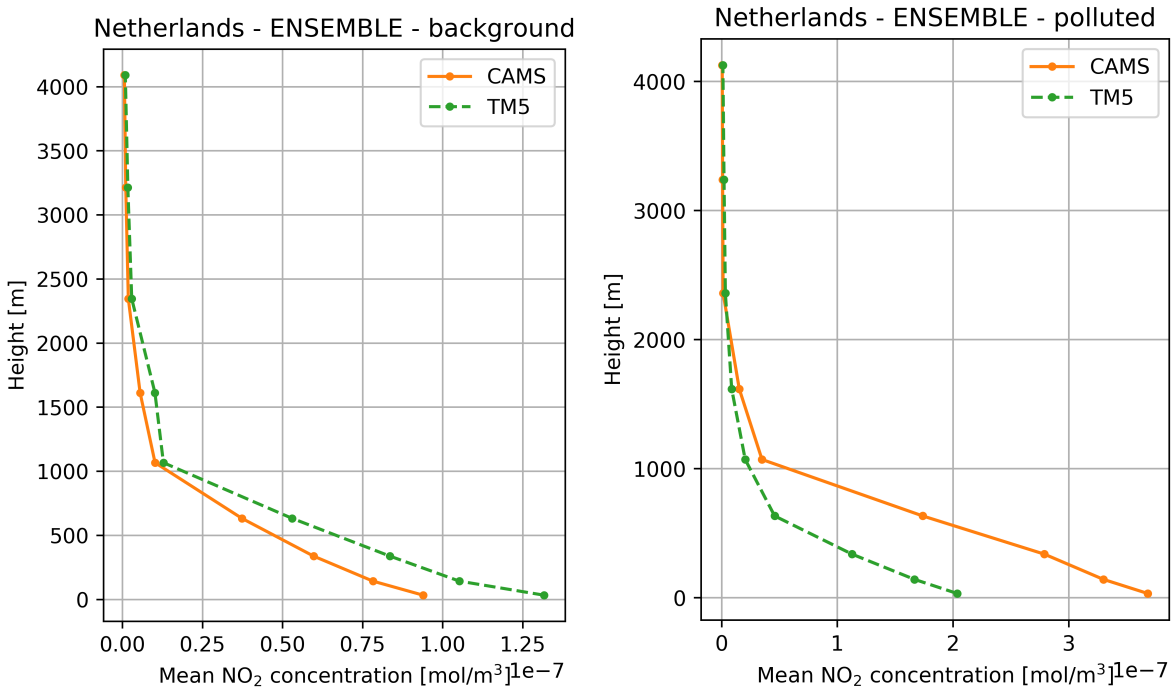

(a) (b)

Figure 5.13: Comparison of the model NO_2 profiles of the Netherlands scene on 05-03-2018 for (a) polluted area (b) the background area. The average profile is taken over the areas indicated with the red and black box, respectively, in Figure 5.12b.

5.1.3 Conclusion

This comparison study has shown the possible impact of using high resolution a priori profile shapes to retrieve tropospheric NO_2 from high resolution measurements, using several example cases.

First of all, when using model profiles at high spatial resolution, one has to be make sure the model resolves the NO_2 enhancements well enough. A model where the plumes are missing or are at the wrong location, either due to discrepancies between the predicted and actual meteorological conditions or due to outdated emission inventories, could lead to a decrease in accuracy of the retrieval. An iterative process could solve this, where the first retrieval is done with coarse model profiles, in order to check if the high resolution profiles

are sufficiently accurate before using them in a second retrieval. Nevertheless, this remains a 'catch-22' problem, as accurate a priori profiles from emission models are required to improve column measurements, and accurate column measurements are required to improve emission models.

The high spatial resolution a priori profiles seem to correct the retrieval for wrongly assumed NO_2 concentrations. For layers the retrieval is sensitive to, an increase in a priori NO_2 concentration leads to a decrease in retrieved NO_2 VCD, since the box-AMF for those layers was underestimated and the contribution of that layer to the column was overestimated. Vice-versa, for layers with little sensitivity, increased a priori concentration leads to an increase in VCD, since the contribution of that layer was underestimated. For the shown cases, increasing the model resolution from 1.0° x 1.0° to 0.1° x 0.1° resulted in local changes of the retrieved VCD in the order of 10-20% increase or decrease, depending on the combination of NO_2 profile and averaging kernel, as described above.

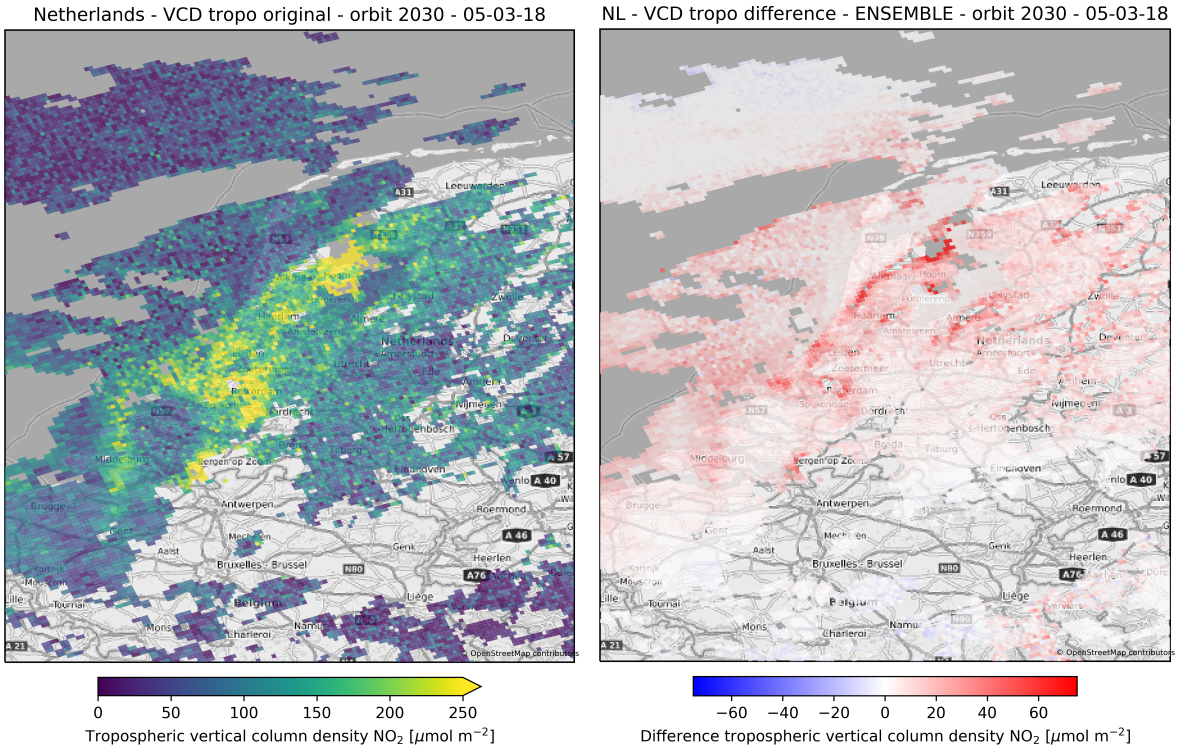

Figure 5.14: Comparison of the retrieved NO_2 VCD's of the Netherlands on 05-03-2018: (a) the original retrieval (b) and relative difference when using the CAMS model profiles.

5.2 High resolution surface albedo database

The TROPOMI L2 retrieval algorithms require surface albedo databases as input, which are currently obtained from an OMI LER climatology (Kleipool et al., 2008) for the NO_2 algorithm (440 nm) and from a GOME-2 LER climatology (Tilstra et al., 2017) for the FRESCO cloud retrieval (758 and 772 nm). Ideally, a bidirectional reflectance distribution function (BRDF) would be used, which describes the reflectivity of a surface as function of incident angle, reflectance angle and wavelength. However, this quantity is not available for the required wavelengths, thus the Lambertian Equivalent Reflectance (LER) is used. The LER assumes the reflecting surface as an isotropic diffuse reflector that reflects light from all incoming directions equally over all outgoing directions. Assuming a Lambertian surface, the reflectivity is equal to the albedo, which causes these terms to be often interchanged in documentation. The OMI LER database is made from 5 years of OMI reflectivity data, sampled globally at monthly and yearly averaged albedo values at a grid of 0.5° x 0.5° for UVIS wavelengths at similar viewing geometry as TROPOMI. The GNOME-2 LER database contains the surface reflectivity values sampled at a resolution of 0.25° x 0.25° for a large wavelength range. However, the OMI LER database is used for the NO_2 retrieval, because the underlying GOME-2 measurements are coarser than the OMI measurements and the overpass time is several hours before TROPOMI (van Geffen et al., 2019).

An accurate and detailed albedo map is crucial to many atmospheric retrieval methods. For example, the TROPOMI cloud support retrieval algorithm (FRESCO) uses the surface albedo to differentiate between low clouds and the surface and the NO_2 retrieval uses the surface albedo to determine the air-mass factors (van Geffen et al., 2019). For areas with homogeneous land cover, the spatial resolution of the albedo map is of less importance than for boundary cases, such as coast lines and water bodies. Furthermore, seasonality in land cover is an important aspect when considering an albedo map. Lorente et al. (2018) has shown the impact of using surface reflectance anisotropy by using a high resolution BRDF database to retrieve cloud cover and NO_2 for OMI and GOME-2 measurements, where under certain conditions the impact on the total NO_2 AMF was up to 30%-35%. A recent aircraft campaign, (Judd et al., 2019, in review), performed NO_2 column measurements at a spatial resolution of 250 m x 250 m. From a multi-variable linear regression they concluded that in their NO_2 retrieval the variability in tropospheric AMF could be explained for 64% by the surface albedo, illustrating the importance of high resolution surface reflectance data for high spatial resolution retrievals. Furthermore, a case study applying high resolution surface reflectances derived from Sentinel-2 on TROPOMI NO_2 retrieval cases, Bossers (2019), has shown an improvement in the accuracy of the AMF values by 10% on average and up to 68% locally on the Rotterdam greater area. These studies indicate the importance of a good quality, high spatial resolution albedo database for cloud and NO_2 retrievals. Especially for future UV-VIS sensors with increasing spatial resolution to 2 x 2 km, an albedo climatology with a mid-latitude resolution of 55 km x 34 km can be considered too coarse.

A new experimental LER database with a grid resolution of 0.05° x 0.05° is being developed at the KNMI. This database is generated from one year of TROPOMI reflectance data and contains a yearly albedo value per pixel, with a resolution of 5.5 km x 3.4 km at mid-latitudes, which is finer than the nominal TROPOMI pixel resolution. There are several drawbacks from this new database compared to the original LER database. Since the TROPOMI LER

database contains yearly albedo values instead of monthly, errors might be introduced in areas prone to seasonality changes in surface reflectivity. In addition, in this experimental version of the LER database, the wavelengths at which the albedo is calculated differs due to technical considerations. In the NIR band only one wavelength is included (754 nm), instead of two wavelengths, and in the VIS band the used wavelength is 426 nm, instead of 440 nm. The expected behaviour is that the processor will extrapolate the input albedo value to the specified albedo wavelength within the window used for the retrieval, however, errors introduced by this are unknown. To improve the quality of the original LER database, several methods are being applied in the processor. For example, using a land, ocean, snow and ice mask, the albedo of pixels which are known to be located over ocean will be corrected accordingly. Furthermore, in the FRESCO cloud algorithm, the surface albedo is corrected to match the measured radiance, by inferring a certain cloud fraction on the pixels. This could give rise to a false cloud cover, when there is a discrepancy between the surface albedo in the database and the actual surface albedo, which would increase the air mass factor. Besides, instrument degradation might decrease the measured reflectance, introducing a discrepancy between the LER database and the zoom-mode reflectance.

The FRESCO algorithm uses the O_2-A band (around 758 nm) to retrieve the cloud pressure and an effective cloud fraction (a radiometric equivalent of the geometric cloud fraction, which results in the correct TOA radiance while assuming a cloud albedo of 0.8) (van Geffen et al., 2019). However, in the NO_2 retrieval, only the cloud pressure from the FRESCO algorithm is used, and the cloud fraction and cloud radiance fraction are retrieved in the NO_2 window (440 nm). This is because the cloud fraction at the O_2-A window is not necessarily representative for the cloud fraction at the NO_2 window, due to large wavelength difference, especially above vegetated areas. Besides, there is a mismatch between the pixel field of view of the NIR and the VIS bands of TROPOMI. In the NO_2 window cloud retrieval a LUT is used, of which one of the parameters is the cloud pressure, as retrieved by the FRESCO algorithm. Thus, indirectly the cloud fraction in the NO_2 window is dependent on the FRESCO cloud fraction, hence, also the surface albedo database used in the FRESCO retrieval.

Changes in the input surface albedo might change the retrieved cloud pressure (height) and cloud fraction, which changes the air mass factor and the surface albedo used in the NO_2 retrieval. In addition, the air mass factor is a function of the albedo, which increases with increasing albedo, as the retrieval becomes more sensitive to the surface layer. An increase in cloud fraction leads to a decrease in air mass factor, as the cloud blocks the light and the retrieval becomes less sensitive to NO_2 in the boundary layer below. For more quantitative examples see Figure 5 in Boersma et al. (2004).

In this section the new albedo database is used to retrieve a few selected TROPOMI zoom mode NO_2 scenes. To assess the importance of the surface albedo spatial resolution at future NO_2 retrievals at high resolution, a comparison will be made between several TROPOMI NO_2 zoom mode retrievals using the OMI LER and the TROPOMI LER databases as input for the cloud and NO_2 processors. Several scenes were selected to see the effect on features where albedo resolution has a increased impact on the retrieval, such as coastlines, cloud contaminated scenes and urban areas: the United Arab Emirates, the Netherlands, Israel and Karachi (Pakistan).

The surface albedo, cloud fraction and air mass factor are complexly coupled, disallowing for confident interpretation. Besides, the possible effects due to the aforementioned uncertainties in the TROPOMI LER database increase the complexity even further. The results shown in this section should be considered preliminary and further research is required to understand the effects of the TROPOMI LER database on the retrieval algorithm. The goal of this section is rather to show the importance of a high resolution a priori surface albedo and demonstrate the potential effect.

United Arab Emirates

The United Arab Emirates (UAE) is a good test case for a coastline with a high contrast in albedo and little cloud cover. The surface albedo maps for the wavelength used in the FRESCO algorithm are shown in Figure 5.15. In the GOME-2 LER database the effect of low spatial resolution is clearly visible, as the albedo values appear smoothed near coast lines due to spatial interpolation. The TROPOMI LER database shows values over land several times larger than in the original database. Figure 5.16 shows the albedo in the NO_2 window, which is underestimated in the Dubai area (west coast) in the OMI LER database. On the east coast, the albedo does follow the coastline, which might be because of the aforementioned albedo correction in the processor for ocean pixels. The correction is not applied to land pixels which have been assigned an ocean albedo value.

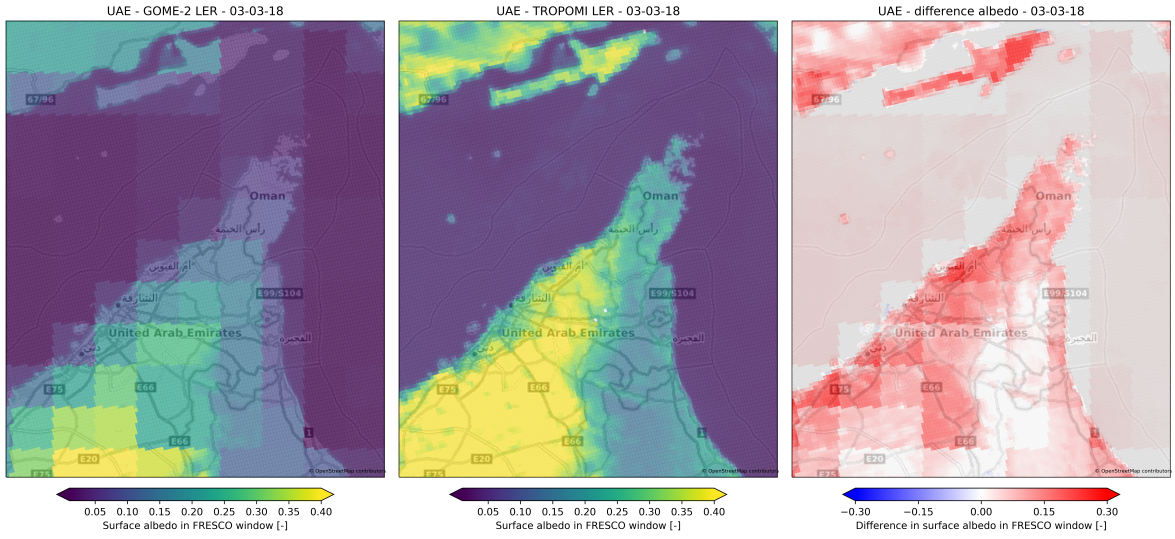

(a) (b) (c)

Figure 5.15: Comparison of the processed FRESCO albedo maps for the United Arab Emirates on 03-03-2018: (a) original GOME-2 LER, (b) new TROPOMI LER, and (c) difference between the two maps.

Figure 5.17a and 5.17b show the retrieved cloud fraction in the NO_2 window for the two LER databases. The cloud fraction over land, visible on the GOME-2 LER version, disappeared almost completely using the TROPOMI LER. The areas with cloud cover are the same areas that experience a change in albedo between the LER databases (Figure 5.15c). From the VIIRS optical image in Figure 5.17c, taken at similar overpass time, it appears there are only a few minor clouds that day above this scene. It seems possible that the cloud fraction is increased by the algorithm to match the database surface albedo to the measured reflectivity. By increasing the resolution of the surface albedo, the discrepancy between the assumed surface

albedo and measured reflectivity was decreased. However, as mentioned before, seasonality and wavelength differences in surface albedo might have be the cause of the differences seen as well.

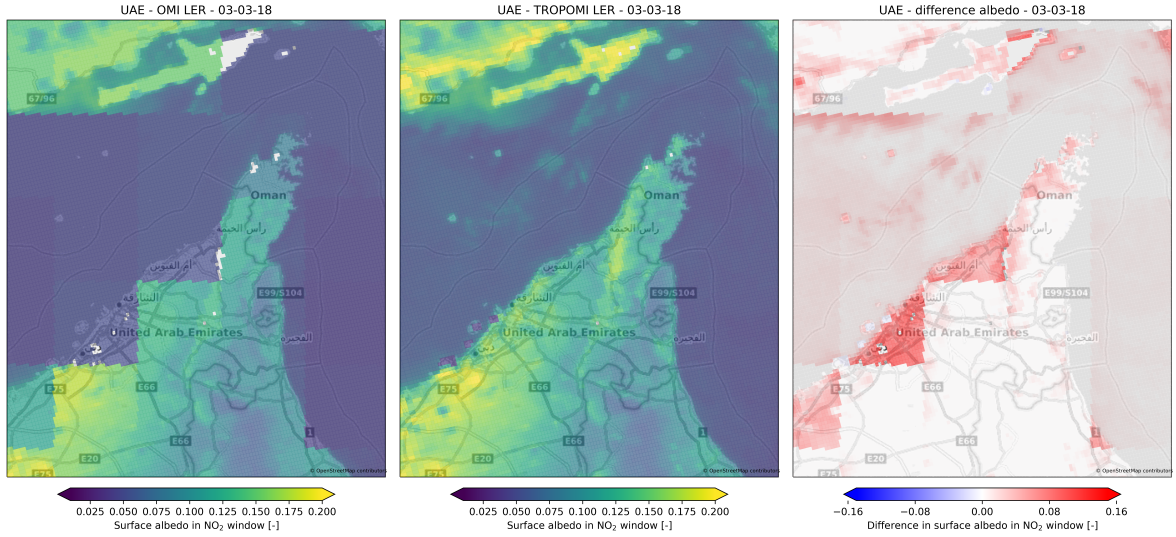

(a) (b) (c)

Figure 5.16: Comparison of the processed NO_2 albedo maps for the United Arab Emirates on 03-03-2018: (a) original OMI LER, (b) new TROPOMI LER, and (c) difference between the two maps.

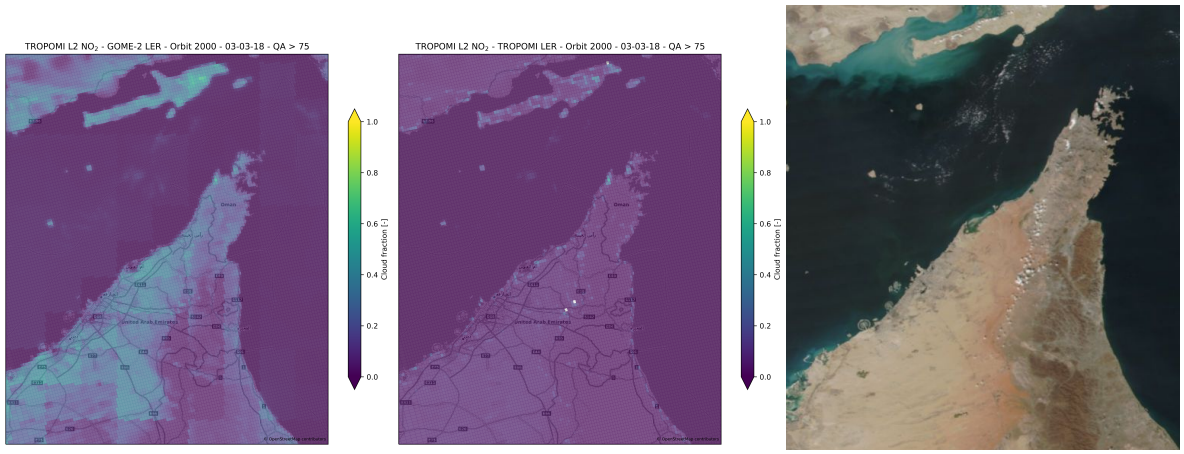

(a) (b) (c)

Figure 5.17: Comparison of the NO_2 window cloud fraction maps for the United Arab Emirates on 03-03-2018: (a) using GOME-2/OMI LER and (b) using TROPOMI LER; and (c) optical image obtained by VIIRS.

The originally retrieved NO_2 vertical column map is shown in Figure 5.18b, together with the difference between the high and low resolution albedo map retrieval in Figure 5.18c. The VCD map using the high resolution albedo map is not shown, since the difference with the original map would not be visible. The tropospheric air-mass factor above Dubai decreases, shown in Figure 5.18a, which increases the VCD. This is unexpected, as the increased albedo and decreased cloud fraction at Dubai theoretically should lead to an increase in AMF. The

reason for the decreasing AMF is unknown. The changes in VCD visible in the middle of the peninsula, above the Al Hajar Mountain range, visible by the different surface color in Figure 5.17c, seem to co-align with the small clouds visible. Although, the elevation differences in that area complicate the case further.

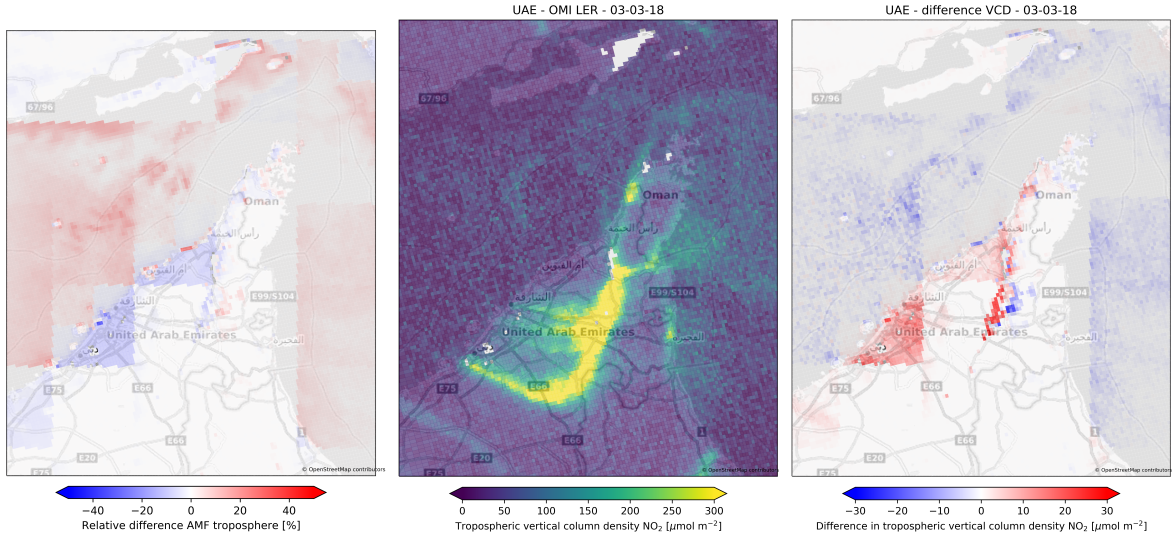

(a) (b) (c)

Figure 5.18: Comparison of the retrieved NO_2 AMF and VCD for the United Arab Emirates on 03-03-2018: (a) relative difference in air mass factor, (b) original VCD, (c) difference between new and original version.

The Netherlands

The case of the Netherlands scene on 05-03-2018 contains complicated coastlines, substantial cloud cover and ice cover, which make it hard to independently assess the impact of a high resolution surface reflectivity database. Nonetheless, it makes for an interesting case to analyse. Figure 5.19 shows the low and high resolution version of the albedo maps in the FRESCO window. The amount of filtered out pixels increases in the TROPOMI LER scene, which turns out to be non-converging pixels in the FRESCO algorithm, caused by the algorithm unable to retrieve the cloud fraction and thus discarding the pixels in the albedo map. Focussing on the converged pixels, the artefacts due to low resolution surface albedo data, visible at the coast, have decreased in the high resolution version. Furthermore, more detail can be seen in the high resolution case: local enhancements above land and albedo signatures due to cloud cover, for example, in Friesland and Noord-Brabant (see Figure 5.21c for the optical image). The NO_2 albedo maps are shown in Figure 5.20, where similar improvements due to resolution increase can be seen. The NO_2 window cloud retrieval has suffered less from the non-converging pixels than the FRESCO cloud retrieval, and different albedo and cloud features can be seen, possible due to difference in wavelength of the NO_2 and O_2-A window.

Figure 5.21a and 5.21b show the cloud cover in the NO_2 window as retrieved by the NO_2 algorithm using the OMI and the TROPOMI LER databases, respectively. Figure 5.21c shows the cloud cover as seen by optical wavelengths obtained by VIIRS at similar overpass time. It appears most cloud features are captured by both versions, however, it does not give clues on the reason of the non-converging areas. This image shows the IJssel and Marker lakes lighter than usual, which might indicate the lakes are covered in ice, which is confirmed by

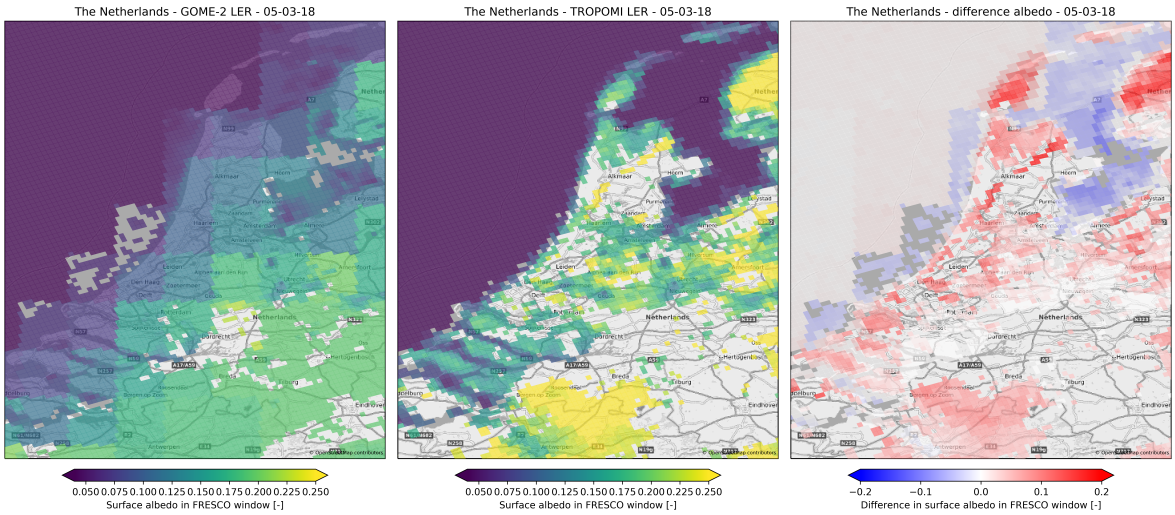

Figure 5.19: Comparison of the processed FRESCO albedo maps for the Netherlands on 05-03-2018: (a) original GOME-2 LER, (b) new TROPOMI LER, and (c) difference between the two maps.

a Dutch article[1]. The surface reflectivity of these pixels is underestimated by the database, as the ice has a larger albedo than water. These areas were not flagged for to contain ice by the used NISE snow and ice cover database. The underestimation of the surface albedo causes an underestimation of the air-mass factor and results in an overestimation of the NO_2 columns (see Figure 5.22b). The discrepancy is only for a minor part of the ice cover, most likely where NO_2 was present, as it acts as a multiplication factor.

The resulting air mass factor is shown in Figure 5.22a, indicating an increase for most pixels above land and a large decrease for pixels at the Marker and IJssel lakes on the upper right and the part of the coastal North and Wadden sea. These changes propagate directly into the retrieved NO_2 VCD, of which the original version is shown in Figure 5.22b and the relative difference between the new and original version in Figure 5.22c. The new version of the VCD map is deliberately not shown, since differences are too small to be visible. The block structures visible in the air mass factor difference reflect the artefacts from the original albedo database. The AMF decrease above the lakes and Wadden Sea might be caused by the increase in cloud fraction. The cloud cover probably increased to compensate for the underestimation of the assumed albedo in the FRESCO wavelength (see Figure 5.19) above the ice. The AMF decrease then causes the overestimation of the NO_2 column above the ice, however, the area that was originally overestimated is not affected, and even decreases. This case highlights the complex interactions in the retrieval between surface reflectivity, cloud parameters, ice cover, air-mass factor and NO_2 column.

[1]Source: https://wintersportweerman.nl/de-late-winter-van-2018-gaf-extreem-veel-ijs-juist-op-dieper-en-stromend-water-100573/

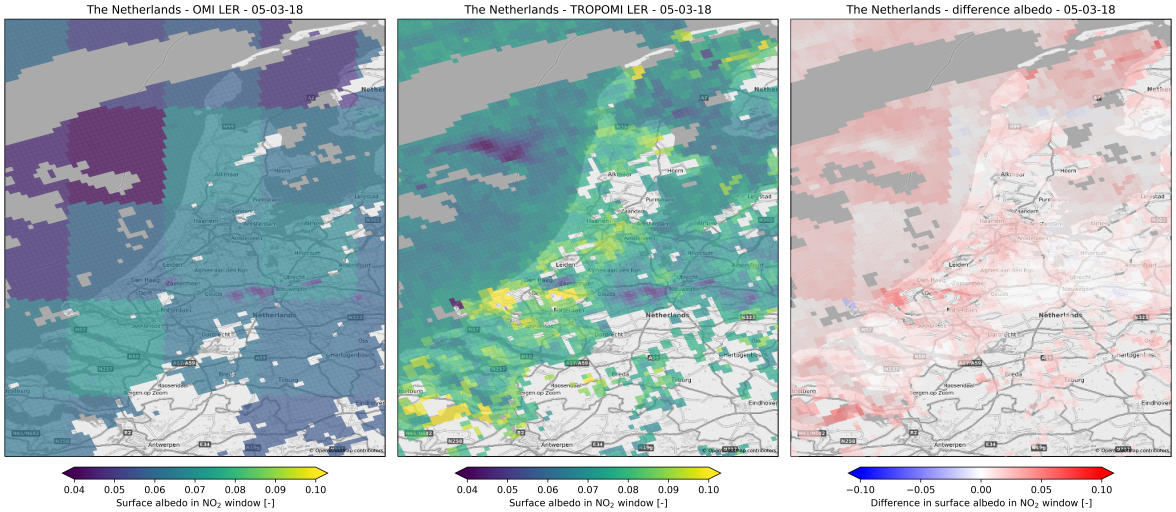

(a) (b) (c)

Figure 5.20: Comparison of the processed NO_2 albedo maps for the Netherlands on 05-03-2018: (a) original OMI LER, (b) new TROPOMI LER, and (c) difference between the two maps.

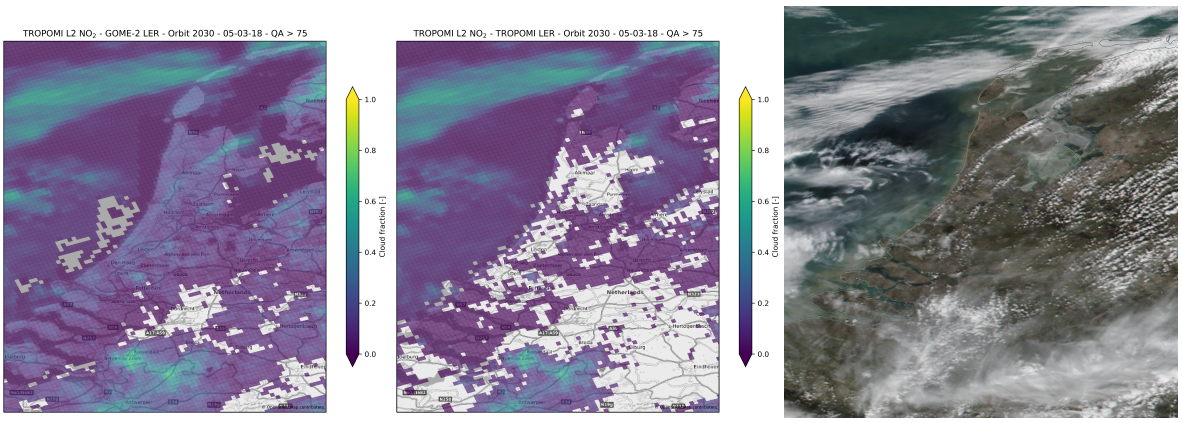

(a) (b) (c)

Figure 5.21: Comparison of the NO_2 window cloud fraction maps for the Netherlands on 05-03-2018: (a) using GOME-2/OMI LER and (b) using TROPOMI LER; and (c) optical image obtained by VIIRS.

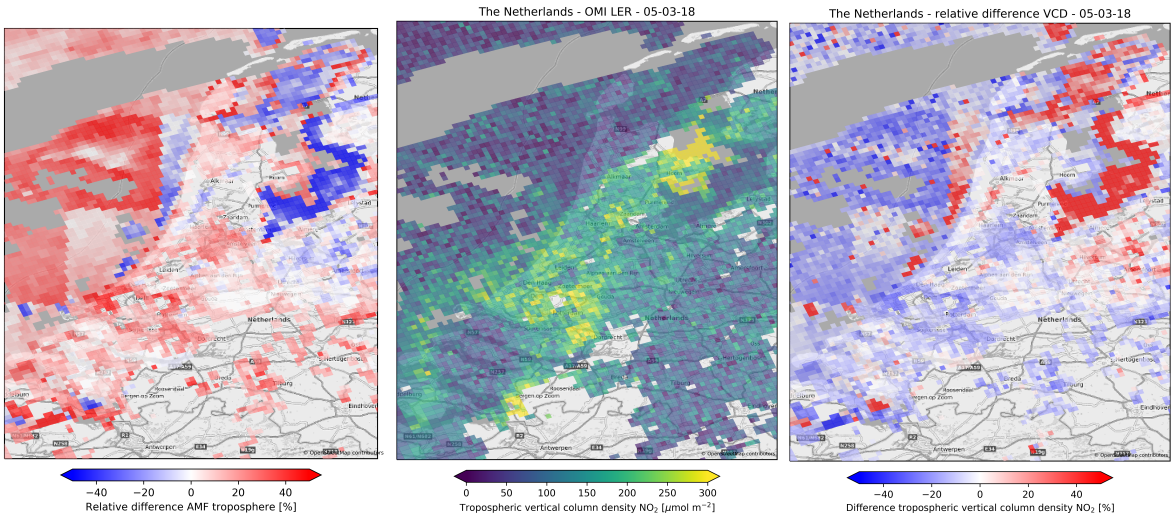

(a) (b) (c)

Figure 5.22: Comparison of the retrieved NO_2 AMF and VCD for the Netherlands on 05-03-2018: (a) relative difference in air mass factor, (b) original VCD, (c) relative difference between new and original version.

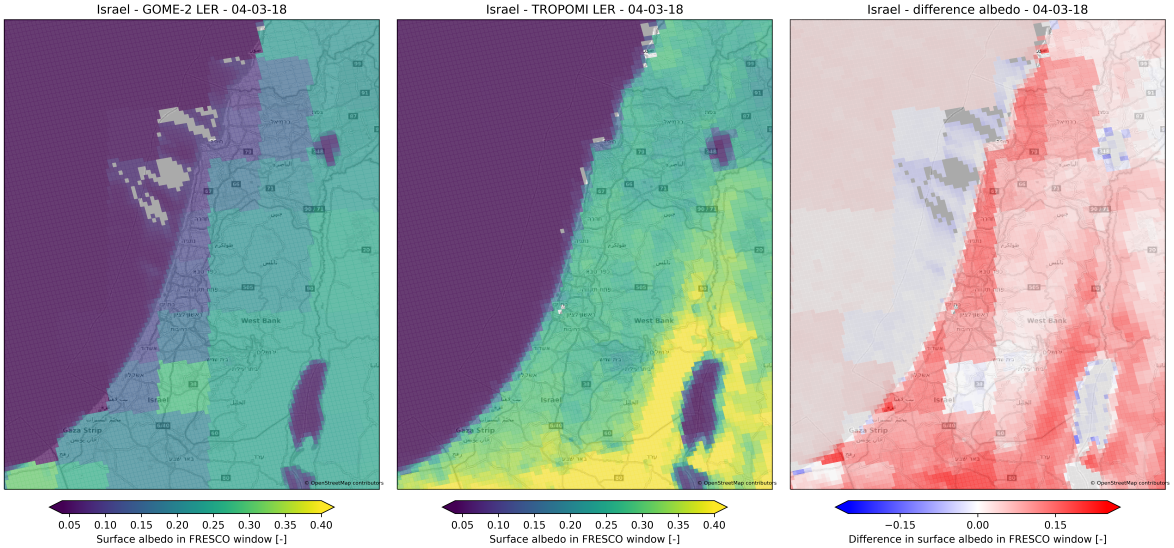

(a) (b) (c)

Figure 5.23: Comparison of the processed FRESCO albedo maps for Israel on 04-03-2018: (a) original GOME-2 LER, (b) new TROPOMI LER, and (c) difference between the two maps.

Israel

The case of Israel contains a coastline and several clouds above the Mediterranean in the north-east. The different versions of the FRESCO window surface albedo maps are shown in Figure 5.23. The non-convergent pixels in the low-resolution albedo map do not appear in the high resolution version, which coincide with part of the clouds, visible in the optical image in Figure 5.25c. In addition, the coastline is much better represented in the high resolution case. In-land there are differences visible as well, for example around the Dead Sea in the south-east, although this might be due to seasonality changes. The surface albedo maps in the NO_2 window show similar differences. The original OMI LER database shows some artefacts in this regions, which have disappeared in the TROPOMI LER database. Also the cloudy area above the Mediterranean is well implemented in the map by the algorithm. The difference in wavelength between the two windows is visible in the local enhancements in albedo in the NO_2 due to different land cover types, which are not present in the FRESCO window.

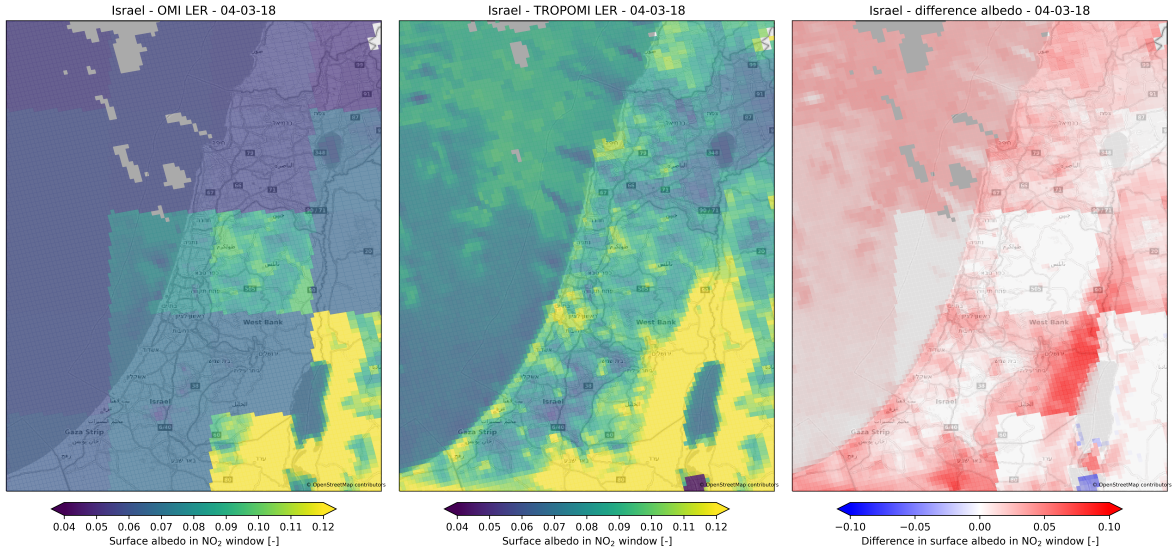

(a) (b) (c)

Figure 5.24: Comparison of the processed NO_2 albedo maps for Israel on 04-03-2018: (a) original OMI LER, (b) new TROPOMI LER, and (c) difference between the two maps.

Similar to the scene of the United Arab Emirates, the artificial cloud cover in the NO_2 window decreases in the high resolution albedo map, as shown in Figure 5.25. Still, artefacts in cloud fraction remain, as features in the optical image (Figure 5.25c) are present in the cloud fraction map (Figure 5.25b) as well.

The resulting original, new and difference VCD maps are shown, respectively, in Figure 5.26. The VCD is reduced significantly in the two hotspot areas near Haifa, which is due to an increased AMF, caused by the increase in surface albedo and decrease in cloud fraction. The VCD around Tel Aviv had decreased slightly as well.

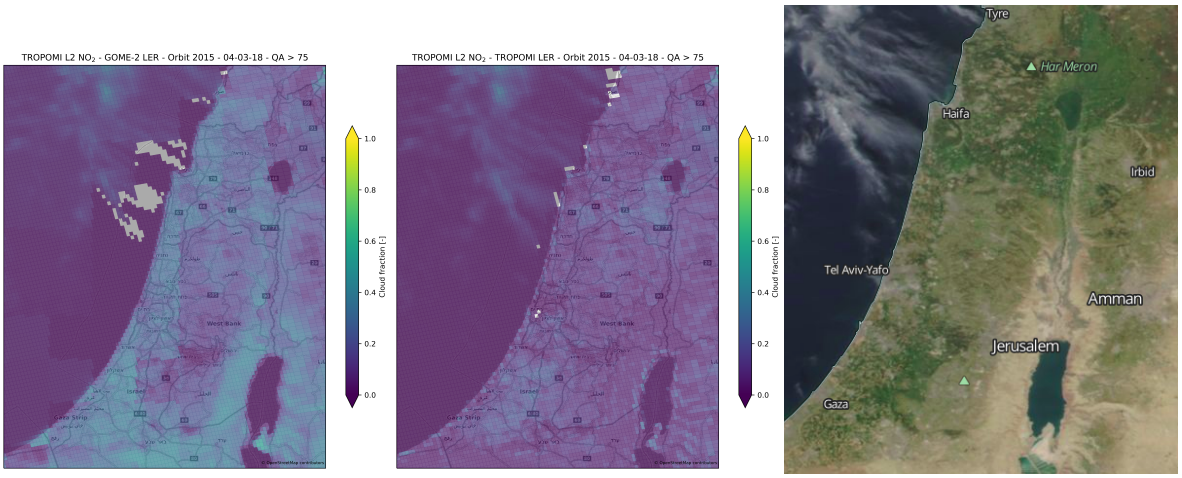

(a) (b) (c)

Figure 5.25: Comparison of the NO_2 window cloud fraction maps for Israel on 04-03-2018: (a) using GOME-2/OMI LER and (b) using TROPOMI LER; and (c) optical image obtained by VIIRS.

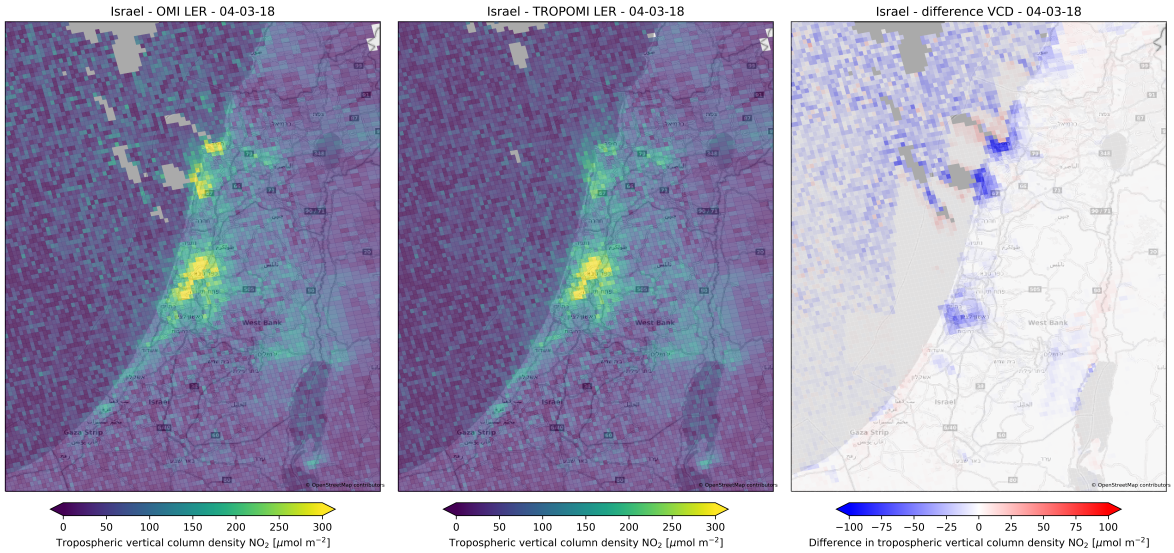

(a) (b) (c)

Figure 5.26: Comparison of the retrieved NO_2 VCD for Israel on 04-03-2018: (a) original version (using OMI LER), (b) new version (using TROPOMI LER) (c) difference between new and original version.

Karachi

The Karachi (Pakistan) scene at 05-03-2018 is similar to the United Arabic Emirates scene, as there is a pollution source next to a coastline with large albedo differences and no clouds present. Figure 5.27 shows the improvement in resolution of the albedo value in the FRESCO window, as the coastline is better represented and the albedo values have increased to more realistic values. In-land there is also a increase in albedo, which might be due to seasonality changes or the small difference in wavelength between the two databases. The albedo maps in the NO_2 window in Figure 5.28 show much less differences, except for the area around the coastline corner.

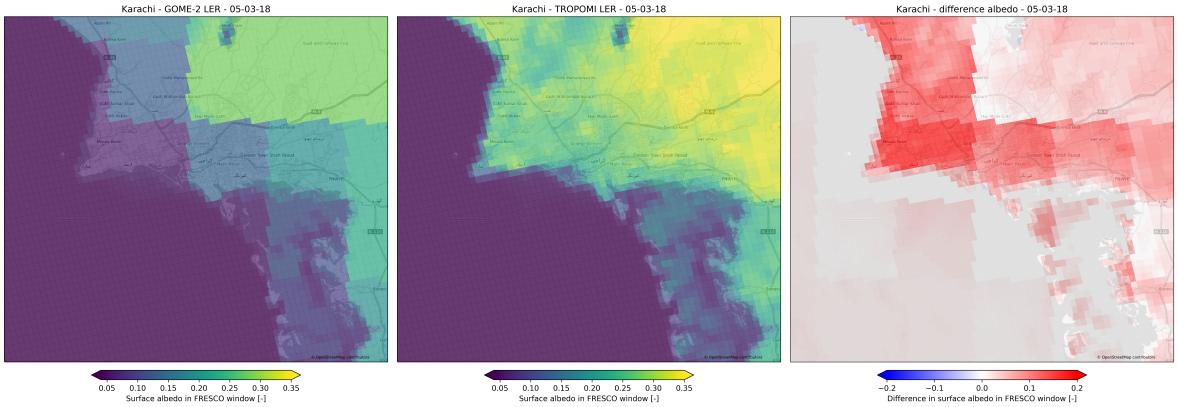

(a) (b) (c)

Figure 5.27: Comparison of the processed FRESCO albedo maps for Karachi on 05-03-2018: (a) original GOME-2 LER, (b) new TROPOMI LER, and (c) difference between the two maps.

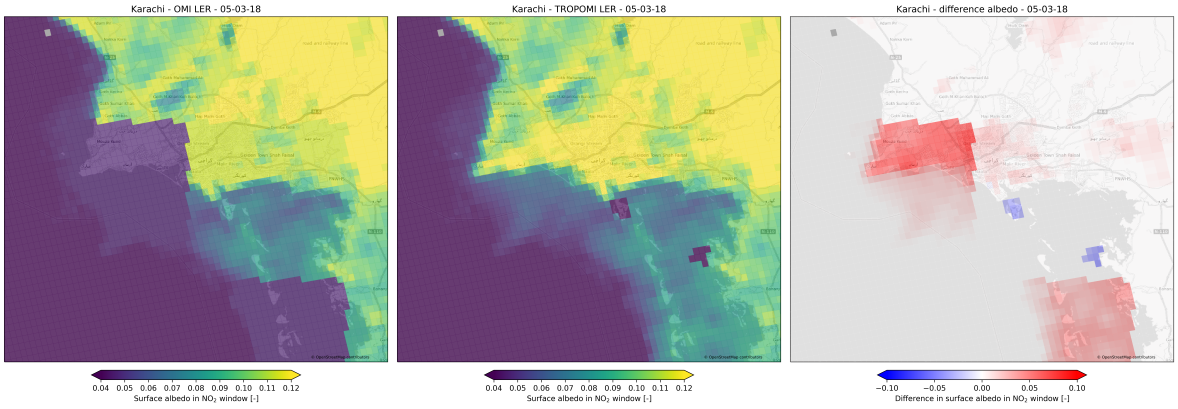

(a) (b) (c)

Figure 5.28: Comparison of the processed NO_2 albedo maps for the Karachi (Pakistan) on 05-03-2018: (a) original OMI LER, (b) new TROPOMI LER, and (c) difference between the two maps.

Again, the cloud cover in the NO_2 window decreases as the TROPOMI LER database is used, shown in Figure 5.29. Also in this scene, the artefacts in the original cloud cover map resemble the changes in surface albedo in the FRESCO window.

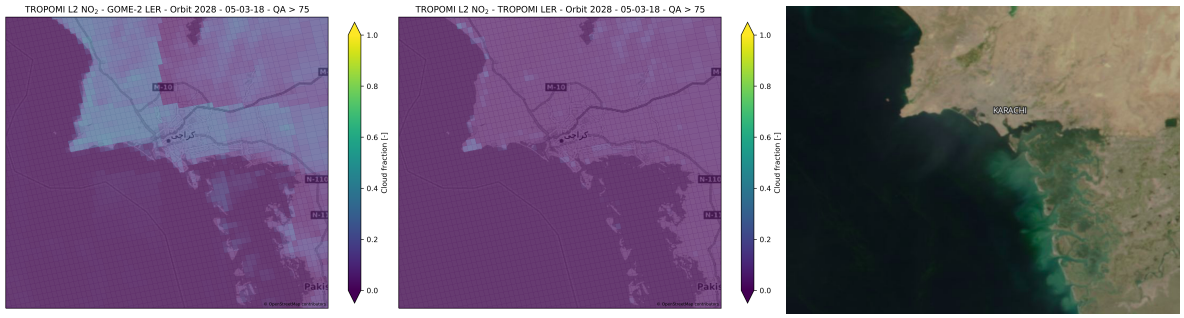

(a) (b) (c)

Figure 5.29: Comparison of the NO_2 window cloud fraction maps for Karachi on 05-03-2018: (a) using GOME-2/OMI LER and (b) using TROPOMI LER; and (c) optical image obtained by VIIRS.

Figure 5.30a shows the originally retrieved NO_2 VCD, which contains a highly polluted area around Karachi. The difference due to the change in surface albedo database is shown in Figure 5.30b, which appears to coincide with the largest difference in surface albedo in the NO_2 window. The change in VCD is relatively small compared to the maximum VCD values measured in the plumes. The increase in VCD is caused by the decrease in AMF, which is unexpected, since the surface albedo increased and the cloud fraction decreased, supposedly leading to an increase in AMF.

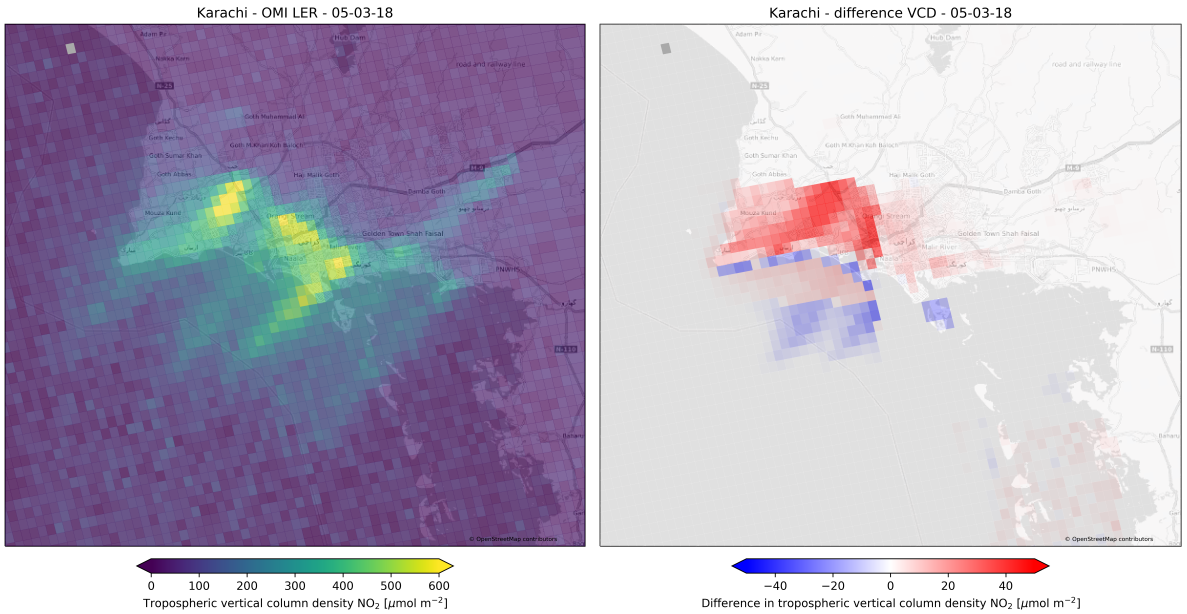

(a) (b)

Figure 5.30: Comparison of the retrieved NO_2 VCD for Karachi (Pakistan) on 05-03-2018: (a) original version (using OMI LER), (b) relative difference between new (using TROPOMI LER) and original version.

Conclusion

This preliminary analysis has shown the improvements in surface albedo representativeness in the FRESCO and NO_2 windows using the high spatial resolution TROPOMI LER database instead of the GOME-2 and OMI LER databases, as artefacts near coastal regions disappeared and surface features were better captured. Furthermore, the changes in retrieved cloud fraction in the NO_2 windows have shown the potential impact of replacing the coarse LER databases with high resolution alternatives. Also in the retrieved tropospheric NO_2 values, discrepancies have been presented due to under-representativeness of the surface albedo databases.

It should be noted once more that there are several other factors that could have influenced these results: the wavelength differences, seasonality and algorithm corrections. Although the effect of surface albedo is complex due to coupled parameters as cloud pressure, cloud fraction, air mass factors and NO_2 columns, this analysis demonstrates the potential effect of using a high resolution surface albedo database in the retrieval of cloud parameters and NO_2 columns at high spatial resolution.

6

Conclusions and Recommendations

In this chapter the found conclusions are collected and an attempt is made to answer the research questions. Furthermore, recommendations for future research regarding this topic are made.

Sub-question 1: What is changed in the instrument settings for TROPOMI in the special zoom science mode and what are the consequences of that?

The TROPOMI instrument operated in the 'Zoom Science Mode' (or simply 'zoom mode') during the E1 Commissioning Phase of the mission for about a week (01-03-2018 to 07-03-2018), resulting in a total of 88 granules. During this mode, measurements were only performed for 4 out of 8 detector bands, due to data volume restrictions, with adjusted instrument configuration (ICID 0114). The binning scheme of the CCD detectors was changed such that no binning was applied in the centre of the swath (310 km out of the total 2700 km), decreasing the ground pixel width by a factor 2 in nadir. Towards the edge of the swath, the binning increased, averaging more pixels together, to reduce the data volume that had to be read from the CCD. Furthermore, the integration time was shortened by a factor three, from 1.08 s to 0.36 s, resulting in a three times smaller ground pixel length. Hence, the pixel size reduced by a factor 6 from 7.1 x 3.6 km to 2.4 x 1.8 km. Due to the changes in the binning scheme, any database depending on the binned ISRF or the pixel viewing angles had to be regenerated in order to use the KNMI TROPOMI L2 processors. The comparison to co-located VIIRS radiance measurements has shown good agreement and no signs of pixel smearing or memory effect of the detector, indicating a proper single pixel response.

Analysis of the propagated NO_2 VCD error indicates the source of error increase to be the SCD uncertainty. The posterior statistical uncertainty of the retrieved SCD was calculated using measurements from the unpolluted Pacific Ocean, which indicated an error increase of factor 2.3 between the nominal TROPOMI measurements and the zoom-mode measurements. The proximity of the found factor to the theoretical random noise factor of 2.45, indicates a minor influence of systematic error. Furthermore, the uncertainty propagated by the retrieval algorithm was found to be conservative compared to the statistical uncertainty, as it was 5% and 18% larger for the nominal and zoom-mode measurements, respectively.

Sub-question 2: What is the increase in NO_2 pollution mapping capabilities due to the spatial resolution increase in the zoom-mode measurements compared to the nominal measurements?

Selected scenes of the processed TROPOMI L2 zoom-mode measurements have imaged NO_2 pollution at unprecedented spatial resolution. Comparisons to measurements simulated at nominal resolution demonstrated the increase in sharpness and detail of the pollution plumes. Furthermore, several sources that were distinguishable at the zoom-mode resolution, appeared as one source in the downscaled measurements. Two methods to quantify increase in image information content have been implemented and compared, of which the *image sharpness measure* method performed best when applied to resolution changes in the selected zoom-mode pollution cases. This method could potentially be helpful in quantifying the effect of resolution changes on pollution mapping. In addition, comparisons between zoom-mode scenes and real measurements at nominal resolution have shown similar advancements in captured detail and shape of the NO_2 plumes. It can be concluded that the increase in resolution from 7.1 x 3.6 km to 2.4 x 1.8 km certainly shows improvement in sharpness and detail in mapping NO_2 plumes. However, the increase in resolution is too small to change the level of representativeness, since no additional features or sources can be detected.

Sub-question 3: How well do high spatial resolution NO_2 measurements compare to model forecasts from CAMS and what can be learned from it?

Comparing the CAMS models with each other and with TROPOMI zoom-mode measurements have shown a wide range in performance of the models. Since several power plant plumes were better resolved in the TROPOMI measurements than in the CAMS forecasts, high resolution satellite measurements could be useful to improve emission inventories used in the models. Furthermore, besides validation with in-situ measurements, validation of the models with high resolution NO_2 measurements might be beneficial, as substantial differences occur between the NO_2 forecasts of the individual models. Finally, several scenes have been identified where the measured NO_2 plumes are represented well by the CAMS models, which were used for testing the retrieval algorithm with high resolution a priori profiles from CAMS later on.

Sub-question 4: How well do high resolution NO_2 column measurements correlate with co-located CO_2 column measurements and how much do they increase plume detection capabilities?

Several cases were found where TROPOMI zoom-mode NO_2 measurements could be compared to co-located OCO-2 CO_2 measurements. The cases with low surface wind velocities have shown a high correlation between the two measurement sets, whereas scenes with moderate wind show weak correlation, most likely due to turbulent diffusion that occurred during the time between the satellite overpasses. The plume detection algorithm from the SMARTCARB study has been demonstrated on several cases from the zoom-mode NO_2 measurements to detect NO_2 plumes. For cases with high albedo, and therefore good signal-to-noise ratios, the algorithm performs well, and most plumes are correctly detected. However, for areas with lower signal-to-noise ratios, for instance higher mid-latitudes, the algorithm suffered from the increased noise and could not identify power plant plumes correctly. Ap-

plied to simulations at nominal TROPOMI spatial resolution, the algorithm still manages to detect the plumes, although the shape of the plumes is not defined as well. The demonstrated ability of detecting the shape of NO_2 pollution plumes with high detail provide further support for a 2 x 2 km resolution NO_2 instrument onboard the Sentinel 7 CO_2 mission to enhance CO_2 detection capabilities. However, the signal-to-noise ratio of the instrument should be sufficiently high to ensure adequate plume detection above all areas, including higher mid-latitudes.

Sub-question 5: What is the effect of using higher spatial resolution a priori input for high spatial resolution NO_2 retrievals in polluted areas?

High resolution a priori tropospheric NO_2 profile shapes from the CAMS models have been used to retrieve NO_2 columns, for several example cases from the zoom-mode data-set. The a priori profiles from the operationally used TM5 model and the CAMS models have been compared and one potential risk has been identified: high resolution model predictions where the plumes are missing or are at the wrong location, either due to discrepancies between the predicted and actual meteorological conditions or due to outdated emission inventories, could lead to a decrease in accuracy of the retrieval compared to the original model. The differences in the retrieved NO_2 show that the high resolution profiles correct the retrieval for wrongly assumed NO_2 concentrations. For layers the retrieval is sensitive to, an increase in a priori NO_2 concentration leads to a decrease in retrieved NO_2 VCD, since the box-AMF for those layers was underestimated and the contribution of that layer to the column was overestimated. Vice-versa, for layers with little sensitivity, increased a priori concentration leads to an increase in VCD, since the contribution of that layer was underestimated.

Improvements in surface reflectivity representativeness in the FRESCO and NO_2 windows have been presented using the experimental high spatial resolution TROPOMI LER database instead of the GOME-2 and OMI LER databases, as artefacts near coastal regions disappeared and surface features were better captured. Test retrievals of the zoom-mode measurements using the high resolution surface reflectivity databases have shown discrepancies in the retrieved cloud fraction in the NO_2 window. This demonstrates the potential impact of replacing the coarse LER databases with high resolution alternatives. Furthermore, changes in the retrieved tropospheric NO_2 columns indicate under-representativeness of the surface reflectivity databases in the retrieval setup. It should be noted once more that there are several other factors that could have influenced these results: wavelength differences in the LER database, seasonality and algorithm corrections. Although the effect of surface reflectivity is complex due to coupled parameters as cloud pressure, cloud fraction, air mass factors and NO_2 columns, the importance of a high resolution surface reflectivity database, including temporal variations, for measurements at high spatial resolution is demonstrated with the shown results.

Main question: What is the additional value of the high spatial resolution NO_2 measurements obtained by TROPOMI in zoom mode compared to the nominal resolution measurements?

The high resolution data-set obtained by TROPOMI operated in zoom mode has shown measurements of tropospheric NO_2 sources from space with unprecedented detail, which demonstrates the technologically capabilities of the TROPOMI instrument and the potential of future space borne air quality monitoring instruments. Although the increase in spatial resolution is insufficient for a noticeable change in spatial representativeness in mapping NO_2 pollution, the improvement in capturing the shape and details of local NO_2 enhancements is substantial, which could be valuable for the identification and/or attribution of local sources in emission estimations and for modelling efforts to better understand the transport of air pollutants. Furthermore, NO_2 measurements with a pixel size of 2.4 x 1.8 km were valuable in providing further evidence for the benefit of using high resolution NO_2 plume detection to enhance CO_2 emission estimation. Finally, the zoom-mode measurements have been useful in highlighting the importance of high resolution a priori NO_2 profiles and surface albedo databases for retrievals of high spatial resolution measurements.

Several recommendations can be made for future research regarding the topics covered in this thesis:

- For future space-borne UV-VIS-NIR instruments that measure tropospheric NO_2 abundance, with spatial resolution as high or higher than the zoom-mode measurements, design choices will have to be made regarding the spatial resolution and noise requirements. The zoom-mode measurements could provide valuable insights for constraining the requirements on these design choices. For example, the equatorial areas, with high albedo and smaller solar zenith angles and thus relatively high SNR, showed results with a low background noise, even though the instrument noise had increased due to the adjusted settings. In the mid-latitudinal areas with low albedo and higher solar zenith angles, the increase in background noise had a larger impact, which could compromise the monitoring of NO_2 sources in those areas.

- The estimation of NO_2 emissions from megacities using measurements from TROPOMI single overpasses has been demonstrated (Beirle, 2013). The impact of the spatial resolution of the measurements used in these inversion techniques could be studied using the TROPOMI zoom-mode measurements. For example, these methods apply integration techniques to quantify the total emissions, on which the effect of varying measurement resolution could be investigated. This could be valuable in determining the resolution of future NO_2 instruments that are to monitor NO_2 emission sources.

- The comparison between the measured (zoom mode) TROPOMI NO_2 columns and the columns obtained from the CAMS models could be extended by using more test cases and more in depth quantification. The original model data at their original spatial and temporal grid should be used, instead of the regridded CAMS versions, for a fairer performance assessment. Furthermore, when quantifying differences, the TROPOMI averaging kernels should be applied when integrating the model profiles to column values, to minimize discrepancies caused by assumptions in the TROPOMI retrieval.

- Further research on the effect of high resolution a priori NO_2 profiles on the TROPOMI NO_2 retrieval would be valuable. Any high resolution model, which resolves individual NO_2 from power plants or cities, should be validated to the measurement data, in order to ensure the retrieval performance would not be decreased due to erroneous plume

information. Then, more statistically robust analysis could gain quantitative insights in the potential benefit for the tropospheric NO_2 product. Furthermore, simulations could be done to quantify the impact of accurate higher resolution a priori profile information.

- More analysis is required regarding the high resolution TROPOMI LER database, under development at the KNMI. The effect of seasonality, wavelength differences and algorithm corrections could be better understood or possibly eliminated. Then, the impact of the spatial resolution increase on the cloud and NO_2 retrieval performance could be investigated in detail. Another option would be to use synthetic spectra and well understood scenarios to simulate the impact of varying resolution of surface reflectivity databases. This could help to estimate the potential error decrease in the NO_2 product due to a more accurate air mass factor by using a surface albedo database with increased spatial resolution.

Bibliography

Aguado, E. and Burt, J.E.: *Understanding Weather and Climate*. Pearson, 2013. ISBN 9780321769633.

Arther, J., World Health Organization, Organization, W.H., et al.: Health aspects of air pollution with particulate matter, ozone and nitrogen dioxide: report on a WHO working group, Bonn, Germany 13-15 January 2003. *Environmental monitoring and assessment*, 12(9):65–80, 2003.

Beirle, S.: Megacity Emissions and Lifetimes of Nitrogen Oxides Probed from Space. 1737(2011):1737–1740, 2013. doi:10.1126/science.1207824.

Bézy, J.L., Sierk, B., Caron, J., et al.: The Copernicus Sentinel-5 mission for operational atmospheric monitoring: status and developments. (October 2014):92410H, 2014. doi: 10.1117/12.2068177.

Boersma, K.F., Eskes, H.J., and Brinksma, E.J.: Error analysis for tropospheric NO2 retrieval from space. *Journal of Geophysical Research: Atmospheres*, 109(D4):n/a–n/a, 2004. doi: 10.1029/2003JD003962.

Boersma, K.F., Eskes, H.J., Richter, A., et al.: Improving algorithms and uncertainty estimates for satellite NO 2 retrievals: results from the quality assurance for the essential climate variables (QA4ECV) project. *Atmospheric Measurement Techniques*, 11(12):6651–6678, 2018.

Boersma, K.F., Eskes, H.J., Veefkind, J.P., et al.: Near-real time retrieval of tropospheric NO 2 from OMI. *Atmospheric Chemistry and Physics*, 7(8):2103–2118, 2007. doi:10.5194/acp-7-2103-2007.

Borsdorff, T., Aan de Brugh, J., Hu, H., et al.: Measuring Carbon Monoxide With TROPOMI: First Results and a Comparison With ECMWF-IFS Analysis Data. *Geophysical Research Letters*, 45(6):2826–2832, 2018. doi:10.1002/2018GL077045.

Bossers, N.: *The impact of high resolution surface reflectance data on the accuracy of the TROPOMI tropospheric NO2 product over the greater Rotterdam region.* Master's thesis, 2019. Delft University of Technology.

Bouwman, A.F., Van Vuuren, D.P., Derwent, R.G., et al.: A global analysis of acidification and eutrophication of terrestrial ecosystems. *Water, Air, and Soil Pollution*, 141(1-4):349–382, 2002. doi:10.1023/A:1021398008726.

Bovensmann, H., Buchwitz, M., Burrows, J.P., et al.: A remote sensing technique for global monitoring of power plant CO2 emissions from space and related applications. *Atmospheric Measurement Techniques*, 3(4):781–811, 2010. doi:10.5194/amt-3-781-2010.

Bovensmann, H., Burrows, J.P., Buchwitz, M., et al.: SCIAMACHY: Mission objectives and measurement modes. *Journal of the atmospheric sciences*, 56(2):127–150, 1999.

Bowman, K.P. and Krueger, A.J.: A global climatology of total ozone from the Nimbus 7 total ozone mapping spectrometer. *Journal of Geophysical Research: Atmospheres*, 90(D5):7967–7976, 1985.

Brewer, A.W., McElroy, C.T., and Kerr, J.B.: Nitrogen dioxide concentrations in the atmosphere. *Nature*, 246(5429):129, 1973.

Brodzik, M.J. and Stewart, J.S.: Near-Real-Time SSM/I-SSMIS EASE-Grid Daily Global Ice Concentration and Snow Extent, Version 5. 2019. doi:https://doi.org/10.5067/3KB2JPLFPK3R.

Bryan N. Duncan: A space-based, high-resolution view of notable changes in urban NOx pollution around the world (2005– 2014). *Geophysical Research: Atmospheres*, (November):1–8, 2015. doi:10.1002/2013JD020225.Received.

Burrows, J.P., Platt, U., and Borrell, P.: *The Remote Sensing of Tropospheric Composition from Space*. Physics of Earth and Space Environments. Springer Berlin Heidelberg, 2011. ISBN 9783642147913.

Burrows, J.P., Weber, M., Buchwitz, M., et al.: The global ozone monitoring experiment (GOME): Mission concept and first scientific results. *Journal of the Atmospheric Sciences*, 56(2):151–175, 1999.

Byers, L., Friedrich, J., Hennig, R., et al.: A Global Database of Power Plants. 2018. www.wri.org/publication/global-database-power-plants.

Chance, K. and Kurucz, R.L.: An improved high-resolution solar reference spectrum for earth's atmosphere measurements in the ultraviolet, visible, and near infrared. *Journal of Quantitative Spectroscopy and Radiative Transfer*, 111(9):1289–1295, 2010. doi:https://doi.org/10.1016/j.jqsrt.2010.01.036.

De, K. and Masilamani, V.: Image sharpness measure for blurred images in frequency domain. *Procedia Engineering*, 64:149–158, 2013. doi:10.1016/j.proeng.2013.09.086.

de Haan, J.F.: DISAMAR: Determining Instrument Specifications and Analyzing Methods for Atmospheric Retrieval, Algorithm description and background information. *KNMI*, 2011.

de Haan, J.F., Bosma, P.B., and Hovenier, J.W.: The adding method for multiple scattering calculations of polarized light. *Astronomy and Astrophysics*, 183:371–391, 1987.

De Smedt, I., Theys, N., Yu, H., et al.: First results of tropospheric formaldehyde retrievals with TROPOMI onboard the Copernicus Sentinel-5 Precursor Mission. In *EGU General Assembly Conference Abstracts*, volume 20, page 7339. 2018.

de Vries, J., Voors, R., Ording, B., et al.: TROPOMI on ESA's Sentinel 5p ready for launch and use. (August 2016):96880B, 2016. doi:10.1117/12.2240839.

Dobson, G.M.B.: Observers' handbook for the ozone spectrophotometer. *Ann. Int. Geophys. Year*, 5(1):46–89, 1957.

Dockery, D.W., Pope, C.A., Xu, X., et al.: An association between air pollution and mortality in six US cities. *New England journal of medicine*, 329(24):1753–1759, 1993.

ESA Mission Science Division: COPERNICUS Sentinels 4 and 5 Mission Requirements Traceability Document. Technical report, 2017. EOP-SM/2413/BV-bv, issue 2, revision 0.

Eskes, H., van Geffen, J., Boersma, F., et al.: High-resolution nitrogen dioxide retrievals from the Sentinel-5P TROPOMI sensor. In *EGU General Assembly Conference Abstracts*, volume 20, page 12435. 2018a.

Eskes, H., van Geffen, J., Boersma, F., et al.: Sentinel-5 precursor/TROPOMI Level 2 Product User Manual Nitrogendioxide. 2018b. S5P-KNMI-L2-0021-MA, issue 2.0.0.

Eskes, H.J. and Boersma, K.F.: Averaging kernels for DOAS total-column satellite retrievals. *Atmospheric Chemistry and Physics*, 3(5):1285–1291, 2003. doi:10.5194/acp-3-1285-2003.

European Environment Agency: Air quality in Europe - 2018 report. 2018. doi:10.2800/55823.

Feixas, M., Bardera, A., Rigau, J., et al.: *Information Theory Tools for Image Processing*, volume 6. 2014. ISBN 9781627053617. doi:10.2200/s00560ed1v01y201312cgr015.

Fuglestvedt, J.S., Berntsen, T.K., Isaksen, I.S.A., et al.: Climatic forcing of nitrogen oxides through changes in tropospheric ozone and methane; global 3D model studies. *Atmospheric Environment*, 33(6):961–977, 1999.

Goldberg, D.L., Lamsal, L.N., Loughner, C.P., et al.: A high-resolution and observationally constrained OMI NO2 satellite retrieval. *Atmospheric Chemistry and Physics*, 17(18):11403–11421, 2017. doi:10.5194/acp-17-11403-2017.

Gulde, S.T., Kolm, M.G., Smith, D.J., et al.: Sentinel 4: a geostationary imaging uvn spectrometer for air quality monitoring - status of design, performance and development. In *International Conference on Space Optics - ICSO 2014*, volume 10563 1056, pages 1–9. 2014. ISBN 9781510616158. doi:10.1117/12.2304099.

Hakkarainen, J., Ialongo, I., Maksyutov, S., et al.: Analysis of Four Years of Global XCO2 Anomalies as Seen by Orbiting Carbon Observatory-2. *Remote Sensing*, 11(7):850, 2019. doi:10.3390/rs11070850.

Heath, D.F., Mateer, C.L., and Krueger, A.J.: The Nimbus-4 Backscatter Ultraviolet (BUV) atmospheric ozone experiment - two years' operation. *Pure and Applied Geophysics*, 106(1):1238–1253, 1973.

Hendrick, F., Mahieu, E., Bodeker, G.E., et al.: Analysis of stratospheric NO2 trends above Jungfraujoch using ground-based UV-visible, FTIR, and satellite nadir observations. *Atmospheric Chemistry and Physics*, 12(18):8851–8864, 2012. doi:10.5194/acp-12-8851-2012.

Hong, J., Hong, Y., Song, C.K., et al.: A New Era of Air Quality Monitoring from Space in East Asia: Korea's Geostationary Environmental Monitoring Spectrometer (GEMS) and an Integrated Korea-US Air Quality (KORUS-AQ) Study. In *AGU Fall Meeting Abstracts*. 2015.

Hu, H., Landgraf, J., Detmers, R., et al.: Toward Global Mapping of Methane With TROPOMI: First Results and Intersatellite Comparison to GOSAT. *Geophysical Research Letters*, 45(8):3682–3689, 2018. doi:10.1002/2018GL077259.

Huijnen, V., Williams, J., van Weele, M., et al.: The global chemistry transport model TM5: description and evaluation of the tropospheric chemistry version 3.0. *Geoscientific Model Development*, 3(2):445–473, 2010. doi:10.5194/gmd-3-445-2010.

IEC BiPM, ILAc IFcc, OIML ISO, et al.: The international vocabulary of metrology—basic and general concepts and associated terms (VIM). *JcGM*, 200:2012, 2012.

Inness, A., Flemming, J., Heue, K.P., et al.: Monitoring and assimilation tests with TROPOMI data in the CAMS system: near-real-time total column ozone. *Atmospheric Chemistry and Physics*, 19(6):3939–3962, 2019. doi:10.5194/acp-19-3939-2019.

Jacob, D.: *Introduction to atmospheric chemistry*. Princeton University Press, 1999.

Judd, L.M., Al-Saadi, J.A., Janz, S.J., et al.: Evaluating the impact of spatial resolution on tropospheric NO2 column comparisons within urban areas using high-resolution airborne data. (2):1–25, 2019. doi:10.5194/amt-2019-161.

Kleipool, Q., Ludewig, A., Babic, L., et al.: Pre-launch calibration results of the TROPOMI payload on-board the Sentinel 5 Precursor satellite. *Atmospheric Measurement Techniques Discussions*, (February):1–67, 2018. doi:10.5194/amt-2018-25.

Kleipool, Q.L., Dobber, M.R., de Haan, J.F., et al.: Earth surface reflectance climatology from 3 years of OMI data. *Journal of Geophysical Research Atmospheres*, 113(18):1–22, 2008. doi:10.1029/2008JD010290.

Krings, T., Neininger, B., Gerilowski, K., et al.: Airborne remote sensing and in situ measurements of atmospheric CO2 to quantify point source emissions. *Atmospheric Measurement Techniques*, 11(2):721–739, 2018. doi:10.5194/amt-11-721-2018.

Kuhlmann, G., Clément, V., Fuhrer, O., et al.: Using NO2 Satellite Observations to Support Satellite-based CO2 Emission Estimates of Cities and Power Plants. In *Hyperspectral Imaging and Sounding of the Environment*, pages HW3C—-3. Optical Society of America, 2018a.

Kuhlmann, G., Clément, V., Marshall, J., et al.: SMARTCARB – Use of satellite measurements of auxiliary reactive trace gases for fossil fuel carbon dioxide emission estimation. 2018b. Final report of ESA study contract n°4000119599/16/NL/FF/mg, project led by Empa (Switzerland).

Lerot, C., Theys, N., De Smedt, I., et al.: The offline total ozone product from TROPOMI/S5p. In *EGU General Assembly Conference Abstracts*, volume 20, page 7850. 2018.

Levelt, P., Joiner, J., Tamminen, J., et al.: The Ozone Monitoring Instrument (OMI): towards a 14 Year Data Record and Applications in the Air Quality and Climate Domain. In *AGU Fall Meeting Abstracts*. 2017.

Levelt, P.F., Van Den Oord, G.H.J., Dobber, M.R., et al.: The ozone monitoring instrument. *IEEE Transactions on Geoscience and Remote Sensing*, 44(5):1093–1100, 2006. doi:10.1109/TGRS.2006.872333.

Lin, J.T., Liu, M.Y., Xin, J.Y., et al.: Influence of aerosols and surface reflectance on satellite NO2 retrieval: seasonal and spatial characteristics and implications for NOx emission constraints. *Atmospheric Chemistry and Physics*, 15(19):11217, 2015.

Loots, E.: Algorithm theoretical basis document for the TROPOMI L01b data processor. Technical report, 2015. S5P-KNMI-L01B-0009-SD, issue 8.0.0.

Lorente, A., Folkert Boersma, K., Stammes, P., et al.: The importance of surface reflectance anisotropy for cloud and NO2 retrievals from GOME-2 and OMI. *Atmospheric Measurement Techniques*, 11(7):4509–4529, 2018. doi:10.5194/amt-11-4509-2018.

Loughner, C.P., Lary, D.J., Sparling, L.C., et al.: A method to determine the spatial resolution required to observe air quality from space. *IEEE Transactions on Geoscience and Remote Sensing*, 45(5):1308–1313, 2007. doi:10.1109/TGRS.2007.893732.

Mauzerall, D.L., Sultan, B., Kim, N., et al.: NOx emissions from large point sources: Variability in ozone production, resulting health damages and economic costs. *Atmospheric Environment*, 39(16):2851–2866, 2005. doi:10.1016/j.atmosenv.2004.12.041.

Meijer, Y.: Status of the Copernicus Anthropogenic CO2 Monitoring Mission. In *AC-VC-14 & GEO-CAPE Joint Meeting*, May. 2018.

Moeller, C. and Moyer, D.: NPP VIIRS Flight 1 Relative Spectral Response (RSR) Overview. Technical Report October, 2011.

Murray, L.T.: Lightning NOx and Impacts on Air Quality. *Current Pollution Reports*, 2(2):115–133, 2016. doi:10.1007/s40726-016-0031-7.

NASA Goddard Space Flight Center: NASA Visible Infrared Imaging Radiometer Suite Level-1B Product User Guide. Technical Report May 2018, Version 1.0, 2018.

Nassar, R., Hill, T.G., McLinden, C.A., et al.: Quantifying CO2 emissions from individual power plants from space. *Geophysical Research Letters*, 44(19):10–45, 2017.

OCO-2 Science Team, Eldering, A., and Gunson, M.: OCO-2 Level 2 bias-corrected XCO2 and other select fields from the full-physics retrieval aggregated as daily files. 2017. doi:10.5067/XR7ZWYSKP7D0.

Osterman, G.B., Eldering, A., Mandrake, L., et al.: OCO-2 XCO2 V8r Lite Products, Warn Levels, and Bias Correction. Technical report, 2017.

Pérez Albiñana, A., Martin, D.D., Erdmann, M., et al.: Sentinel-5: the new generation European operational atmospheric chemistry mission in polar orbit. *Infrared Remote Sensing and Instrumentation XXV*, 10403(August 2017):23, 2017. doi:10.1117/12.2268875.

Platt, U., Perner, D., and Pätz, H.W.: Simultaneous measurement of atmospheric CH2O, O3, and NO2 by differential optical absorption. *Journal of Geophysical Research: Oceans*, 84(C10):6329–6335, 1979.

Platt, U. and Stutz, J.: *Differential Optical Absorption Spectroscopy: Principles and Applications*. Physics of Earth and Space Environments. Springer Berlin Heidelberg, 2008. ISBN 9783540757764.

Pope, R.M. and Fry, E.S.: Absorption spectrum (380–700 nm) of pure water. II. Integrating cavity measurements. *Appl. Opt.*, 36(33):8710–8723, 1997. doi:10.1364/AO.36.008710.

Reuter, M., Buchwitz, M., Schneising, O., et al.: Towards monitoring localized CO2 emissions from space: co-located regional CO2 and NO2 enhancements observed by the OCO-2 and S5P satellites, 2019. doi:10.5194/acp-2019-15.

Rozanov, A., Bovensmann, H., Bracher, A., et al.: NO2 and BrO vertical profile retrieval from SCIAMACHY limb measurements: Sensitivity studies. *Advances in Space Research*, 36(5):846–854, 2005. doi:10.1016/j.asr.2005.03.013.

Russell, A.R., Perring, A.E., Valin, L.C., et al.: A high spatial resolution retrieval of NO2 column densities from OMI: method and evaluation. *Atmospheric Chemistry and Physics*, 11(16):8543–8554, 2011. doi:10.5194/acp-11-8543-2011.

Serdyuchenko, A., Gorshelev, V., Weber, M., et al.: High spectral resolution ozone absorption cross-sections Part 2: Temperature dependence. *Atmospheric Measurement Techniques*, 7(2):625–636, 2014. doi:10.5194/amt-7-625-2014.

Shindell, D.T., Faluvegi, G., Koch, D.M., et al.: Improved attribution of climate forcing to emissions. *Science*, 326(5953):716–718, 2009.

Silvern, R.F., Jacob, D.J., Mickley, L.J., et al.: Using satellite observations of tropospheric NO2 columns to infer long-term trends in US NO2 emissions: the importance of accounting for the free tropospheric NO2 background. *Atmospheric Chemistry and Physics Discussions*, (2):1–26, 2019. doi:10.5194/acp-2019-168.

Sneep, M.: Regenerating the semi-static input for the Sentinel 5 precursor KNMI and SRON Level 2 processors. Technical report, 2018. S5P-KNMI-L2-0131-TN, issue 2.0.0.

Sneep, M.: Sentinel 5 precursor / TROPOMI KNMI and SRON level 2 Input Output Data Definition. Technical report, 2019. S5P-KNMI-L2-0009-SD, issue 11.0.0.

Sneep, M. and Pedergnana, M.: S5P / TROPOMI Static input for Level 2 processors. Technical report, 2015. S5P-KNMI-L2CO-0004-SD, issue 3.0.0.

Stammes, P., Sneep, M., Wang, P., et al.: A sharper view of clouds and aerosols with TROPOMI. In *EGU General Assembly Conference Abstracts*, volume 20, page 12078. 2018.

Stull, R.B. and Ahrens, C.D.: *Meteorology for Scientists and Engineers*. Earth Science Series. Brooks/Cole, 2000. ISBN 9780534372149.

Thalman, R. and Volkamer, R.: Temperature dependent absorption cross-sections of O2–O2 collision pairs between 340 and 630 nm and at atmospherically relevant pressure. *Phys. Chem. Chem. Phys.*, 15(37):15371–15381, 2013. doi:10.1039/C3CP50968K.

Theys, N., De Smedt, I., Lerot, C., et al.: TROPOMI SO2 retrievals: first results and initial validation. In *EGU General Assembly Conference Abstracts*, volume 20, page 7732. 2018.

Tilstra, L.G., Tuinder, O.N., Wang, P., et al.: Surface reflectivity climatologies from UV to NIR determined from Earth observations by GOME-2 and SCIAMACHY. *Journal of Geophysical Research*, 122(7):4084–4111, 2017. doi:10.1002/2016JD025940.

Valin, L.C., Russell, A.R., Bucsela, E.J., et al.: Observation of slant column NO2 using the super-zoom mode of AURA-OMI. *Atmospheric Measurement Techniques*, 4(9):1929–1935, 2011a. doi:10.5194/amt-4-1929-2011.

Valin, L.C., Russell, A.R., Hudman, R.C., et al.: Effects of model resolution on the interpretation of satellite NO2 observations. *Atmospheric Chemistry and Physics*, 11(22):11647–11655, 2011b. doi:10.5194/acp-11-11647-2011.

van Geffen, J., Eskes, H., Boersma, K., et al.: TROPOMI ATBD of the total and tropospheric NO2 data products. Technical report, 2019. S5P-KNMI-L2-0005-RP, issue 1.4.0.

van Geffen, J., Eskes, H., Sneep, M., et al.: TROPOMI NO2 slant column retrieval: details, uncertainties and comparisons with other satellite based NO2 data. In *EGU General Assembly Conference Abstracts*, volume 20, page 6593. 2018.

Van Weele, M., Levelt, P., Aben, I., et al.: Science Requirements Document for TROPOMI, Volume 1, KNMI & SRON. Technical report, RS-TROPOMI-KNMI-017, 2008.

Vandaele, A., Hermans, C., Simon, P., et al.: Measurements of the NO2 absorption cross-section from 42 000 cm−1 to 10 000 cm−1 (238–1000 nm) at 220 K and 294 K. *Journal of Quantitative Spectroscopy and Radiative Transfer*, 59(3-5):171–184, 1998. doi:10.1016/S0022-4073(97)00168-4.

Veefkind, J.P., Aben, I., McMullan, K., et al.: TROPOMI on the ESA Sentinel-5 Precursor: A GMES mission for global observations of the atmospheric composition for climate, air quality and ozone layer applications. *Remote Sensing of Environment*, 120(2012):70–83, 2012. doi:10.1016/j.rse.2011.09.027.

Veefkind, P., Kleipool, Q., Ludewig, A., et al.: Overview of Early Results from TROPOMI on the Copernicus Sentinel 5 Precursor. In *EGU General Assembly Conference Abstracts*, volume 20, page 12216. 2018.

Vlemmix, T., Ge, X.J., de Goeij, B.T.G., et al.: Retrieval of tropospheric NO2 columns over Berlin from high-resolution airborne observations with the spectrolite breadboard instrument. *Atmospheric Measurement Techniques Discussions*, 15(2):1–34, 2017. doi:10.5194/amt-2017-257.

Williams, J.E., Boersma, K.F., Sager, P.L., et al.: The high-resolution version of TM5-MP for optimized satellite retrievals: description and validation. *Geoscientific Model Development*, 10(2):721–750, 2017.

Zara, M., Boersma, K.F., De Smedt, I., et al.: Improved slant column density retrieval of nitrogen dioxide and formaldehyde for OMI and GOME-2A from QA4ECV: Intercomparison, uncertainty characterisation, and trends. *Atmospheric Measurement Techniques*, 11(7):4033–4058, 2018. doi:10.5194/amt-11-4033-2018.

Zeldovich, Y.A., Frank-Kamenetskii, D., and Sadovnikov, P.: *Oxidation of nitrogen in combustion.* Publishing House of the Acad of Sciences of USSR, 1947.

Zoogman, P., Liu, X., Suleiman, R.M., et al.: Tropospheric emissions: Monitoring of pollution (TEMPO). *Journal of Quantitative Spectroscopy and Radiative Transfer*, 186:17–39, 2017.